Fabrication and characterization of highly-ordered TiO$_2$-CoO, CNTs@TiO$_2$-CoO and TiO$_2$-SnO$_2$ nanotubes as novel anode materials in lithium ion batteries

Dissertation

zur Erlangung des akademischen Grades

Doktor rerum naturalium

(Dr. rer. nat.)

vorgelegt

dem Bereich Mathematik und Naturwissenschaften

der Technischen Universität Dresden

von

Mahmoud Madian, M.Sc.

geboren am 01.01.1983 in Asiut (Ägypten)

Eingereicht am 24.07.2017

Datum der Verteidigung: 18.12.2017

Die Dissertation wurde in der Zeit vom April 2013 bis Juli 2017 an der Professur für Physikalische Chemie in Kooperation mit dem Leibniz-Institut für Festkörper- und Werkstoffforschung (IFW) Dresden e. V. angefertigt.

1. Gutachter: Prof. Dr. Alexander Eychmüller

2. Gutachter: Prof. Dr. Jürgen Eckert

To my generous parents

and beloved family, Samar, Muaz and Leen

Abstract

Developed rechargeable batteries are urgently required to make more efficient use of renewable energy sources to support our modern way of life. Among all battery types, lithium batteries have attracted the most attention because of the high energy density (both gravimetric and volumetric), long cycle life, reasonable production cost and the ease of manufacturing flexible designs. Indeed, electrode material characteristics need to be improved urgently to fulfil the requirements for high performance lithium ion batteries. TiO_2-based anodes are highly promising materials for LIBs to replace carbon due to fast lithium insertion/extraction kinetics, environmentally-friendly behavior, low cost and low volume change (less than 4%) therewith, high structural stability as well as improved safety issues are obtained. Nevertheless, the low ionic and electric conductivity ($\approx 10^{-12}$ S m^{-1}) of TiO_2 represent the main challenge. In short, the present work aims at developing, optimization and construction of novel anode materials for lithium ion batteries using materials that are stable, abundant and environmentally friendly.

Herein, both of two-phase $Ti_{80}Co_{20}$ and single phase Ti-Sn alloys (with different Sn contents of 1 to 10 at.%) were used to fabricate highly ordered, vertically oriented and dimension-controlled 1D nanotubes of mixed transition metal oxides (TiO_2-CoO and TiO_2-SnO_2) *via* a straight-forward anodic oxidation step in organic electrolytes containing NH_4F. Surface morphology and current density for the initial nanotube formation are found to be dependent on the crystal structure of the alloy phases. Various characterization tools such as SEM, EDXS, TEM, XPS and Raman spectroscopy were used to characterize the grown nanotube films.

The results reveal the successful formation of mixed TiO_2-CoO and TiO_2-SnO_2 nanotubes under the selected voltage ranges. The as-formed nanotubes are amorphous and their dimensions are precisely controlled by tuning the formation voltage. The electrochemical performance of the grown nanotubes was evaluated against a Li/Li$^+$ electrode at different current densities. The results revealed that

TiO_2-CoO nanotubes prepared at 60 V exhibited the highest areal capacity of ~ 600 µAh cm^{-2} (i.e. 315 mAh g^{-1}) at a current density of 10 µA cm^{-2}. At higher current densities TiO_2-CoO nanotubes showed nearly doubled lithium ion intercalation and a coulombic efficiency of 96 % after 100 cycles compared to lower effective TiO_2 nanotubes prepared under identical conditions. To further improve the electrochemical performance of the TiO_2-CoO nanotubes, a novel ternary carbon nanotubes (CNTs)@TiO_2-CoO nanotubes composite was fabricated by a two-step synthesis method. The preparation includes an initial anodic fabrication of well-ordered TiO_2-CoO NTs from a Ti-Co alloy, followed by growing of CNTs horizontally on the top of the oxide films using a simple spray pyrolysis technique. The unique 1D structure of such a hybrid nanostructure with the inclusion of CNTs demonstrates significantly enhanced areal capacity and rate performances compared to pure TiO_2 and TiO_2-CoO NTs without CNTs tested under identical conditions. The findings reveal that CNTs provide a highly conductive network that improves Li$^+$ ion diffusivity promoting a strongly favored lithium insertion into the TiO_2-CoO NT framework, and hence results in high capacity and extremely reproducible high rate capability.

On the other hand, the results demonstrate that TiO_2-SnO_2 nanotubes prepared at 40 V on a Ti-Sn alloy with 1 at.% Sn display an average 1.4 fold increase in areal capacity with excellent cycling stability over more than 400 cycles compared to the pure TiO_2 nanotubes fabricated and tested under identical conditions.

The thesis is organized as follows:

Chapter 1: General introduction, in which the common situation of energy demand, along with the importance of lithium ion batteries in renewable energy systems and portable devices are discussed. A brief introduction to TiO_2-based anode in lithium ion batteries and the genera strategies for developing TiO_2 anodes are also presented. The scope of this thesis as well as the main tasks are summarized.

Chapter 2: The basic concepts of lithium ion batteries with an overview about their main components are discussed, including a brief information about the anode materials and the crystal structure of TiO_2 anode. A detailed review for TiO_2 nanomaterials for LIBs including the fabrication methods and the electrochemical performance of various TiO_2 nanostructures (nanoparticles, nanorods, nanoneedles, nanowires and nanotubes) as well as porousTiO_2 nanostructures is presented. The fabrication of TiO_2 nanotubes by anodic oxidation, along with the growth mechanism are highlighted. The factors affecting the electrochemical performance of anodically fabricated pure TiO_2, TiO_2/carbon composites and TiO_2-mixed with another metal oxide are reviewed.

Chapter 3: In this chapter, the synthesis of TiO_2-CoO, (CNTs)@TiO_2-CoO and TiO_2-SnO_2 nanotubes, along with the characterization techniques and the electrochemical basics and concepts are discussed.

Chapter 4: Detailed results and discussion of synthesis, characterizations and the electrochemical performance of TiO_2-CoO nanotubes and ternary (CNTs)@TiO_2/CoO nanotube composites are presented.

Chapter 5: Detailed results and discussion of synthesis, characterizations and the electrochemical performance of ternary (CNTs)@TiO_2-CoO nanotube composites are explained.

Chapter 6: Detailed results and discussion of synthesis, characterizations and the electrochemical performance of TiO_2-SnO_2 nanotubes are presented.

Chapter 7: Summarizes the results presented in this work finishing with realistic conclusions, and highlights interesting work for the future.

Zusammenfassung

Um die zur Aufrechterhaltung unserer modernen Lebensweise unabdingbaren erneuerbaren Energiequellen effizient nutzen zu können, werden hochentwickelte wiederaufladbare Batterien dringend benötigt. Lithium-Ionenbatterien gelten aufgrund ihrer hohen Energiedichte (sowohl gravimetrisch als auch volumetrisch), ihrer langen Lebensdauer, moderater Produktionskosten und aufgrund der Möglichkeit, vielfältige Konzepte einfach herstellen zu können, als vielversprechend. Dennoch müssen die Elektrodenmaterialien dringend verbessert werden, um den Ansprüchen an zukünftige hochentwickelte Lithium-Ionenbatterien gerecht zu werden. TiO_2-basierte Anoden gelten aufgrund ihrer schnellen Lade- und Entladekinetik, ihres umweltfreundlichen Verhaltens und niedriger Kosten als aussichtsreiche Alternativen zu Kohlenstoffen. Durch die geringe Volumenänderung beim Lithiumeinbau (unter 4%) werden außerdem eine hohe strukturelle Stabilität und erhöhte Sicherheit gewährleistet. Die hauptsächlichen Herausforderungen stellen die niedrige ionische und elektrische Leitfähigkeit ($\approx 10^{-12}$ S m^{-1}) von TiO_2 dar. Zusammengefasst liegt das Ziel der vorliegenden Arbeit in der Entwicklung, Optimierung und Herstellung neuartiger Anodenmaterialien für Lithium-Ionenbatterien unter Verwendung stabiler, verfügbarer und umweltfreundlicher Materialien.

In dieser Arbeit wurden sowohl zweiphasiges $Ti_{80}Co_{20}$ und einphasige Ti-Sn-Legierungen (mit verschiedenen Sn-Gehalten zwischen 1 und 10 at-%) zur Herstellung hochgeordneter, vertikal orientierter eindimensionaler Nanoröhren aus gemischten Übergangsmetalloxiden (TiO_2–CoO und TiO_2–SnO_2) mittels anodischer Oxidation in NH_4F-haltigen organischen Elektrolyten genutzt. Dabei wurden Abhängigkeiten der Oberflächenmorphologie und der Stromdichte für die Bildung der Nanoröhren von der Kristallstruktur der zugrundeliegenden Legierung beobachtet. Vielfältige Methoden wie REM, EDXS, TEM, XPS und Ramanspektroskopie wurden genutzt, um die Nanoröhren zu charakterisieren. Die Ergebnisse zeigen, dass gemischte TiO_2-CoO und TiO_2-SnO_2 Nanoröhren in den

gewählten Spannungsfenstern erfolgreich gebildet werden konnten. Die so hergestellten Nanoröhren sind amorph und in ihren Dimensionen präzise durch die Wahl der Spannung einstellbar. Eine elektrochemische Beurteilung der Nanoröhren erfolgte durch Tests gegen eine Li/Li$^+$-Elektrode bei veschiedenen Stromdichten. Die Resultate zeigen, dass TiO$_2$-CoO-Nanoröhren, welche bei 60 V hergestellt wurden, die höchsten Flächenkapazitäten von ~ 600 μAh cm^{-2} (d.h. 315 mAh g^{-1}) bei einer Stromdichte von 10 μA cm^{-2} aufweisen. Bei höheren Stromdichten zeigen TiO$_2$-CoO-Nanoröhren nahezu verdoppelte Lithiuminterkalation und eine Coulomb-Effizienz von 96 % nach 100 Zyklen, verglichen mit weniger effektiven TiO$_2$–Nanoröhren, welche unter identischen Bedingungen hergestellt wurden. Um die elektrochemischen Eigenschaften der TiO$_2$-CoO-Nanoröhren weiter zu verbessern, wurde ein neuer Komposit aus Kohlenstoff-Nanoröhren und TiO$_2$-CoO-Nanoröhren ((CNT)s@TiO$_2$/CoO) durch eine zweistufige Synthese hergestellt. Die Herstellung beinhaltet zunächst die anodische Bildung geordneter TiO$_2$/CoO-Nanoröhren, ausgehend von einer Ti-Co-Legierung, gefolgt von einem horizontalen Kohlenstoff-Nanoröhren-Wachstum auf dem Oxid mittels einer simplen Sprühpyrolyse. Die einzigartige 1D-Struktur einer solchen hybriden Nanostruktur mit eingebundenen CNTs zeigt deutlich erhöhte Flächenkapazitäten und Belastbarkeiten im Vergleich zu Nanoröhren aus TiO$_2$ und TiO$_2$/CoO-Nanoröhren ohne CNTs, die unter identischen Bedingungen getestet wurden. Die Ergebnisse zeigen, dass die CNTs ein hochleitfähiges Netzwerk bilden, welches die Diffusion von Lithium-Ionen und deren Einbau in die TiO$_2$/CoO-Nanoröhren begünstigt und somit hohe Kapazitäten und reproduzierbare hohe Belastbarkeiten bewirkt.

Außerdem zeigen die Resultate, dass TiO$_2$-SnO$_2$ Nanoröhren, welche bei 40 V auf einer Ti-Sn-Legierung mit 1 at.% Sn hergestellt wurden, im Mittel eine 1,4-fache Erhöhung der Flächenkapazität und eine exzellente Zyklenstabilität über mehr als 400 Zyklen, verglichen mit unter identischen Konditionen hergestellten und getesteten TiO$_2$-Nanoröhren, zeigen.

Die Arbeit ist wie folgt organisiert:

Kapitel 1: Allgemeine Einführung, in der die Energienachfrage und die Bedeutung von Lithium-Ionenbatterien in erneuerbaren Energiesystemen und tragbaren Geräten diskutiert wird. Eine kurze Einleitung zu TiO_2-basierten Anoden in Lithium-Ionenbatterien und allgemeine Strategien zur Entwicklung von TiO_2-Anoden werden ebenfalls gezeigt. Das Ziel der Arbeit und hauptsächliche Aufgaben werden zusammengefasst.

Kapitel 2: Das grundlegende Konzept der Lithium-Ionenbatterie mit einem Überblick über ihre Hauptkomponenten wird diskutiert. Dies beinhaltet auch eine kurze Darstellung der Anodenmaterialien und der Kristallstruktur von TiO_2-Anoden. Eine detaillierte Übersicht über TiO_2-Nanomaterialien für LIB, welche Herstellungsmethoden und die elektrochemische Performance verschiedener TiO_2-Nanostrukturen (Nanopartikel, Nanostäbe, Nanonadeln, Nanodrähte und Nanoröhren) und poröser TiO_2-Nanostrukturen beinhaltet, wird gezeigt. Die Bildung von TiO_2-Nanoröhren durch anodische Oxidation und der Wachstumsmechanismus werden hervorgehoben. Faktoren, welche die elektrochemische Performance anodisch hergestellter TiO_2-Materialien, TiO_2/Kohlenstoff-Komposite und TiO_2 als Gemisch mit anderen Metalloxiden beeinflussen, werden diskutiert.

Kapitel 3: In diesem Kapitel werden die Synthese von TiO_2-CoO, (CNTs)@TiO_2/CoO und TiO_2-SnO_2-Nanoröhren, die Charakterisierungsmethoden, elektrochemische Grundlagen und Konzepte diskutiert.

Kapitel 4: Detaillierte Resultate und die Diskussion der Synthese, Charakterisierung und der elektrochemischen Performance der TiO_2-CoO-Nanoröhren und der ternären (CNTs)@TiO_2/CoO-Nanoröhrenkomposite werden gezeigt.

Kapitel 5: Detaillierte Resultate und die Diskussion der Synthese, Charakterisierung und der elektrochemischen Performance der der ternären (CNTs)@TiO$_2$/CoO-Nanoröhrenkomposite werden diskutiert.

Kapitel 6: Detaillierte Resultate und die Diskussion der Synthese, Charakterisierung und der elektrochemischen Performance von TiO$_2$-SnO$_2$-Nanoröhren werden gezeigt.

Kapitel 7: Eine Zusammenfassung der Resultate, die in dieser Arbeit gezeigt wurden und Schlussfolgerungen, sowie interessante Ansatzpunkte für zukünftige Arbeiten werden präsentiert.

Contents

Chapter 1

Introduction and scope of the thesis

1.1 Batteries for renewable energy systems and portable devices

The need for green energy becomes an obvious fact to meet the growing humankind's demand of energy which expected to be doubled by 2050 [1,2]. Particularly, the current supply of fossil fuel is limited, in addition to its negative impact on the environment. Among all energy forms, electricity represents the main usable energy form in our everyday life. This fact in turn has created a great interest to generate electricity from environmentally-friendly and renewable sources, such as

solar and wind. Europe has set a target of 20% of the total electricity should be generated from renewable sources by 2020 [3]. Although an intensive research has been conducted in solar and wind areas. However, further improvements are still needed to maximize the electricity production. This necessity is due to the fact that, only 12% of the total electricity is generated from such sources. One of the main requirements for developing energy conversion plants and smart grids for power distribution is an efficient electricity storage system. This storage system is a vital issue, as the electricity generation is a weather dependent process and mitigation of the output is required, especially when the production exceeds the consumption at a given time. The stored energy will be used later when required. Photovoltaic (PV) systems usually compatible with grid-tie systems with "net metering" in the developed countries to support the electricity production. These plants usually work without battery systems as the electricity directly transformed through the grid using smart controllers. In addition, the every day's use of portable devices such as cameras, laptops, tablets, music players and mobile phones are well-established in order to suit our modern life. The portable devices are not only important for the healthy persons but they also represent an urgent need especially for the handicapped or disabled people to power particular portable medical devices. Nowadays, there is a similar strong desire to replace the current gasoline vehicles with hybrid or electric powered vehicles (EVs) to reduce the adverse effect of the emitted gases, such as carbon oxides on the environment which have a great impact on the global warming. One of the most obstacles for the development of electric vehicles and their market is the availability of high performance rechargeable batteries. Therefore, production of efficient and low cost Li-ion batteries is crucial for commercializing electric vehicles. In short, efficient and cost-effective rechargeable lithium ion batteries are strongly needed.

Lithium ion batteries indisputably become the first choice as primary power sources for portable devices and electric vehicles. They offer valuable properties, *i.e.* long cycle life, high energy density, reasonable production cost and the ease of

manufacturing flexible designs. These properties are the main reasons behind populating lithium ion batteries as the main part in portable devices, in addition to play a central role in the miniaturization of electronics and medical devices. Indeed, developing anode materials for lithium ion batteries with higher performance and competitive price is still the main hurdle to reduce weight and improve performance of LIBs.

1.2   TiO₂-based anode in lithium ion batteries

TiO₂-based anodes are alternative anode materials to overcome the graphite problems due to their high structural stability. This is referred to their low volume change during cycling ($\approx 4\%$), excellent capacity retention and fast kinetics for lithium intercalation/extraction [4]. Furthermore, lithium dendrite and solid electrolyte interface (SEI) formation is unlikely due to the higher delithiation potential (1.7 V *vs.* Li/Li$^+$) turning TiO$_2$ into a safe operating anode material. On top of that, they are highly abundant, nontoxic and obtained at reasonable production costs [5]. These properties are not only essentially required for employing lithium ion batteries (LIBs) in EVs, but also for stationary energy storage. Nevertheless, the low theoretical capacity of TiO$_2$ (335 mAh g^{-1}) and the poor ionic and electric conductivity are the main obstacles hindering the production of high-performance LIBs from titania [4,6,7].

1.3   Strategies for developing TiO₂ anodes

Up-to-date, research focuses on two strategies in order to improve the lithium ion diffusion into TiO$_2$ anodes. The first strategy aims at reducing their size down to the nanoscale by fabrication of various nanostructures, *i.e.* nanoparticles, nanobelts, nanotubes and hierarchical tubular structures [8–10]. Among the different reported nanostructures, anodically fabricated TiO$_2$ nanotubes show a good electrochemical

performance. This behavior is ascribed to their well-ordered nature, perfect alignment and high surface area [11]. Such properties are highly required to increase the electrode/electrolyte contact and reduce the lithium ion diffusion pathway [12]. The second strategy is to improve the ionic conductivity and therewith enhancing the electrochemical performance of TiO_2-based anodes. This property is achieved by coating or doping them with other relatively more conductive materials, e.g. graphene and carbon nanotubes (CNTs) [13,14]. However, these strategies have shown a relative success to overcome the low conductivity of TiO_2. But the reported reversible capacity is still far away from the theoretical capacity. Mixing TiO_2 with other transition metal oxides with higher conductivity and theoretical capacity is another approach. This approach is expected to bundle the advantages of both materials resulting in an improvement of the ionic conductivity as well as the reversible capacity. Various mixed oxide nanotubes have been synthesized by coating or electrodeposition techniques, for instance, TiO_2 with Co_3O_4 and NiO coatings [15,16]. Both TiO_2 deposited coaxially onto SnO_2 nanotubes and MoO_3 deposited onto $TiO_{2,}$ have been investigated as anode materials and showed higher lithium insertion [17,18]. The main problem for metal oxide coatings on TiO_2 nanotubes is that Li^+ ions migrate slowly into the metal oxide nanoparticles that cover the nanotube surface [18]. Alternatively, the fabrication of mixed oxide nanotubes by anodic oxidation of Ti-based alloys is even more promising, as it bundles the advantage to form different metal oxides from one starting material. To this end, various binary and ternary Ti-based systems have recently been explored regarding the formation of mixed oxide nanotubes. Such mixed oxide nanotubes were shown to have a respected potential for applications, for example, oxide nanotubes obtained from Ti-V [19], Ti-Ni [20], Ti-Fe [21], Ti-Mo-Ni [22] and Ti-6Al-4V [23] alloys were implemented in rechargeable batteries, supercapacitors, solar hydrogen production systems.

In this regard, Ti-Co-O and Ti-Sn-O systems are very promising candidates to significantly contribute to the physicochemical properties, such as the relatively high electric and ionic conductivity of both SnO_2 and CoO compared to those of TiO_2 [24–

28]. This protocol is expected to improve the ionic conductivity and the reversible capacity of the mixed oxide anodes. Such systems represent an ideal solution to obtain an anode material of unique structural stability and good electronic properties resulting in an excellent electrochemical performance.

1.4   Scope of work

The proposed work aims at developing, optimization and construction of lithium ion batteries using materials that are stable, abundant and environmentally friendly. In details, the possibility to fabricate self-organized Ti-Co-O and Ti-Sn-O nanotubes on current collectors of Ti-Co and Ti-Sn alloys and study the effect of mixed oxides on the lithium ion storage for TiO_2 nanotubes was investigated. 1D architectures are known to overcome the pulverization or the structure collapse resulting from the large volume changes during Li^+ ion insertion/extraction[12]. The resulting nanotubes will be used as anode materials in lithium ion batteries. Moreover, overlapping each of CoO and SnO_2 with TiO_2 nanotubes in an excellent texture will overcome the structural instability and the resistivity, which may result from other synthesis techniques. The ability to precisely tune the tube dimensions will maximize the contact area between the electrode material and the electrolyte. Consequently, the diffusion distance of Li^+ ions across the electrode is shortened and high electrochemical performance will be achieved. In addition, using the as-grown nanotubes as binder and additive-free electrodes will add a unique advantage to save the extra costs during battery manufacturing. Furthermore, utilizing Ti-Co and Ti-Sn substrates as current collector will result in a particularly good contact between active material and current collector. To the best of our knowledge, no reports have discussed the use of Ti-Co and Ti-Sn alloys to grow TiO_2-CoO and TiO_2-SnO_2 nanotubes, respectively by anodic oxidation. With respect to Ti-Co-O system, Co_3O_4-coated TiO_2 nanotube composites have been formed *via* a two-step method and enhance the conductivity of TiO_2 which therefore improved the lithium storage performance[15]. Furthermore, a different strategy is proposed to realize deposition

of CNTs on anodically fabricated TiO_2-CoO NTs using a simple spray pyrolysis technique. CNTs function as conductive networks that connect TiO_2 nanotubes from the opposite side of the current collector allowing for better electrical and ionic conductivities, paving the way for superior lithium ion insertion with excellent rate performance. Regarding the Ti-Sn-O system, SnO_2 is chosen. It is characterized as n-type semiconductor with superior electronic properties and high theoretical capacity (781 mAh g^{-1}) [29]. Jeun *et al.* [30] reported the fabrication of double-shell SnO_2@TiO_2 nanotubes by atomic layer deposition (ALD) using polyacrylonitrile (PAN) nanofibers as templates. Such nanotubes showed improved electrochemical performance when utilized as anode material in lithium ion batteries. Only a recent study reported the growth of TiO_2-SnO_2 nanotubes on a Ti substrate for the application of solar hydrogen production *via* a two-steps synthesis route. In this attempt, Sn layers were sputtered [31]. SnO_2 nanotubes themselves were fabricated on titanium substrates using ZnO nanowire arrays as sacrificial templates for the application of lithium ion batteries [32]. Despite several attempts that have been explored to prepare self-ordered SnO_2 nanotubes from pure Sn substrates by anodic oxidation, only mesoporous morphologies without well-defined tubular structures were formed [33]. The results presented here are not only important for research on electrochemical energy storage materials but can also be interdisciplinarily used in solar cells, water splitting and photocatalysis.

1.5 Tasks

1. Synthesis of Ti-Co and Ti-Sn alloys with various atomic compositions

Discs of $Ti_{80}Co_{20}$ and Ti-Sn_x (x = 1, 5 and 10 at.%) alloys have to be prepared by an arc-melting technique and will be used as starting materials to fabricate mixed TiO_2-CoO and TiO_2-SnO_2 nanotubes with different compositions. Their composition will be controlled by XRD and a wet-chemical analysis by ICP-OES. In addition, the alloy substrates before the anodization are also explored using SEM and EDX.

2. Fabrication of vertically oriented and highly ordered mixed oxide nanotube arrays.

Self-organized mixed TiO_2-CoO and TiO_2-SnO_2 nanotube arrays will be grown on the surface of $Ti_{80}Co_{20}$ and Ti-Sn alloys with various tin concentrations (1 - 10 at.%), respectively, *via* a single anodic oxidation step. By tuning the applied voltage and the anodic oxidation electrolytes, the nanotube morphologies and surface areas could be controlled. The resulting highly ordered 1D nanotubes of Ti-Co-O and Ti-Sn-O mixed oxides will be tested and evaluated as anode materials in lithium ion batteries instead of the random network of nanowires and nanotubes. These combinations of metals are purposely chosen as they exhibited enhanced electrochemical performance compared to pure TiO_2 NTs. The formation of ordered mixed metal oxide nanotubes from Ti-based alloys by single and simple anodic oxidation step is more attractive and expected to demonstrate perfect intercalation properties for Li^+ ions are expected to be demonstrated.

3. Characterization of the grown mixed oxide nanotube arrays

Variable characterization tools will be used to investigate the fabricated mixed oxide nanotube arrays in order to optimize morphological appearances, such as tubes length and diameters. The structures, crystallinity and the surface areas of the present phases are also investigated. These tools include X-ray diffraction (XRD), scanning electron microscopy (SEM), energy-dispersive X-ray spectroscopy (EDXs), transmission electron microscopy (TEM), X-ray photoelectron spectroscopy (XPS), Raman scattering spectroscopy and nitrogen adsorption isotherms.

4. Fabrication of (CNTs)@TiO_2/CoO nanotubes

Ternary carbon nanotubes (CNTs)@TiO_2-CoO nanotubes composite will be fabricated by a two-step synthesis method. The preparation includes an initial anodic fabrication of well-ordered TiO_2-CoO NTs from a Ti-Co alloy, followed by growing of CNTs horizontally on the top of the oxide films using a simple spray pyrolysis

technique. The as-fabricated ternary composite will be directly used as binder- and additive-free electrode and tested for lithium ion insertion.

5. Electrode preparation, battery assembly and testing

The grown oxide nanotubes are used directly as electrodes without adding binders or conductive additives. The battery will be assembled as Swagelok cells. The prepared cells will be tested by typical electrochemical methods, like cyclic voltammetry, galvanostatic cycling with potential limitation and impedance spectroscopy.

6. Investigation the electrode stability after cycling

The morphological changes after electrochemical cycling will be explored using SEM. In addition, TEM will be used to investigate the stability of tubular structures over Li^+ ion insertion/extraction cycles.

Chapter 2

Basics and literature review

2.1   Lithium ion battery system

Generally, a lithium ion battery is a device able to convert chemical energy to electric energy, and vice versa, through electrochemical reactions (oxidation/reduction) between the active materials (anode/cathode) that have a potential difference in presence of an electrolyte. Mainly, a lithium ion battery is composed of three main components: two electrodes with different electrical potential, and a separator, which electrically isolates the electrodes from each other and allows the Li^+ ions to migrate between the electrodes. The electrolyte is mainly the liquid

negotiating medium between the electrodes allowing the migration of Li^+ ions while the separator is completely soaked with the liquid to also avoid being a Li^+ ion barrier.
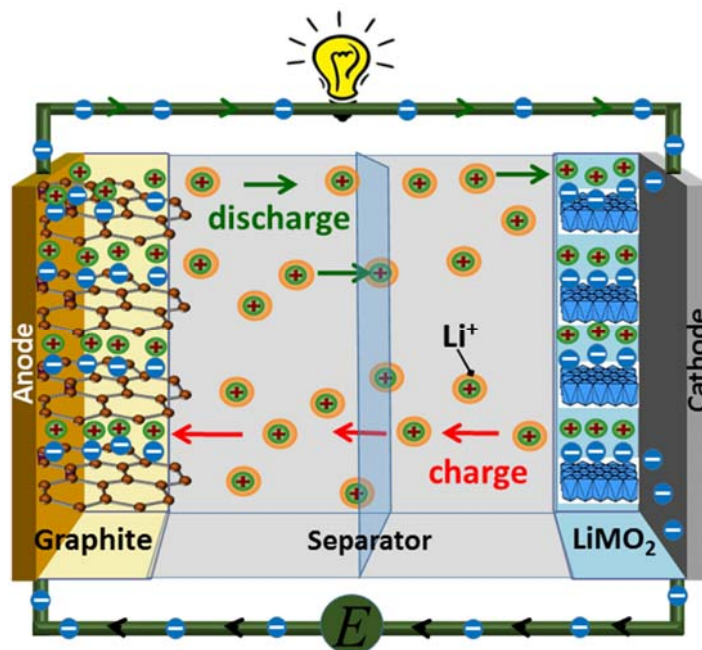
Fig. 2.1. *Schematic of the operation principles for rechargeable lithium ion batteries.*

In commercial cells the negative electrode (anode) composed of intercalation compounds that can host lithium ions *i.e.* carbonaceous materials. The positive electrode (cathode) consists of other intercalation materials that have more positive redox potential such as transition-metal oxide/chalcogenide e.g., MnO_2, TiS_2, $NiPS_3$, or MoS_2 and lithium transition metal oxide e.g., $LiMO_2$, M = Co, Ni, Mn or lithium transition metal phosphates e.g., $LiFePO_4$ [34]. The electrolyte is commonly a solution containing lithium salt (i.e. $LiPF_6$) and mixed with liquid alkyl carbonates [34]. The electrochemical reactions of the electrodes undergo a process, in which Li^+ ions are transported between the cathode and the anode (see **Fig. 2.1**), and accordingly these processes are called "rocking-chair" reactions [35]. During discharge, Li^+ ions de-intercalate from the anode material and the ions are transported through the electrolyte to intercalate the cathode, which also acts as electron acceptor [36]. Accordingly, the electrons are shuttled through the external circuit providing the current flow.
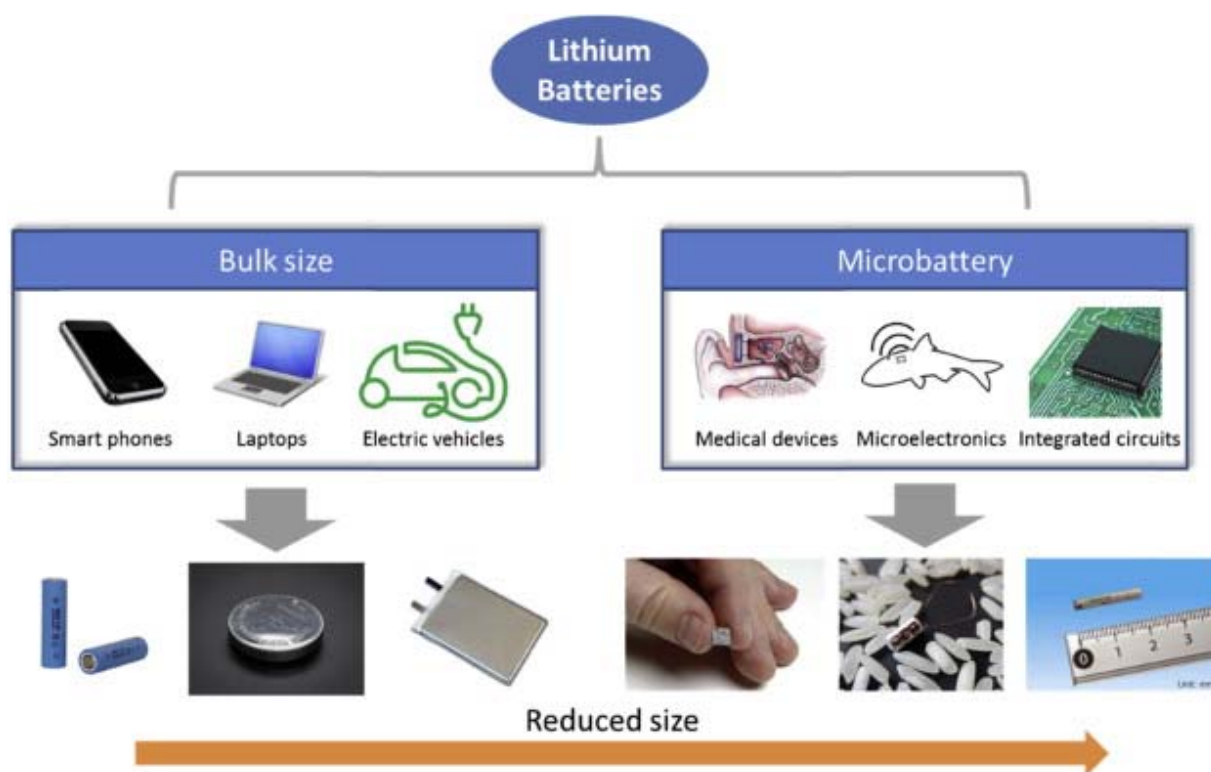
Fig. 2.2. *Flexible size and designs for lithium ion batteries adapted with permission from ref.* [37].

This process is thermodynamically favorable due to reduction the cathode materials in which they spontaneously convert from high to a thermodynamically more stable low valance. On charge, Li$^+$ ions de-intercalate in reverse from the cathode to intercalate the negative electrode (anode), which acts as electron donor [38]. This oxidation requires an external trigger allows a reaction of the anode material   to its previous state. **Figure 2.2** presents a variety of sizes and designs of lithium ion batteries according to their application [37]. **Table (2.1)** shows the superiority of lithium ion batteries over other commercial battery systems explained by specific capacity (W h/kg) and energy density (W h/L) [39]. Although Li-based batteries have received extensive attention at both fundamental and applied research, since further improvement in their electrochemical performance is still required, which is hindered by some restrictions in the electrode materials. The electrode materials represent the most important part for development as they

mainly determine the efficiency of batteries. To construct high performance lithium ion batteries, the electrode materials should meet the following requirements: (1) high surface area and large pore size, as they are important to provide large exposed surface and more channels for lithium ion insertion. This results in short paths and faster diffusion rates for lithium ions. This plays a crucial role to improve the rate of capability. (2) Low volume expansion/shrinkage during lithium insertion/extraction to avoid the cracking and miss-contact between the current collector and the electrode materials and increase the cycling stability. (3) High ionic and electric conductivity which is required to achieve fast charging and discharging as well as facilitating Li^+ ion insertion. (4) Abundant (5) Low production cost. (6) Environmentally friendly.

Table 2.1. Specific energy and energy densities of commercial rechargeable batteries [39].

Rechargeable battery	Specific energy, W h/kg	Energy density, W h/L
Pb–acid	30	80
Ni–Cd	40	90
Ni–MH	55	165
Ni–Zn	70	145
Ag–Zn	75	200
Li ion	265	690

2.2   Anode materials

Lithium is the lightest metal (density of 0.534 g/cm^3) in comparison with others [40]. It has a high electrochemical potential -3.0 V *vs.* standard hydrogen electrode and a high theoretical capacity up to 3860 mAh/g. Lithium metal has been employed as active anode materials in primary batteries for longer time. The situation in secondary batteries with metallic lithium anodes is quite critical because lithium causes serious safety problems in addition to the low cycling stability which is mainly attributed to the formation of lithium dendrites on the anode surface. Therefore,

replacement of metallic lithium with another insertion material was a vital key factor for developing rechargeable lithium ion batteries. In the early 1991, Sony has introduced the first lithium ion battery to the market in which graphite was used as active anode material, owing to its abundance, reasonable production cost and reasonable theoretical capacity (372 mAh/g). This important event has aroused the attention of many researchers and urged them to do an extensive work to improve the performance of lithium ion batteries. However, using graphite as anode material is accompanied with several drawbacks. It suffers from severe structure collapse and cracking over cycling that originally starts with the formation of solid electrolyte interface (SEI) followed by rapid capacity fading. The low operating voltage of ~ 0.1 V *vs.* Li/Li$^+$ represents another problem [6,40]. Such a low potential allows for lithium electroplating at the electrode surface which requires implementing of extra materials in the sense of carbon or other materials for safety issues [41]. At a high charge/discharge current rate, lithium dendrites can easily be formed on the graphite surface due to its high polarization. Such dendrites can move through the separator resulting in an internal short circuit, cell damaging and warming up until fire (thermal runaway) [42]. Moreover, using of a graphite-based anode is particularly restricted to low temperatures [41]. As the HEVs, EVs are usually charged/discharged at high current rates in a wide temperature range (- 30 - 60 °C), where using of graphite is not suitable and does not meet the EVs requirements. Therefore, replacing graphite with another material becomes an urgent need. A variety of materials are proposed as promising candidates for the negative electrode in lithium ion batteries including lithium-metal alloys (Li$_x$M where, M = Sn[43], Al [44], Ga [45], Ge [46], Pb [47], Sb [48], etc.), silicon-based materials (Si nanostructures, Si/C [49], Cu-Si-Al$_2$O$_3$ [50], Ni$_3$Si$_2$/Si [51], etc.), layered metal dichalcogenides (MS$_2$, M = Mo, W, Ga, Nb and Ta) and transition metal oxides (MO, M = Ti, Sn, etc.) [52]. In this following sections, detailed information about the TiO$_x$-based anodes will be discussed, as they represent the main focus of this thesis.

2.3   Crystal structure of TiO$_2$

TiO$_2$ has eight known polymorphs; rutile, anatase, brookite, TiO$_2$-B, TiO$_2$-R, TiO$_2$-H, TiO$_2$-II, TiO$_2$-III [53]. Among them rutile, anatase and TiO$_2$-B are intensively reported as anode materials for lithium ion batteries during the last decades. Rutile is the thermodynamically most stable phase while anatase and TiO$_2$-B have a metastable nature [54]. However, previous studies showed that nanosized anatase (below 20 nm) becomes the most thermodynamically stable [55]. At high temperature anatase undergoes a phase transformation to rutile [56]. The electrochemical lithiation/delithiation of TiO$_2$ polymorphs are described by equation no. 2.1 [57].

$$x\text{Li}^+ + \text{TiO}_2 + x\text{e}^- \leftrightarrow \text{Li}_x\text{TiO}_2 \tag{2.1}$$

Where x is the mole fraction of Li in TiO$_2$ and $0 \leq x \leq 1$, depending on the crystallinity, particle size, morphology, surface area and their polymorphs. For instance, negligible amounts of Li$^+$ ions (0.1 Li atoms per Ti atom) are inserted by the rutile structure at room temperature owing to a Li$^+$ ion diffusion into rutile which is thermodynamically favorable only along the c-axis channels instead of ab-planes [56,57].

The crystal structures of rutile, anatase and TiO$_2$-B are shown in **Figure 2.3**. Rutile crystallizes in a tetragonal symmetry with the space group $P4_2/mnm$ with TiO$_6$ octahedra sharing edges along c-direction while the corners are located along the ab-planes [58]. A slight orthorhombic distortion is found for the TiO$_6$ octahedra [59]. During intercalation, Li$^+$ ions have to move into the tetrahedral sites that neighbor to ab-planes. This explains the difficulty of Li$^+$ ions to reach the TiO$_6$ octahedral sites [60]. Therefore, the diffusion coefficient through the c-direction is 10^{-6} cm^2 s^{-1} which is much larger than that of ab-planes (10^{-14} cm^2 s^{-1}) [61–63]. With time, Li$^+$ ions insertion into bulk rutile structure is prohibited due to the repulsion forces among lithium ions and small capacity can obtained.
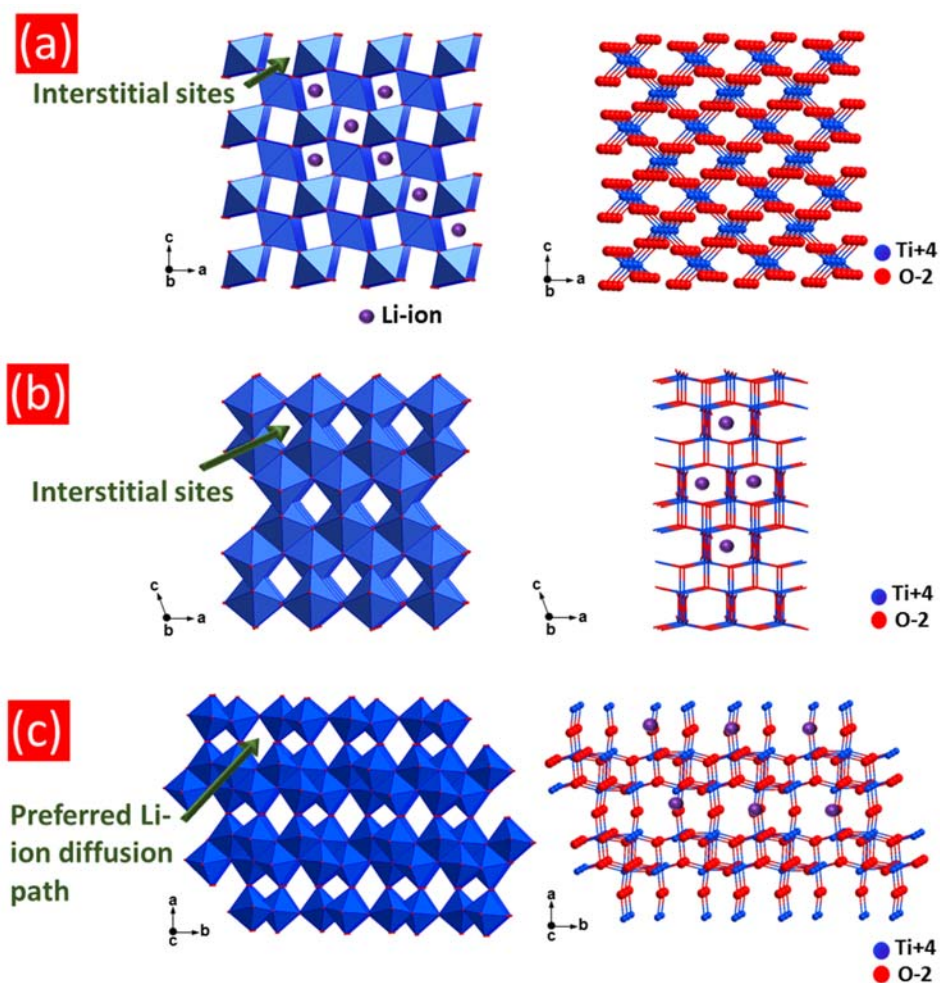
Fig. 2.3. *Structure of rutile (a), anatase (b) and TiO₂(B) (c) drown with Diamond software; the arrows point to the interstitial sites that can host lithium ions into each structures.*

TiO_2-B has monoclinic *C2m* crystal and its structure contains corrugated sheets of edge-end corner sharing TiO_6 [65]. A distorted square based pyramid is noticed in its structure instead of octahedron due to some Ti-O bonds (2.20 - 2.25 Å), which are larger than the Ti-O bonds in both anatase (1.937 - 1.966 Å) and rutile (1.946 - 1.983 Å) [61,65]. The open structure of TiO_2-B provides one dimensional infinite channels which can accommodate the volume changes during lithium ion insertion without lattice deformation [66]. Pseudocapacitive behavior was also

reported for TiO$_2$-B, which results in a faster diffusion rate during charging/discharging [67].

Anatase has a tetragonal structure $I4_1/amd,$ in which distorted edge-sharing TiO$_6$ octahedra are in a stacking of one dimensional zigzag chains [61,65]. The empty TiO$_6$ zigzag channels represent diffusion paths for Li$^+$ ions intercalation. Usually, a phase transition in the tetragonal anatase phase takes place due to the strong Li-Li repulsive forces resulting in an orthorhombic distortion[6,59]. Owing to the Li$^+$ ions insertion into anatase exceeds Li$_{0.05}$TiO$_2$, the changes occurred in its unit cell usually resulting in decreasing the c-axis and increasing the b-axis. The total volume changes from lithium ion insertion is less than 4% [59,68].

2.4   TiO$_2$ nanomaterials for LIBs

The reported reversible capacity of bulk TiO$_2$ is only 180 mAh g^{-1} i.e. half of its theoretical capacity [69,70]. Further Li$^+$ ion storage into TiO$_2$ framework is restrained because of the strong repulsive forces among the Li ions. Basically the lithium ion insertion/extraction in TiO$_2$ materials is a diffusion controlled process which depend on the diffusion coefficient and the diffusion length of TiO$_2$ [6,62]. The diffusion coefficient is determined by the nature of the materials and the diffusion length depends on the particle size of TiO$_2$. Therefore, several approaches have been developed to synthesize various TiO$_2$ nanostructures such as nanoparticles, nanotubes and nanowires of pure titania or as composites with other materials [70].

2.4.1 TiO$_2$ nanoparticles

TiO$_2$ nanoparticles have been approved as effective anode materials in LIBs. The particle size of TiO$_2$ represents the key factor, which defines its reversible capacity and the rate performances. When the particle size decreases to nanometer ranges, the surface area increases in consequence and the lithium ion diffusion path will be shortened resulting in an improved Li$^+$ ion insertion capacity. Wagemaker *et*

al. [71] conducted a comparative study among TiO_2 nanoparticles with different particle sizes (7 - 40 nm) to explore the impact of particle sizes on the insertion reactions. They found a dramatically increase of Li capacity and Li-ion solubility with decreasing sizes of the TiO_2 nanoparticles. Moreover, the small particle sizes improve the rate capability of the electrodes. **Figure 2.4a** schematically explains that anatase microparticles can accommodate only up to half a mole of Li^+ ions while the nanosized particles can deliverer up to one mole of Li^+ ions per mole TiO_2 [71].
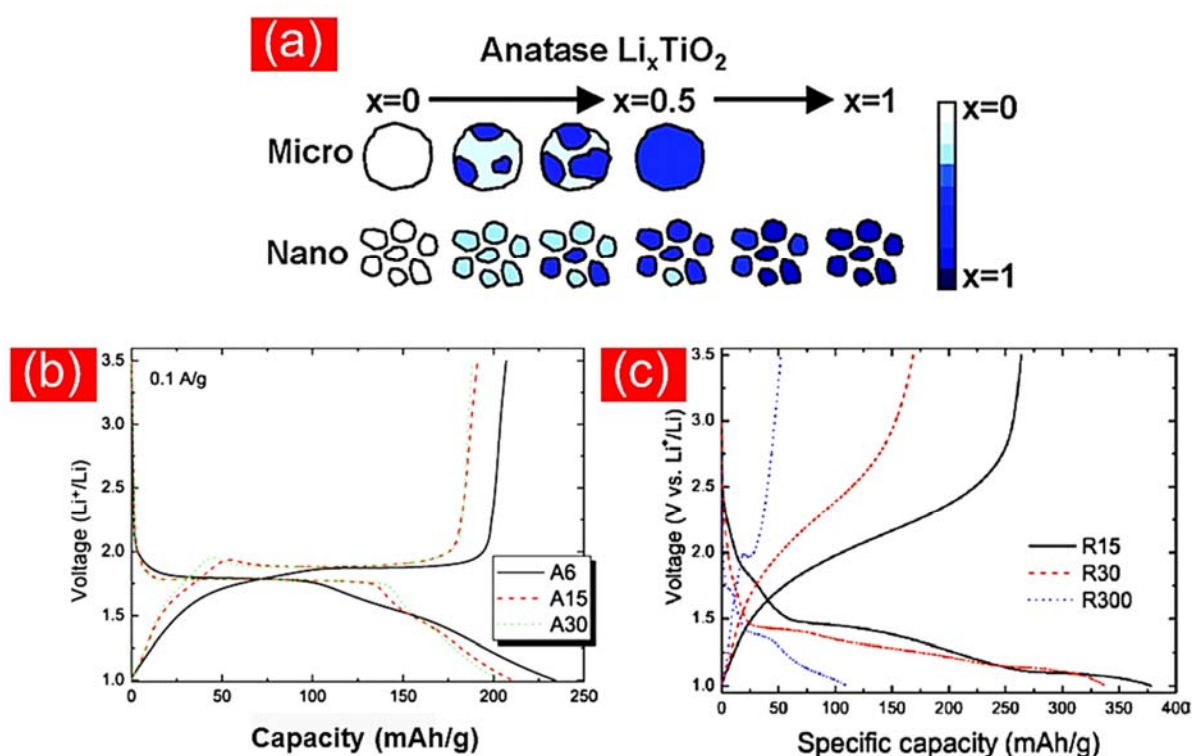
Fig. 2.4. *Schematic of the impact of particle sizes on the insertion capacity of anatase TiO_2 (a) reprinted from ref.* [71]*; Voltage profile of anatase nanoparticles with 6 (A6), 15 (A15) and 30 (A30) nm in diameter (b)* [72]*; The initial capacity profiles of rutile nanoparticles with 15 (R15), 30 (R30) and 300 (R300) nm in diameter (c)* [73]*.*

This behavior has been confirmed in another study, in which very fine anatase particles with an average size of 6 nm and a specific surface area of 258 m^2 g^{-1} showed a higher specific capacity in comparison with particles of 15 and 30 nm in diameter and specific areas of 83 and 57 m^2 g^{-1}, respectively, as shown in **Figure 2.4b**. Beside

that the rate capability was also increased by decreasing the particle size [72]. Size-dependent performance of rutile nanoparticles was investigated by Jiang *et al* [73]. The highest initial capacity of about 378 mAh g^{-1} is demonstrated for rutile with a particle size of 15 nm (**Fig. 2.4c**) at 0.05 A/g. A capacity of 207 mAh g^{-1} was retained by that electrode after 20 discharging cycles.

Theoretical modeling studies have been performed by Sushko *et al.* [74] to investigate the relation between particle size and ionic conductivity of TiO$_2$. These studies demonstrated that the ionic conductivity can be remarkably improved if the particle size of TiO$_2$ is below 20 nm due to the higher charge transport of Li$^+$ ions and electron accumulation at the nanoparticle boundaries. In contrast, when the nanoparticles are larger than 20 nm, the charge separation is dominant, hence, lower ionic conductivity is obtained [74]. Controlling the TiO$_2$ morphology in terms of particle size and surface area was studied through different synthesis techniques such as sol-gel and solvothermal methods. For instance, Kubiak *et al.* [75] used sol-gel and miniemulsion techniques to produce mesoporous TiO$_2$ with different particle sizes (9 - 12 nm) and pore diameters (7 - 15 nm). The electrochemical tests showed the lithium insertion capacity is dramatically improved by the high surface area and the small particle sizes [75]. The authors also found that there is a relation between the particle size and pseudocapacitive effect, where double layer capacity and pseudocapacitity are also increased by reducing the particle size. Nanocrystalline anatase with an average particle size of 5 nm displayed enhanced Li$^+$ ion storage capacity compared to the 10 nm size. In addition, faster charging and discharging rates were observed for these nanoparticles owing to the Faradic reactions, which occur at the electrode surface and control the whole insertion reactions. Similar improvement in the electrochemical performance of anatase nanoparticles, prepared by a sol-gel method followed by a hydrothermal treatment, with average sizes of 8 nm was reported by Wilhelm *et al.* [76]. The prepared nanoparticles can deliver 140 mAh g^{-1}. The solvothermal method was used to fabricate anatase nanoparticles anodes.

The electrochemical evaluation tests for the electrode showed a reversible capacity of 196 mAh g^{-1}, which is sustained over 100 cycles at a current rate of 0.2 C [77].

However, formation of TiO_2 particles in the nanoscale is not always useful to improve its Li^+ ion storage, whereas there is only an optimal size range which can positively affect their performance and the others do not. For instance, well-dispersed anatase nanoparticles fabricated by a sol-gel method exhibited considerable enhancement in their Li^+ ion insertion when the particle size ranges between 8 to 25 nm [78].

Great interest was paid to further improve the lithium storage performance of zero dimensional TiO_2 by coating the TiO_2 surface with carbon to overcome the poor lithium ion diffusivity and low electronic conductivity. In typical traditional synthesis methods, incorporation of carbon into TiO_2 is conducted by hydrothermal heating of metal salts in presence of carbon sources such as glucose. However, controlling the carbon content as well as obtaining homogeneous carbon distribution over the TiO_2 surface is hardly to be achieved. Liu *et al.* [79] reported on the hydrothermal carbon-coating treatment to fabricate a sandwich-like structure of a TiO_2@C hollow sphere composite. As a result of combining carbon and TiO_2, the TiO_2@C hollow spheres showed enhanced reversible capacity (240 mAh g^{-1}) with good capacity retention and high rate capability compared to the lower capacity (120 mAh g^{-1}) of uncoated TiO_2 nanoparticles (Degussa P25). Incorporation of carbon into porous TiO_2 nanoshells was studied by Wang *et al.* [80] who succeeded to control the carbon content in TiO_2@C composites to realize a highly reversible lithium ion storage (**Fig. 2.5a**). The preparation method includes two steps where the first is a coating of TiO_2 hollow spheres with a resorcinol-formaldehyde layer via a sol-gel method. The second step involves thermal treatment of the sample to carbonize the polymer and to form a crystalline TiO_2 shell. The TiO_2@C electrode exhibited about 425 mAh g^{-1} at a current rate of 1/10C. The specific capacity of this electrode decreased to ~150 mAh g^{-1} when the current rate was increased to 10C (**Fig. 2.5b**). In addition, such a composite has demonstrated a reversible capacity of ~190 mAh g^{-1}, which is slightly decreased to

170 mAh g^{-1} after more than 300 charging/discharging cycles at a rate of 2C (**Fig. 2.5c**). The ability to precisely control the carbon content in the TiO$_2$@C composites makes this preparation route is much more attractive than a traditional hydrothermal preparation.
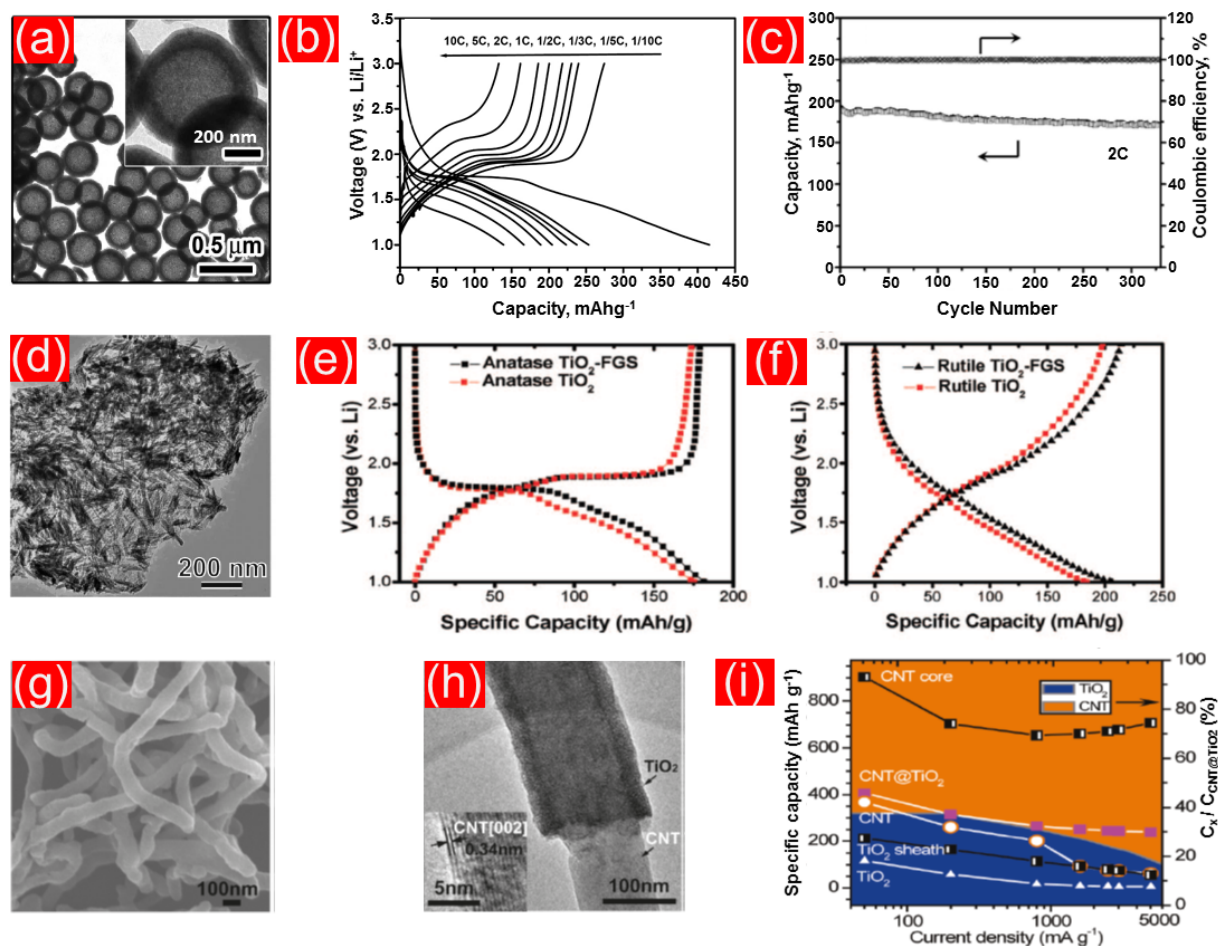

Fig.2.5. *SEM image of TiO$_2$/C shell (a), its first discharge−charge voltage profiles at different current density (b) and cycling performance (c), adapted from ref.* [80]*; SEM image of TiO$_2$-functionalized graphene sheet hybrids (d) and their voltage profiles for anatase (e) and rutile phases (f) adapted from ref.* [81]*; SEM and TEM micrographs of TiO$_2$-coated CNTs (g), (h) and their cycling performance (i) adapted from ref.*[82]*.*

Graphene is a promising candidate of the carbon family to be incorporated into TiO$_2$ as it considered is an excellent electron transport material. Coating of TiO$_2$

nanoparticles with a graphene layer provides conductive boundaries for electron transport resulting in a higher electrical conductivity which overcomes the internal resistance of TiO_2. Furthermore, these conductive boundaries serve as protective layers, which prevent the direct contact between the TiO_2 and the electrolyte resulting in enhanced stability of the active materials. Various successful studies report on the fabrication of TiO_2-graphene hybrid nanostructure for improved Li-ion insertion. Wang *et al.* [81] used an *in-situ* technique to fabricate self-assembled nanocrystalline TiO_2 with graphene utilizing anionic sulfate surfactants to stabilize graphene in aqueous solutions (**Fig. 2.5d**). The obtained hybrid nanostructure showed a doubling of the Li^+ ion insertion capacity of the pure TiO_2 as a result of an increased electrical conductivity induced by graphene (**Fig. 2.5e, f**). In another study [83], TiO_2 nanoparticles@graphene were also prepared by an *in-situ* synthesis. The obtained TiO_2-graphene composites were tested for Li^+ ion intercalation as anodes demonstrating a reversible capacity of 60 mAh g^{-1} at a high current rate of 5 A g^{-1} with negligible fade over 400 cycles. The unique conductivity of graphene sheets and the well dispersion of TiO_2 nanoparticles in combination lead to a superior electrochemical performance in Li^+ ion storage.

Owing to their high conductivity, stability and the ease of manufacturing, CNTs were used as excellent candidates to synthesize TiO_2/CNTs composite anodes. Core-shell TiO_2/CNTs (**Fig. 2.5g,h**) were prepared by hydrolysis of tetrabutyl titanate and showed a specific capacity of ~ 240 mAh g^{-1} at a current density of 5 A g^{-1} exhibiting a threefold increase in capacity than pure TiO_2 (62 mAh g^{-1}) at the same current density (**Fig. 2.5i**). The enhancement in capacity was attributed to the better electron supply due to the CNTs enable the TiO_2 shells to store higher lithium ion concentrations [82].

2.4.2 TiO$_2$ nanorods, nanoneedles and nanowires

The main drawback of TiO$_2$ nanoparticles as anodes in LIBs is the missing contact among the particle boundaries, which results in poor electronic and ionic conductivity [71,74]. In addition, the random motion of the electrons through the particles, as there are no defined pathways for the electron transport, hinders the electron separation at the current collectors [77,84]. Furthermore, the nanoparticles with high surface area possess higher surface energies compared to bulk materials. These particles can aggregate during the synthesis process or even during they undergo an electrochemical intercalation and thus the surface area decreases accordingly [85]. Indeed, the formed aggregates restrain the electrolyte to reach the particle surface causing a severe capacity drop.

Fabrication of TiO$_2$ with particular one-dimensional morphologies such as nanorods, nanoneedles and nanowires could significantly overcome the nanoparticles's drawbacks and improve their lithium ion insertion ability. Experimental work showed that the porous nature of the nanowires allowing a good contact between the electrolyte and the anode material and accommodates the strains resulting from changing the crystal dimensions after the electrochemical insertion reaction. As an example flower-like rutile nanorods (**Fig. 2.6a**) were synthesized by hydrolysis of a TiCl$_4$/ethanol solution at 50 °C [86]. The obtained nanorods showed a considerable higher reversible capacity and cycling stability than spherical rutile nanoparticles (**Fig. 2.6b**). The significant improvement in battery performance was attributed to the rod geometry of rutile lying along its c-direction, which is thermodynamically favorable for lithium ion insertion [86]. Fabrication of anatase nanotubes can be performed through an easy way in which the rutile powders are hydrothermally treated at 500 and 700 °C in alkaline media (10 M NaOH) (**Fig. 2.6c**). Reproducible discharge capacity ($\sim$ 175 mAh g^{-1}) was also noticed for anatase nanotubes after 10 cycles at a C/10 rate (**Fig. 2.6d**) [87]. Similar synthesis route was reported by Kim *et al.* [88] who further treated the obtained nanotubes/nanorods at a temperature between 300 - 400 °C to transform the present nanotubes into nanorods.

Bao *et al*. [89] succeeded to hydrothermally produce porous anatase nanorods at a lower temperature (200 °C) using NaOH/KOH as alkaline medium. The resultant nanorods showed a high initial discharge capacity (212 mAh g^{-1}) at a current density of 60 mA g^{-1}, which was retained for 30 discharging/charging cycles. Gao *et al*. [90] developed a method to prepare anatase nanorods. For this, $TiCl_4$ undergoes a hydrolysis with caustic soda and the obtained hydrolysate is hydrothermally treated at 110 °C. The materials exhibits lithium insertion capacity of 206 mAh/g with good reversibility at a current density of 50 mA g^{-1}. Rutile nanoneedles with about 25 nm in diameter and 100 nm length were prepared from titanium isopropoxide by reverse microemulsion mediated sol-gel method (**Fig. 2.6e**). The nanoneedle electrode was capable to achieve an initial specific capacity of 305 mAh g^{-1} (**Fig. 2.6f**) [91]. Wang *et al*. [92] reported on the fabrication of anatase nanowires with a minor $TiO_2(B)$ phase content via the hydrothermal treatment of commercial P25 powders (Degussa) followed by the an annealing step at 400 °C (**Fig. 2.6g**). These nanowires demonstrated a high specific capacity of 280 mAh g^{-1} at a current density of 140 mA g^{-1} upon 40 cycles with a Coulombic efficiency of 89% (**Fig. 2.6h**). Wu *et al*. [93] developed a room temperature hydrothermal method without using Teflon-lined autoclave to prepare anatase nanowires from $Ti(OC_4H_9)_4$. This material exhibited a reversible capacity of 216 mAh g^{-1} at a current density of 20 mA g^{-1}. Anatase particles were converted into $TiO_2(B)$ nanowires with diameters ranging from 20 to 40 nm by the hydrothermal method in presence of an aqueous solution of NaOH [94].
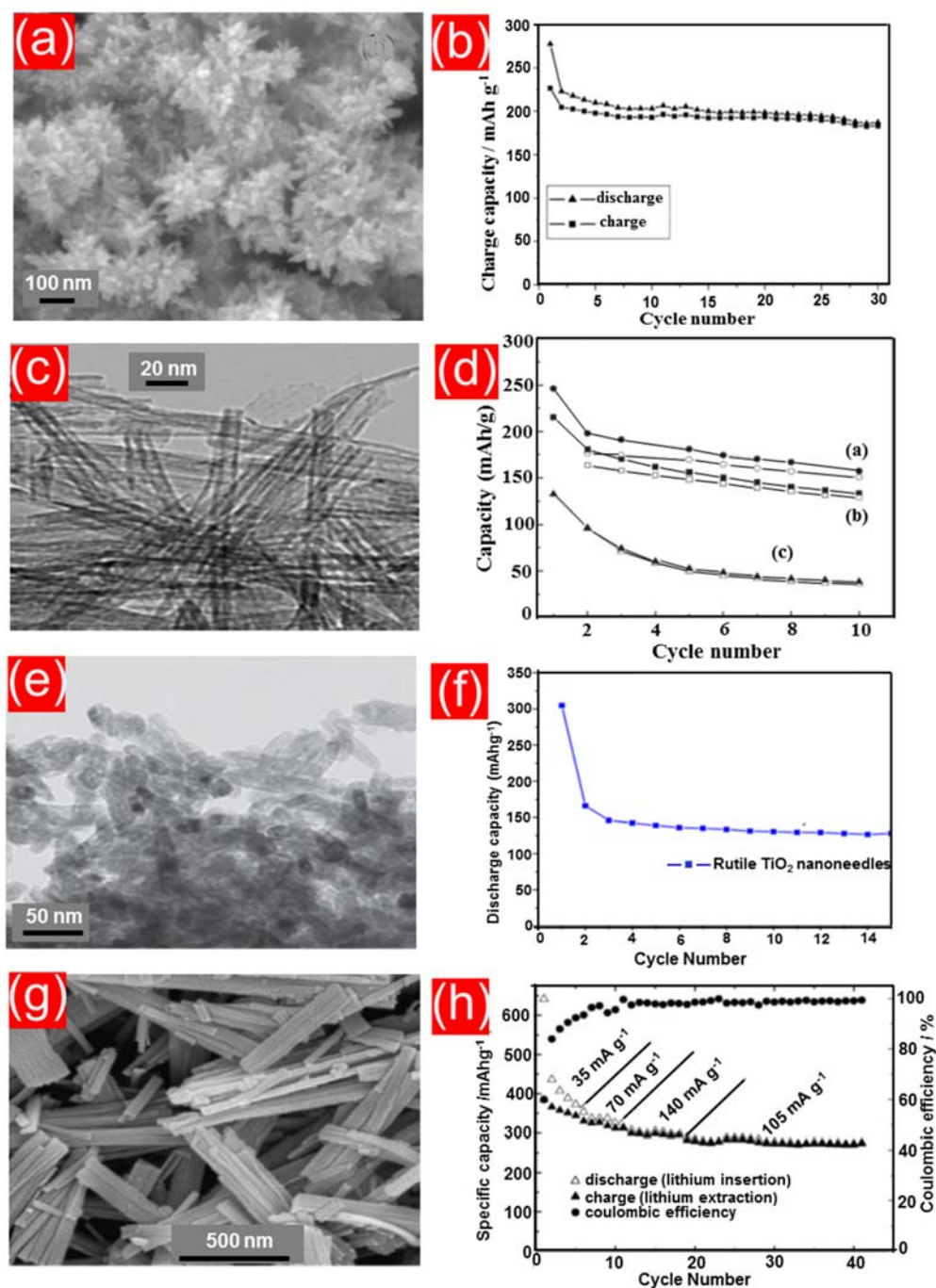
Fig. 2.6. *SEM image of the flower-like rutile nanorods (a) and their galvanostatic cycling at C/10 (b) adapted from ref.*[86]; *TEM image of TiO₂ nanotubes synthesized by treating of rutile with NaOH at 125 °C (c); and their performance denoted in image (d) with symbol (a)   adapted from ref.* [87].*TEM image of as-prepared rutile nanoneedles (e), their discharge cycling (f) and voltage profiles appear in the inset adapted from ref.*[91]; *SEM image of the as-prepared TiO₂ nanowires (g), their*

discharge capacity and Coulombic efficiency at the different current densities (h) adapted from ref. [92].

The electrochemical performance of 1D TiO_2 nanoarchitectures can be further improved by coating or doping with carbonaceous materials that improve both the electrical and ionic conductivities. Goriparti *et al.* [95] synthesized carbon-doped TiO_2 nanowires by a hydrothermal method and employed them as anodes in LIBs. The as-prepared C-TiO_2 nanowires showed enhanced reversible capacity of 306 mAh g^{-1} at a current rate of 0.1C with long term cycling (1000 charging/discharging cycles) compared to the undoped TiO_2 nanowires.

As already explained, high conductivity and good electron transport, especially at high temperature, make graphene a good additive to form composites with TiO_2 in order to reduce the internal resistance and decrease the irreversible heat which is produced from charging and discharging processes. TiO_2 nanotube/graphene composites were explored by Wang *et al.* [96] prepared by a single-step hydrothermal synthesis. The composites presented a high storage capacity of 357 mAh g^{-1} at 10 mA g^{-1} when they used as anodes in LIBs. The tubular structure of TiO_2 and the good electronic properties of graphene are the main reasons behind the excellent performance of such composites. In addition, TiO_2 nanorod arrays were grown onto graphene sheets by a modified seed-assisted hyrothermal preparation. It was observed that the sandwich-like nanocomposite of rutile nanorods/graphene exhibited largely improved revisable charging/discharging capacities as well as an enhanced rate capability compared to pure TiO_2 nanorods. The noticed better performances have been mainly attributed to superior conductivity and the unique structure of such composite that triggers excellent insertion reactions [97].

2.4.3 Porous TiO_2 nanostructures

Application of porous TiO_2 nanostructures is another promising approach to decrease the diffusion path of Li^+ ions in the electrode material, and, thus developing

their insertion performance. The specific nature of porous nanostructures and the high surface area allow for good wettability and better permeability of the electrolyte facilitating excellent charge transfer across the electrode material at the electrode/electrolyte interface. Particular attention has been given to synthesize nanoporous TiO_2 with different morphologies including 0D, 1D, 2D and 3D structures. The fabrication of such porous structures is commonly performed by template-free and template-assisted methods [6]. In the template-free approach, a hydrothermal process is used to obtain core-shell structured mesoporous TiO_2 spheres. In template-assisted approach, surfactants are utilized for producing mesoporous TiO_2. The main advantages of this preparation route is the ability to fabricate well-ordered and uniform mesopores with high surface area. Zero-dimensional (0D) nanoporous hollow spheres have been synthesized using carboxyl functionalized polystyrene TiO_2 spheres as a template (**Fig. 2.7a**). As anode materials, such hollow spheres showed a reversible capacity of 230 mAh g^{-1} when they are cycled at a current density of 33.5 mA g^{-1} (**Fig. 2.7b**). With this measure additional surface capacities may be generated for such porous structures resulted in a good Li^+ ion storage properties [98]. The relation between porosity and lithium storage characteristics has been investigated by Saravanna and co-workers [99]. They fabricated various mesoporous TiO_2 nanoparticles (10 - 20 nm particle size) with different pore sizes (5.7 - 7 nm) by a soft template method in which a titanium isopropoxide is utilized as a titanium source and different cationic surfactants of various chain lengths. The specific surface area of the prepared samples increases from 90 to 135 $m^2 g^{-1}$ with increasing pore diameters. The electrochemical results showed a high specific capacity (268 mAh g^{-1}) of the sample with the high surface area. The improved performance was ascribed to the high surface area which provides much larger voids for increased Li^+ ion accommodation. Wang *et al.* [100] developed a facile microwave-assisted hydrothermal reaction to produce porous TiO_2 spheres with a subsequent annealing step at 500 °C. When tested as anodes in LIBs, they showed a stable Li^+ ion storage capacity of 184 mAh g^{-1} at 1C (170 mA g^{-1}). In another study, porous TiO_2 nanospheres were fabricated by a simple sol-gel method followed

by thermal annealing. The electrochemical measurements indicate that the obtained material with such porous structure was able to deliver higher reversible capacities than dense TiO_2 nanospheres without porosity [101].

However, coating mesoporous TiO_2 with carbon not always results in a high specific capacity for instance, Zhang *et al.* [102] reported the synthesis of a C-coated mesoporous TiO_2@graphene sheets composite *via* a one-step solvothermal reaction. The sandwich-like structure of this hybrid composite is utilized as anode for LIBs exhibiting an initial capacity of 145 mAh g^{-1} at a current density of 0.2 A g^{-1}. Only a specific capacity of 111 mAh g^{-1} is achieved after 100 cycles. One-dimensional (1D) structure of TiO_2 with a mesoporous rod-like morphology has been reported by Jiang *et al.* [103] by the ultraviolet irradiation of titanium glycolate subsequent with heat treatment. A reversible capacity of 161 mAh g^{-1} at a current density of 1 A g^{-1} was demonstrated for these porous nanorods and retained for 40 cycles. Anatase nanorods were also synthesized by a low temperature colloidal synthesis by a thermal decomposition of titanium precursors containing a coordinating agent such as oleic acid. In this preparation route oleic acid is utilized as a capping agent to prevent the nanoparticle agglomeration during the synthesis process as well as it provides a carbonaceous percolating networks that cover the porous nanorods. The composite anode showed a specific capacity of 250 mAh g^{-1} at a rate of 1C confirming the superiority of such porous coated structure [104].
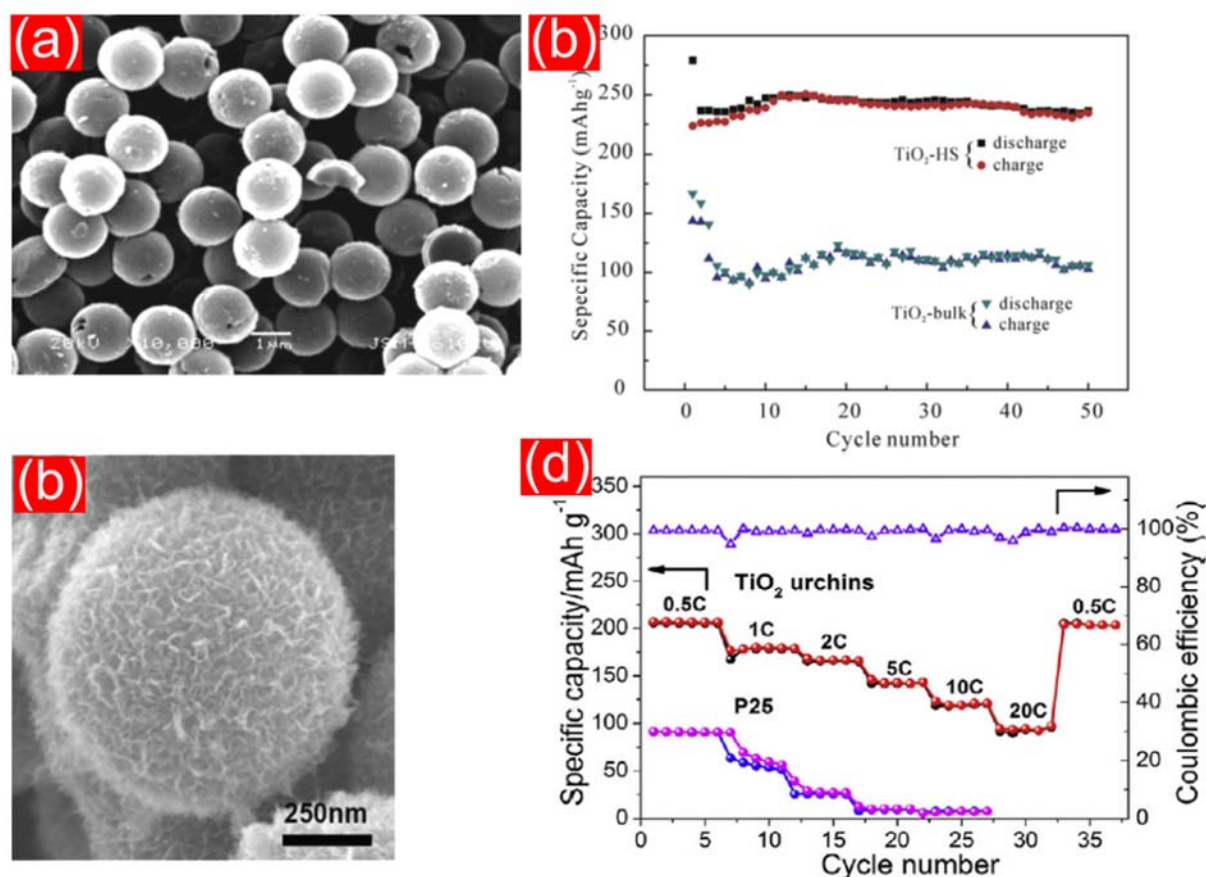
Fig.2.7. *SEM micrograph (a) and galvanostatic cycling (b) of TiO₂ hollow spheres (HS) in comparison with bulk TiO₂ at 0.1 C adapted from ref.* [98]*; SEM image (c) and rate capability (d) of the porous TiO₂ urchins compared to commercial P25 nanoparticles adapted from ref.*[105].

Hierarchically porous TiO$_2$ with 2D structures received a great interest especially as negative electrodes in LIBs. These unique porous nanostructures provide a rapid reactant transport through the larger pore diameters as well as a high surface area which is obtained from the smaller pores acting as active sites for the adsorption/desorption of the reactants. Recently, 2D hierarchically porous anatase with a specific surface area of 486 m^2 g^{-1} is synthesized by chemical etching of amorphous TiO$_2$ powder using acetic acid [106]. The obtained texture is characterized by micropores with arrange of 2 to 6 nm and mesopores of 15 to 80 nm. A reversible specific capacity of 191 mAh g^{-1} was demonstrated for this hierarchical structure at a current rate of 1A g^{-1} and this capacity is retained for 60 cycles [106].

Jin *et al.* [84] prepared hierarchical nanosheets with yolk-shell structure with highly porous microspheres shell and dense mesoporous core by a solvothermal alcoholysis. The pore diameter of the outer 2D nanosheet shell is about 15 nm and the inner mesoporous core shows a 3 nm pore size. These particular structures offer a stable porous framework that allows for electrolyte diffusion by capillary attraction and it also buffer the volume increase along with lithium ion intercalation/extraction reactions. Prolonged galvonostatic cycling over 700 cycles were performed by such electrode exhibiting a reversible specific capacity of 225 mAh g^{-1} [84].

Three-dimensional (3D) porous structure have also been studied for the application of lithium ion storage. The synthesis of 3D interconnected hierarchical structures composed of porous urchins have been reported by Cai *et al.* [105] (**Fig. 2.7c**). They synthesized them from hydrothermal TiO_2/oleylamine as precursor followed by an ion-exchange and a calcination process. When evaluated as anode material, the 3 D structure showed a lithium storage capacity of 206 mAh g^{-1} at 0.5 C after 100 cycles (**Fig. 2.7d**). The formation of 3D hierarchical nanoporous anatase *via* the hydrolysis of titanium glycolate was reported by Shin *et al.* [107]. A lithium-ion storage capacity of 302 mAh g^{-1} was observed for such nanoporous anodes with superior cycling stability. The experimental results of this study have proven that 64 % of the achieved capacity is attributed to two major storage processes which are the bulk insertion and the pseudocapacitive interfacial storage modes. The electrochemical performance of such a material reflects the importance of the high surface area of nanoporous TiO_2 to generate additional pseudo-capacitance. Recent work demonstrated a simple *in-situ* preparation of ordered 3D macroporous TiO_2 anodes using a polystyrene templated carbon cloth. The 3D electrodes provided a specific capacity of 174 mAh g^{-1} when cycled at a current density of 2 A g^{-1} [108]. The pore size and the thickness effects on the electrochemical performance of the 3D porous electrodes prepared by atomic layer deposition were optimized during a systematic study conducted by Ye *et al.* [109]. The results revealed that decreasing

the pore sizes and thickness of the 3D electrode, improve its power performance and the diffusivity of Li^+ ions across the electrode/electrolyte interface.

2.5   TiO$_2$ nanotubes prepared by electrochemical anodization

The one dimensional (1D) tubular structure of TiO_2 is of great scientific interest as well as practical significance particularly if the nanotubes are highly ordered and aligned perfectly in close packed arrays. These outstanding characteristics are realized by the potentiostatic anodization of Ti substrates as it is a simple, straightforward and cheap preparation technique (see **Fig. 2.8**). The majority of reported preparation methods only result in random networks of TiO_2 nanotubes with uncontrolled dimensions. However, template-assisted atomic layer deposition (ALD) can produce nanotubes with controlled geometries. It requires long time and complicated preparation steps which is reflected in the high cost, and thus, a limit in use [110]. The first anodic oxidation study of pure Ti and Ti-6Al-4V substrates resulted in uniform porous films of TiO_2 as reported by Zwilling *et al.* [111] in 1999. However a previous report before Zwilling's work had explored the anodization of Ti substrates in the presence of fluoride ions only results in a porous structure [112]. In 2001, Grimes and co-workers [113] reported that well-defined nanotube arrays were synthesized by the anodic oxidation of Ti substrates in HF containing electrolyte. These results aroused numerous attention and pushed the research towards the optimization of synthesis parameters (i.e. electrolyte configurations, applied voltage, reaction time, pH, agitation and temperature, etc.), to understand the formation mechanism and to employ these nanotubes in various research applications.
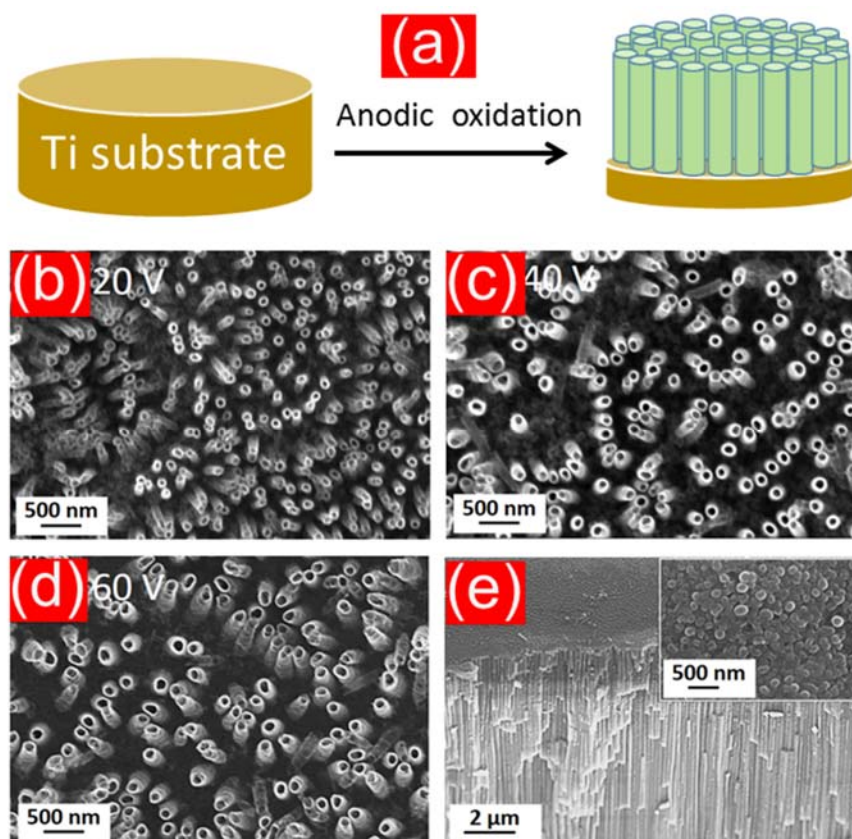
Fig.2.8. *Schematic illustration of the formation of TiO₂ nanotubes by the anodization of Ti substrate (a); SEM micrograph of anodized Ti substrates in formamide based electrolyte containing 0.2 M NH₄F at different anodization voltage 20 V (b), 40 V (c) and 60 V (d); The cross-sectional view (e) while the inset shows the bottom view of the nanotubes prepared at 60 V reprinted from ref.* [114].

Extensive studies proved that the TiO₂ nanotubes obtained by anodic oxidation are self-organized, well-aligned perpendicular to the substrate, and exhibit uniform tube diameters, wall thicknesses as well as high surface areas. Furthermore, the nanotube dimensions (i.e. diameter, wall thickness and tube length) can be precisely controlled by tuning the applied voltage, the used temperature the electrolyte composition especially F⁻ concentration [113–117]. The anodization is normally performed in a two-electrode electrochemical cell with the metal/alloy sheets as the working electrode and platinum foil or graphite as counter electrode in aqueous or

organic electrolytes containing F$^-$ ions as shown in the schematic of **Figure 2.9**. Aqueous HF solutions were firstly used as electrolytes to manufacture TiO$_2$ nanotube arrays with tube lengths below 500 nm [113,118]. Replacing the aqueous solutions with organic electrolytes composed of ethylene glycol as solvent in addition to a fluorine source such as NH$_4$F at high pH values allows for TiO$_2$ nanotube formation with lengths reach up to 1000 micrometer [119–121].
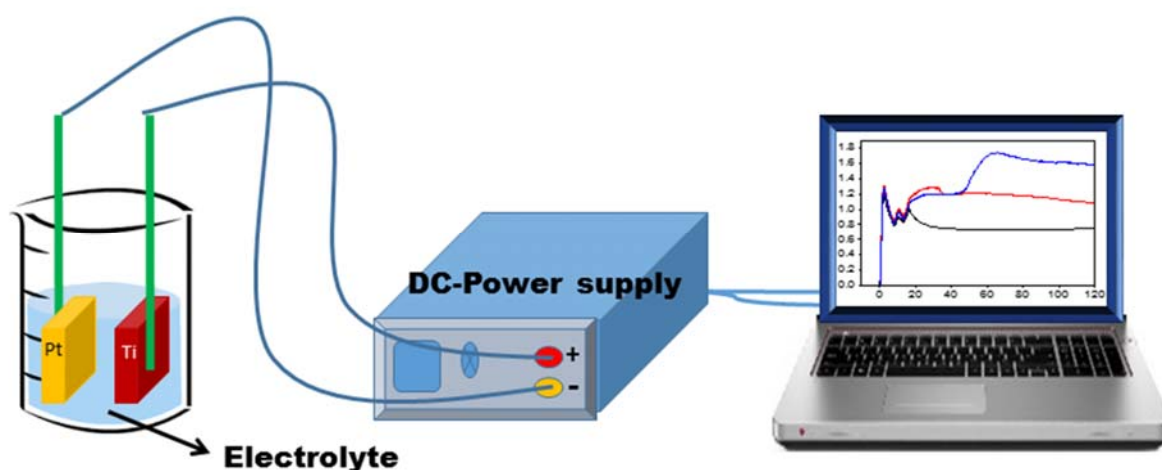

Fig. 2.9. *Schematic illustration of anodic oxidation.*

The nanotubes fabricated with these electrolytes always exhibited average diameters and wall thicknesses larger than 50 nm and 15 nm, respectively. Using neutral electrolytes such as those containing (NH$_4$)$_2$ SO$_4$ with NH$_4$F leads to a reduced dissolution rate of TiO$_2$ resulting in nanotube arrays with length in the micrometer range [122]. These electrolytes are considered as mild oxidation conditions for Ti substrates. Note that, the chemical composition of the electrolyte also plays a central role in the physical properties of the fabricated nanotubes [123]. For instance, addition of acetic acid results in the formation of robust tubes. Furthermore, increasing the F$^-$ concentration allows control of the tube wall thickness [124,125].

2.6   The mechanism of nanotubes formation by anodic oxidation

The formation mechanism of TiO_2 nanotubes is basically similar to the mechanism of porous alumina [126–128]. At the beginning of an anodization process, the Ti substrate is exposed to the electrolyte and a compact oxide layer of TiO_2 will be formed on the substrate surface due to the interaction between Ti metal and H_2O as described in equations 2.3 - 2.3 [128]. In addition, the initially obtained oxide layer is subjected to an electric field aided dissolution to produce Ti^{4+} cations where the Ti-O bonds can easily be broken due to the high polarization effect originating from the electric field [129,130].

$Ti \rightarrow Ti^{4+} + 4e^-$ $\hspace{6cm}$ (2.2)

$Ti + 6H_2O \rightarrow TiO_2 + 4H_3O^+ + 4e^-$ $\hspace{3.2cm}$ (2.3a)

$Ti^{4+} + 8H_2O \rightarrow Ti(OH)_4 + 4H_3O^+$ $\hspace{3.5cm}$ (2.3b)

$Ti(OH)_4 \rightarrow TiO_2 + 2H_2O$ $\hspace{5cm}$ (2.4)

At the same time, a hydrogen evolution is occurred at the cathodic side as the complementary reaction according to equation no. 4 [131].

$8H_3O^+ + 8e^- \rightarrow 4H_2 \uparrow + 4H_2O$ $\hspace{4.3cm}$ (2.5)

Note that, as soon as the voltage is applied, the electric field induces the anodic dissolution the Ti surface to form Ti^{4+} ions (eq. 2.2) as well as the generation of oxygen anions (O^{2-}) by deprotonation of H_2O molecules or OH^- ions that are present in the electrolyte (eq. 2.3 - 3.4) [127,128]. The created oxygen anions migrate from the electrolyte/oxide interface across the previously formed oxide layer to reach the metal surface while the Ti^{4+} ions diffuse from the metal surface at the metal/oxide interface towards the oxide/electrolyte interface [130]. Therefore, the growth of the oxide layer described in eq. 2.2 mainly depends on the ion formation (Ti^{4+} and O^{2-}) process. The interaction between Ti^{4+} and O^{2-} and the diffusion rate of both Ti^{4+} and O^{2-} into the oxide layer aided by the electrical field. Indeed, the presence of fluoride ions in the electrolyte represents the main key to produce self-organized tubular morphology in

the previously formed compact oxide layer. In the main, two reactions are forced by fluoride ions, the first is complexation reaction in which they react with the Ti^{4+} cations ejected to the oxide/electrolyte interface to form $[TiF_6]^{2-}$ species as displayed in equations no. 5, 6 [132].

$$Ti^{4+} + 6F^- \rightarrow [TiF_6]^{2-} \qquad\qquad (2.6)$$

$$TiO_2 + 6HF^- \rightarrow [TiF_6]^{2-} + 2H_2O + 2H^+ \qquad\qquad (2.7)$$

The second reaction is a chemical attack of the compact oxide layer explained in **Figure 2.10**.
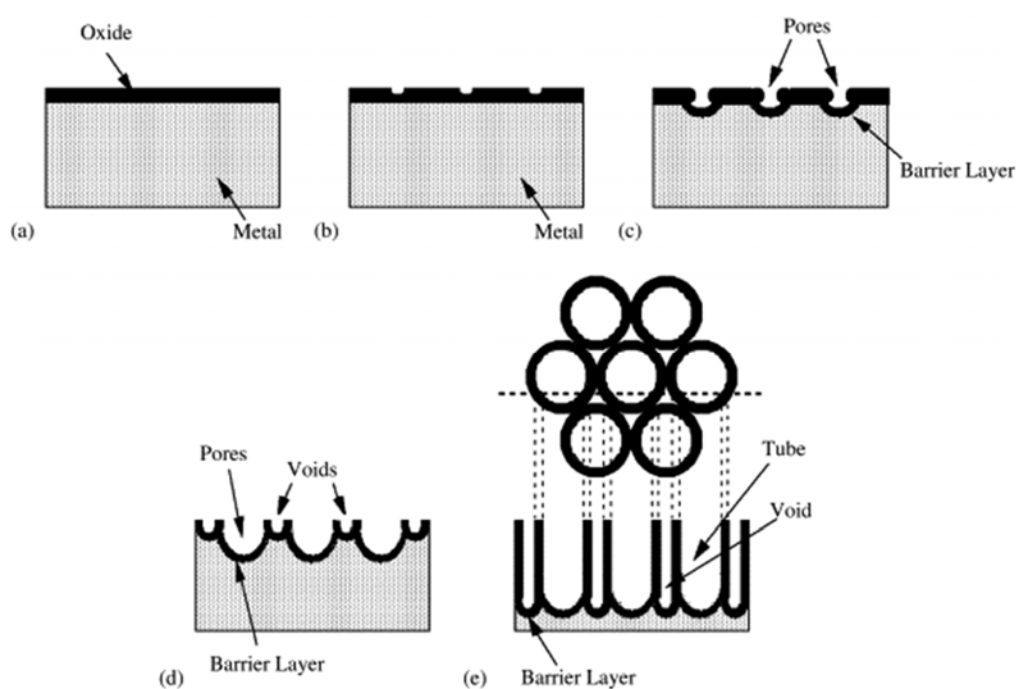
Fig. 2.10. Schematic diagram of the formation mechanism of a nanotube array at constant anodization voltage: (a) compact oxide layer formation, (b) pit formation on the oxide layer, (c) growth of the pit into scallop shaped pores, (d) metallic part between the pores undergoes oxidation and electric field assisted dissolution, and (e) fully developed nanotube array with the corresponding top view taken from ref. [115].

Fluoride ions chemically dissolve TiO_2 by and forming $[TiF_6]^{2-}$, which are water soluble species, causing small pits (eq. no. 6) [115,133]. These pits represent preferential sites for the electric field assisted chemical dissolution. With time, these pits become deeper and wider and the materials converted into tubes upon the high

dissolution rate at these active sites [129]. Therefore, the nanotube heights during the anodization process are controlled by the balance between the rate of electrochemical oxidation and chemical etching. Application of a high anodization voltage leads to an increased electrochemical oxidation compared to the rate for chemical etching. Consequently, a thick layer of TiO_2 nanotubes can be formed before reaching the equilibrium between both rates.

2.7   Anodically fabricated TiO$_2$ nanotubes as anodes in LIBs

As discussed above, the anodic oxidation offers the ability to tune the nanotube dimensions producing well-ordered and high surface area TiO_2 nanotube arrays perpendicularly attached to the Ti substrate. These easily tunable properties open up the possibility for various applications, especially as anodes in lithium ion batteries. The porous nature of such nanotubes can effectively decrease the lithium ion pathway, thus allowing for high lithium ion accessibility of the electrode material [134]. This property, in turn, decreases the polarization of the anode material and triggers a high charging/discharging rate. The high surface area enlarges the contact area between the electrode materials and the electrolyte causing a low current density. The one-dimensional structure of the nanotubes can buffer volume change gained from the lithium ion insertion and extraction.

Systematical studies supported with theoretical analysis were carried out to evaluate the Li^+ ion storage of bare anodically fabricated TiO_2 and the conventional randomly oriented TiO_2 nanotubes mixed mechanically with 10% conductive carbon [12]. The results presented excellent electrochemical performance for the nanotubes prepared by anodization with a six-fold increase in capacity of at a current density of 10C compared to randomly organized TiO_2 nanotubes even after mixing with conductive carbon. These superior performances are ascribed to the good electrical contact between the oxide layer and the Ti substrate, which serves as current collector. This arrangement leads to an increased electrical conductivity of the whole electrode [12]. Wei *et al.* [135] reported the effect of nanotube diameters and wall

thicknesses on the storage performance and cycling stability of TiO_2. The results showed 96.4% of the initial capacity can be retained after 140 cycles for TiO_2 with 50 nm pore diameter and 25 nm wall thickness. When the tube diameter and wall thickness increase to 100 nm and 40 nm, respectively, a rapid capacity fading to only 53% of the original capacity was observed.

In the next sections, various approaches are discussed which affect the electrochemical properties of TiO_2 prepared by anodization such as the anodization electrolyte, the degree of crystallinity, the annealing atmosphere, structure modifications with carbonaceous materials, post-anodization and the influence of other transition metal oxides.

2.7.1 Anodization electrolyte

Ionic liquids as anodization bath were explored in different reports to produce defect-free TiO_2 NTs with good mechanical strength and to improve the charge transfer efficiency. These electrolytes are characterized by the higher electrical conductivity which helps to decrease the decomposition of the electrolyte during the anodization process. However, the TiO_2 nanotubes fabricated with liquid ionic electrolytes showed a good cycling stability for more than 1000 cycles. The obtained reversible capacity is relatively low ($\sim$ 140 mAh g^{-1}) at a low charging rate (C/10) [136].

2.7.2 Amorphous and crystalline TiO₂ anodes

Generally, TiO_2 nanotubes prepared by the electrochemical anodization are amorphous. Previous studies showed that the crystalline anatase phase is formed by annealing of the NTs at a temperature above 280 °C in air. At temperatures higher than 450 °C a mixture of well crystalline anatase and small amounts of rutile are obtained [115]. The temperature from 600 to 900 °C are required for the complete phase transition from anatase to rutile [137]. Other studies showed single-phase

anatase is obtained after annealing the mixed or the coated TiO_2 nanotubes at 450 °C. Nevertheless, the crystallization process of the NT is depending on the specific chemical composition of the used base metal and by the local diffusion of the alloying element. For example, Nb increases the conversion temperature of anatase to rutile [138]. Hence rutile is not formed in the grown nanotubes on Ti6Al7Nb even when they are annealed at 550 °C. Alternatively, Fe concentration in a Ti-Fe alloy can promote the formation of rutile and decreases the anatase phase [21].

Particular interest was paid to investigate the relation between the degree of crystallinity and the electrochemical performance of TiO_2 nanotubes as anodes for lithium ion batteries. Experiments measurements have been conducted by Ivanov *et al.* [139] which revealed that the amorphous TiO_2 structure promotes a higher lithium ion diffusion rate than the crystalline anatase structure. The reason was attributed to larger amount of disorders and defects in the amorphous structure than the crystalline one. These defects offer bigger channels or more diffusion paths for Li^+ ion migration. In addition, the low mechanical stress and less rigid nature owned by amorphous TiO_2 facilitate the intercalation with large amounts [134,135]. Furthermore, Ryu *et al.* [140] reported a comparison study between the amorphous and crystalline TiO_2 NTs and their storage capacity, rate capability and cycling stability. The as-prepared and post-annealing NTs showed similar pore diameters (30 - 50 nm) and tube heights (8.2 µm). Cycling performance and rate capability of the amorphous tubes were found to be much better than the crystalline TiO_2 due to the higher Li^+ ion diffusivity in the amorphous structure. The rate capability of amorphous and crystalline anatase TiO_2 NTs was investigated by Fang *et al.* [141]. Amorphous TiO_2 exhibited high rate capability compared to crystalline anatase fabricated with same morphological features (**Fig. 2.11**). This phenomenon is proven by the higher Li^+ ions diffusion coefficient of amorphous TiO_2 compared to anatase. However, higher ionic conductivity for anatase than for amorphous nanotubes indicated by electrochemical impedance spectroscopy (EIS).
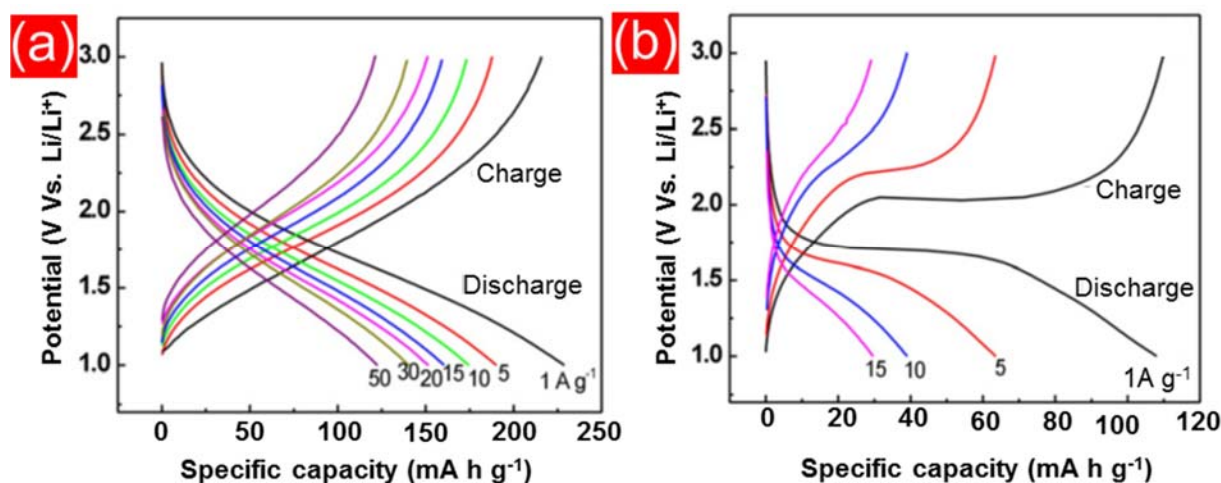
Fig. 2.11. *Voltage profiles of amorphous (a) and anatase (b) TiO₂ nanotubes measured at different current densities. Adapted from ref.* [141].

Tighineanu *et al.* [142] studied the influence of annealing temperature and time on the ionic conductivity of TiO$_2$ nanotube arrays. The ionic conductivity of TiO$_2$ mainly depends on the conversion process from amorphous TiO$_2$ to the crystalline phases, where anatase showed a higher electric conductivity than rutile containing tube arrays. The optimal annealing temperature to obtain low resistance materials was found between 250 - 450 °C. That work also showed the crystalline anatase is obtained by annealing amorphous TiO$_2$ at 250 °C for longer time up to 20 hours [142]. Mixed composition of anatase and rutile in the TiO$_2$ nanotube arrays, obtained by thermal treatment carried out at a temperature higher than 580 °C, demonstrated higher areal capacity than that achieved by single anatase NTs [143]. The authors associate enhanced insertion capacity to the higher Li ion diffusion coefficient of rutile plays a stronger role than the improved electrical conductivity of anatase.

2.7.3 Influence of the annealing atmosphere on the properties of TiO₂ nanotube anodes

Considerable attention has been drawn to the annealing atmosphere of the TiO$_2$ nanotubes as an important factor for their electrochemical storage properties. Experiments explored that the annealing atmosphere can affect the morphology and

the present crystalline phases of the nanotube arrays. Free-standing TiO_2 nanotubes annealed in Ar atmosphere showed morphological features which differ from those obtained from annealed in air as presented in **Figure 2.12a**,**b** [144]. Furthermore, the electrochemical tests showed better performances for the sample annealed in Ar than that annealed in air (**Figure 2.12c**).
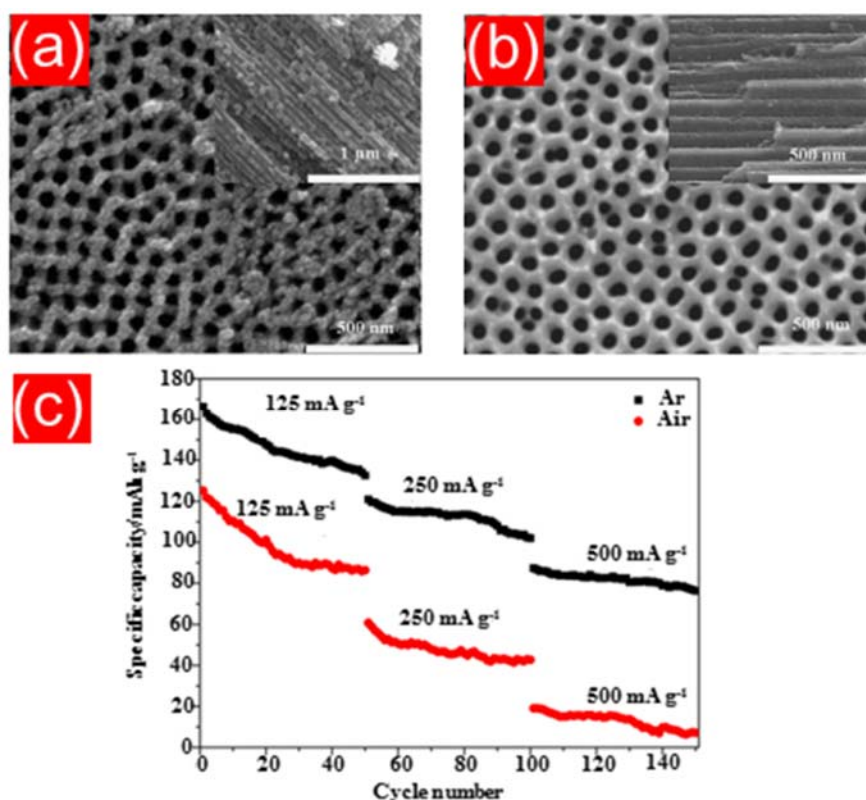
Fig. 2.12. *SEM micrographs of the TiO_2 nanotubes thermally treated in Ar (a) in air (b) atmosphere and the rate capability of each electrode (c). Adapted from ref.*[144].

This behavior was attributed to the presence of significant amounts of carbon mixed with the TiO_2 nanotubes led to an improvement of their electronic conductivity. Enhanced initial lithium ion insertion capacity up to 240 mAh g^{-1} at a current density of 320 mA g^{-1} was reported by Liu *et al.* [145] for anatase nanotube arrays when they were annealed in N_2 atmosphere at 300 °C. The achieved capacity decreased as the annealing temperature increased. The authors correlated that observation to the

lower storage ability of rutile obtained by phase transformation from anatase at high temperatures leading to a reduced overall electrode capacity. Lu *et al.* [146] investigated the use of H_2/95%Ar as a reducing atmosphere to thermally treat the anodized TiO_2 NTs. Structural and morphological changes have been observed for the annealed nanotubes in the reducing atmosphere associated with an improvement in their electrochemical rate performance during lithium insertion measurements. Results of detailed experiments indicate the hydrogenation treatment produced large number of oxygen vacancies inside the crystal lattice of TiO_2 which represent active sites for Li^+ ions intercalation [146].

2.7.4   Free-standing TiO_2 nanotube membranes

In addition to the nanotubes grown on Ti foils, there is a great interest in using the TiO_2 nanotube membranes after the detachment from the substrates, especially when they can be used in the application of microbattteries. Wei *et al.* [10] reported a two-step anodization process followed by a thermal treatment to fabricate TiO_2 nanotube films [10]. The TiO_2 membranes were separated from the Ti substrates by sonication. The resultant 3-D free-standing TiO_2 nanotube layers were evaluated as anodes for microbatteries and exhibited an areal capacity of 0.46 mA cm^{-2} (i.e. 184 mAh g^{-1}) at a current density of 0.05 mA cm^{-2}. Furthermore, these membrane electrodes demonstrated excellent cycling stability over 500 cycles with a capacity loss of about 6 %. The found areal capacity was found depends on the nanotube length. Interestingly, using of a two anodization steps provides TiO_2 nanotubes with small pore diameter. This aspect was utilized by Liu *et al.* [147] to produce nanotubes with 20 nm which showed excellent enhancement in the electron transport.

As the above-mentioned approaches aimed at enhancing the lithium-ion storage performance by optimizing the nanotube dimensions, annealing temperature and the environment to reduce the internal resistivity of the TiO_2 materials, the poor electrical conductivity problems need to be solved. Doping or coating TiO_2 nanotubes

with other materials that are more conductive such as graphene or CNTs usually is the general protocol to overcome the conductivity obstacles.

2.7.5 TiO$_2$ nanotubes/carbon composites

Similar to TiO$_2$ nanoparticles and nanowires, doping of TiO$_2$ nanotubes with highly conductive materials were explored. Here, the aim was to improve the electronic conductivity of TiO$_2$ using carbon composites which provide more electrons to the TiO$_2$ surface to achieve a higher Li$^+$ ion storage at very fast charging/discharging rates. Kilinic *et al.* [148] succeeded to fabricate C-doped TiO$_2$ nanotubes grown on Ti foils by anodic oxidation. Doping was performed through two different methods. The first is an *in-situ* synthesis during the anodic oxidation process. The key point here is the anodic oxidation electrolyte which must contain a carbon source such as polyvinyl alcohol. The second is a heat treatment method in which the anodized TiO$_2$ nanotubes are subjected to a thermal treatment at 500 °C under a N$_2$ and C$_2$H$_2$ flux (1:1). Furthermore, carbon-modified anodically prepared TiO$_2$ nanotubes were also investigated by Mole *et al.* [149] by thermal treatment in a CH$_4$/H$_2$ atmosphere in the presence of Fe. A three-time increase in the double layer capacitance was demonstrated by C-TiO$_2$ nanotubes compared to the pure TiO$_2$ nanotube electrodes due to the improved charge transfer obtained by the presence of carbon and iron dopants. In addition, Chen *et al.* [13] developed a simple method to fabricate Au/RGO-TiO$_2$ NTs composites via electrolysis of chloroauric acid and graphene oxide on the surface of anodically fabricated TiO$_2$ nanotubes. These composite materials were only tested as photocatalysts and exhibited enhanced photocatalytic activity towards the degradation of methyl orange.

2.7.6 Mixed oxide nanotubes

The fabrication of ordered mixed transition metal oxide nanotubes is usually obtained by two approaches, the first includes more than one preparation step in which the nanotubes are firstly fabricated *via* the usual synthesis means discussed

above (such as anodization or atomic layer deposition) and then they are subjected to doping or coating processes. The second approach is realized by a single preparation step in which Ti-based alloys were used as substrates for the anodization and the mixed oxide tubes are formed directly on their surface. For instance, Co_3O_4 nanoparticles@TiO_2 nanotubes were synthesized by the electrodeposition of the grown TiO_2 nanotubes (**Fig. 2.13a**). The Co_3O_4/TiO_2 composite was explored for lithium ion storage as anode material [15]. The coated Co_3O_4 layer leads to an increase of the Li^+ ion insertion capacity which is related to the improved ionic conductivity as well as it contributes to the overall electrode capacity. An interesting *in-situ* preparation process during the anodization of Ti foils was reported by Cao *et al.* [150] to produce Co_3O_4-doped TiO_2 nanotubes in which $Co(NO_3)_2.6H_2O$ utilized as cobalt source in the anodic oxidation electrolyte. This composite material showed enhanced photoelectrochemical properties under visible light. Self-doping and electrodeposition techniques were employed to achieve uniform copper filling from the bottom to the top of the TiO_2 nanotubes [151]. This strategy was proposed to enhance the conductivity of the tube bottoms using a conductive copper coating. Similar to copper-filled TiO_2 nanotubes, α-Fe_2O_3 was selected and prepared by a pulse electrodeposition to finally form Fe_2O_3 nanorod/TiO_2 nanotube composites [152]. This approach allows for growing Fe_2O_3 rods with various lengths ranging between 50 - 550 nm according to the deposition time. In another study, Fe_2O_3 hollow nanorods were formed on the outer and inner surface of anodically fabricated TiO_2 to prepare 3D hierarchical structures of Fe_2O_3@TiO_2 [153].
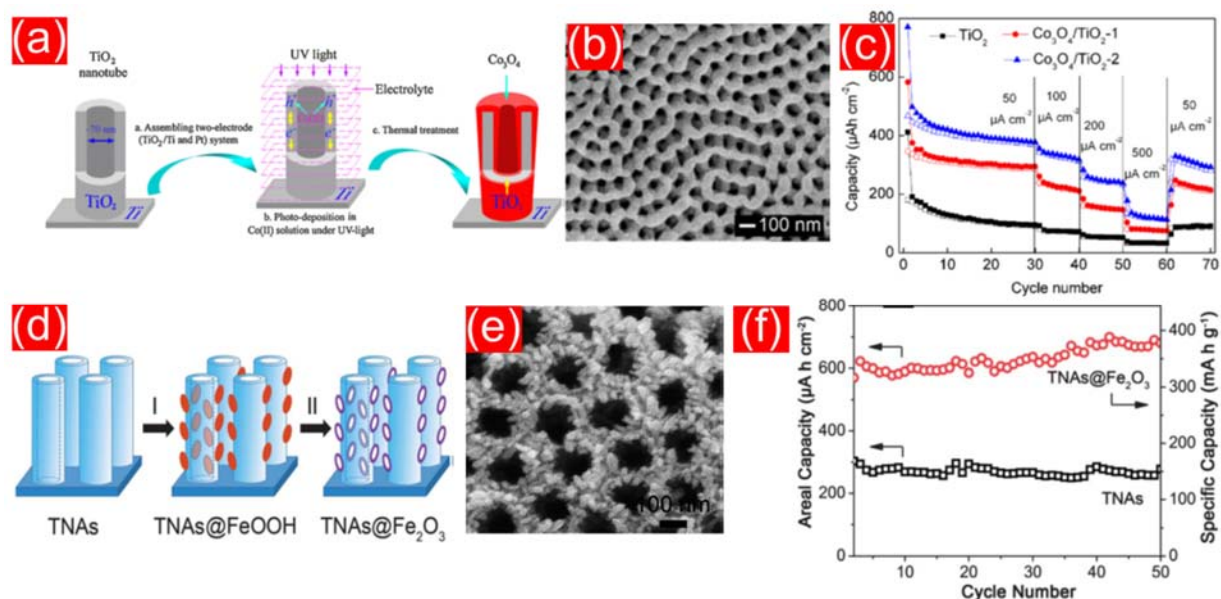
Fig. 2.13. *Schematic for the fabrication of Co_3O_4/TiO_2 nanotube composites through photo-deposition techniques (a); SEM images of Co_3O_4-coated TiO_2 nanotubes obtained at photodeposition time of 4 h (b) and their areal capacities measured at different current densities (c) adapted from ref. [15]; Schematic of synthesis of Fe_2O_3 hollow nanorods@TiO_2 nanotube arrays (d): (I) growth of FeOOH nanospindles on TiO_2 by hydrolysis of Fe^{3+} ions; (II) thermal transformation of FeOOH nanospindles to Fe_2O_3 hollow nanorods on the surface of TiO_2 nanotube. SEM image of Fe_2O_3 nanorod onTiO_2 (e); cycling performances of Fe_2O_3@TiO_2 in comparison with bare TiO_2 adapted from ref. [153].*

The preparation technique includes the hydrolysis of Fe^{3+} ions to grow FeOOH nanospindles followed by the thermal transformation to Fe_2O_3 nanorods as presented in **Figure 2.13d,e** This heterojunctional composite was integrated as anode in a LIB and demonstrated an outstanding electrochemical performance with an areal capacity of about 600 µA cm^{-2} that was retained for 50 cycles at a current density of 100 µA cm^{-2} (**Fig. 2.13f**). Homogenous VO_x nanoparticles were also deposited onto TiO_2 nanotube arrays by CVD. The well-disperses VO_x on the nanotube surface makes TiO_2 to a highly attractive catalytic material for different reactions [154]. Guan *et al.* [18] reported a controllable synthesis of MoO_3-doped TiO_2 nanotube arrays *via* anodic oxidation followed by electrodeposition. The MoO_3 modified nanotube anodes can deliver twice the areal capacity of bare TiO_2. However, the

electrochemical impedance spectra (EIS) analysis demonstrated that the Li^+ ion transfer into TiO_2 is blocked by the presence of MoO_3 nanoparticles. Gobal *et al.* [155] investigated the electrodeposition of Zn-Ni onto TiO_2 nanotubes in alkaline solution subsequently after thermal annealing at 300 °C to form NiO-ZnO/TiO_2 nanoporous/cracked composites. The assembled electrodes demonstrated good capacitive behavior as supercapacitor.

Interestingly, SnO_2 nanowires were grown on the surface of TiO_2 NTs by a two-step method in which the anodized TiO_2 nanotubes were subjected to an electrodeposition process. Sn and SnO_2 present in the mixed oxide electrodes were tested for the Li^+ ion storage by limiting the voltage ranges to 1.2 - 0.01 V *vs.* Li^+/Li^0 [156]. An areal capacity of 140 μAh cm^{-2} was demonstrated by a 2 μm thick Sn/SnO_2 layer with a capacity retention of up to 85 % after 50 cycles. The TiO_2 nanotubes help to buffer the volume changes of the Li-Sn alloys and, thus, improves the overall electrode performance [156]. SnO_2 deposited coaxially onto TiO_2 nanotubes were synthesized by the post electrodeposition. The SEM image is presented in **Figure 2.14a** [17]. The prepared monohybrids displayed a good electrical conductivity and, thus, an enhanced electrochemical performance for Li^+ ion storage (**Figure 2.14b**). As previously mentioned template-assisted atomic layer deposition (ALD) is considered as alternative technique to fabricate TiO_2 with controlled tubular geometry but it is a complicated time consuming procedure. Kim *et al.* [30] reported on the fabrication of SnO_2/TiO_2 NT heterostructures by ALD. The resulting mixed oxide anodes exhibited a specific capacity of 100 mAh g^{-1} in the second cycle. However, a capacity of 300 mAh g^{-1} was only maintained by this electrode even after 50 cycles. The surface modification by SnO_2 is designated to enhance the lithium insertion rate and, thus, increases the specific capacity of such anode composite compared to pure TiO_2 (250 mAh g^{-1}).
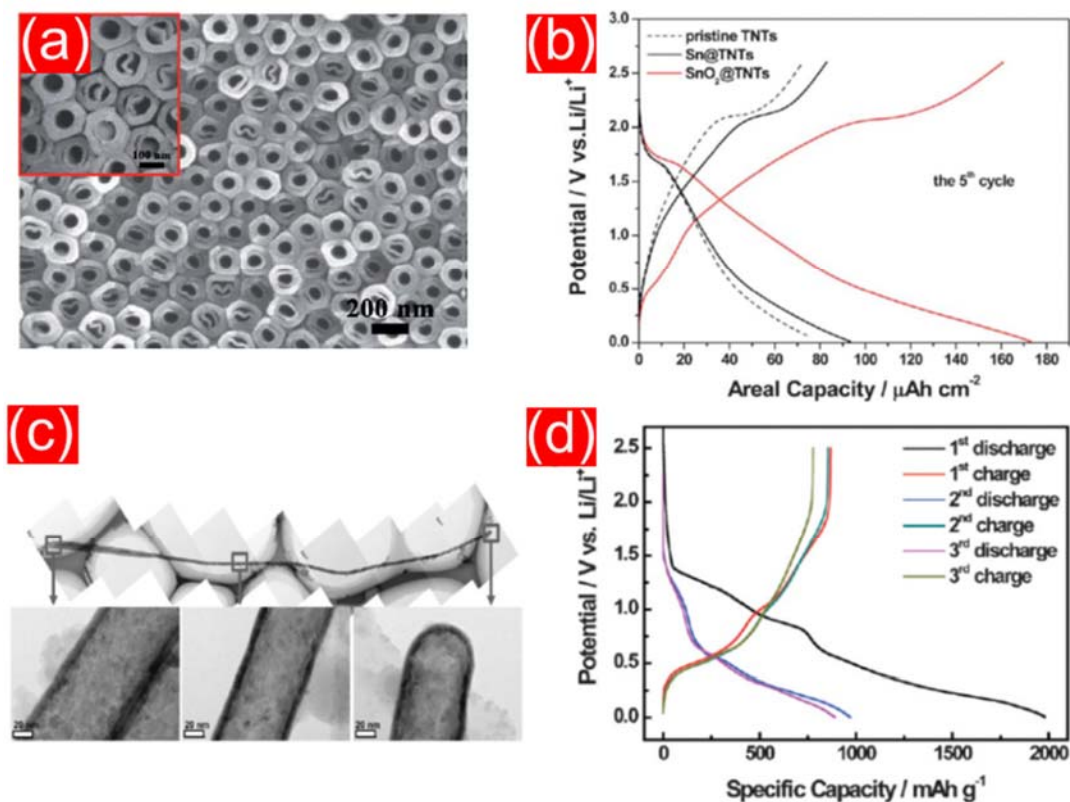
Fig.2.14. *SEM image of coaxial SnO₂@TiO₂ nanotubes synthesized by the post electrodeposition (a); their galvanostatic charging-discharging curves obtained at a current rate of 100 μA/cm⁻² (b) adapted from ref.* [17]*; TEM images of an ALD-grown SnO₂. The magnified images obtained from three different regions are presented as insets (c); their galvanostatic charging-discharging curves measured at a current rate of C/10 (d) adapted from ref.* [30]*.*

Another surface modification to TiO₂ nanotubes was carried out by Lopez *et al.* [157] who deposited Li₃PO₄ films on the nanotubes surface. The obtained 3D structure of Li₃PO₄-coated TiO₂ was assembled as anode and was tested for lithium ion storage. The electrochemical results revealed a reversible capacity of 110 mAh g⁻¹ achieved for over 190 cycles at a rate of 5C. The lithium phosphate was proposed in this composite as ionic conductor which improves the electrical and ionic conductivity of TiO₂ [157]. Alternatively, a straightforward approach used to fabricate self-organized mixed oxide nanotube arrays is found in the anodic oxidation of Ti-based alloys. Although several binary and ternary mixed oxide nanotubes were fabricated

by the anodization of Ti-Fe [21], Ti-Ta, Ti-Nb [158], Ti-Pd [159], Ti-Al [160], Ti-Mo [161], Ti-V [19], Ti-W [162], Ti-Mn [163], Ti-Ni [16],Ti-Mo-Ni [22] and Ti-6Al-4V [164] alloys, but only some of them were used as anodes in lithium ion batteries. As an example, well-ordered mixed Ti-Mn-O nanotubes were grown on the surface of a Ti-8Mn alloy by anodization [163]. The mixed oxide anodes were integrated with $LiCoO_2$ cathode to assemble a full cell battery. These mixed oxide nanotubes exhibited a capacity of 474 mA g^{-1} which was kept for 30 cycles. A decent electrode of ordered TiO_2/Nb_2O_5 nanotubes demonstrated long-term cycling stability and higher reversible lithium storage capacity than pure TiO_2 nanotube arrays prepared under similar conditions [165].

Chapter 3

Materials and methods

3.1 Methodology

3.1.1 Synthesis of TiO$_2$-CoO and TiO$_2$ Nanotubes

The Ti$_{80}$Co$_{20}$ (at.%) prealloy was prepared by arc-melting of Ti (99.8 %, ARA-T Advance, Germany) and Co (99.9 % VEB Mansfeld Kombinat, Germany) metals under argon atmosphere. The prealloy was subsequently cast into rods of 12 mm in diameter using a cold crucible device. Discs of 1 mm thickness were cut from the rods and ground with SiC abrasive paper up to a grit size of P1400 and were then polished.

Prior to the anodic oxidation, the substrates were sonicated for 30 min in acetone, rinsed with deionized water and finally dried in air. The anodic oxidation experiments of the Ti-Co alloy substrates were realized inside Teflon cells using a programmable DC-power supply (Keithley 2400 source master). A platinum foil was used as counter electrode and placed at a distance of 1 cm from the Ti-Co alloy substrate used as working electrode. The electrolyte consisted of a formamide-based solution containing 0.2 M NH_4F (99 % purity, Merck), 0.1 M H_3PO_4 (85 %, Merck) and 3 % v/v H_2O [22].

The anodic oxidation experiments were carried out at room temperature applying different voltages (20, 40 and 60 V) for 5h [166] with a sweep rate of 20 mV s^{-1}. After anodization, the substrates were washed with deionized water and sonicated for a few seconds. The grown nanotubes were thermally treated at 450 °C for 3 h in air to enhance crystallinity. For comparison, TiO_2 nanotube arrays were fabricated from Ti substrates (0.25 mm thick, 99.8 % purity, Alfa Aesar) employing the same electrolyte and anodic oxidation conditions as used for the Ti-Co alloy. The obtained nanotubes were thermally annealed at 450 °C for 3 h in air.

3.1.2 Synthesis of CNTs@TiO$_2$-CoO NT composite

Multi-walled CNTs were synthesized on the surface of TiO_2/CoO NT arrays by a single-step spray pyrolysis technique. A mixture of 1.25 g ferrocene ($C_{10}H_{10}Fe$, 99.5 % purity, Alfa Aesar) and 0.5 g benzeneboronic acid ($C_6H_7BO_2$, 98 % purity, Alfa Aesar) in 100 mL toluene (C_7H_8, 99.99% purity, Merck) was used as precursor solution. A steady precursor spray was generated with the help of a spray system and the fine spray was carried by argon gas into a horizontal quartz tube, maintained at a temperature of 860 °C. The as-prepared TiO_2/CoO NT sample was placed in the middle of the quartz tube. The synthesis was carried out until the precursor solution was exhausted (~25 min). Fe from ferrocene nucleates the growth of CNTs, whereas toluene serves as the carbon precursor. Boron, from the benzeneboronic acid, aids in the formation of stable bends in the CNTs and significantly increases the aspect ratio

of the nanotubes, resulting in a uniformly covered CNT layer on the substrates [167]. The CNTs synthesis in this section was performed by Dr. Raghunandan Ummethala.

3.1.3 Synthesis of TiO_2-SnO_2 and TiO_2 nanotubes

The Ti-Sn prealloys with different Sn contents (1, 5 and 10 at.%) were prepared by arc-melting Ti (99.8 %, ARA-T Advance, Germany) and Sn (99.999 % Auerhammer Metallwerk GmbH, Germany) metals under an argon atmosphere. The obtained ingots were then cast into rods of 12 mm diameter inside a cold crucible device. These rods were cut into discs of 1 mm thickness and ground with SiC abrasive papers from P400 to P1400 grit size and then polished. All alloy substrates were ultrasonically cleaned for 30 min in acetone and ethanol, rinsed with deionized water and dried in air. The anodization processes were conducted at room temperature inside Teflon cells, in which a platinum foil was used as the counter electrode placed at a distance of 1 cm from the Ti-Sn alloy substrate as working electrode with an ethylene glycol-based solution containing 0.2 M NH_4F (99 % purity, Merck), and 3 % v/v H_2O as electrolyte. Different formation voltages (10, 20 and 40 V) were applied for 5h with a rate of 20 mV s^{-1} using a programmable DC-power supply (Keithley 2400 source master).

The anodized substrates were subsequently washed with deionized water and sonicated for a few seconds to remove the residual debris. The nanotubes grown on the $TiSn_1$, $TiSn_5$ and $TiSn_{10}$ alloy substrates will be further denoted as T1S, T5S and T10S, respectively. Pure TiO_2 nanotubes were prepared from Ti substrates (0.25 mm thickness, 99.8 % purity, Alfa Aesar) for comparison employing identical anodization conditions.

3.2   Characterization techniques

3.2.1   X-ray diffraction (XRD)

Phase identification of the as-fabricated/annealed TiO_2-CoO nanotubes was performed by X-ray diffraction (PANalytical X'Pert Pro diffractometer) using Co K_α radiation of wavelength λ = 1.7889 Å and PIXcel detector in Bragg-Brentano geometry. The phase composition of the Ti-Co and Ti-Sn alloy substrates with a thickness of about 100 µm was examined by X-ray diffraction (STOE Stadi P diffractometer, Mo $K_{\alpha1}$ radiation of wavelength λ = 0.7093 Å, transmission geometry). X-ray diffraction is a powerful characterization tool used for identifying crystalline phases in materials where the atoms are arranged in regular distances describing a three dimensional crystal. The technique is based on diffraction of X-rays by the atoms of a crystal along specific directions. In laboratory scale, X-rays are generated by a cathode ray tube and subjected to a filtration to produce monochromatic radiation. The diffracted X-rays are collected by a detector. The obtained diffraction plot consists of a pattern of observed intensities *versus* the scattering angle 2θ.
Diffracted X-rays from different atomic planes may undergo constructive interference based on the X-ray scattering coefficients, which in turn depend on the crystal structure. The constructive interference leads to significantly enhanced intensities which are observed as peaks in the observed data. The peaks are observed at specific scattering angles (2θ) which are determined by the Bragg's law ($n\lambda$ = 2d sin θ, where λ= wavelength of X-ray, θ = scattering angle, d = inter-planar distance along a specific atomic plane, n=1,2,3...) [168].

Rietveld analysis was performed using Fullprof software for phase analysis and evaluation of lattice parameters [169]. In the Rietveld method, user-selected parameters are refined by a least squares approach to minimize the difference between an experimental pattern (observed data) and a model based on the hypothesized/identified crystal structure and instrumental parameters (calculated pattern).

3.2.2 Scanning electron microscopy (SEM)

The scanning electron microscopy (SEM) is one of the most important technique widely used for characterization, especially to get detailed information regarding surface morphologies of materials. In this technique, the imaging is performed by scanning a sample (in a raster scan mode) with a focused beam of high-energy electrons generated from an electron gun. As this beam undergoes an accelerating process using specific magnetic lenses, it possess a high kinetic energy that is sufficient to produce signals from the electron-sample interactions. The resultant signals contain several components which are backscattered and diffracted backscattered electrons, secondary electrons which used for the imaging process, photons, visible light and heat. By detecting these signals by the secondary electron detector and processing the obtained data, several information including the 2D image describe the morphology of the sample surface, chemical composition and crystalline structure can be obtained for the investigated material. A modification in SEM is performed by integration of a field-emission cathode into the electron gun in order to produce narrower probing beams at low and high electron energy. This possibility in turn allows for improved spatial resolution, minimized sample charging and providing a high resolution reaching 1.5 nm in aided case. Therefore this property is called field emission scanning electron microscopy (FESEM). In this work, the surface morphology of polished alloy substrates before and after anodization was investigated by field emission scanning electron microscopy (Gemini LEO 1530, Zeiss). The accelerating voltage was 20 kV.

3.2.3 Energy-dispersive X-ray spectroscopy (EDXS)

Energy-dispersive X-ray spectroscopy is an analytical tool used for analyzing the elemental compositions by the interaction between the electron source and the sample under investigation. In this technique, the sample is exposed to focused beam of electron that cause an excitation of electrons from the ground state to the excited

state generating an electron hole. The quantity of the X-rays energies emitted from the sample is detected and counted by an energy-dispersive spectrometer. The counted energies represent a specific characteristic of a certain atomic concentration of the sample to be measured. EDX analysis were performed to investigate the elemental composition of the as-cast alloys using a Bruker XFlash®4010 detector equipped with QUANTAX evaluation software.

3.2.4 Transmission electron spectroscopy (TEM)

Transmission electron microscopy (TEM) is one of the electron microscopy techniques which are based on a focused beam of accelerated electron, obtained by electromagnetic lenses, interacting with and transmitting ultra-thin specimen. The unscattered electrons are then collected in a fluorescent screen at the bottom of the microscopy providing a 2D shadow image of the specimen which can directly recorded with a camera. Transmission electron microscopy (TEM) was conducted using a FEI Tecnai F30 with field emission gun at 300 kV acceleration voltage to characterize the electrodes after the electrochemical cycling. The sample preparation for TEM investigation includes dispersion of scratched oxide films in acetone using an ultrasonic bath for 5 min. A droplet of the suspended solution was spread on a cupper grid and dried in air for 10 min before investigation.

3.2.5 X-ray photoelectron spectroscopy (XPS)

The chemical composition of the fabricated nanotubes was explored using X-ray photoelectron spectroscopy (XPS, PHI 5600CI, Physical Electronics). The hemispherical analyzer worked on a pass energy of 29 eV, base pressure of the system was around 2×10^{-8} Pa. Monochromatic Al K_{α} radiation (350 W) and a low energy flood gun were used for charge neutralization. Binding energy shifts by charging were corrected to the carbon contamination for C 1s at 284.8 eV. The atomic concentrations of elemental Ti and Sn in the grown mixed oxide nanotube electrodes were determined before and after sputtering the nanotubes surface with Ar^{+} ions for 8 min

(beam energy 3.5 keV) with a sputter rate of approximately 3.5 nm min^{-1}. Concentration quantification was carried out with standard single element sensitivity factors. XPS is an effective surface-sensitive characterization technique used for identifying the elemental composition, oxidation state and the empirical formula of transition metal oxides. In this method, a specimen is irradiated with X-ray beams under ultra-high vacuum (UHV) conditions ,allowing the electron to be excited from the ground state to above the Fermi level, and simultaneously measuring the kinetic energy as well as the electron that escaped at the top specimen surface ($\geq$ 10 nm). The X-ray photoelectron spectra contain asset of peaks located at certain values of binding energies correspond to the electron configurations of specific atoms and their chemical environment being analyzed.

3.2.6 Raman spectroscopy

Raman spectra of the fabricated TiO_2-CoO and TiO_2-SnO_2 nanotubes were recorded at a laser power of 8 mW and an excitation wavelength of 532 nm (Thermo Scientific, DXR Smart Raman). Raman scattering spectroscopy is a rapid and powerful characterization technique used for providing further insights about the vibration properties and the composition of the present phases of fabricated oxide nanotubes. This technique is frequently used to identifying both anatase and rutile phases in TiO_2 compounds where, the presence of a well-defined peak located around 144 and 446 cm^{-1} corresponding to E_g vibration modes for anatase and rutile phases, respectively [170]. The principles of this technique is based on the interaction between a monochromatic light, *i.e.* laser beam, and the molecular vibrations of a specimen which causes up or down shifts in energy of laser photons. The calculated energy shifts corresponded to the vibration modes of a system.

3.2.7 Nitrogen sorption isotherms

The nitrogen sorption experiments were carried out for the synthesized TiO_2-CoO and TiO_2-SnO_2 nanotubes after carefully scratching off the nanotube films from

the substrates using a Quantachrome Quadrasorb SI apparatus. Prior to the measurement, the samples were degassed under dynamic vacuum at 150 °C for 24 h. The specific surface areas and the pore size distributions were calculated in the region of relative pressure p/p_0 = 0.05 - 0.2 using the multi-point Brunauer-Emmett-Teller (BET) method [171].

3.2.8 Inductively coupled plasma optical emission spectroscopy (ICP–OES)

The elemental concentrations of the as-cast Ti-Co and Ti-Sn alloys were analyzed by inductively coupled plasma optical emission spectroscopy (ICP-OES) using an IRIS Intrepid II XUV (Thermo Fisher Scientific) apparatus. The sample solution was initially prepared for ICP-OES analysis by dissolving a piece of each alloy in 3 ml of HCl (37%, Merck), 1 ml HNO_3 (65%, Merck), 0.5 ml HF (40%, Merck). The obtained mixture was diluted with deionized water to reach a ratio of 1 g of solid sample to 20 g of total solution. The final solution was placed into a high pressure microwave Teflon vessel and heated to 80 °C for 1 h.

3.3   Basic definitions and electrochemical concepts

3.3.1 Faraday's law

Faraday's law states that the required amount of electricity to change one mole of material is equal to 96485 coulomb as expressed by eq. 3.1 [172]:

$$m = R_F \cdot \frac{M\,Q}{n\,F}$$

(3.1)

where m is the mass of substances formed at the electrode in gram; R_f is the Faradic efficiency which is considered to be equal to 1; M is the molar mass of the substance (g/mol); Q is the amount of electricity transferred in the electrochemical reaction (in

C); n is the number of electrons released per one mole reaction and F is the Faraday's constant (96485 C mol^{-1}).

3.3.2 Capacity

The theoretical capacity of a battery is defined as the quantity of electricity contributed in the electrochemical reactions [173]. It is given in terms of coulomb (C) or Ampere-hour (A.h). Theoretically, it is calculated with Faraday's law, where one gram-equivalent weight of active material releases 96485 C or 26.8 Ah. By dividing the theoretical capacity by the mass of active material, the theoretical is obtained gravimetric capacity as given by equation 3.2 [172].

Theoretical gravimetric capacity: $C_{m\,th}(C\ g^{-1}) = \frac{n \cdot F}{M}$ (3.2)

Coulomb is converted into Ah, as 1 Ah = 1000 mAh = 3600 C, so the theoretical gravimetric capacity is expressed with equation 3.3.

$$C_{m\,th}(mAh\ g^{-1}) = \frac{1000 \cdot n \cdot 96485}{3600 \cdot M} = 26801 \cdot \frac{n}{M} \qquad (3.3)$$

The term specific capacity can be given to gravimetric or volumetric capacity and it may refer to an electrode or a full battery. The practical specific capacity is defined as the ratio between the amount of electricity that can be delivered at a certain discharge/charge current to the total mass of the battery.

3.3.3 Discharge

A process in which an external consumer is applied to an electrochemical cell results in an electron flow from the anode which is oxidized to the cathode across the external circuit. This process is completed by moving the anions and cations inside the electrochemical cell to the anode and cathode, respectively.

3.3.4 Charge

A process in which the ions and the electron flow of a rechargeable cell transport in the opposite directions of the discharge mode. Note that, by definition,

the oxidation and reduction take place at the positive and negative electrodes, respectively. Therefore, the positive electrode now becomes the anode and the negative electrode becomes the cathode.

3.4   Electrochemical techniques

3.4.1 Cyclic voltammetry

Cyclic voltammetry (CV) is one of the potentiodynamic measurements in which a voltage is applied linearly between two values to an electrode at a fixed time against a reference electrode which has a constant potential. This technique is mainly used for providing specific information about the electrochemical reactions of electrodes such as redox reactions and charge-transfer kinetics as well as adsorption processes. The rate of voltage change with time during the measurement is known as scan rate (Vs^{-1}). In typical voltammograms, the current of the working electrode is plotted *versus* the applied voltage. From voltammograms, the location of redox potentials of electroactive materials as well as diffusion properties for the redox reactions can be easily determined.

3.4.2 Galvanostatic discharging/charging cycling

In a galvanostatic discharging/charging process, a fixed current is applied to the electrode with simultaneously measuring the voltage. This test provides valuable insights about the capacity, electrochemical performance, stability, reversibility and cycle life of electrode materials. Usually the electrode performance of a battery depends on the current rate which is applied during the measurements expressed in C/h. The charging/discharge rate is basically calculated from the mass of active material of an electrode according to its capacity. When the battery is completely charged or discharged in a time of a one hour, the applied current rate is equal to 1C. To calculate the capacity, the obtained current is multiplied by the duration of a single charge or discharge step and it is expressed as ampere-hour (Ah). Accordingly,

the specific capacity is the obtained capacity per mass of electrode and, hence, it is expressed in mAh g^{-1}.

3.4.3 Electrochemical impedance spectroscopy (EIS)

It is an electrochemical test used to determine the equivalent resistance R in direct current (DC) measurements. In this technique, a small AC signal (~5 - 10 mV) is applied to an electrochemical cell at a fixed DC bias potential and the impedance Z is measured over a wide range of frequency usually between 0.01 Hz and 1 MHz. The obtained spectrum contains an imaginary part (*Im(Z))* as a function of the real part (*Re(Z)*) using a frequency as a variable parameter.

3.5   Electrode preparation and measurement conditions

3.5.1 TiO$_2$-CoO nanotube electrodes

Binder and carbon-free electrodes were assembled in an Ar-filled glove box under controlled O_2 and H_2O content (< 0.1 ppm). The electrochemical tests were performed in Swagelok-type cells, in which the anodized TiO$_2$-CoO nanotubes were used as working electrodes, lithium foil (Alfa Aesar, 99.9 %) as counter electrode and standard LP30 electrolyte (1 M LiPF$_6$, 1:1 DMC/EC, BASF). All electrochemical measurements were conducted by a multichannel potentiostat/galvanostat (VMP3 potentiostat/galvanostat, Bio-Logic).

Cyclic voltammetry tests (CV) were carried out between 1 - 3 V *versus* Li/Li$^+$ at a scan rate of 0.1 mV s^{-1}. Swagelok cells were cycled (galvanostatic cycling with potential limitation) at various current densities of 10 - 400 μA cm^{-2} between the charging/discharging potentials of 1 and 3 V *versus* Li/Li$^+$. The working electrodes consist of thin oxide films of low significant weights, and their applications would be mostly microbatteries, which recommends normalization of the capacity to the area instead of weight. However, the gravimetric capacities are shown in the text. As a reference, TiO$_2$ nanotubes were assembled and tested at the same parameters. The average weight of the grown oxide nanotubes was determined after removing the

nanotubes from the alloy substrate by sonication in a mixture of ethanol and deionized water (volume ratio 9:1) [174]. Three samples from each anodization voltage were weighted before and after sonication and drying the substrate for 3 h at 120 °C. The mass of each electrode was ≈1.066 mg. The electrochemical impedance spectroscopy (EIS) experiments were conducted after 100 charge/discharge cycles between 100 kHz to 0.1 Hz at a potential of 1.7 V. For *post mortem* analysis the cells were disassembled in the glove box and thoroughly washed with DMC. During transfer to the TEM and the SEM air exposure was minimized as good as possible by short outside handling times.

3.5.2 CNTs@TiO$_2$ and CNTs@TiO$_2$/CoO NTs electrodes

Half cells were assembled as coin cells of the CR2025 type in an Ar-filled glove box under controlled O$_2$ and H$_2$O content (< 0.1 ppm), in which CNTs@TiO$_2$ and CNTs@TiO$_2$/CoO NTs were used as working electrodes, a lithium foil (Alfa Aesar, 99.9 %) as counter electrode, a Celgard 2500 polypropylene separator with 16 mm diameter and 25 µm thickness, and the standard LP30 electrolyte (1 M LiPF$_6$, 1:1 v/v DMC/EC, BASF). The mass of the deposited CNTs was determined by weighing the electrode before and after the spray pyrolysis step. The average CNT mass per electrode area was ≈0.12 mg. Cyclic voltammetry tests (CV) were carried out in a potential range of 0.1 - 3 V *vs.* Li/Li$^+$ at a scan rate of 0.1 mV s^{-1}. The assembled cells were then galvanostatically cycled at a current density of 50 µA cm^{-2}, corresponding to a current density of 1C between 0.1 and 3 V *vs.* Li/Li$^+$. For comparison, pure TiO$_2$ and TiO$_2$/CoO NTs were assembled and tested under identical conditions. Electrochemical impedance spectroscopic (EIS) tests were conducted between 100 kHz to 0.1 Hz at a potential of 1.7 V after 50 charging/discharging cycles at a current density of 50 µA cm^{-2}.

3.5.3 TiO$_2$-SnO$_2$ nanotube electrodes

The as-fabricated nanotubes were directly used without additional binder or conductive additives. The Ti-Sn substrates served as current collectors. Swagelok-type cells, in which the TiO$_2$-SnO$_2$ nanotubes were used as working electrodes, a lithium foil (Alfa Aesar, 99.9 %) as counter electrode, two pieces of glass fiber (Whatman) as separator and standard LP30 electrolyte (1 M LiPF$_6$, 1:1 DMC/EC, BASF) were assembled in an Ar-filled glove box under controlled O$_2$ and H$_2$O content (< 0.1 ppm). Cyclic voltammetry tests (CV) were carried out between 0.1 - 3 V *versus* Li/Li$^+$ at a scan rate of 0.1 mV s^{-1}.

All cells were cycled (galvanostatic cycling with potential limitation) at a current density of 504 µA cm^{-2} i.e. 335 mAhg^{-1} corresponds to a current density of 1C (1C means complete discharging in 1 h) between the charging/discharging potentials of 0.1 and 3 V *versus* Li/Li$^+$. We normalized the capacity to the area instead of the weight, however, the gravimetric capacities are shown in the text due to the fact that the working electrodes are thin oxide films of low significant weights. For comparison, TiO$_2$ nanotubes were assembled and tested under the same conditions. To determine the average weight of the grown oxide nanotubes, the anodized substrates were sonicated in a mixture of ethanol and deionized water (volume ratio 9:1) in order to separate the nanotubes from the alloy substrates. The anodized substrates from each alloy were dried for 3 h at 120 °C and weighed before and after sonication. The mass of each electrode was ≈1.9 mg. Electrochemical impedance spectroscopic (EIS) experiments of assembled cells were performed between 100 kHz to 0.1 Hz at a potential of 1.7 V before and after 100 cycles at a current density of 50 µAh cm^{-2}.

Chapter 4

TiO₂-CoO nanotubes as anodes in lithium ion batteries
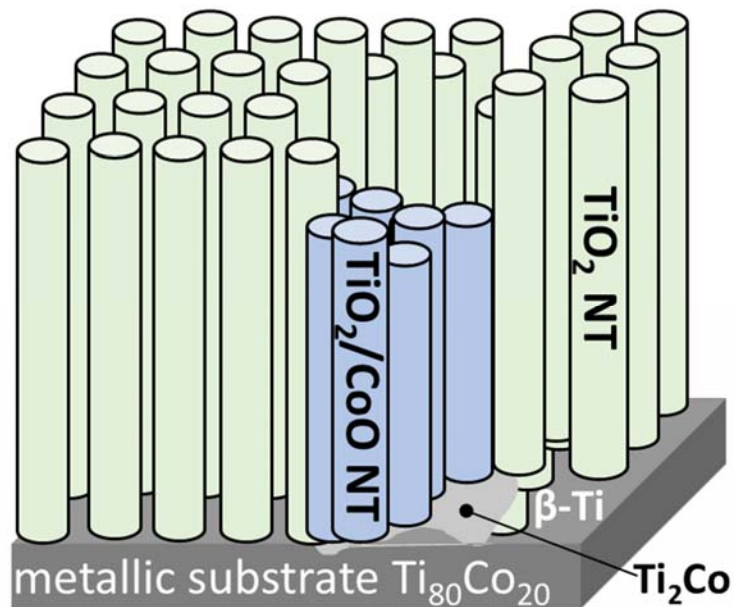
In this chapter detailed results and discussion of characterizations and the electrochemical testing of TiO₂-CoO NT electrodes are presented.

4.1 Introduction

As it is discussed previously, TiO_2 nanotubes fabricated by anodic oxidation are well-aligned, and exhibit uniform tube diameters, wall thicknesses as well as high surface areas. These properties help to maximize the contact between electrode and electrolyte and to reduce the lithium ion diffusion path. The Ti-Co-O system is a very promising candidate to significantly contribute to the physicochemical properties such as the relatively high electric and ionic conductivity of CoO to those of TiO_2. Additionally, 1D architectures can effectively hinder pulverization and the structure failure resulting from the large volume changes during lithium ion insertion/extraction. Therefore, combining of CoO to TiO_2 nanotubes in an elegant 1D nanostructure results in durable electrodes with high structural stability that fit the Li^+ ion insertion and extraction process. Furthermore, the nanotubes grown on the substrate, which concurrently serves as current collector, allows for the good contact between the active materials and the current collector and save the extra cost for binder and additive materials during battery assembly. In this chapter, detailed results and discussion related to the characterization of TiO_2-CoO NT will be presented to emphasize the possibility to fabricate self-organized TiO_2-CoO nanotubes on a current collector of atomic composition $Ti_{80}Co_{20}$. Results of electrochemical testing of TiO_2-CoO NT electrodes will be discussed to explore the effect of the presence such mixed oxides on the lithium ion storage for TiO_2 nanotubes.

4.2 Characterization

4.2.1 Phase identification of as cast Ti-Co alloy

In the current work, a Ti_{80}-Co_{20} alloy was casted at 1210 °C to prepare substrates for the anodic oxidation synthesis. **Figure 4.1** represents the phase diagram of the Ti-Co alloy. X-axis shows the cobalt concentration in atomic percent

increases towards the left direction reaching a 100% at the end. Y-axis displays the corresponding temperature at which the phases are formed. In molten form at 1210 °C the composition was Ti$_{80}$-Co$_{20}$. According to the phase diagram, ß-Ti starts to precipitate in the liquid. As ß-Ti can only dissolve up to 14.5 at.% Co [175] therefore, during the precipitation of ß-Ti the rest of the Co (up to 5.5 at.%) will be ejected out in the liquid. This shifts the composition of liquid towards the Eutectic composition. At 1020 °C, all of the remaining liquid is transformed into Eutectic mixture (ß-Ti + Ti$_2$Co). By cooling down the alloy to 685 °C, an α-Ti phase is formed.
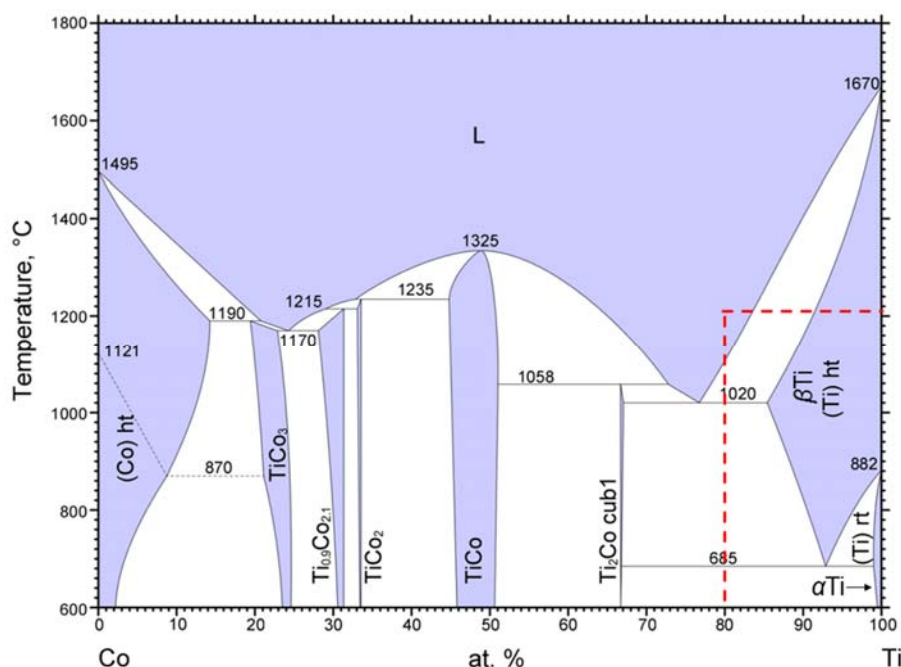
Fig. 4.1. *Ti-Co phase diagram adapted from ref.* [175].

The elemental concentrations of the as-cast Ti-Co alloy was analyzed by inductively coupled plasma optical emission spectroscopy (ICP-OES analysis) The concentrations of elemental Ti and Co are 79.845 and 20.155 ± 0.001 at.%, which are in good agreements with the desired chemical compositions, indicating the high quality of the as-cast alloy. The phase composition of the as-cast Ti-Co substrates was investigated by XRD and the corresponding pattern is shown in **Figure 4.2a**. The as-

cast alloy consists of two phases; the first is a ß-Ti phase and the second is a Ti$_2$Co phase. All measured reflections of the two phases are in agreement with the cubic structure of ß-Ti ($Im\bar{3}m$) [176] and the cubic structure of Ti$_2$Co ($Fdm\bar{3}m$) [177].
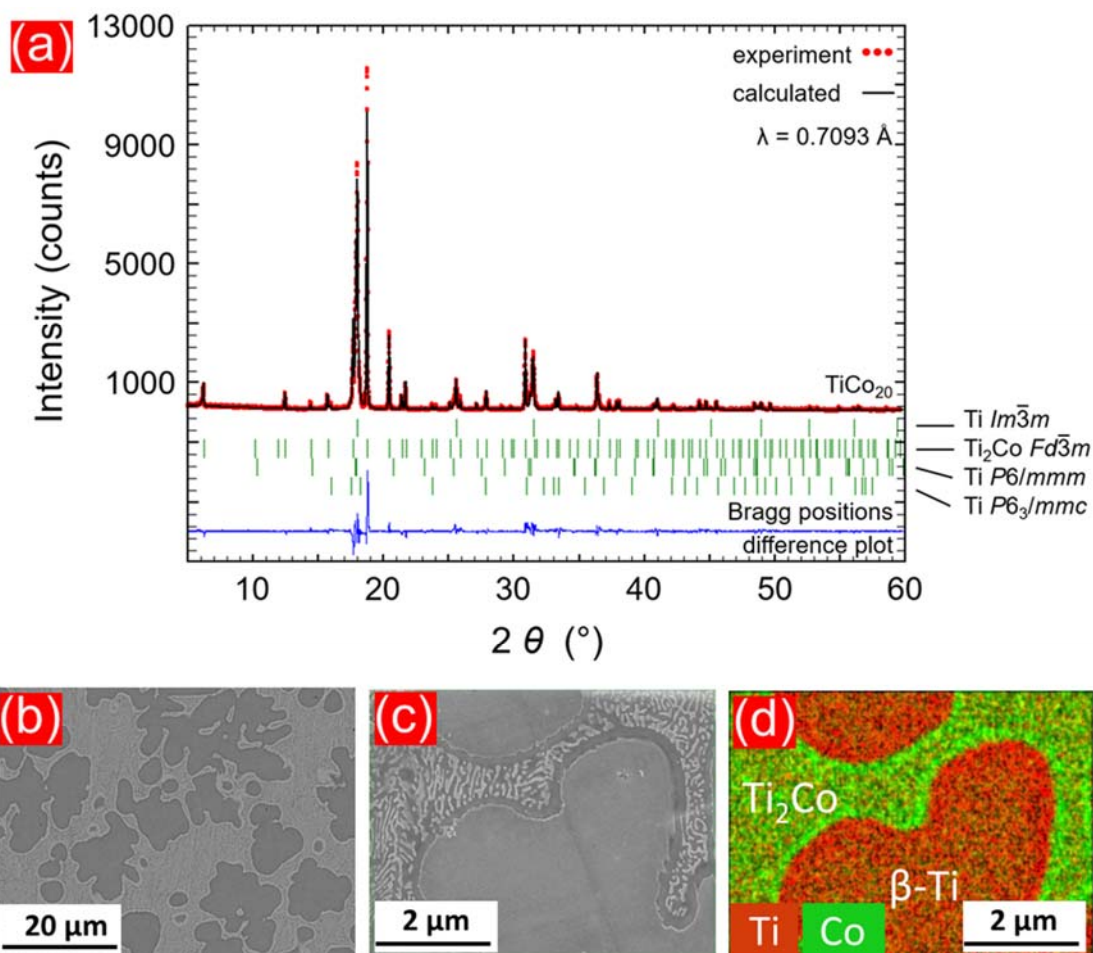
Fig. 4.2. *X-ray diffraction pattern (a), SEM micrographs (b,c) and EDXS element mapping (d) of the as-cast Ti-Co alloy with green color for the Co signal and red for the Ti signal.*

Other phases such as *α*-Ti ($P6_3/mmc$) [178] or ω-Ti ($P6/mmm$) [179] may be present in traces and cannot be completely excluded. The microstructures of the as-cast Ti$_{80}$Co$_{20}$ alloy is presented in **Figure 4.2 b** and **c**. Two different phases are distributed over the as-cast sample cross-section. The dark areas are related to ß-Ti

whereas the bright areas represent the Ti$_2$Co phase. Additionally the lamellar structure in **Figure 4.2c** corresponds to an eutectic mixture of ß-Ti and Ti$_2$Co.

EDX element mapping for Ti and Co, as presented in **Figure 4.2d,** exhibits the allocation of both Ti and Co with different contents in each phase. According to the phase diagram of the Ti-Co system, the maximum solubility of cobalt in ß-Ti and Ti$_2$Co is ~ 14.5 % (at 1020 °C) and ~ 33 %, respectively, which indicates the possibility to grow mixed oxide nanotubes in both phases [175].

4.2.2 Time-current density relationship

Figure 4.3a explains the time-current density relationship during the anodic oxidation of Ti$_{80}$Co$_{20}$ substrates measured at different anodization potentials. At the beginning the current density rapidly increases due to the growing of metal oxide films. At the peak maximum (P1), the metal surface becomes totally oxidized. Afterwards, the drop in the current density occurs because of the passivation effect of the formed oxide layer. Compared to the current density transients of pure Ti (**Figure 4.3b),** an additional peak (P2) was observed for Ti$_{80}$Co$_{20}$ at 10.8 V that corresponds to an anodization time of 9 min. The origin of this peak is related to crack formation as well as to a fresh surface oxidation resulting from an internal surface stress in the ß-Ti phase as shown in **Figure 4.4**. The stress at the initial stage of the NT growth is attributed to the presence of the two phases, ß-Ti and Ti$_2$Co, with different and unrelated crystal structures. Both phases retain their stability without any cracking before an anodization time of 9 min (**Fig. 4.4**). After relaxation, the current density decreases due to oxide formation. At point P3, the current density increases again induced by field-assisted chemical dissolution of the oxides by the fluoride ions in the sense of an etching process [21,143].
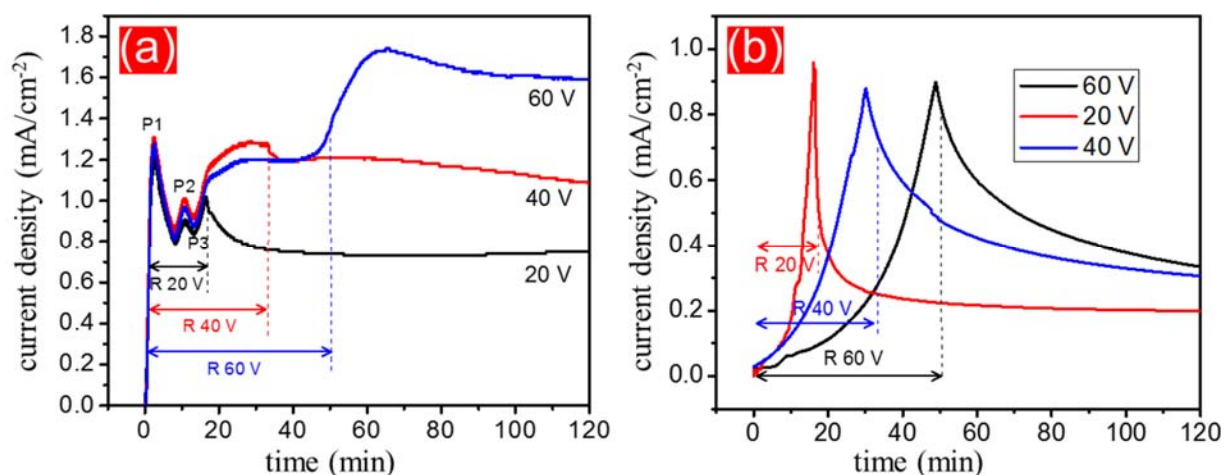
Fig. 4.3. Time-current density relationship of fabricated nanotubes at different anodic oxidation potentials of a Ti$_{80}$Co$_{20}$ substrate (a) and pure Ti substrate (b).

Ramping periods reaching constant anodization potentials are displayed as R20V, R40V and R60V (**Fig. 4.3a**). Subsequently, the current density ends in a plateau at steady-state conditions corresponding to an equilibrium between the rate of metal oxidation and chemical etching. SEM images of the early stage of anodization prove the possibility of grown nanotubes on both alloy phases as presented in **Figures 4.4** and **S1** (supplementary information).
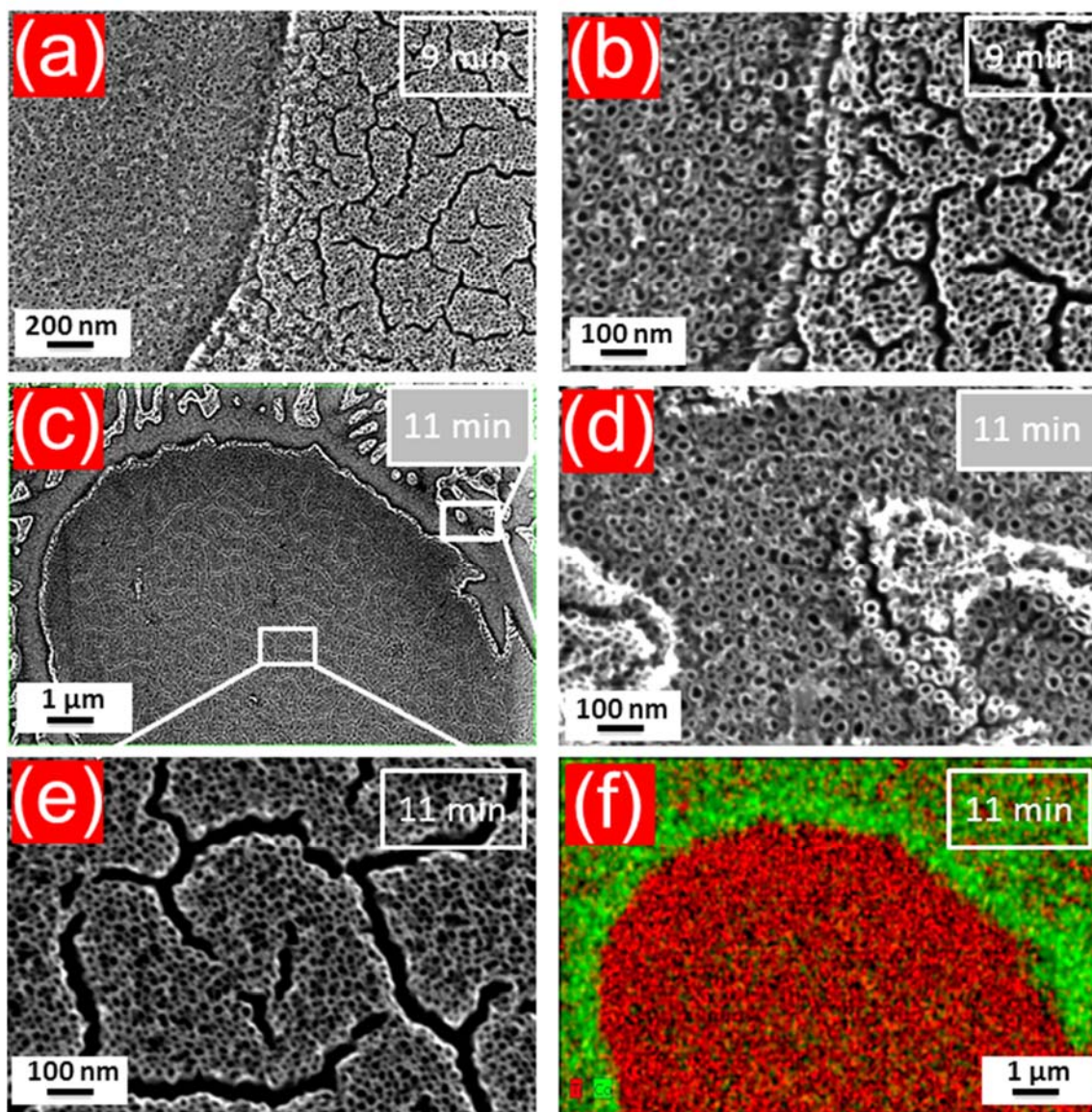
Fig. 4.4. *SEM micrographs of the Ti-Co alloy anodized for 9 min. (a,b), anodized for 11 min. (c), the β-Ti phase anodized for 11 min as magnification (d) of (c), the Ti₂Co phase anodized for 11 min as magnification (e) of (c) and EDXS element mapping (f) of (c) with green color for the Co signal and red for the Ti signal.*

4.2.3 Morphology of the fabricated TiO₂-CoO nanotubes

Representative images of the Ti-Co alloy microstructures after anodic oxidation are shown in **Figure 4.4.** Micrographs **a, c** and **e in Figure 4.5** represent highly magnified images of the ß-Ti phase, whereas micrographs (b), (d) and (f)

correspond to the Ti$_2$Co phase both anodized at 20, 40 and 60 V, respectively. Cross section views in the insets of **Figure 4.5 c** and **d** underline the successful fabrication of nanotubes on both phases of the prepared alloy. The nanotubes grown on the ß-Ti phase are self-organized, well-aligned and uniform in length. However, the nanotube arrays fabricated on the Ti$_2$Co phase are distributed irregularly and are defined by much shorter length than those grown on the ß-Ti region. The mean lengths of the nanotubes on the ß-Ti phase and Ti$_2$Co after 5 h at 60 V were determined to 27 ± 1 μm and 24 ± 1 μm, respectively, as presented in **Figure 4.6a and b.** A similar behavior was reported for a Ti-6Al-7Nb alloy and was attributed to different etching rates of two different Ti phases during the anodic oxidation [180]. The nanotube diameters and wall thicknesses of both alloy phases are independent of the applied potential. For the ß-Ti phase, the inner tube diameters range from 37 - 45 nm. The inner tube diameters of Ti$_2$Co are smaller than those of the ß-Ti phase ranging from 33 - 40 nm. The thickness of the tube walls of both phases reaches 10 ± 3 nm.

The bottom view of the fabricated nanotubes after mechanically scratched off the substrate are shown in the insets of **Figure 4.5e** and **f.** The bottoms of the nanotubes grown on both phases are closed. EDX mapping of the anodized alloy in **Figure 4.4** showed that the nanotubes formed on the ß-Ti phase mainly contain Ti species with some Co whereas the Ti$_2$Co phase clearly shows both Ti and Co species. From these results, a mixture of TiO$_2$ nanotubes with CoO nanotubes is deduced for both phases but with differing characteristic and behavior depending on the amount of Co or, later, CoO involved in the anodization process. This difference may be expressed in different growth kinetics of the TiO$_2$ and the CoO nanotubes which leads to different tube heights and growth homogeneities as well as an inhomogeneous tube alignment on the array. This phenomenon is also observed for various Ti-based alloys [180–182] that contain minimum two phases during the anodic oxidation process. The main reason is attributed to a differing etching behavior of the individual phases. This unequal etching results in a partial chemical dissolution of one phase and a

complete dissolution of the second phase could occur. Consequently, irregular surface morphologies of the grown nanotube arrays are obtained.
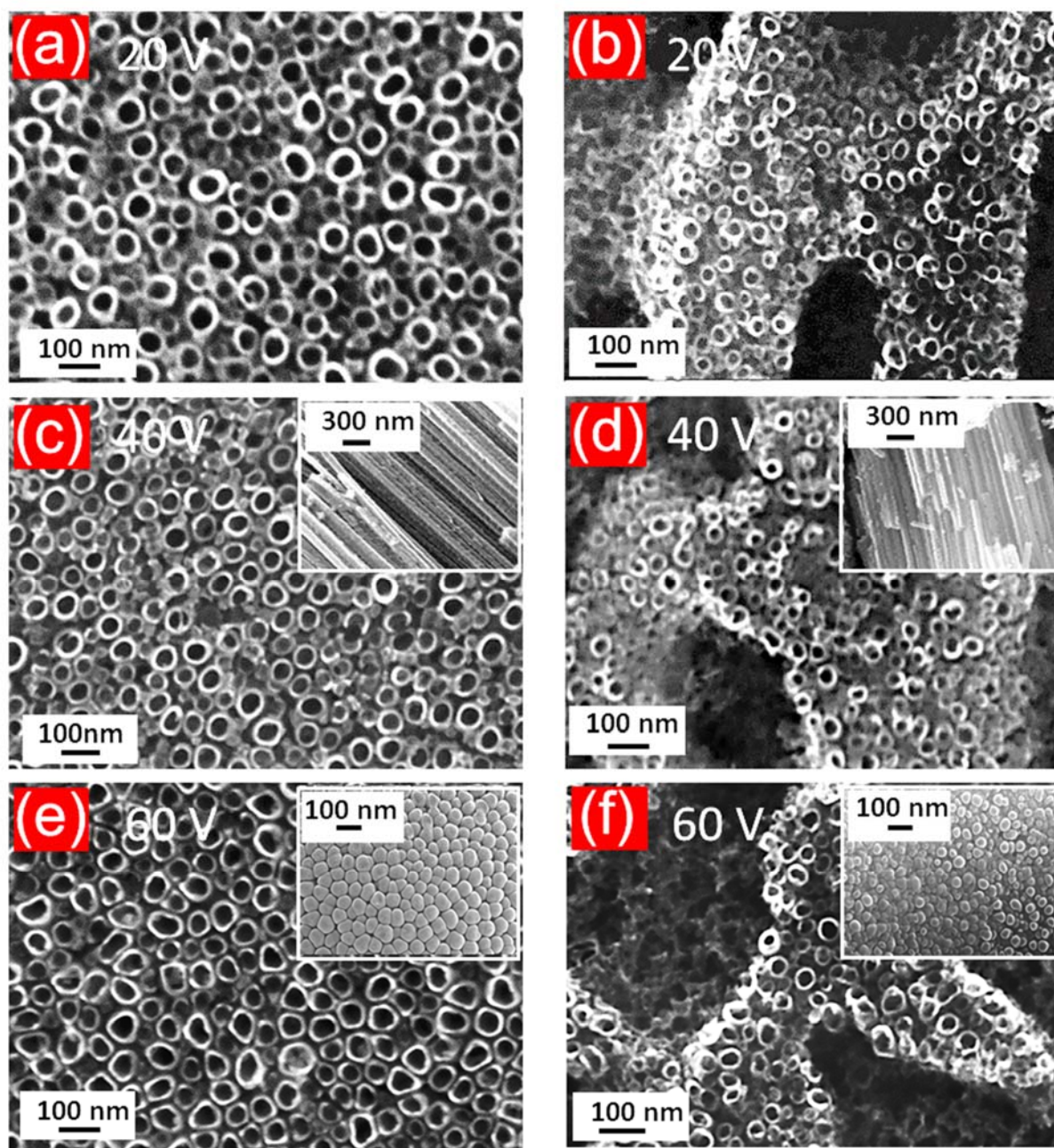
Fig. 4.5. *SEM micrographs of the Ti-Co alloy with the β-Ti phase anodized at 20 V (a), 40 V (c) and 60 V (e), respectively and the Ti₂Co phase anodized at 20 V (b), 40 (d) and 60 V (f) for 5 h. Both phases are visible by element contrast and tube growth behavior.*
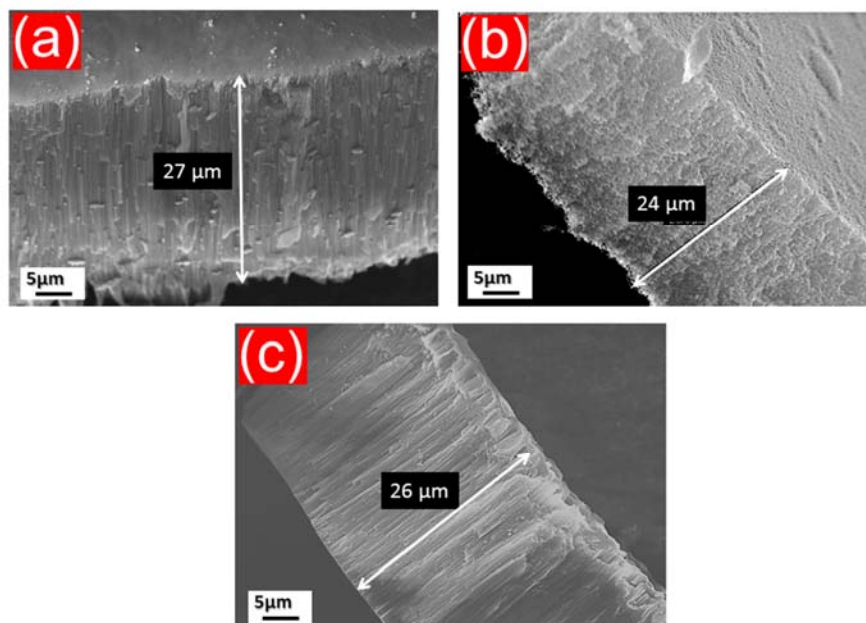
Fig. 4.6. *SEM micrographs with cross sectional views of the alloy Ti₂Co substrate anodized at 60 V for the β-Ti phase (a) and the Ti₂Co phase (b). Cross sectional view of the pure Ti substrate anodized at 60 V (c).*

The average elemental ratio of the anodized alloy, obtained by EDX analysis, was 86:14 for Ti and Co, respectively, which matches the element content of the as-cast alloy. The different etching rates of the alloy phases can be affected by its atomic ratio. SEM images of TiO$_2$ nanotubes fabricated under identical anodic oxidation conditions at 20, 40 and 60 V are presented in **Figure 4.7a, b** and **c**, respectively. The growth of the nanotube diameters is proportional to the formation voltage which is in agreement with the literature [183]. The mean nanotube diameters measured are 75, 105 and 130 nm for the samples prepared at 20, 40 and 60 V, respectively. Image **d** in **Figure 4.7** shows the tubular structure of the formed tubes which are closed at the bottoms as seen in the inset. The average nanotube lengths for the TiO$_2$ nanotubes formed at 60 V are determined with 26 ± 1 μm as presented in **Figure 4.6c**.
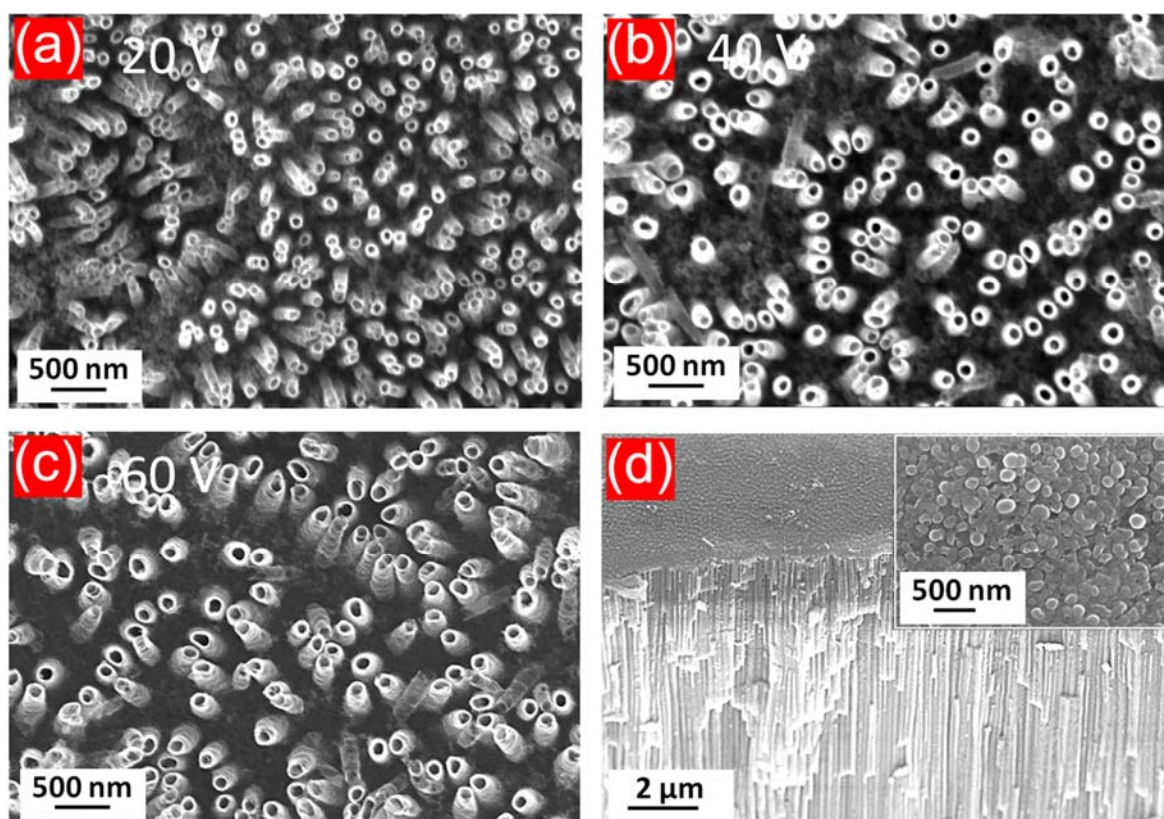
Fig. 4.7. *SEM micrographs of the pure Ti, anodized at 20 V (a), 40 V (b) and 60 V (c), respectively. Cross sectional view for the sample treated at 60 V (d). The inset in (panel d) shows the nanotube bottoms.*

Compared to the ß-Ti phase on the Ti-Co alloy, the nanotubes grown on the Ti substrate exhibit small gaps between the tube walls. Therefore, the contact between the neighboring nanotubes is lower than for the nanotubes formed on the ß-Ti phase of the Ti-Co alloy. From the more intense contact of the tubes formed on the Ti-Co alloy, a better ion transfer and therewith a faster diffusion of ions are expected in the electrochemical measurements described below.

4.2.4 Phase identification of the fabricated TiO$_2$-CoO nanotubes

The structural characterization of the obtained nanotubes on the Ti-Co alloy was performed using X-ray diffraction and the patterns corresponding are presented in **Figure 4.8a**. Due to the absence of specific reflections, no hint on the growth of a crystalline oxide film is found. An amorphous state or a very low degree of

crystallization is concluded from this observation before annealing. To enhance the crystallinity, the as-anodized substrates were subjected to a thermal treatment for 3 h at 450 °C in air with a heating rate of 1 °C min^{-1}. For the annealed substrates, reflections are observed at $2\theta = 29.5°$ corresponding to the 101 reflection of the tetragonal anatase phase (space group $I4_1/amd$) [184].
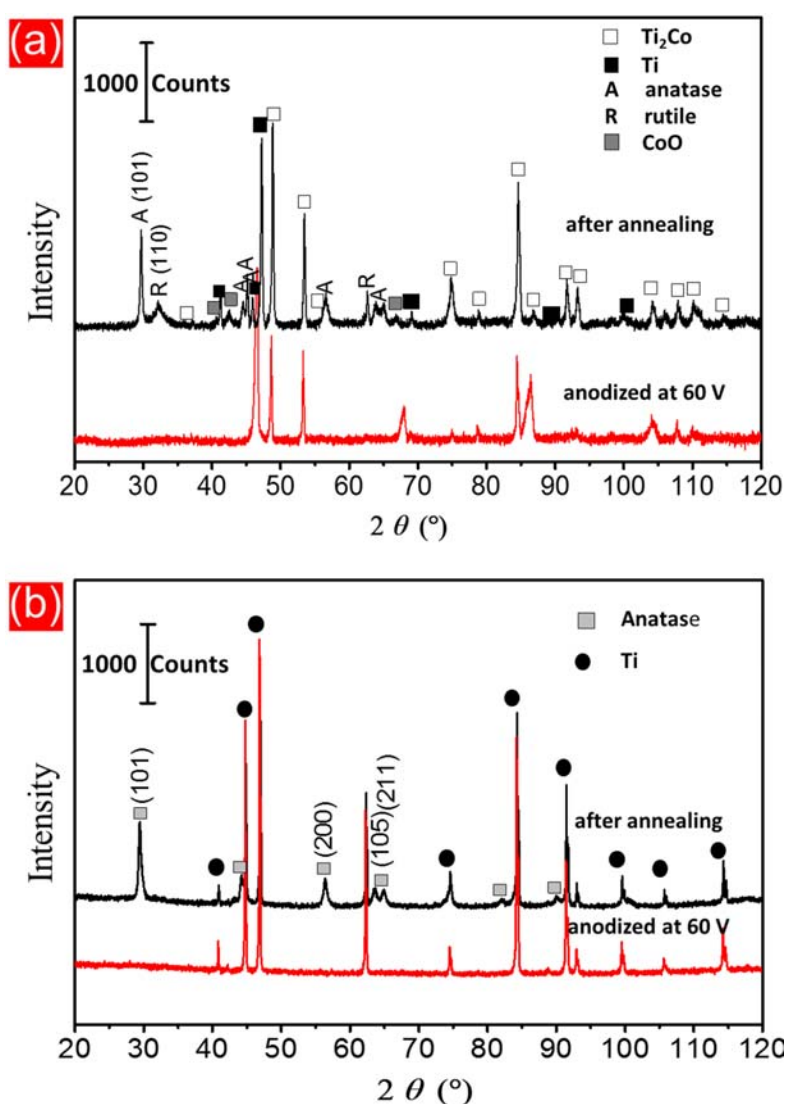
Fig. 4.8. *X-ray diffraction patterns of the anodized alloy substrate at 60 V before and after annealing (a) and the anodized Ti substrate treated at 60 V before and after annealing (b).*

An additional reflection is found at $2\theta = 32°$ that is related to the 110 reflection of the tetragonal rutile structure (space group $P4_2/mnm$) [185]. Moreover, the signal

appearing at $2\theta = 42.7°$ is assigned to the 101 reflection of hexagonal CoO (space group $P6_3mc$) confirming the formation of an additional oxide phase [186]. After the thermal treatment, the reflections of the ß-Ti phase are diminished and the reflections of α-Ti appeared. This behavior may be due to separation of cobalt from the ß-Ti phase by oxidation and oxide formation. The cobalt concentration together with applied temperature (450 °C) may not reach the formation temperature and necessary composition for ß-Ti and ends up with α-Ti. In the X-ray pattern of the anodically oxidized and the annealed sample (**Fig. 4.8a**), this separation is recognized as the reflection at 67.5° 2θ splits into reflections corresponding to CoO and α-Ti. **Figure 4.8b** shows the XRD patterns for the as-grown nanotubes on the Ti substrate. The strong 101 reflection was observed for the pure Ti corresponding to the α-Ti phase (space group $P6_3/mmc$) [176]. No noticeable reflections for TiO$_2$ are observed indicating the as-formed nanotubes to be amorphous. Reflections are indexed by the structure model for (space group $I4_1/amd$) [187] after annealing of the formed nanotubes at 450 °C in air.

4.2.5 Specific surface area of the fabricated TiO$_2$-CoO nanotubes

Nitrogen physisorption experiments were carried out in order to determine the porosity and the specific surface area of the samples. In both cases the nitrogen adsorption and desorption isotherms shown in **Figure 4.9a** and **c** exhibit type-H1 shapes which are considered to be indicative for the presence of mesopores with a pore diameter (2 nm < d < 50 nm). This result is in accordance with the observations from SEM investigations (**Fig. 4.6**). In addition, the voids between individual tubes or bundles thereof can be viewed as macropores (d > 50 nm), thus leading to the quickly increasing amount of adsorbed nitrogen in the high-pressure regions of the isotherms.
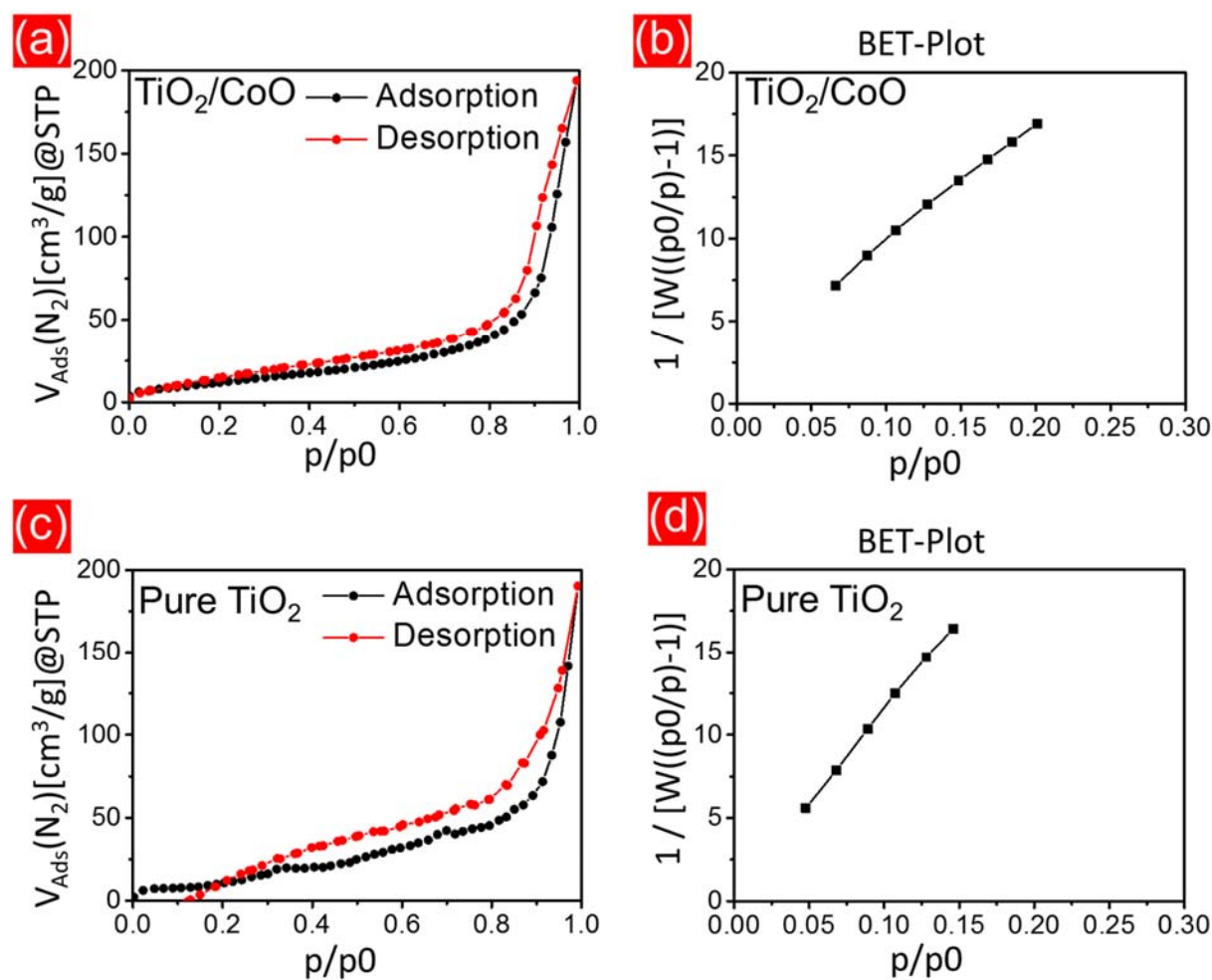
Fig. 4.9. *Nitrogen sorption analysis for the TiO$_2$-CoO (a,b) and pure TiO$_2$ NT (c,d), anodized at 60 V.*

The BET method [171] was used to determine the specific surface area of the samples revealing a higher specific surface area and a larger pore volume for TiO$_2$-CoO nanotubes (46 m^2 g^{-1} and 0.19 cm^3 g^{-1}) in comparison to pure TiO$_2$ nanotubes (38 m^2 g^{-1} and 0.16 cm^3 g^{-1}). The respective BET plots of TiO$_2$-CoO and pure TiO$_2$ nanotubes are presented in **Figure 4.9b** and **d**, respectively.

4.2.6 XPS investigation of the grown TiO₂-CoO nanotubes

To elucidate the chemical composition of the grown nanotubes on the Ti-Co alloy, XPS analyses were performed. The spectra of the annealed nanotubes are presented in **Figure 4.10a-d**. Charging effects of the samples make corrections to the binding energy (BE) scale necessary. The Ti 2p spectra (**Fig. 4.10a**) show no broadening and are similar in shape and binding energy position as reported for TiO$_2$ [21,22], thus titanium is present as tetravalent Ti. The observed peak of Ti 2p$_{3/2}$ is therefore suited for BE referencing. Consequently, spectra are shifted to the Ti 2p$_{3/2}$ signal at 459 eV by 0.4 eV.

Strong Co 2p peaks are observed with maxima at 781.5 eV (2p$_{3/2}$) and 797.5 (2p$_{1/2}$) eV with a spin-orbit splitting of 16 eV that agrees well with the Co 2p signal of CoO [188]. No indication for metallic cobalt is recognized (**Fig. 4.10b**). The shake-up satellite peaks are usually situated 6 eV above the main peaks of Co 2p [189]. It has been widely discussed in literature that the satellite structure at this BE value is characteristic for divalent cobalt in CoO [190]. The observed O 1s peak at 531 eV is another indication for the presence of metal oxides [21] and at 533.2 eV for hydroxyl groups [11] (**Fig. 4.10c**). The P 2p peak in **Figure 4.10d** appears at 134.2 eV indicating a pentavalent-oxidation state of an oxygen-bound cationic phosphorus species [190]. From these results a successful formation of TiO$_2$-CoO nanotube films from a Ti-Co alloy are deduced but mixed Ti-Co-O nanotubes cannot be excluded. The latter is possible since TiO$_2$ always assimilates certain amounts of other, especially transition metal, elements. Phosphorus remains chemically-sorbed on the surface of the nanotubes with a content of about 1 at.% from H$_3$PO$_4$ due to its presence in the anodic oxidation bath.
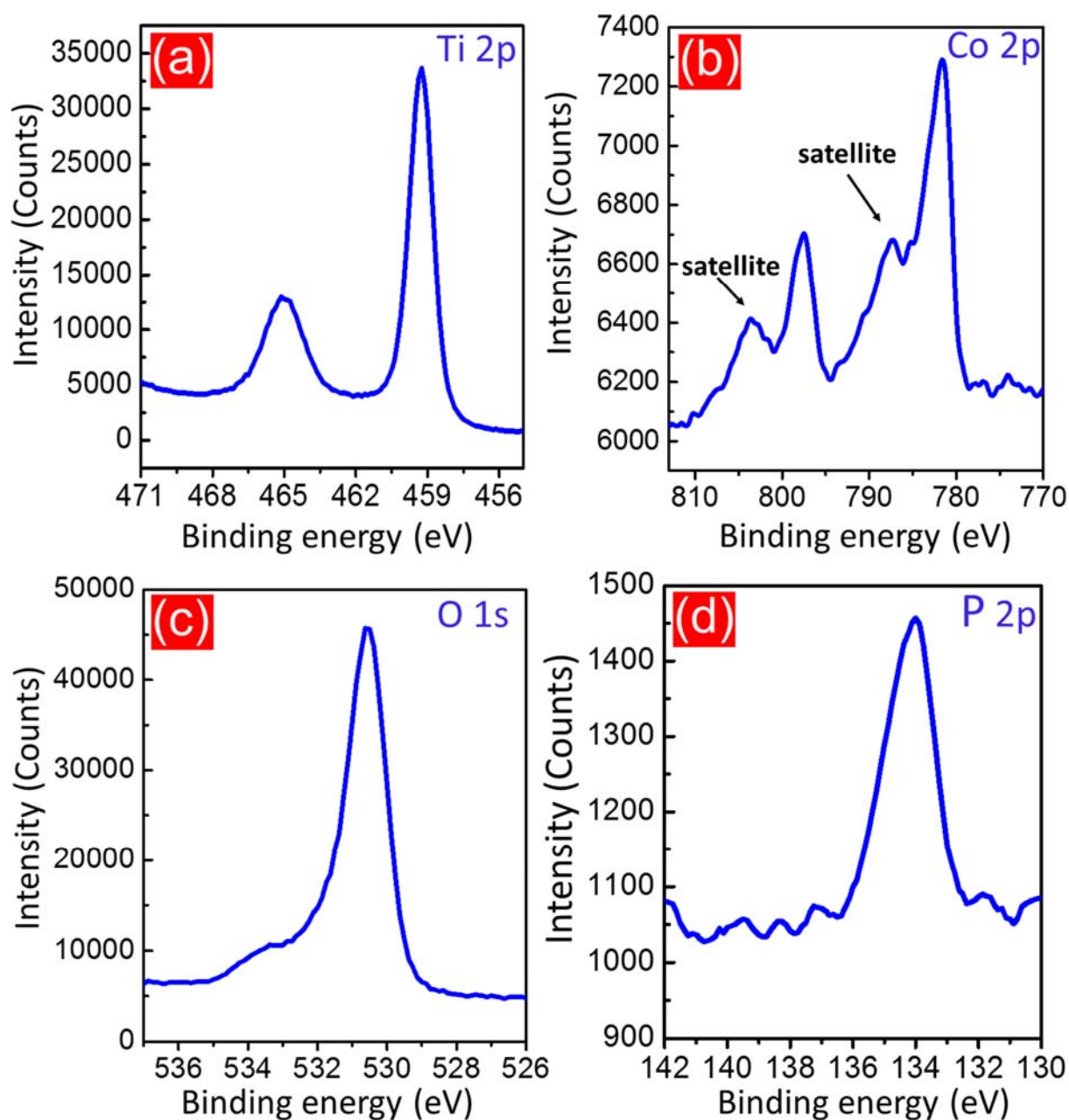
Fig. 4.10. *X-ray photoelectron spectra of the grown nanotubes on the Ti-Co alloy at 60 V after annealing for the binding energies Ti 2p (a), Co 2p (b). O 1s (c) and P 2p (d).*

4.2.7 Raman spectroscopy of TiO₂-CoO nanotubes

In order to provide further details about the structure properties of the fabricated oxide nanotubes, Raman scattering spectroscopic investigation was performed as another effective characterization tool. **Figure 4.11** shows Raman spectra of the pure TiO_2 and TiO_2-CoO nanotubes, grown at 60 V after annealing. Five pronounced peaks located 146, 198, 396, 517 and 639 cm^{-1} are clearly seen in all spectra. These peaks are assigned to the E_g, E_g, B_{1g}, A_{1g} and E_g vibration modes, respectively of the tetragonal anatase of TiO_2 [191–193].
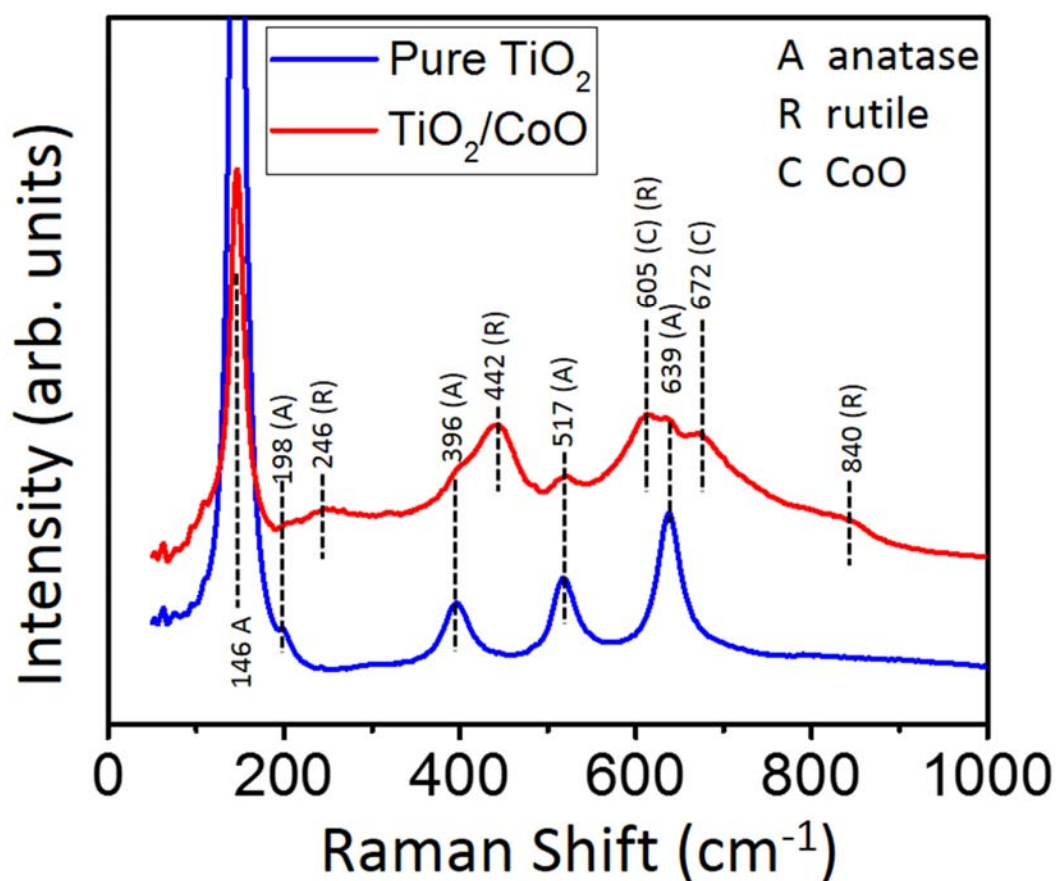
Fig. 4.11. *Raman spectra of the pure TiO₂ and TiO₂-CoO grown at 60 V after annealing.*

The Raman spectrum of the TiO$_2$-CoO nanotubes exhibits two additional peaks at 672 and 605 cm^{-1} match those of CoO [194,195]. Note three peaks are appeared at 246, 442 and 840 cm^{-1} which are characteristic for a multi-photon process, E$_g$, and B$_{2g}$ modes of rutile phase [170]. Moreover, the ca. 605 cm^{-1} peak could also be associated with that reported for rutile [192] (610 cm^{-1}) with a slight Raman shift of 5 cm^{-1}. The Raman analysis is in a good agreement with results of XRD and XPS measurements, indicating the successful formation of TiO$_2$-CoO nanotubes.

4.3 Electrochemical testing of TiO$_2$-CoO electrodes

4.3.1 Cyclic voltammetry tests

Cyclic voltammograms of TiO$_2$ nanotubes and TiO$_2$-CoO nanotubes formed at 60 V after annealing at 450 °C are shown in **Figure 4.12a** and **4.12b**, respectively. Both samples were tested between 1 and 3 V at a scan rate of 0.1 mV s^{-1} *versus* Li/Li$^+$ electrode. Lithium ions easily intercalate into tetragonal anatase by solid state diffusion to yield in orthorhombic Li$_x$TiO$_2$ according to equation (4.1) where $0 \leq x \geq 1$ [196].

x Li$^+$ + TiO$_2$ + x e$^-$ $\leftrightarrow$ Li$_x$TiO$_2$ (4.1)

For the TiO$_2$ sample, anodic and cathodic peaks are located at 1.64 and 2.24 V *vs.* Li/Li$^+$, respectively, and are typically ascribed to lithium insertion and extraction from the anatase phase (**Fig. 4.12a**). The presence and almost identical height of the peaks in both the oxidic and reductive branch of the cyclic voltammograms indicates the reversible Li$^+$ insertion and extraction. The potential separation between the anodic and cathodic peaks in the voltammogram is 0.6 V. For the annealed TiO$_2$-CoO nanotubes sample (**Fig. 4.12b**), a pair of anodic/cathodic peaks is observed at 1.7 and 2.06 V *versus* Li/Li$^+$, respectively. Two irreversible cathodic peaks present at 1 and 1.4 V appear in the first cycle which is attributed to the formation of a stable solid electrolyte interface (SEI). Compared to the TiO$_2$ electrode, the potential difference between the anodic and cathodic peaks is 0.36 V which is much lower than that of the TiO$_2$ electrode. This remarkable reduction in the voltage separation for TiO$_2$-CoO nanotubes is an indication for better reversibility as well as faster Li$^+$ ion diffusion as

reported in the literature [174]. Therefore, larger lithium ion storage is expected for TiO$_2$-CoO nanotubes sample.
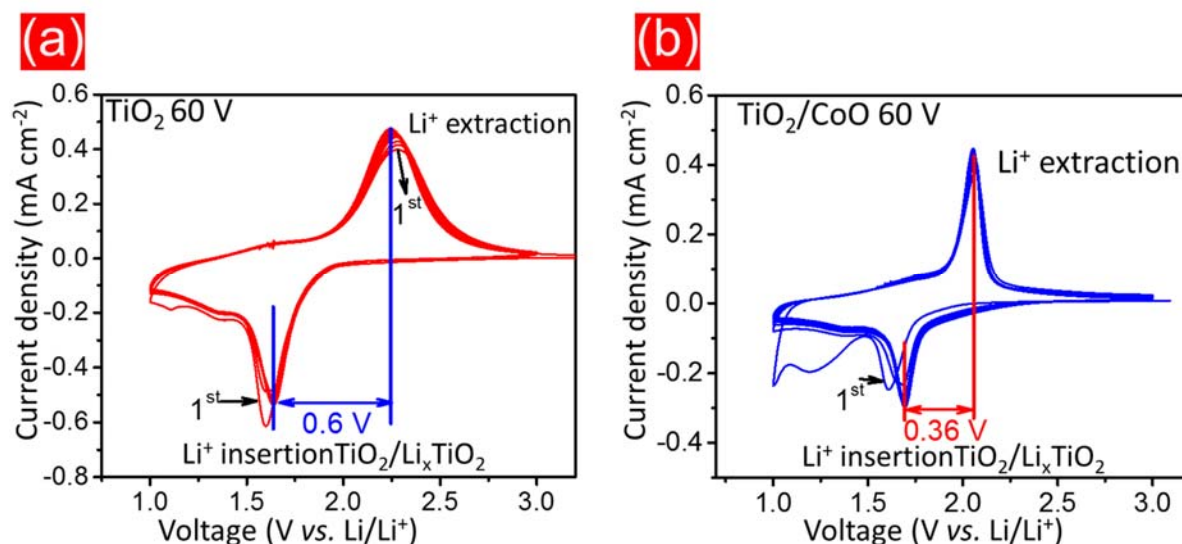
Fig. 4.12. *Cyclic voltammograms of TiO$_2$ (a) and TiO$_2$-CoO nanotubes (b), prepared at 60 V, measured at scan rates of 1 mVs^{-1}.*

4.3.2 Galvanostatic Cycling with Potential Limitation

Galvanostatic discharging (lithium insertion) and charging (lithium extraction) measurements were carried out between 1 - 3 V *versus*. Li/Li$^+$. **Figure 4.13a** displays the charging/discharging curves at a current density of 50 µA cm^{-2} for both TiO$_2$-CoO and pure TiO$_2$ samples formed at 60 V and the inset of **Figure 4.13a** represents the corresponding Coulombic efficiency. The TiO$_2$-CoO electrode show initial discharging/charging capacities of 435 and 325 µAh cm^{-2}, respectively (*i.e.* 229 and 171 mAh g^{-1}) with Coulombic efficiencies of ~ 75 %. The initial discharging/charging capacities of the pure TiO$_2$ electrode reach 250 and 182 µAh cm^{-2} (*i.e.* 150 and 109 mAh g^{-1}) corresponding to a Coulombic efficiency of around 72 %.
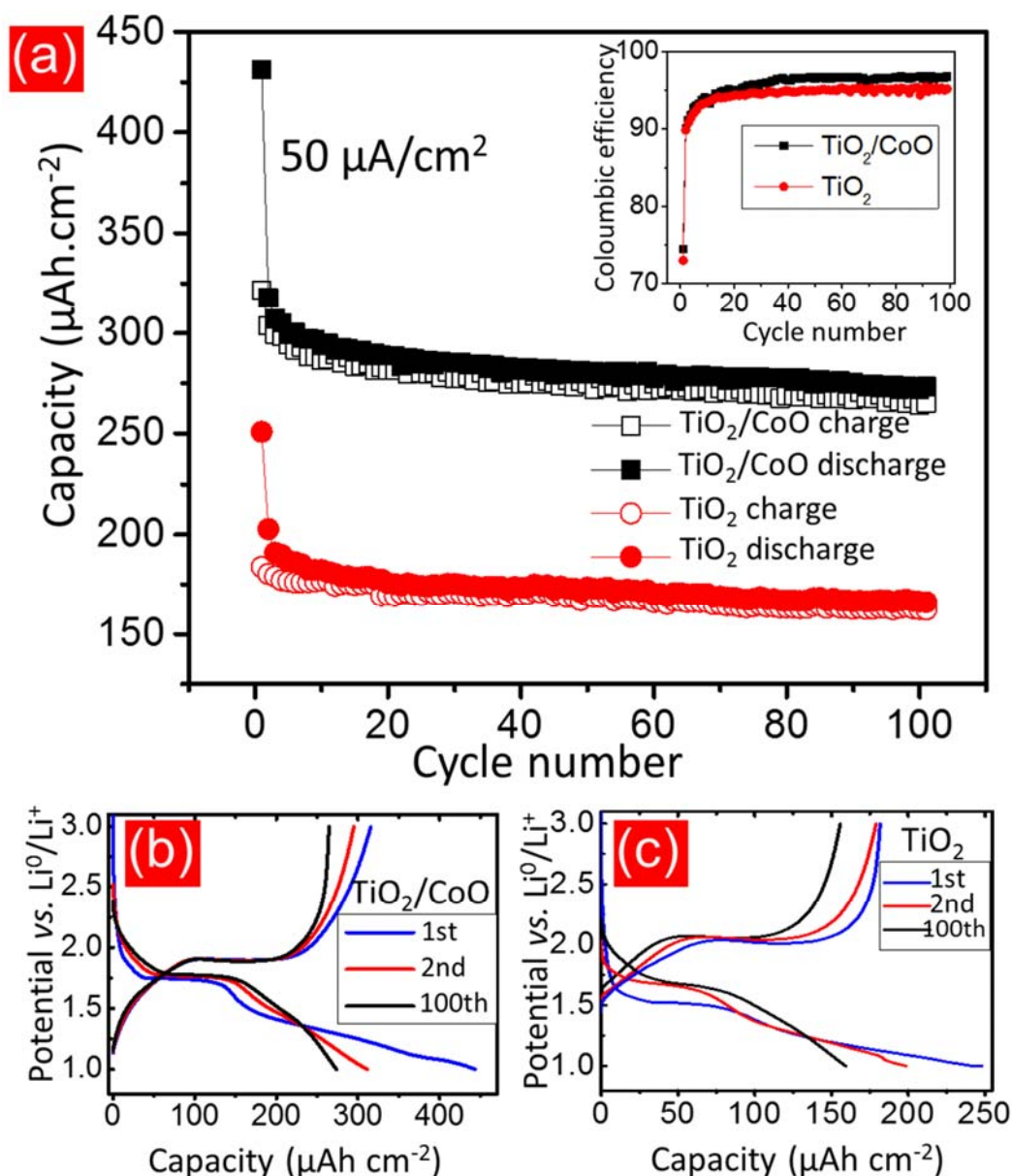
Fig. 4.13. *Galvanostatic areal charging and discharging capacities as a function of cycle number obtained at a current density of 50 μA cm⁻² for pure TiO₂ (a, red circles) and TiO₂-CoO anodes (a, black squares) prepared at 60 V anodization voltages. The filled symbols stand for the discharging and open symbols for the charging processes. The inset shows the corresponding Coulombic efficiency. Typical voltage profiles for the 1st, 2nd and 100th cycle against areal capacity for pure TiO₂ (b) and TiO₂-CoO anodes (c), respectively.*

The irreversible capacity noticed in the first cycle is ascribed to the formation of a stable solid electrolyte interface (SEI) due to the interaction between the electrolyte and the electrode material. **Figure 4.13b** and **c** showed the voltage profiles of the 1st, 2nd and 100th discharging/charging cycles for the TiO$_2$-CoO and the pure TiO$_2$ electrode, respectively. During the first cycle the discharge voltage decreases gradually from the open circuit voltage *vs.* Li/Li$^+$ until a plateau at 1.78 V is reached attributed to the phase transition from the tetragonal anatase to orthorhombic Li$_x$TiO$_2$ due to lithium insertion [67]. The potentials continue to decrease to reach their initial capacities afterwards. After 100 discharging/charging cycles, TiO$_2$-CoO was still able to deliver a discharge capacity of 280 µAh cm^{-2} which is 1.6 times higher as compared to the pure TiO$_2$ nanotube sample (160 µAh cm^{-2}) with a capacity retention of about 88 %.

To demonstrate the electrochemical rate capability, both electrodes were examined for Li$^+$ ion insertion and extraction at different current densities from 10 to 400 µA cm^{-2} as presented in **Figure 4.14.** The areal capacity of each sample is directly proportional to its formation voltage which is related to their weights. It is reported that the tube heights increase by increasing the anodization voltage at a constant time using the same electrolyte [120,197]. Therefore, the oxide layer thickness is related to its weight. The TiO$_2$-CoO electrode, prepared at 60 V (**Figure 4.14a**), demonstrated the highest areal capacity of about 600 µAh cm^{-2} (i.e. 315 mAh g^{-1}) at a current density of 10 µA cm^{-2} with a cycle stability up to 83%. The remarkable better rate capabilities of the TiO$_2$-CoO electrode means that it carries more potential for practical applications compared to pure TiO$_2$ (**Figure 4.14b**) formed under identical conditions. The obtained areal capacity of TiO$_2$-CoO electrodes in our study are significantly higher than some previously reported values for other systems containing TiO$_2$ nanotube-based array electrodes such as TiO$_2$/Fe$_2$O$_3$ and MoO$_3$ deposited on TiO$_2$ [18,156] and comparable with the areal capacity of similar system such as for Co$_3$O$_4$-coated TiO$_2$ evaluated at a current density range of 100 - 200 µA cm^{-2} [15].
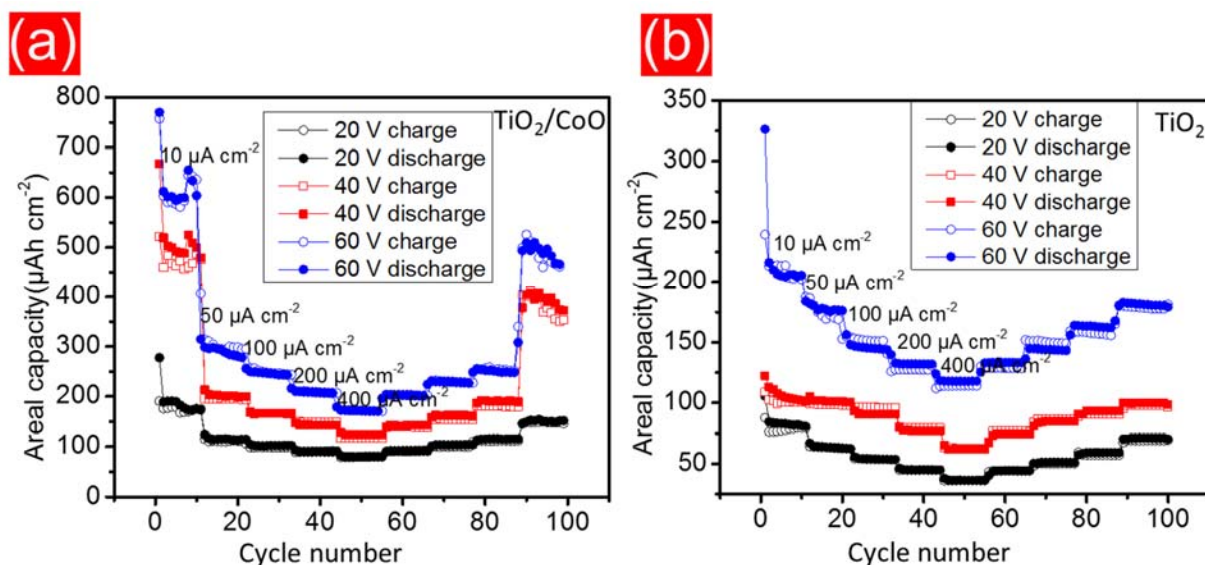
Fig. 4.14. *Rate capability of TiO₂-CoO (a) and TiO₂ anodes (b), prepared at anodization voltages of 20 V (black circles), 40 V (red squares) and 60 V (blue circles), as a function of cycle number. The filled symbols explain the discharging and open symbols the charging process.*

The improved electrochemical performance of TiO$_2$-CoO nanotubes is ascribed to the high surface area of the mixed oxide nanotubes with high aspect ratio, *i.e.* small diameter and long length, compared to pure TiO$_2$. The electrochemical performance of TiO$_2$ nanotubes depends on their specific surface area [67,139]. The specific surface area (S$_{BET}$) calculated from nitrogen adsorption isotherms shows a higher apparent S$_{BET}$ as well as a larger total pore volume of the TiO$_2$-CoO nanotubes, (46 m^2 g^{-1} and 0.19 cm^3 g^{-1}) compared to the pure TiO$_2$ nanotubes (37.61 m^2 g^{-1} and 0.16 cm^3 g^{-1}). The smaller tube diameter and wall thickness of TiO$_2$-CoO, compared to pure TiO$_2$, leads to an increase of the specific surface area and a decrease of the Li ion diffusion length. Also, the tube wall contact in TiO$_2$-CoO is higher than that of pure TiO$_2$, as confirmed by SEM images, which allows for faster ion transfer and higher conductivity. Moreover, an enlargement of the internal surface area of the fabricated tubes may stimulate their capacitive surface for lithium storage resulting in pseudocapacitance [199,200].

4.3.3 Electrochemical impedance spectroscopy (EIS) tests

In order to further understand the reason behind the superior electrochemical performance of the TiO$_2$-CoO electrode, electrochemical impedance spectroscopy (EIS) tests were performed for both the pure TiO$_2$ and the TiO$_2$-CoO sample after conducting 100 charging/discharging cycles. The Nyquist plots, for the samples measured at 1.78 V, are presented in **Figure 4.15**.
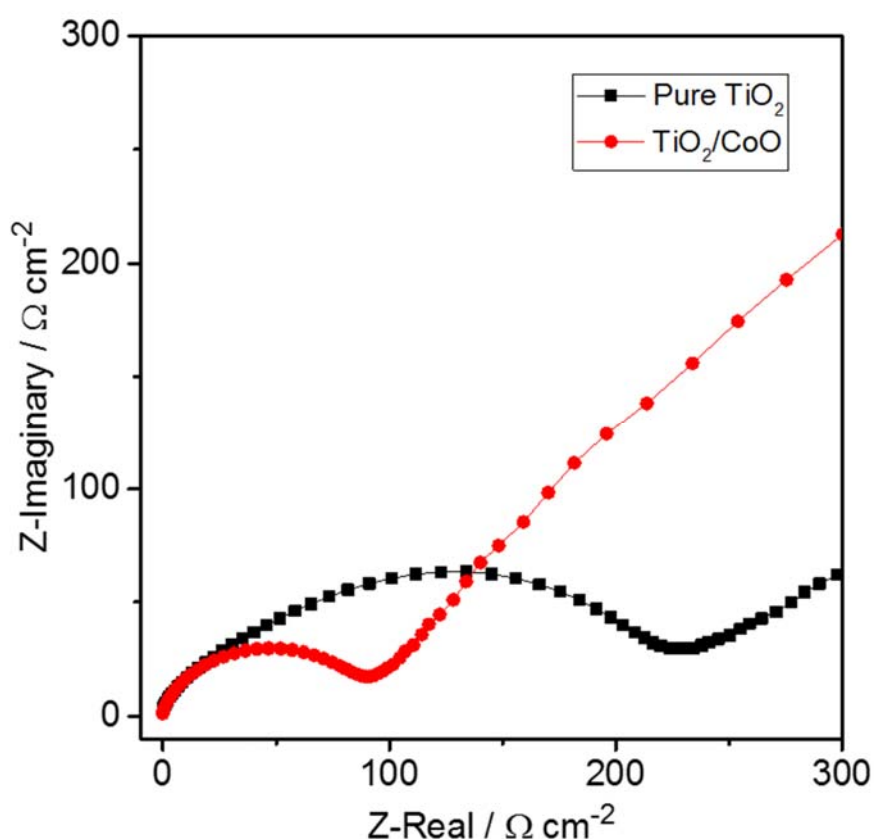
Fig. 4.15. *Nyquist plots of TiO$_2$ (red circles) and TiO$_2$-CoO anodes (black squares) after conducting 100 charging/discharging cycles, in the frequency range of 100 kHz to 0.1 Hz at a potential of 1.78 V vs. Li/Li⁺.*

Both samples exhibit semicircles from high to medium frequency and an inclined line in the low frequency region. Such semicircles describe the charge transfer resistance when lithium ions diffuse from the electrolyte into the electrode interface [174,201]. Lithium diffusion from the inside electrode is represented by the

inclined line. A significant decrease of the semicircle diameter for TiO$_2$-CoO compared to pure TiO$_2$ was observed. The presence of CoO positively affects the conductivity of TiO$_2$, resulting in faster lithium ion insertion/extraction processes and better electrochemical performance.

4.3.4 Structural stability TiO$_2$-CoO anodes over cycling

SEM and TEM investigations after 100 charging/discharging cycles at a current density of 400 µA cm^{-2} are conducted to investigate the morphological stability of the TiO$_2$-CoO NT upon cycling. Image **(a)** in **Figure 4.16** shows the top overview at low magnification of the TiO$_2$-CoO electrode (prepared at 60 V).
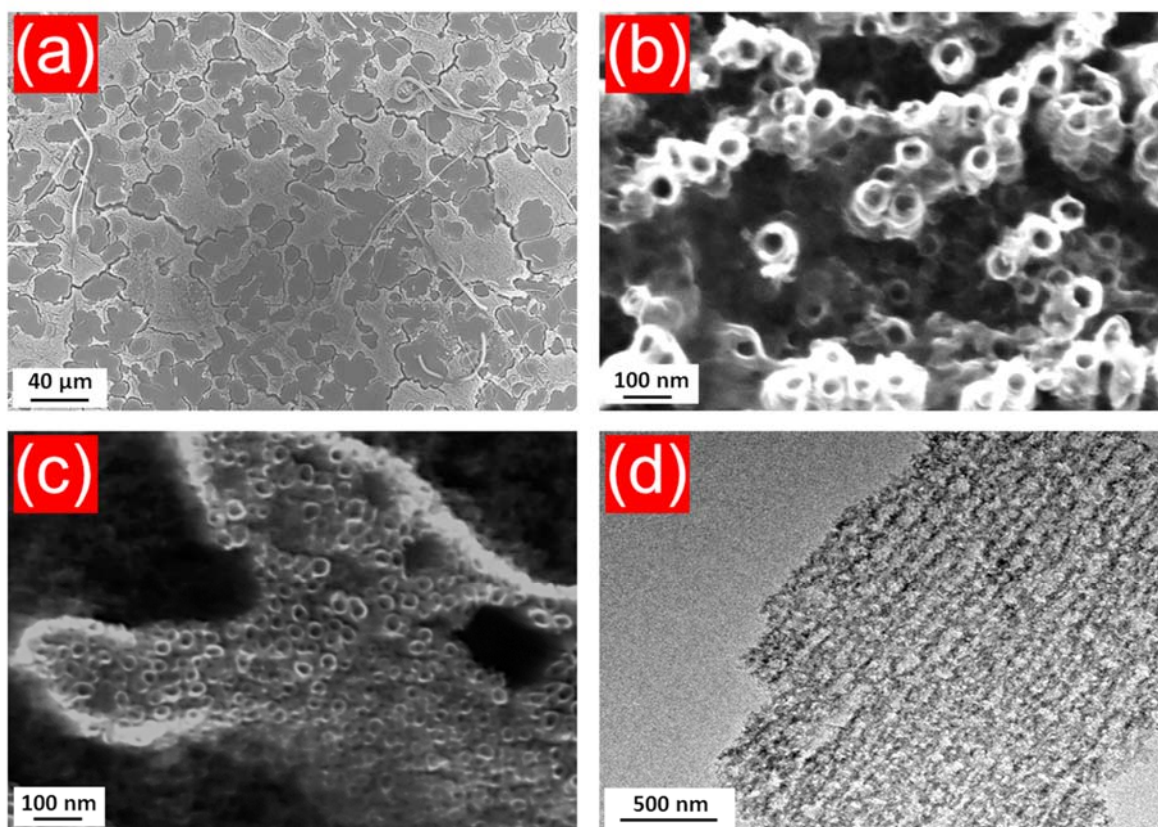
Fig. 4.16. *Morphological characterization of the TiO$_2$-CoO electrode formed at 60 V after 100 charging / discharging cycles at a current density of 400 µA cm^{-2}; SEM images of the top view of the electrode (a); nanotubes grown on the β-Ti phase (b) and*

Ti$_2$Co phase (c), respectively; TEM image of the TiO2-CoO electrode after 100 charging/discharging cycles (d).

Some fibers appear on the surface which could be came from the separator material. At a high magnification, the NTs grown on both the β-Ti (**Figure 4.16b**) and the Ti$_2$Co (**Figure 4.16c**) phase of the electrode maintain their tubular shape without discernible collapse of the nanotube walls. Moreover, the nanotube features of the cycled electrode are slightly changed compared to the as-prepared nanotubes (**Figure 4.5**). Nevertheless, the TEM image of the TiO$_2$-CoO electrode after cycling in **Figure 4.16d** shows a marginal deformation of the nanotube. A stable morphology is also important characteristic for the practical applications

4.4 Summary of chapter 4

In this chapter, the electrochemical growth of well-aligned titanium and cobalt oxide nanotubes on the two-phase alloy Ti$_{80}$Co$_{20}$ have been investigated. Different voltages (20 - 60 V) during the anodic oxidation process do not affect the mean nanotube diameters. The current density changes during the dynamic anodization processes and correlates with the morphology depending on the crystal structure of the two phases. The crystallinity of the fabricated oxides was tuned by heat treatment at 450 °C. The structural and spectroscopic characterizations of the oxide films confirm the formation of TiO$_2$-CoO mixed nanotubes. TiO$_2$-CoO nanotube anodes displayed a 1.6 times increased areal capacity compared to pure TiO$_2$ nanotube anodes fabricated under the identical conditions with a capacity retention of 88 % over 100 cycles. The improved electrochemical performance of TiO$_2$-CoO nanotubes is attributed to the following reasons: (1) the high surface area of the TiO$_2$-CoO mixed nanotubes, and (2) the presence of CoO leading to improved conductivity of TiO$_2$. Such improvement essentially facilitates the Li ion insertion and enhances its reversible capacity. The tubular structure of the TiO$_2$-CoO nanotubes is well-retained even after electrochemical cycling.

Chapter 5

Ternary CNTs@TiO₂/CoO nanotube composites: improved anode materials for high performance lithium ion batteries
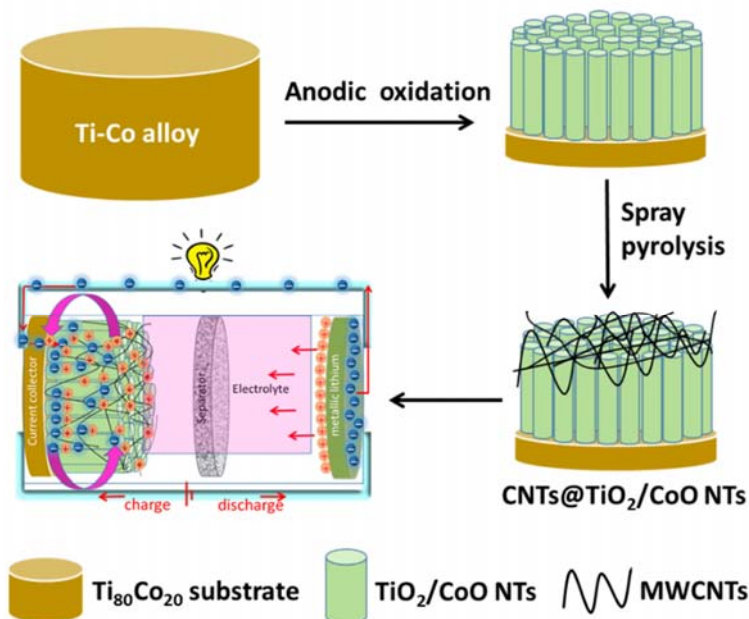
In this chapter, a brief introduction explains the motivation for the fabrication of ternary (CNTs)@TiO$_2$/CoO nanotubes composites in addition to detailed results and discussion of characterizations and the electrochemical testing of ternary composite electrodes are presented.

5.1 Introduction

Electrochemical performance of pure TiO$_2$ can be improved by mixing them mechanically with some carbon derivatives such as graphene, carbon black or CNTs during a slurry preparation [202–204]. Unfortunately, it is not possible to use the mechanical mixing for TiO$_2$ NT arrays, as this technique destroys their tubular structure. Another alternative has been oriented to the thermal treatment of anodically synthesized TiO$_2$ NTs in a methane/hydrogen-containing atmosphere in the presence of Fe precursors to perform carbon coating. Such carbon-coated TiO$_2$ NTs showed a remarkable improvement in the electrical conductivity when tested for supercapacitor applications [149]. CNTs are very attractive materials to synthesize elegant heterojunction composite anodes with TiO$_2$ NTs, owing to their high electronic conductivity, structural stability and the ease of manufacturing through mass production routes [205–208].

Other previous studies address the synthesis of many binary composites from CNTs and pure TiO$_2$ for lithium ion batteries. The prepared TiO$_2$ commonly exhibits forms like nanoparticles or nanospheres, which require additional polymeric binder and conductive carbon in the electrode manufacturing [206–211]. Additionally, most of these studies show that CNTs are utilized as a support for TiO$_2$ or TiO$_2$ is filled into spacings between the CNTs in a CNT array.

In the present study, a new strategy was proposed to realize deposition of CNTs on anodically fabricated TiO$_2$/CoO NTs using a simple spray pyrolysis technique. CNTs function as conductive networks that connect TiO$_2$ nanotubes from the opposite side of the current collector allowing for better electrical and ionic conductivities, paving the way for superior lithium ion insertion with excellent rate performance. In

addition, the as-fabricated ternary composite is directly used as binder- and additive-free electrode, taking the advantage of utilizing the alloy substrate as current collector and recommend them for low cost and high performance batteries.

5.2 Characterization

The typical fabrication process of CNTs@TiO$_2$/CoO NTs is presented in **Figure 5.1a**. Firstly, the TiO$_2$/CoO NTs were grown on the two-phase Ti$_{80}$Co$_{20}$ alloy. The as-grown TiO$_2$/CoO NTs were subsequently subjected to a surface modification with CNTs through spray pyrolysis. The as-formed CNTs@TiO$_2$/CoO NTs were then assembled and tested as anodes against lithium in a coin cell battery. A photograph of the pristine and CNT-covered electrode is shown in **Figure 5.1b**.
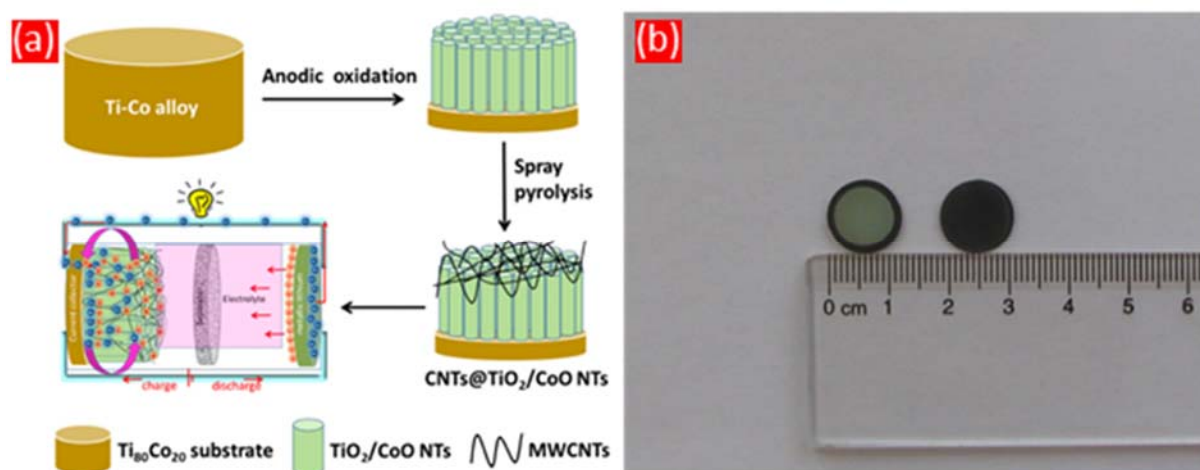
Fig. 5.1. *Schematic illustration of the fabrication strategy of ternary CNTs@TiO$_2$/CoO NTs (a); a photograph of the TiO$_2$/CoO NTs before (left electrode) and after CNT covering (right electrode) (b).*

5.2.1 Morphology and Raman analysis of the fabricated CNTs@TiO$_2$/CoO NTs

The surface morphologies of the as-formed TiO$_2$/CoO NTs and after growing CNTs were examined using SEM. **Figure 5.2a** shows a low magnification view of the

alloy substrate after the anodization process, where the dark and bright areas represent β-Ti and Ti$_2$Co phases, respectively of the Ti-Co alloy. The high magnification top view of β-Ti and Ti$_2$Co are displayed in micrographs (b) and (c) of **Figure 5.2.** Evidently, well-ordered clear-cut TiO$_2$/CoO NTs are successfully formed on the entire surface of the Ti-Co alloy. The average diameter of the nanotubes grown on β-Ti is 40 nm. The nanotubes grown on the Ti$_2$Co phase showed an average diameter of 37 nm. The tubular structure of the oxide film is also indicated from the cross-sectional view of the oxide layer presented in the inset of image **2b**. STEM-EDXS measurements shown in **Figure S2** (Supplementary Information) reveal that the fabricated nanotubes are composed of Ti and Co oxides, implying the good mixing of Co-O and Ti-O species in the framework. Further characterization details of TiO$_2$/CoO NTs are addressed in **chapter 4**.

Panel (2d) manifests the entire overview of the oxide surface after performing the CNT growth. It clearly shows that the CNT layer covers the whole surface of the oxide NT array, indicating a uniform coverage. **Figure 5.2e** demonstrates the high magnification top-view of the as-fabricated CNTs@TiO$_2$/CoO NTs sample. The outer nanotube diameter of the CNTs ranges from 20 to 27 nm, which is a characteristic feature of the multi-walled carbon nanotubes grown by this technique [167,212]. It obviously shows that the CNTs are formed horizontally in an interwoven web-like structure, suggesting that CNTs can effectively connect the individual TiO$_2$/CoO nanotubes through a high conductive network and may serve as a rather charge collector. Thus, the electrical and the ionic conductivities of the CNTs@TiO$_2$/CoO NT electrode are expected to be improved allowing for a higher Li$^+$ ion diffusion and storage efficiency. Successful CNTs deposition on pure TiO$_2$ was also revealed from SEM micrographs in **Figure S3** (Supplementary information).
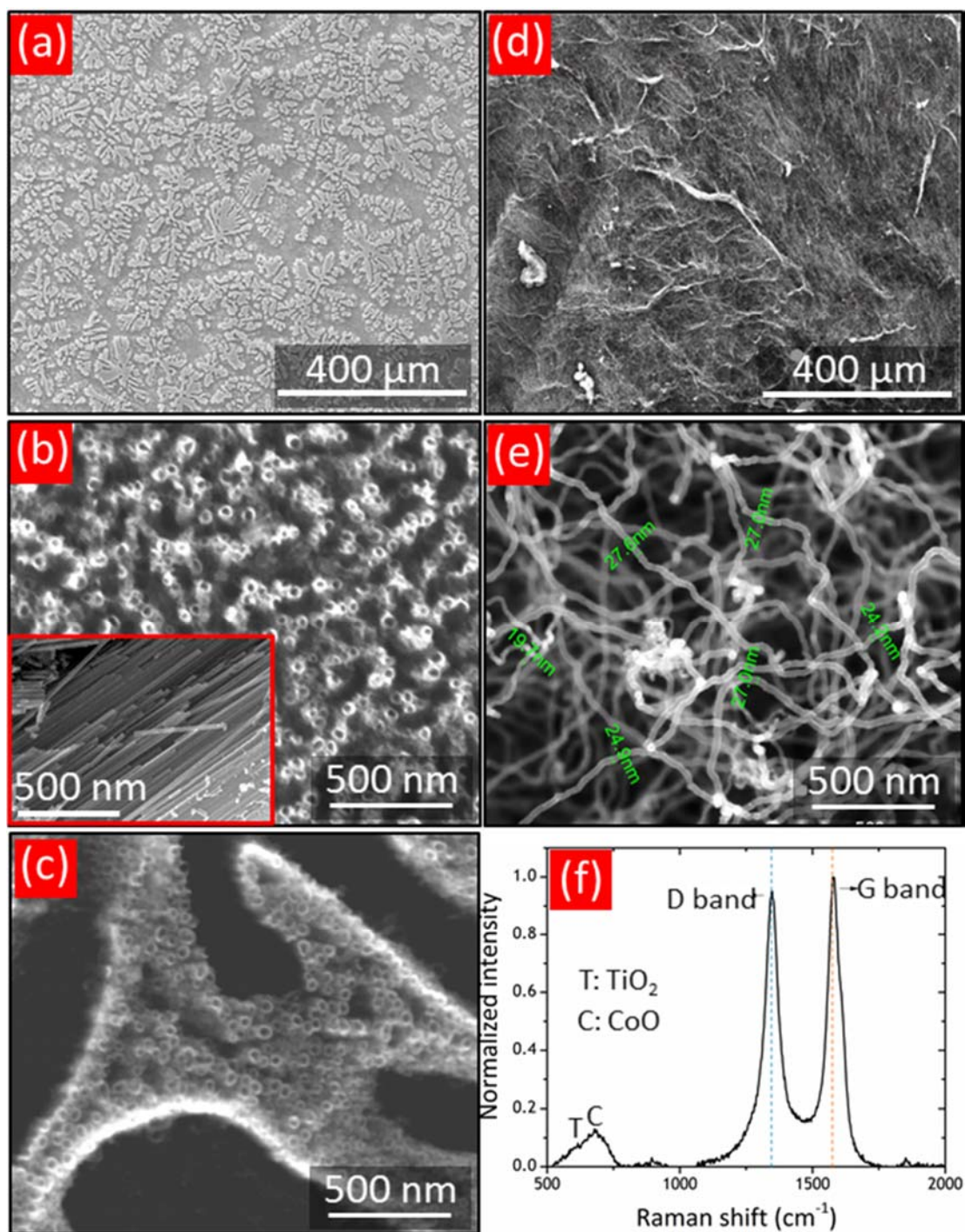
Fig. 5.2. *SEM micrographs, an overview of anodized Ti-Co alloy (a) high magnification of the β-Ti (b) and the Ti₂Co (c) phases anodized at 60 V; low (d) and high (e) magnifications of the ternary CNTs@TiO₂/CoO NTs; Raman spectra of ternary CNTs@TiO₂/CoO NTs (f).*

Raman spectroscopy provides important information about the carbon species like details related to the C-C bonds and defects that can be effectively obtained from the change in the signal shift. **Figure 5.2f** displays the Raman spectrum of the CNTs@TiO$_2$/CoO NTs sample. The typical disorder-induced D band (~1335 cm^{-1}) and tangential modes (G band, ~1587 cm^{-1}) are observed. The D band indicates the presence of defects in sp^2 hybridized carbon, while the G band is a characteristic of the in-plane vibration mode of sp^2-bonded carbons. The recorded D and G values are in accordance with those previously reported for CNTs/TiO$_2$ composites [206, 213-214]. It is interesting to point out that a small shift to higher values was observed for both D and G bands compared to the Raman characteristics of pure CNTs [213–215], revealing the possible interaction between the CNTs and TiO$_2$ [213, 214]. Notably, a broad peak centered with its maximum at 680 cm^{-1} is observed in the spectra. This peak matches very well with the reported A$_{1g}$ vibration mode of CoO species [216]. Additionally, a peak hump is noticed at 610 cm^{-1} which is assigned to rutile [192]. The small peak appeared at 892 cm^{-1} may possibly be related to C-C or C-O stretching vibrations of organic carbon traces that originate from the electrolyte used for the anodic oxidation [218, 218]. In conclusion, the Raman investigation confirms the successful deposition of CNTs on the TiO$_2$/CoO NT surface.

5.2.2 XRD analysis of the fabricated TiO$_2$/CoO NTs before and after CNTs coating

XRD analysis of the TiCo$_{20}$ alloy in **Figure 5.3a** showed reflections in good agreement with those reported for both β-Ti [176] and Ti$_2$Co [177] phases. No or hardly detectable reflections are further observed in the as-anodized TiO$_2$/CoO sample indicating an amorphous state of the prepared nanotubes. Also, reflections for Ti metal can only be distinguished for the as-prepared TiO$_2$ NTs (**Figure 5.3b**) proving a similar amorphous nature of such nanotubes. Sharp reflections are clearly shown in the diffractograms of both CNTs@TiO$_2$/CoO NTs (**Figure 5.3a**) and CNT@TiO$_2$ NTs samples which are in accordance with the Bragg positions of rutile [219]. It is known from the literature [220] that rutile is obtained at a temperature

higher than 800°C which matches with the temperature required for spray pyrolysis to form CNTs.
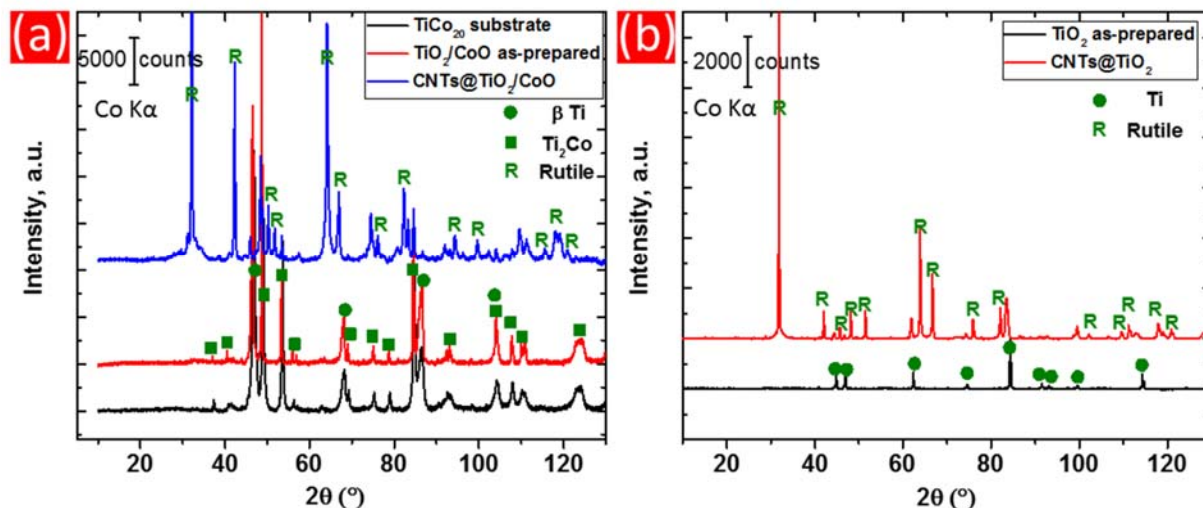
Fig. 5.3. *XRD patterns of the Ti₈₀Co₂₀ alloy substrate, the as-anodized TiO₂/CoO NTs and the as-prepared CNTs@TiO₂/CoO NTs (a); diffractograms of the as-anodized TiO₂ and CNT@TiO₂ NTs samples (b).*

5.3 Electrochemical properties

5.3.1 Cyclic voltammetry

The electrochemical characteristics of bare TiO₂/CoO and CNTs@TiO₂/CoO NT nanocomposite electrodes were investigated in order to underline the synergetic effect of CNTs in the composite backbone. Since the lithium ions intercalate the CNTs at a potential lower than 1 V, the cells were measured between 0.1 and 3 V. **Figure 5.4a** shows typical CV curves obtained at a scan rate of 0.1 mV s⁻¹ of a pureTiO₂/CoO NT electrode, without CNTs. The recorded cyclic voltammograms of the TiO₂ (shown in **Figure S4**, Supplementary Information) and TiO₂/CoO NTs are in general consistent with previous studies suggesting a similar intercalation behavior [221,222,141]. Two broad signals are observed in the anodic and cathodic branches at 1.6 and 1.7 V *vs.* Li/Li⁺, respectively. This broadening in the anodic and cathodic sweeps is a special characteristic for an amorphous state of TiO₂ and TiO₂ mixed with another transition

metal oxide [221,222]. No or hardly distinguishable signals are further detected in the following cycles.
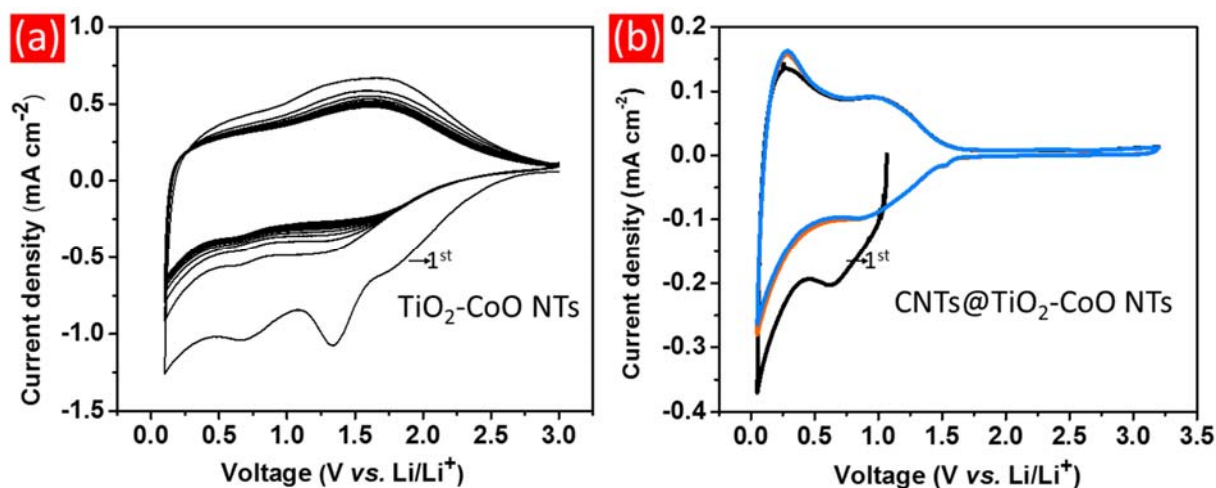
Fig. 5.4. *Cyclic voltammograms of TiO₂/CoO nanotubes (a) and CNTs@TiO₂/CoO NTs (b), measured at scan rates of 0.1 mV s⁻¹.*

These results indicate that the electrochemical insertion/removal reactions into/out of TiO_2 and TiO_2/CoO NT frameworks take place without phase transformation as usually found for crystalline materials [71,202,223]. **Figure 5.4b** depicts the CV curves of the CNTs@TiO₂/CoO NT electrodes. The absence of sharp peaks and presence of two broad peaks in the anodic and cathodic branches at similar peak positions are consistent with the general CV behavior of rutile [224] and are attributed to a typical Li^+ ion intercalation/deintercalation mechanism into or out of solid solution domains [224]. The corresponding anodic/cathodic signals are significantly shifted to the lower voltage of around 1 V *vs.* Li/Li⁺ compared to 1.6 and 1.8 V *vs.* Li/Li⁺ for the unmodified TiO₂/CoO NTs (**Figure 5.4a**) and rutile [224], respectively. This shift in the peak potential is attributed to the presence of CNT layers that interconnect the TiO₂/CoO NTs and enable high electrical conductivity as well as a good lithium ion transport and therewith faster diffusion kinetics [90]. Unlike TiO₂/CoO NTs, no decrease in the current density of the redox signals occurs over cycling, indicating the good stability and better reversibility of CNTs@TiO₂/CoO

NT electrode compared to the CNT-free electrode. These results already suggest that this composite electrode has a great potential as a promising anode for lithium ion batteries.

5.3.2 Galvanostatic cycling with potential limitation

Figure 5.5a depicts the galvanostatic cycling performance of CNTs@TiO₂ and CNTs@TiO₂/CoO NT electrodes and the corresponding Coulombic efficiencies (CE) evaluated at a current density of 50 µA cm^{-2} between 0.01 and 3 V *vs.* Li/Li$^+$. In the first cycle both electrodes show a relatively low areal capacity compared with the following cycles. This observation is in accordance with the previously described analysis of the cyclic voltammograms where the current density in the first scan is slightly smaller (0.13 mA cm^{-2}) than those of the next sweeps (0.15 mA cm^{-2}). A possible activation of the electrode surface may be concluded to be the origin of this behavior [226].
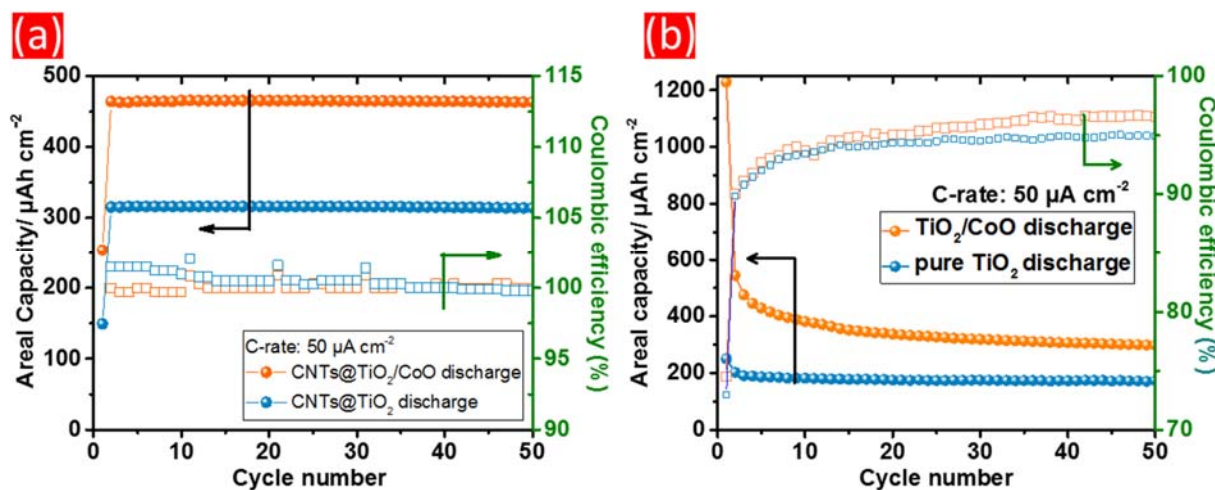
Fig. 5.5. *Galvanostatic areal discharging capacities as a function of cycle number obtained at a current density of 50 µA cm^{-2} for CNTs@TiO₂ and CNTs@TiO₂/CoO NT anodes and their corresponding CE (a); cycling performance of uncovered TiO₂ and TiO₂/CoO NT electrodes with the corresponding CE (b).*

Remarkably, the ternary CNTs@TiO$_2$/CoO NT composite electrode exhibits an areal capacity of 460 µAh cm^{-2} demonstrating excellent cycling stability over 50 charging/discharging cycles with a CE of ≈100 %. Binary CNTs@TiO$_2$ NT composite electrodes can deliver a capacity of 310 µAh cm^{-2} with a relatively higher CE (ca. 104 %) in the first ten cycles reaching an efficiency of ca. 100% at the end of the 50th charging/discharging cycle. It is clear that the ternary CNTs@TiO$_2$/CoO NT electrode displays around a 1.5-fold increase in capacity compared to the CNTs@TiO$_2$ NT anode.

Surprisingly, the binary CNTs@TiO$_2$ and ternary CNTs@TiO$_2$/CoO NT composites show significantly enhanced capacities reaching up to an 1.5-fold increase in the 50th discharge cycle compared to the areal capacity of uncovered TiO$_2$ and TiO$_2$/CoO NT electrodes which were tested at the same electrochemical conditions (**Figure 5.5b**). The remarkable increase in the reversible capacity of the ternary composite is attributed to a good adhesion between the highly conductive, interlaced CNTs and the mixed oxide NTs. The boron-induced 'elbow junctions' of the robust CNT network further enhance the connectivity of the oxide NTs than the commonly used carbon additives and thereby result in higher conductivities facilitating easier and faster electron transport and ion insertion/removal processes. The high CE also implies a stable SEI formed on the surface of the CNTs and the oxide NTs as well as a very low degradation of the electrolyte due to a very low number of side reactions. As one of the components of the ternary oxide electrodes, CNTs may also contribute to the overall capacity of the cells. Hence, based on the capacity measurements conducted on the CNTs without the transition metal oxide nanotubes under identical electrochemical test conditions, it is determined that the CNTs contribute only about 3.6 % (16.8 µAh cm^{-2}) to the overall capacity (**Fig. S5**, Supplementary information). Hence, the CNTs in the ternary composite electrodes mainly improve electrical connectivity and diffusion kinetics in the composite and their storage ability can be neglected especially when optimizing the potential window to higher potentials.

Now it is worth to underline the effect of the amorphicity and crystallinity of the TiO$_2$ and TiO$_2$/CoO NTs on the Li$^+$ ion storage capacity at a current density of 50 μA cm^{-2} based on the results of **Figure 5.5b** and **Figure 4.12** of chapter 4. At the 50th charging/discharging cycle, the amorphous TiO$_2$/CoO NTs deliver an areal capacity of 305 μAh cm^{-2}, which is higher than found for TiO$_2$/CoO NTs containing a phase mixture of crystalline anatase and rutile (280 μAh cm^{-2}). In addition, amorphous TiO$_2$ NTs also show an improved areal capacity of 180 μAh cm^{-2} compared to anatase (170 μAh cm^{-2}). The noticed enhancement in the insertion capacity of amorphous TiO$_2$/CoO and TiO$_2$ NTs is in accordance with previous observations and is attributed to larger amount of disorders and defects in the amorphous structure than the crystalline one[141,226,227]. These defects offer bigger channels or more diffusion paths for Li$^+$ ion migration. Nevertheless, crystallization of nanotube arrays during the CVD process carried out under 860 °C does not affect electrochemical performance since still much higher capacities are observed compared to amorphous or crystalline electrodes without a carbon coverage.
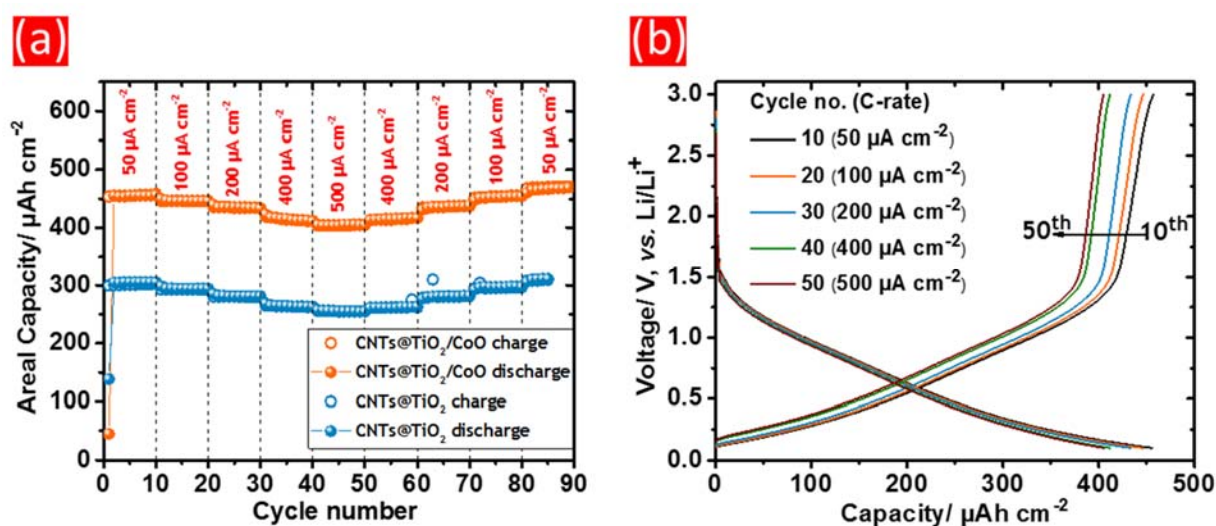
Fig. 5.6. *Rate capability of CNTs@TiO$_2$ and CNTs@TiO$_2$/CoO NT anodes (a); typical voltage profiles for the 10th, 20th, 30th, 40th and 50th cycles against areal capacity of TiO$_2$/CoO NT anodes (b), measured at a current rate of 50, 100, 200, 400 and 500 μA cm^{-2}, respectively.*

In order to determine the electrochemical performance of the CNT-covered anodes, the electrodes were cycled at different current densities (50 - 500 µA cm^{-2}), which are shown in **Figure 5.6a**. The CNTs@TiO$_2$/CoO NT electrode is able to deliver an areal capacity of 455 µAh cm^{-2} when cycled at a current rate of 50 µA cm^{-2}. Only an insignificant decrease in the areal capacity is observed when the current rate is increased from 50 to 500 µA cm^{-2}, still displaying an excellent areal capacity of about 400 µAh cm^{-2}. It is crucial to note that the electrode can reversibly retain the same areal capacity even after 80 charging/discharging cycles when the current rates are gradually decreased, demonstrating the outstanding rate performance of the composite electrode.

The corresponding charging/discharging voltage profiles of CNTs@TiO$_2$/CoO NT anodes obtained at various current densities (50 - 500 µA cm^{-2}) are shown in **Figure 5.6b**. Apparently, no distinct plateaus are detected in the voltage curves matching the cyclic voltammograms discussed above (**Figure 5.4**). Similar behavior in the rate capability was also detected for CNTs@TiO$_2$ NT, however, it can only reach an areal capacity of around 300 and 256 µAh cm^{-2} at current densities of 50 and 500 µA cm^{-2}, respectively. Interestingly, the voltage profile curves of CNTs@TiO$_2$/CoO NT indicate that only a small decrease in the areal capacity will be achieved if the potential window is limited to 1.5 V. In consequence, the possibility to use such materials for practical applications is underlined. These findings clearly demonstrate the effectiveness of the tightly interlaced CNT network in greatly enhancing the rate performance of the CNTs@TiO$_2$ and CNTs@TiO$_2$/CoO NT electrodes.

5.3.3 Electrochemical impedance spectroscopy (EIS)

To gain further understanding on the effect of CNTs on the ionic conductivity of the synthesized composite anodes, electrochemical impedance spectroscopy (EIS) tests were performed for all the cells after 50 charging/discharging cycles. The Nyquist plots of all measured electrodes at 1.7 V *vs.* Li/Li$^+$ are depicted in **Figure 5.7a**. The spectra show semicircles at high-to-medium frequency ranges followed by

inclined lines at the low frequency domain. It is known that the semicircles at high-to medium frequencies correspond to the charge transfer resistance accompanying lithium ion diffusion from the electrolyte towards the electrode/electrolyte interface [12,144,221]. The inclined lines represent lithium ion diffusion inside the electrode frameworks [12,114]. The CNTs@TiO₂/CoO NT electrode exhibits the smallest semicircle indicating the enhanced ionic conductivity compared to the other electrodes. Apparently, the CNT-covered electrodes show a smaller semicircle diameter than uncovered electrodes, confirming that the deposition of CNTs indeed lead to an improved ionic conductivity and hence, enhances the electrochemical performance of lithium-ion insertion/extraction processes.
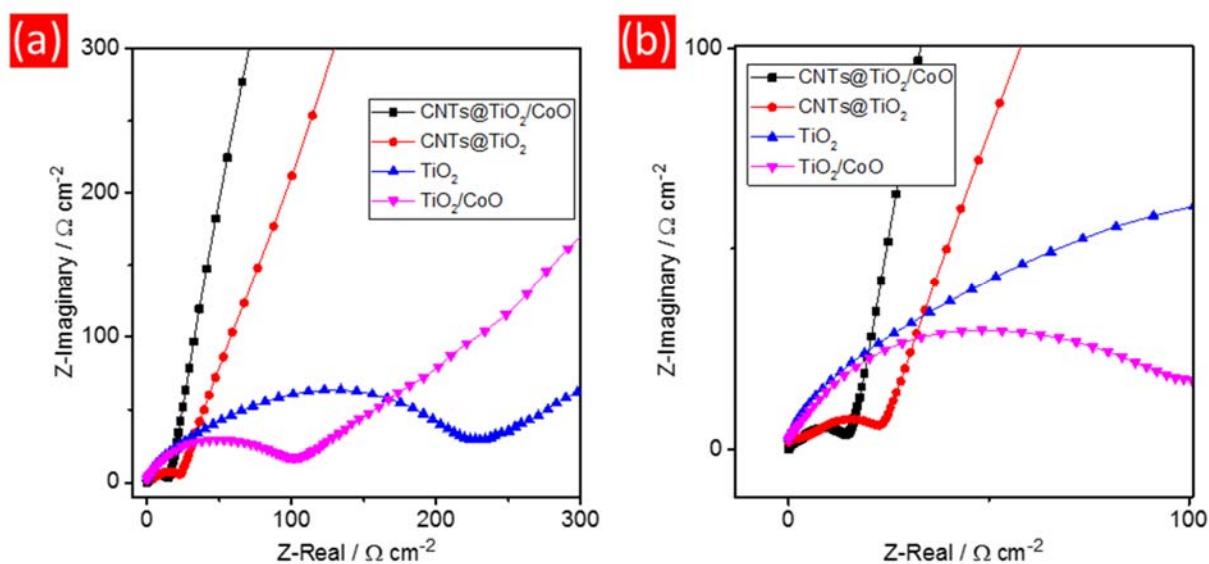
Fig. 5.7. *Nyquist plots of pure TiO₂ NTs (pink triangles), TiO₂/CoO NTs (blue triangles), TiO₂ NTs covered with CNTs (red circles) and TiO₂/CoO NTs covered with CNTs (black squares) after 50 charging/discharging cycles, in the frequency range of 100 kHz to 0.1 Hz at a potential of 1.7 V vs. Li/Li⁺ (a); zoomed view of Fig. 5.7a (b).*

5.4 Summary of chapter 5

In this chapter, it is demonstrated that a robust network of interconnected CNTs can be synthesized laterally on the surfaces of anodically grown TiO$_2$ and TiO$_2$/CoO nanotubes by a simple and quick, single-step spray pyrolysis technique, leading to a successful fabrication of binary CNTs@TiO$_2$ and ternary CNTs@TiO$_2$/CoO nanotube composite electrodes. The electrochemical evaluation *vs.* the typical Li/Li$^+$ reference electrode showed that the CNT-coated electrodes exhibit a 1.5-fold increase in the specific capacity compared to the uncoated anodes, along with a phenomenal rate performance between current densities of 50 - 500 µA cm^{-2}. The ternary CNTs@TiO$_2$/CoO NT composite displays the best electrochemical performance among all tested electrodes. The remarkable electrochemical performance of the composite electrodes is attributed to the highly conductive CNTs interfacing the mixed TiO$_2$/CoO NT framework, leading to an exceptional electronic conductivity and charge transport. Secondly, the tightly interwoven CNT network may also serve as a second charge collector in conjunction with the alloy substrate, resulting in outstanding electrochemical performance. With this kind of composite electrode, it is possible to achieve excellent energy storage properties even with electrically isolating oxide tube arrays and the electrical conductivity of the oxide nanotube electrodes can be significantly improved, and thereby achieve a remarkable enhancement in their electrochemical performance, independent of the oxide morphology, by a simple surface modification step.

Chapter 6

TiO$_2$-SnO$_2$ nanotubes as anodes in lithium ion batteries
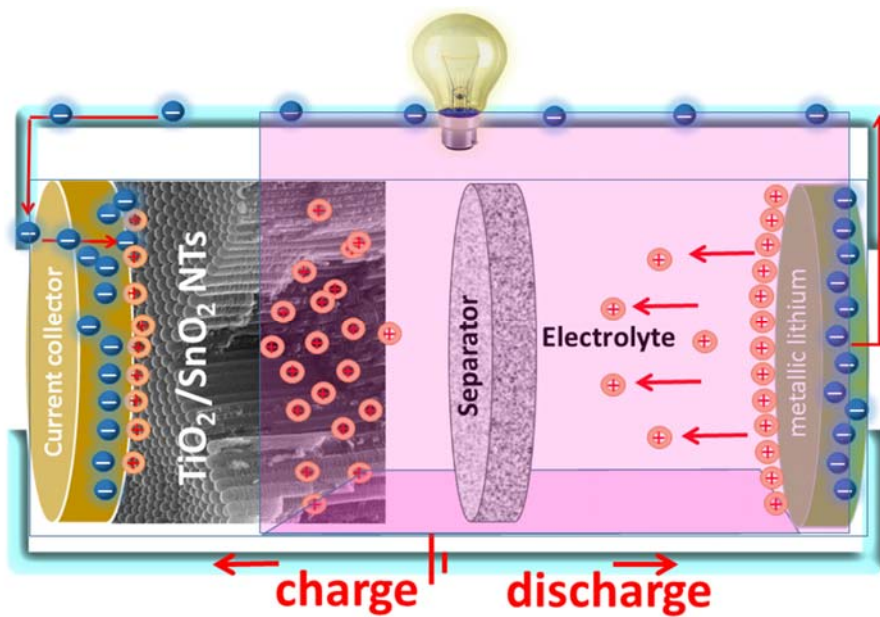
6.1   Introduction

Mixing TiO$_2$ with other transition metal oxides with higher ionic conductivity and theoretical capacity is a vital approach. As presented in chapter 4, TiO$_2$-CoO nanotubes showed enhanced electrochemical performance as electrode material for lithium ion batteries compared to the pure TiO$_2$ nanotubes. Ti-Sn-O system is another promising system to be investigated as potential anode materials in lithium ion batteries. In previous work, double-shell SnO$_2$@TiO$_2$ nanotubes have been synthesized by atomic layer deposition (ALD) using polyacrylonitrile (PAN) nanofibers as templates [30]. Such nanotube electrodes displayed enhanced electrochemical performance when they are used as anode materials in lithium ion batteries. Tin dioxide (SnO$_2$) is an n-type semiconductor with excellent electronic properties and high theoretical capacity (781 mAh g^{-1}). A remarkable contribution of SnO$_2$ to the physicochemical properties of TiO$_2$ nanotubes is proposed by offering the advantage of the 1D nanostructure to accommodate the large volume change upon cycling. In the current work, the anodic oxidation method was used to fabricate mixed TiO$_2$-SnO$_2$ nanotubes on the surface of Ti-Sn alloys with various tin concentrations (1 - 10 at.%). The resulting nanotubes are used as anode materials in lithium ion batteries. Such a system is an ideal solution to obtain an anode material of unique structural stability and good electronic properties resulting in excellent electrochemical performance. In addition, using the as-grown nanotubes as binder and additive-free electrodes will add a unique advantage to save the extra costs for the battery manufacturing. Moreover, utilizing Ti-Sn substrates as current collector will result in a particularly good contact between the active material and the current collector. Detailed results and discussion of synthesis, characterizations and the electrochemical performance of TiO$_2$-SnO$_2$ nanotubes are presented and systematically analysed in this chapter.

6.2   Characterization

6.2.1 ICP-OES analysis of the as-cast Ti–Sn alloys

The elemental concentrations of the as-cast Ti-Sn alloys were analyzed by inductively coupled plasma optical emission spectroscopy (ICP-OES analysis) and the results are shown in **Table 6.1**. The concentrations of elemental Ti and Sn are in good agreement with the desired chemical compositions, indicating the high quality of the as-cast alloys.

Tab. 6.1. ICP-OES analysis of the as-cast Ti-Sn alloys.

Alloy	Sn content at.%	Ti content at.%
Ti-Sn$_1$	1.003 ± 0.001	98.997 ± 0.001
Ti-Sn$_5$	5.003 ± 0.001	94.997 ± 0.001
Ti-Sn$_{10}$	10.014 ± 0.001	89.986 ± 0.001

6.2.2 SEM analysis of the as-cast Ti-Sn alloys

The SEM micrographs of the as-cast alloys (1, 5 and 10 at.% Sn) in **Figure 6.1a**, **d** and **g** respectively, show typically single phase materials present at room temperature matching with the reported phase diagram [228] of the Ti-Sn system (**Fig. S6** in the supplementary information). From the EDXS element mapping presented in **Figures 6.1b**, **c**, **e**, **f**, **h** and **i** the allocation of Ti and Sn is indicated proving the homogenous distribution of Sn metal through the entire alloy substrates. Nevertheless, as shown in the image in **Figure 6.1i** the TiSn$_{10}$ alloy exhibits less homogeneous distribution of Sn across the substrate and agglomerations of metallic Sn are noticed in some areas. This result suggests that the nanotubes grown on the substrate could undergo inhomogeneous mixed oxide formation.
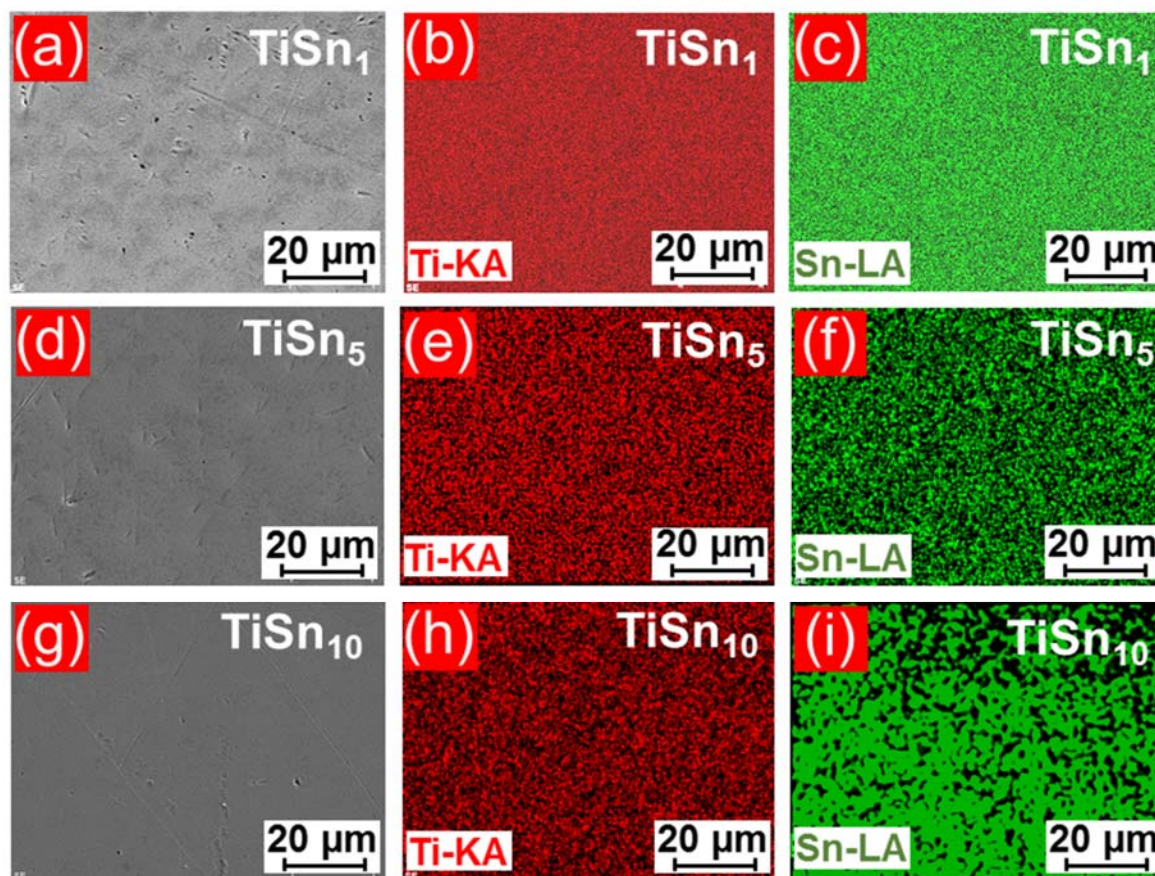
Fig. 6.1. *SEM micrographs of the as-cast alloys; TiSn₁ (a), TiSn₅ (d), TiSn₁₀ (g). EDXS element mapping; for TiSn₁ (b), (c), TiSn₅ (e), (f) and TiSn₁₀ (h) and (i) prove the presence of Sn in all alloy substrates.*

6.2.3 Phase analysis of the as-cast Ti-Sn alloys

The phase composition of the as-cast Ti-Sn substrates was explored by XRD and the recorded patterns are shown in **Figure 6.2**. Only a single phase was detected from the patterns for all as-cast alloys allowing the possible growth of mixed oxide nanotubes on all alloy substrates. The observed phase is in agreement with the hexagonal structure of Ti-Sn (space group $P6_3/mmc$) [229,230]. The patterns of pure Ti and TiSn₁ are indexed based on a Mg-based structure model described in Ref. [229] while the patterns of TiSn₅ and TiSn₁₀ are assigned to the structure model outlined in Ref. [230]. **Table 6.2** summarizes the results obtained from the Rietveld analyses

for pure Ti and the Ti-Sn alloys. The lattice parameters increase with increasing Sn content which is in accordance with the larger atomic radius of the Sn atoms substituting Ti atoms in the Ti lattice. This result validates the incorporation of Sn into Ti-Sn alloys. The differences in intensities compared to the original structure are mainly based on the large crystallites of the alloys (**Tab. 6.2**) which partially exhibit preferred orientations or lattice strain.
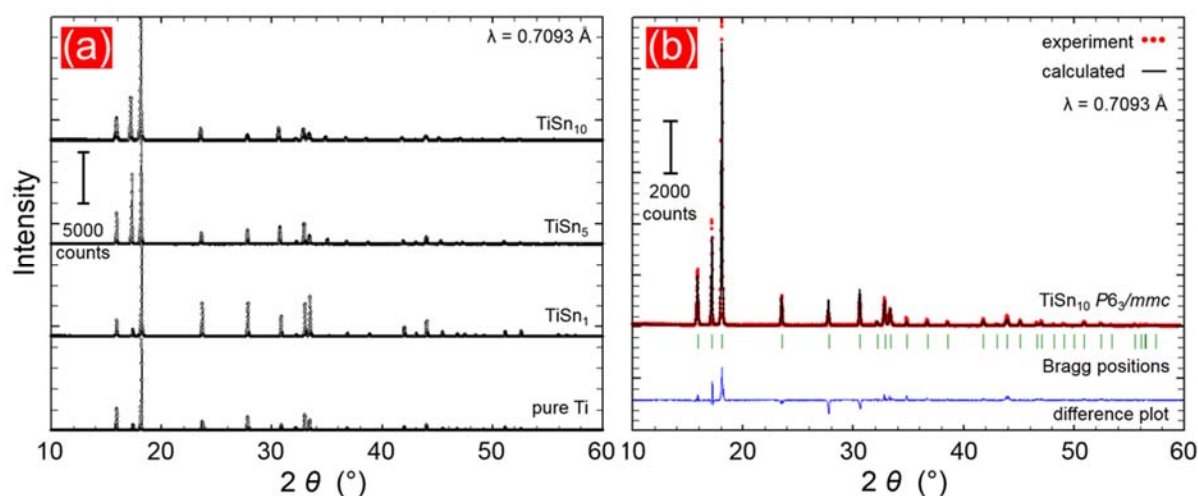
Fig. 6.2. *X-ray diffraction patterns of pure Ti and the as-cast Ti-Sn alloy substrates (a) and an exemplary result of the Rietveld analysis for the TiSn$_{10}$ sample (b).*

Tab. 6.2. Results obtained from the Rietveld analyses of the XRD data of pure Ti and the as-cast Ti-Sn alloys, phase composition, lattice parameters, phase contents and crystallite sizes.

sample	structure model	space group	a / Å	c / Å	γ (°)	V / Å^3	wt.%	crystallite size / nm
pure Ti	Ti#	$P6_3/mmc$	2.9517(1)	4.6848(2)	120	35.3548(3)	100	647
TiSn$_1$	Ti#	$P6_3/mmc$	2.9511(1)	4.6916(4)	120	35.384(6)	100	270
TiSn$_5$	Ti0.95Sn0.05*	$P6_3/mmc$	2.9525(2)	4.7134(3)	120	35.582(6)	100	431
TiSn$_{10}$	Ti0.9Sn0.1+	$P6_3/mmc$	2.9550(3)	4.7355(5)	120	35.810(1)	100	69
# structure model taken from Ref. [229].								
* structure model: based on Ref. [230], occupancy adapted to 5 at.% tin content.								
+ structure model taken from Ref. [230].								

After the detailed characterization of the alloys, these were used as discs for the nanotube growth. **Figure 6.3** represents the variation in the current density as a function of the anodic oxidation time recorded at 40 V during nanotube formation on the different Ti-Sn alloys.
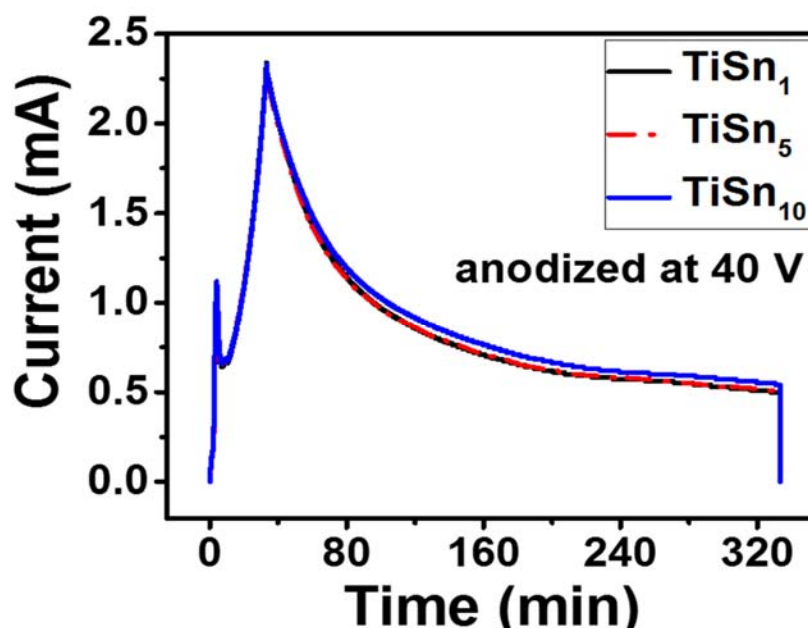
Fig. 6.3. *Time-current density relationship during the nanotube formation on the TiSn$_1$, TiSn$_5$ and TiSn$_{10}$, respectively, at an anodization voltage of 40 V.*

At the beginning the current density increases in less than 1 min due to the interaction between the alloy surface and the oxygen ions O^{2-} (generated from H_2O or OH^- ions of the electrolyte) induced by the electrical field at the interface [11,120]. Afterwards, an exponential decay in the current density occurs due to the passivation effect of the formed compact metal oxide layer. After 10 min. the current density starts to increase again until reaching the final voltage value due to the field-assisted chemical dissolution of the previously formed oxide layer by the fluoride ions causing small pits. The abrupt current decrease with a subsequent increase at the initial anodization time of 10 min. agrees well with previous literature [231,232], in which a ramping voltage was applied during the anodization process. These previously formed pits are gradually converted into pores with time. With increasing anodization time,

these pores continuously and uniformly grow in diameter and depth to finally cover the whole oxide layer resulting in a tube array structure. In the following, the current density decreases reaching steady state conditions where the rate of metal oxidation and electrochemical etching compete [11,231]. In the following sections, the nanotubes grown on the TiSn$_1$, TiSn$_5$, TiSn$_{10}$ and pure Ti substrates will be further denoted as T1S, T5S, T10S and T0S, respectively.

6.2.4 Morphology of the fabricated TiO$_2$-SnO$_2$ nanotubes

The surface morphologies of the TiSn$_1$, TiSn$_5$ and TiSn$_{10}$ substrates after the anodic oxidation carried out at different anodization voltages (10 - 40 V) in the ethylene glycol electrolyte containing 0.3 M NH$_4$F and 3.0 % v/v deionized water are shown in **Figures 6.4**, **6.5** and **6.6**, respectively. For comparison, SEM images of TiO$_2$ nanotubes fabricated under the same anodization conditions at 10, 20 and 40 V are presented in **Figures 6.7a**-**c**. In all cases, the nanotube formation is clearly observed over the entire substrates. Indeed, clear-cut nanotube arrays are featured when the alloy substrates are anodized at a voltage higher than 10 V.

Figure 6.8 summarizes the relationship between the anodization voltage, the inner nanotube diameter and tube wall thickness. It is noticed that the mean nanotube diameter and wall thickness are dependent on the anodization potential i.e. they are increased by increasing the applied voltage during the anodic oxidation processes. Controlling the nanotube dimensions (diameter and length) by varying the formation voltage was explored for pure Ti [120] and various Ti-based alloys such as Ti-Ni and Ti-Pd anodized in similar electrolytes [16,159]. As presented in **Figure 6.8a** for all Ti-Sn substrates, the mean nanotube diameter increases by increasing the formation voltage matching with the reported behavior for pure Ti [31,230]. The main reason for increasing nanotube dimensions was attributed to the enhanced electrical field intensity resulting from the increased applied voltage. Such increase in the electrical field intensity promotes an acceleration of the diffusion rate of the transported ions across the barrier layer (alloy/oxide interface) causing a higher

etching rate in the oxide layer resulting in the formation of tubes with higher lengths and larger diameters [159]. The cross sectional SEM images demonstrate closed nanotube bottoms and typically close-packed arrays with high aspect ratios i.e. small diameter and long length. It is interesting to observe that the nanotube wall thicknesses seem to grow directly proportional to the Sn contents (**Fig.6.8b**), indicating that the easiest lithium ion diffusion is found for T1S similar to nanotubes with thin wall thickness [174]. On top of the nanotubes a partial cover of nanograss is formed. This phenomenon was reported for pure Ti when anodized in ethylene glycol containing fluoride ions [233].
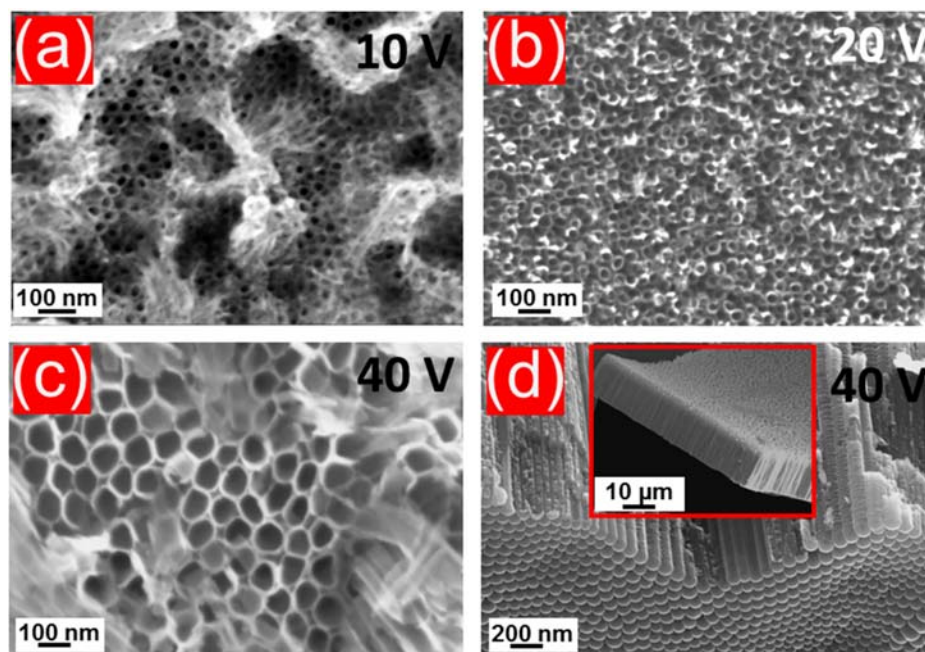
Fig. 6.4. *SEM micrographs of the TiSn$_1$ alloy anodized at 10 V (a), 20 V (b) and 40 V (c), respectively, for 5 h. Cross sectional view for the sample formed at 40 V (d). The inset in (d) shows the uniform growth of the nanotubes.*
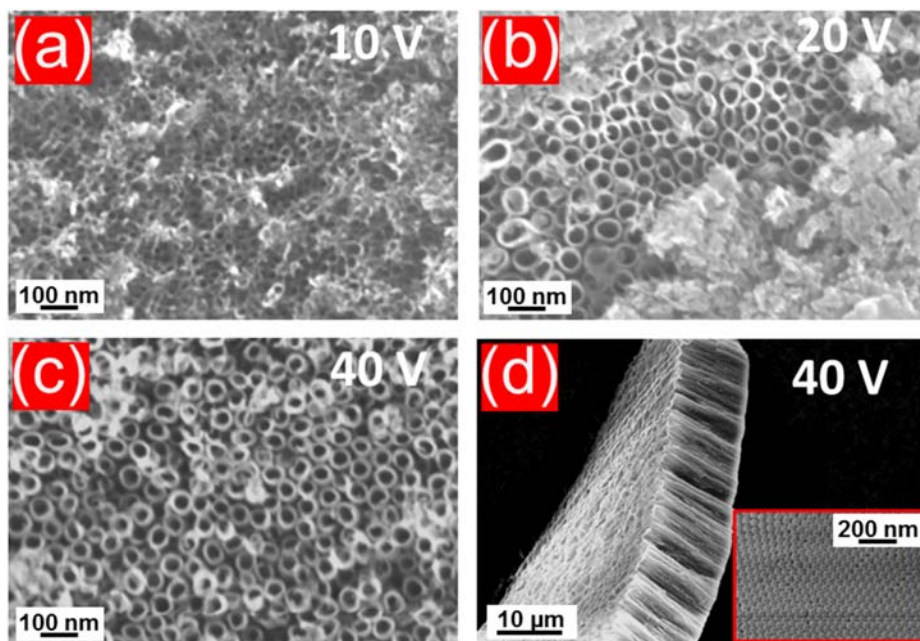
Fig. 6.5. *SEM micrographs of the TiO₂-SnO₂ nanotubes (T5S sample) grown on the TiSn₅ alloy at 10 V (a), 20 V (b) and 40 V (c), for 5 h. Cross sectional view for the sample formed at 40 V (d). The inset in (d) shows the nanotube bottoms.*
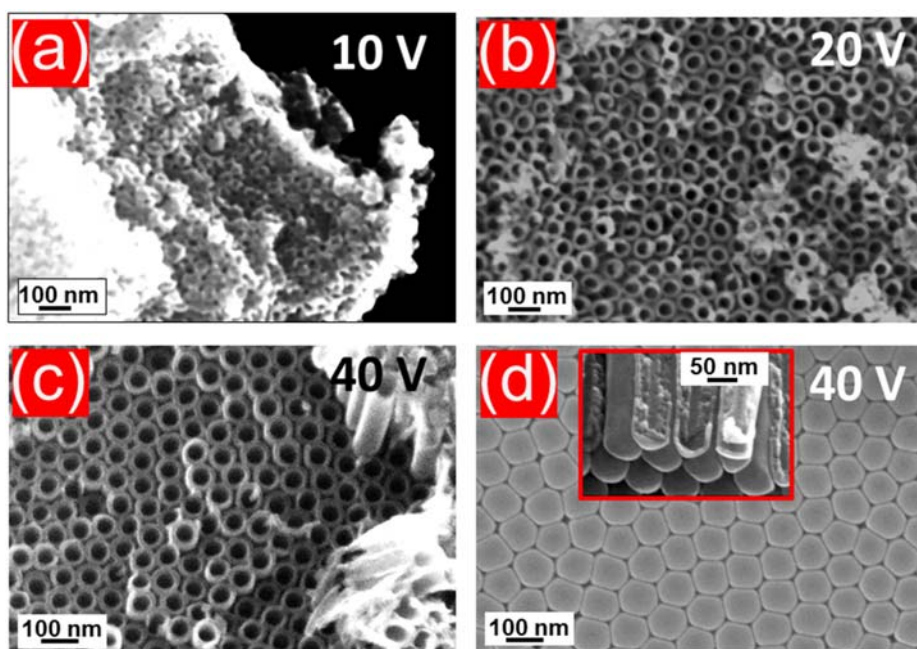
Fig. 6.6. *SEM micrographs of the TiO₂-SnO₂ nanotubes (T10S sample) grown on the TiSn₁₀ alloy at 10 V (a), 20 V (b) and 40 V (c), for 5 h. Bottom view of the sample formed at 40 V (d). The inset in (d) shows the cross sectional nanotube walls.*
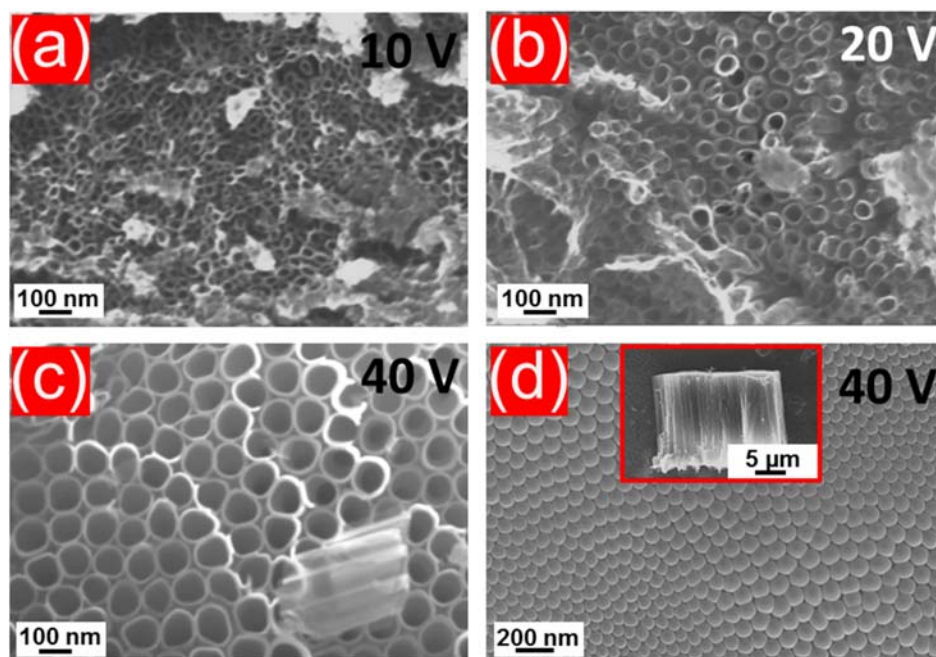
Fig. 6.7. *SEM micrographs of pure TiO$_2$ nanotubes formed at 10 V (a), 20 V (b) and 40 V (c), for 5 h. Bottom view of the sample formed at 40 V (d). The inset in (d) shows the cross-sectional view.*
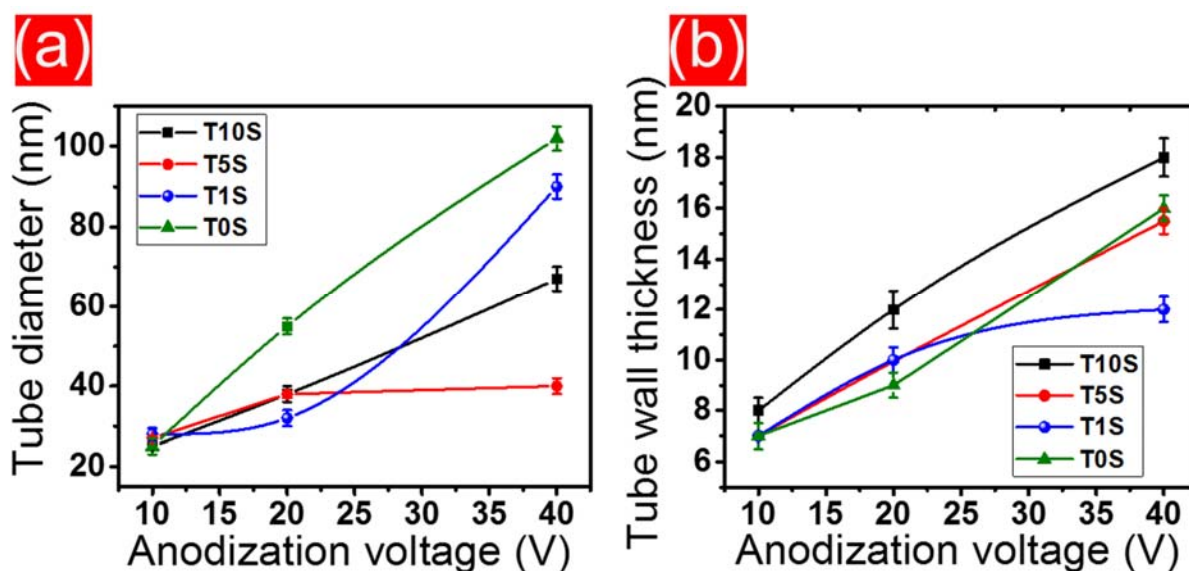
Fig. 6.8. *Effect of the anodization voltage on the nanotube diameter (a) and wall thickness (b) formed by the anodic oxidation of the TiSn$_1$ (T1S), TiSn$_5$ (T5S), TiSn$_{10}$ (T10S) and pure Ti (T0S) substrates, for 5 h.*

The origin of this grass-like structure is ascribed to a partial chemical dissolution of the nanotube surface that takes place by the extended anodization time leading to a thinning of the top tube walls as shown in the cross-sectional image in **Figure 6.9**.
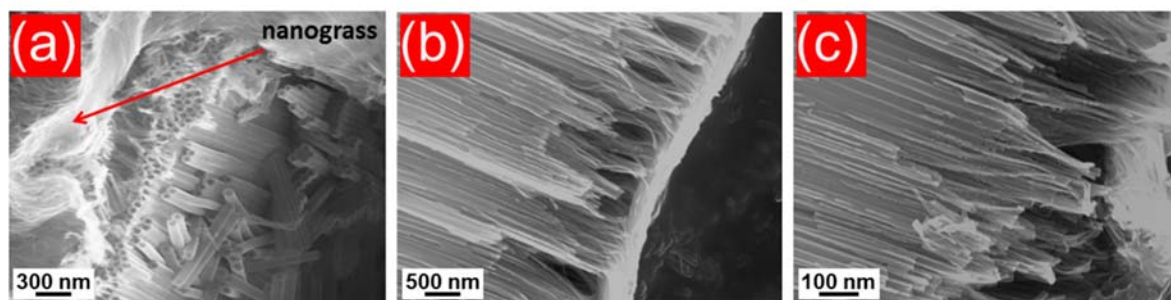
Fig. 6.9. SEM micrographs of TiO₂-SnO₂ nanotubes (T10S sample) prepared at 40 V; Top view showing the nanograss formed on the top of some nanotubes (a), cross-sectional view at low magnification (b), cross-sectional view at high magnification showing the separation of the nanotube walls into nanograss (c).

As the etching is typically non-uniform, internal stresses in the outer walls occur resulting in a separation of nanoneedles or nanograss-like structures [11,233]. One of the useful approaches to reduce this nanotube disorders, is sweeping the voltage to reach desired formation magnitude as used in the present study [234]. Despite all uniform growth the material is amorphous as demonstrated by the XRD pattern in **Figure S7** (in the supplementary information), where no reflections were detected.

EDXS quantitative analysis (**Fig. S8** in the supplementary information) of the grown nanotube films showed that the Sn/Ti contents are 1.21/98.79, 5.22/94.78 and 8.90/91.10 at.% for T1S, T5S and T10S, respectively. These analyses indicate that the Sn contents in the formed nanotube oxides in agreement with those of the alloy substrates. Moreover, ICP-OES analysis showed that T1S, T5S and T10S samples contain similar contents of Ti and Sn (1.2: 98.8, 94.4: 5.6 and 88.8: 11.2 at%,

respectively). Both EDXS and ICP-OES analysis prove no change in the Sn concentrations in both the alloy substrates and the formed oxide films.

The nanotubes grown on the $TiSn_{10}$ substrate at 40 V were further analyzed by TEM. **Figure 6.10a** displays a bright-field TEM image of the tubular nanotubes in dimensions which are comparable to the SEM images (**6.6**). The TEM-EDXS shown in **Figure 6.10c** was carried out in scanning mode (**Figure 6.10b**) and proved that the nanotubes are composed of both Ti and Sn.
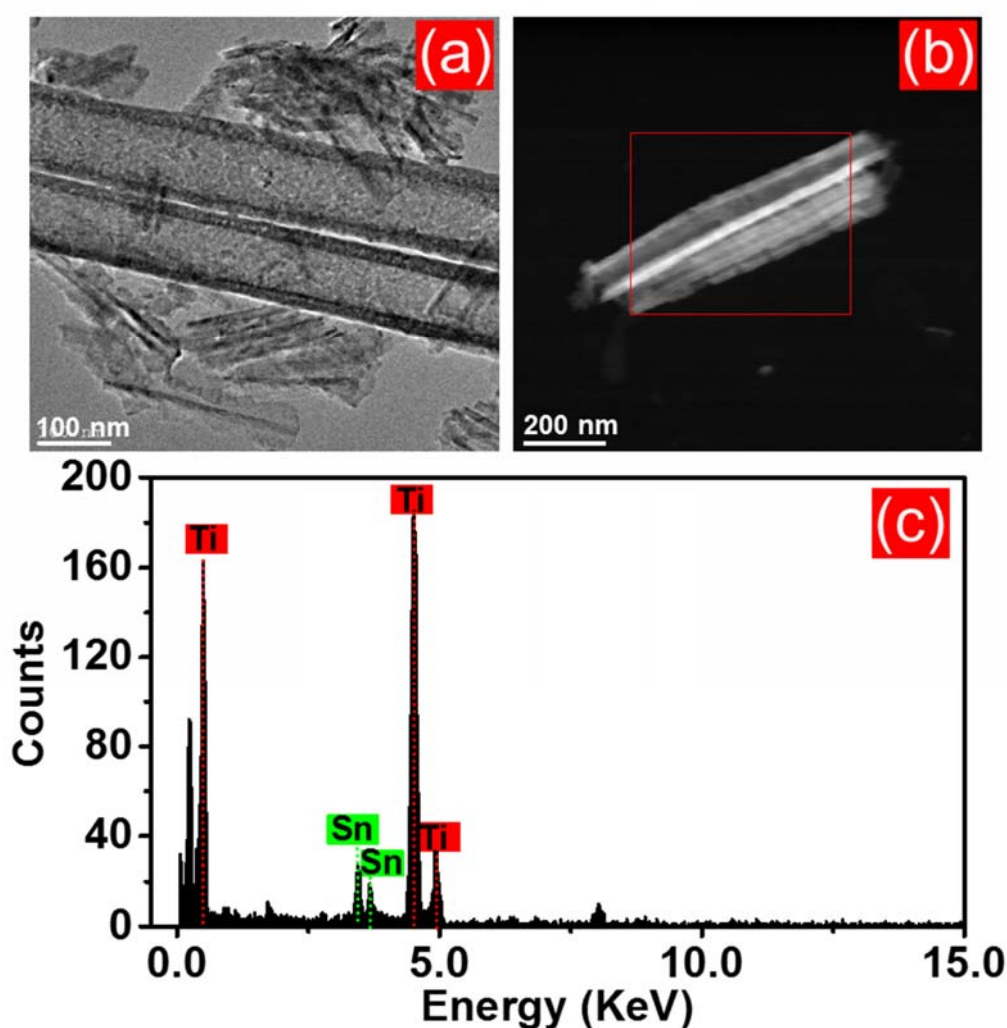
Fig. 6.10. *TEM bright-field images for the as-grown nanotubes on the $TiSn_{10}$ substrate formed at 40 V (a); STEM image for individual nanotubes (b) and the STEM-EDX analysis confirming that the tubes are composed of Ti and Sn oxides (c).*

6.2.5 XPS investigation of the grown TiO₂-SnO₂ nanotubes

To provide further information about the chemical composition of the fabricated nanotubes, X-ray photoelectron spectroscopy was conducted. The obtained XPS survey spectra of the grown nanotubes on the TiSn$_{10}$ substrate are displayed in **Figure 6.11**. The Ti 2p spectrum (**Figure 6.11a**) shows two defined peaks with maxima located at 465 and 459 eV, which are characteristic for the spin-orbit coupling for the Ti 2p$_{1/2}$ and Ti 2p$_{3/2}$ orbitals, respectively. The binding energy (BE) position of the peaks confirms the presence of TiO$_2$ and allows to identify the BE as reference [114,159]. The Sn 3d spectrum is shown in **Figure 6.11b**. Two peaks are observed with maxima at 486.8 and 495.2 eV corresponding to the spin-orbit coupling of the Sn 3d$_{5/2}$ and Sn 3d$_{3/2}$ orbitals, respectively. The position of the two peaks clearly proves the presence of tin in the oxidation state +IV which is assigned to SnO$_2$ [235]. Additionally, the existence of metal oxides is indicated by the O 1s spectra (**Figure 6.11b**), where a single peak at 531 eV is observed [13].Representative spectra for carbon with C 1s in **Figure 6.11d** and for fluorine with the F 1s binding energy in **Figure 6.11e** show apparent peak maxima located at 284.8 and 684.8 eV, corresponding to carbon and fluorides, respectively [236].

Ethers and alcoholic groups as well as carbonyl groups cannot be excluded as shown by the shoulder at higher binding energies with a local maximum at about 287 eV. The presence of significant amounts of carbon (9.18 %) and fluoride (13.59 %) species adsorbed on the formed nanotubes is attributed to a partial decomposition of the electrolyte as it particularly happens in organic electrolytes during anodization [11]. Based on the XPS results, it is deduced a successful formation of TiO$_2$-SnO$_2$ nanotube films from the Ti-Sn alloys. The atomic concentrations of Ti and Sn metals of the grown nanotube films were determined at the nanotube surface and after sputtering time of 8 min corresponding to abrasion of approximately 28 nm from the oxide surface. The depth-profiling analysis are shown in **Table 6.2**. At the nanotube surface, in general the atomic Sn contents of all samples show a good representation of the relative alloy concentration and agree well with EDXS and ICP-OES analysis.
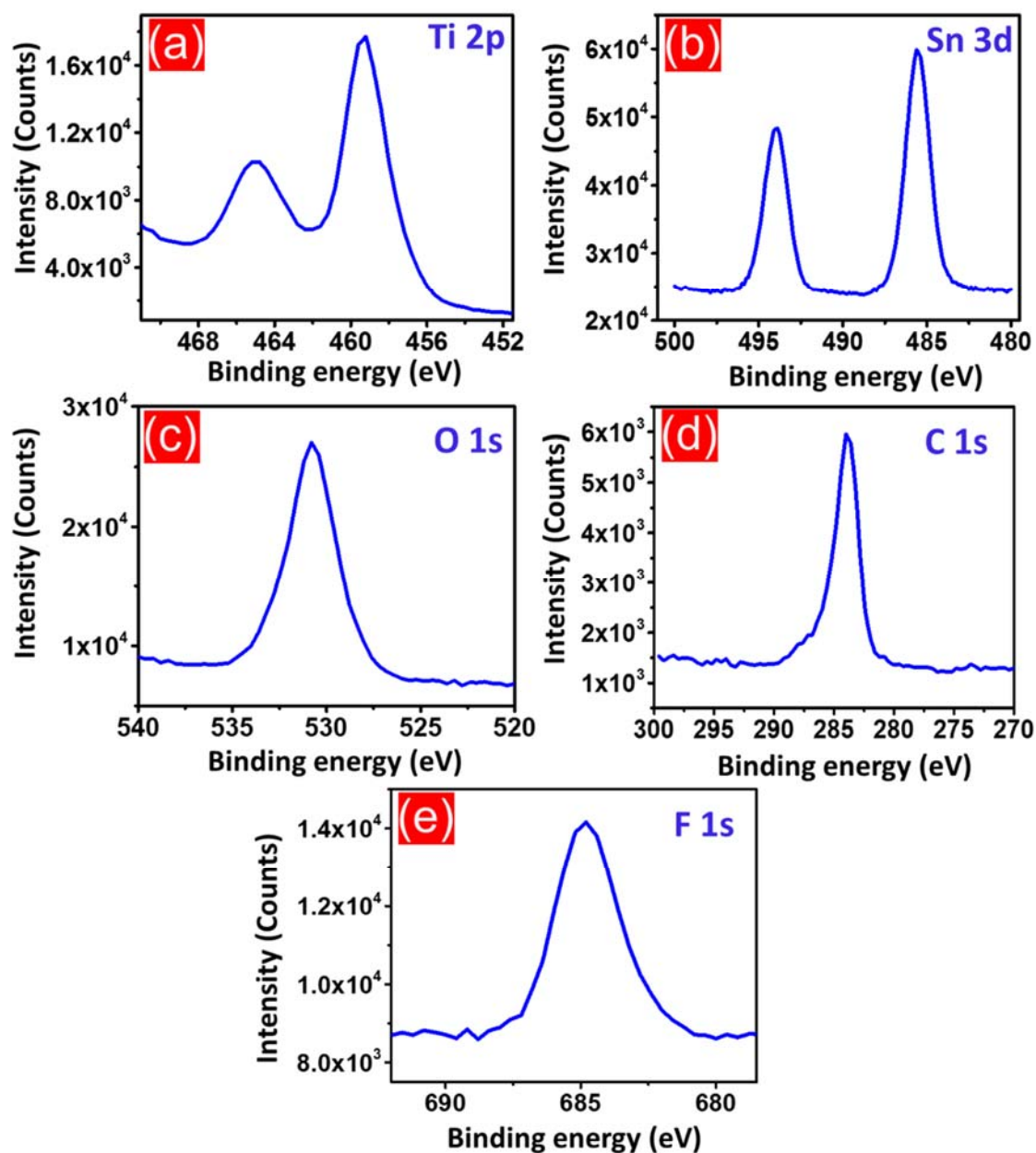
Fig. 6.11. *X-ray photoelectron spectra of the grown nanotubes on the TiSn₁₀ substrate at 40 V for the binding energies Ti 2p (a), Sn 3d (b), O 1s (c), C 1s (d) and F 1s (e).*

The presence of relatively higher Sn contents in the formed nanotubes than those in the alloy substrates could be attributed to the etching rate of Sn by anodic oxidation, which is much faster than for Ti in the alloy substrates [239]. Little

changes in the Sn concentrations to lower values were observed after etching for T1S and T5S samples. T10S shows a larger change in the Sn concentration (from 11.09 to 6.46 ± 0.1) which in accordance with the EDXS mapping results in **Figure 6.1** indicating the inhomogeneous distribution of the Sn metal over the alloy substrate.

Tab. 6.2. *The atomic concentration of elemental Ti and Sn of the grown nanotube arrays obtained by XPS depth-profiling.*

Sample	Measurement condition	Atomic concentration	
		Ti	Sn
T1S	on surface	98.26 ± 0.1	1.74 ± 0.1
T5S	on surface	93.56 ± 0.1	6.44 ± 0.1
T10S	on surface	88.91 ± 0.1	11.09 ± 0.1
T1S	after sputtering	98.44 ± 0.1	1.56 ± 0.1
T5S	after sputtering	95.36± 0.1	4.64 ± 0.1
T10S	after sputtering	93.54± 0.1	6.46 ± 0.1

6.2.6 Raman spectroscopy of TiO$_2$-SnO$_2$ nanotubes

To provide further insights about the composition of the present phases, Raman scattering measurements were conducted for the as-fabricated TiO$_2$-SnO$_2$ nanotubes grown at 40 V. As displayed in **Figure 6.12**, six broad signals located at 394, 443, 505, 612, 772 and 891 cm^{-1} are observed and assigned to amorphous TiO$_2$. These peaks fit very well with the reported spectrum of amorphous TiO$_2$ nanotubes obtained by anodization of a Ti foil [192]. The pronounced peaks at about 177 and 579 cm^{-1} are consistent with the typical Raman spectra of amorphous SnO$_2$ nanomembranes [236]. The peak broadening between 400 and 700 cm^{-1} is attributed to the overlapping Raman modes of TiO$_2$ and SnO$_2$. The Raman analysis is also in

accordance with the results derived from XRD and XPS, corroborating the successful formation of TiO$_2$-SnO$_2$ nanotubes.
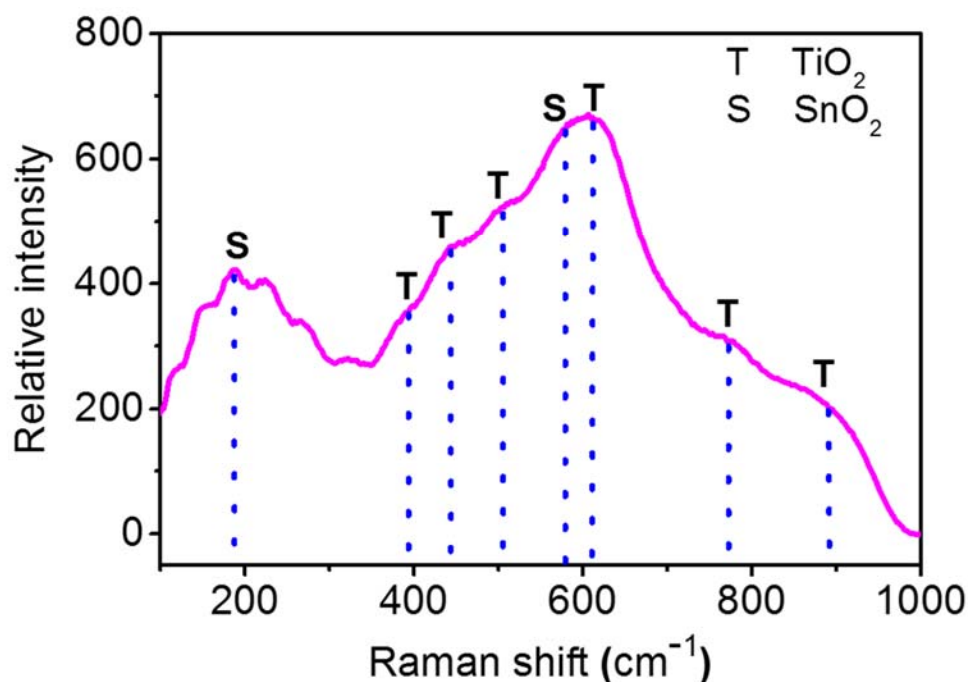
Fig. 6.12. *Raman spectrum of the as-formed TiO₂-SnO₂ grown on the TiSn₁₀ substrate at 40 V.*

6.3   Electrochemical properties

6.3.1 Cyclic voltammetry

The as-formed TiO$_2$ and TiO$_2$-SnO$_2$ nanotubes were directly tested at a cutoff voltage range of 0.1 - 3 V at a scan rate of 1 mV s^{-1} *vs.* Li/Li$^+$, since previous studies have shown that amorphous TiO$_2$ exhibits a better performance than crystalline TiO$_2$ because of larger spatial channels created from disorders and defects in amorphous TiO$_2$ [140,141]. Additionally, the annealing process conducted at 450 °C causes a detachment of the nanotube films from the Ti-Sn substrates. This detachment and which may be due to the increased stress on the barrier layer which is the tube/metal

interface [237]. Typical cyclic voltammograms at the second charging/discharging cycle for the as-grown TiO$_2$-SnO$_2$ and the pure TiO$_2$ nanotubes formed at 40 V are shown in **Figure 6.13**. For the TiO$_2$-SnO$_2$ electrode, the CV behavior, in general, matches well with previous literature reports [30,238].
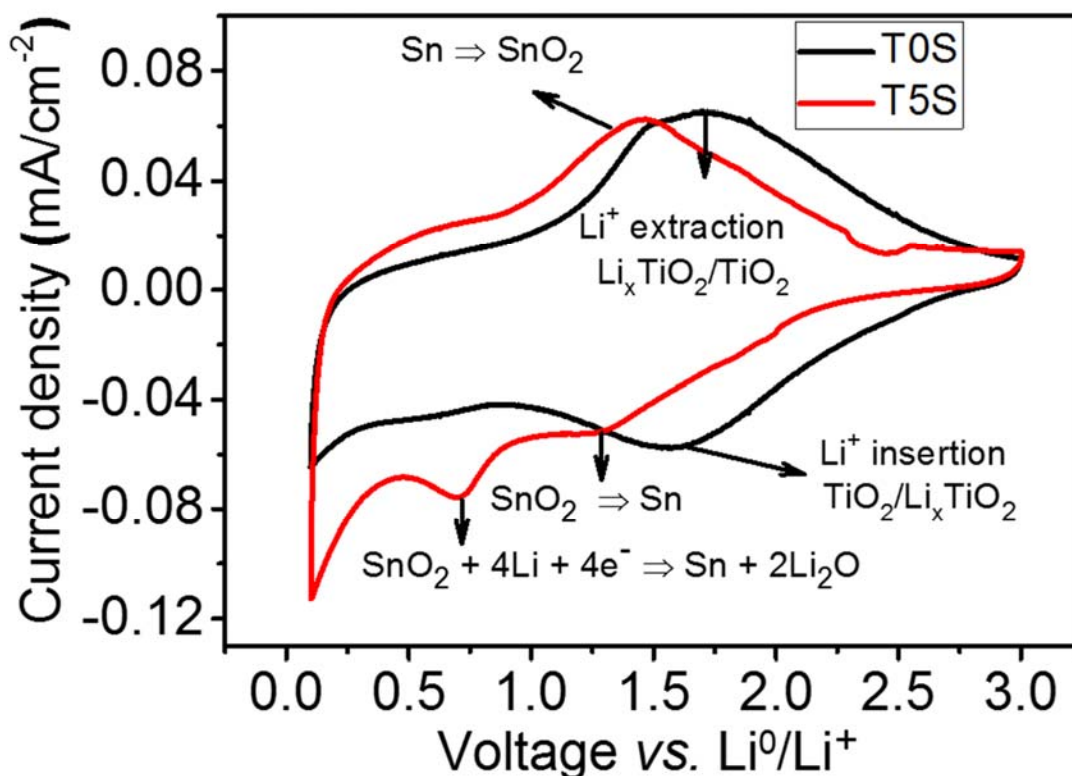
Fig. 6.13. Cyclic voltammograms of TiO$_2$ and TiO$_2$-SnO$_2$ nanotubes (formed on the TiSn$_5$ alloy), prepared at 40 V, and measured at scan rates of 1 mV s^{-1}.

In the reduction branch of the voltammogram, an apparent peak located at 0.77 V *vs.* Li/Li$^+$ appears. This peak is typically ascribed to the irreversible decomposition of SnO$_2$ into metallic Sn and the formation of Li$_2$O. Another peak located at 1.25 V *vs.* Li/Li$^+$, is attributed to the partially reversible conversion reaction of SnO$_2$ into metallic Sn [30]. This reaction is also evident in the cathodic branch from the significant sharpness of the main peak at approximately 1.4 V. In addition, a pair

of anodic/cathodic peaks is noticed at 0.1 and 0.6 V *versus* Li/Li$^+$, respectively, which are associated with the alloying and dealloying reactions to form Li$_x$Sn$_y$ compounds [235]. For pure TiO$_2$, two main broad peaks in the anodic and cathodic branches are detected at the selected voltage range. Related to the insertion and extraction of Li to form Li$_x$TiO$_2$.

6.3.2 Galvanostatic cycling with potential limitation

Galvanostatic discharging/charging curves were obtained from cycling the electrodes at a current density of 504 µA cm^{-2} (i.e. 335 mA g^{-1}) corresponding to a current rate of 1C (1C refers to full charging or discharging in one hour) in Swagelok-type cells between 0.1 - 3 V *vs.* Li/Li$^+$. **Figure 6.14a** shows the voltage profile curves for the first charging (lithium insertion)/discharging (lithium extraction) of the as-formed TiO$_2$ and the TiO$_2$-SnO$_2$ nanotubes. For all electrodes, no well-defined plateaus are noticed in the charging/discharging curves according to the general behavior of amorphous TiO$_2$-based electrodes and the results are compatible to the CV curves in **Figure 6.14**. The T1S, T5S and T10S electrodes exhibit higher initial discharging/charging capacities, i.e. 2525/1127, 2010/1117 and 1831/1105 µAh cm^{-2}, respectively. The gravimetric capacities,1323/590, 1057/585 and 959/579 mAh g^{-1}, follow the same trend corresponding to Coulombic efficiencies (CE) of 44.6, 55.6 and 60.3 %, respectively (**Fig. 6.14b**), compared to pure TiO$_2$ nanotubes with 1272/815 µAh cm^{-2} (i.e. 666/427 mAh g^{-1}) and 64.1 %. The specific capacities of the electrodes proportionally decreases due to the Sn contents of the alloy substrates which relates to the SnO$_2$ mass, suggesting that SnO$_2$ contributes to the whole specific capacity of the electrodes.
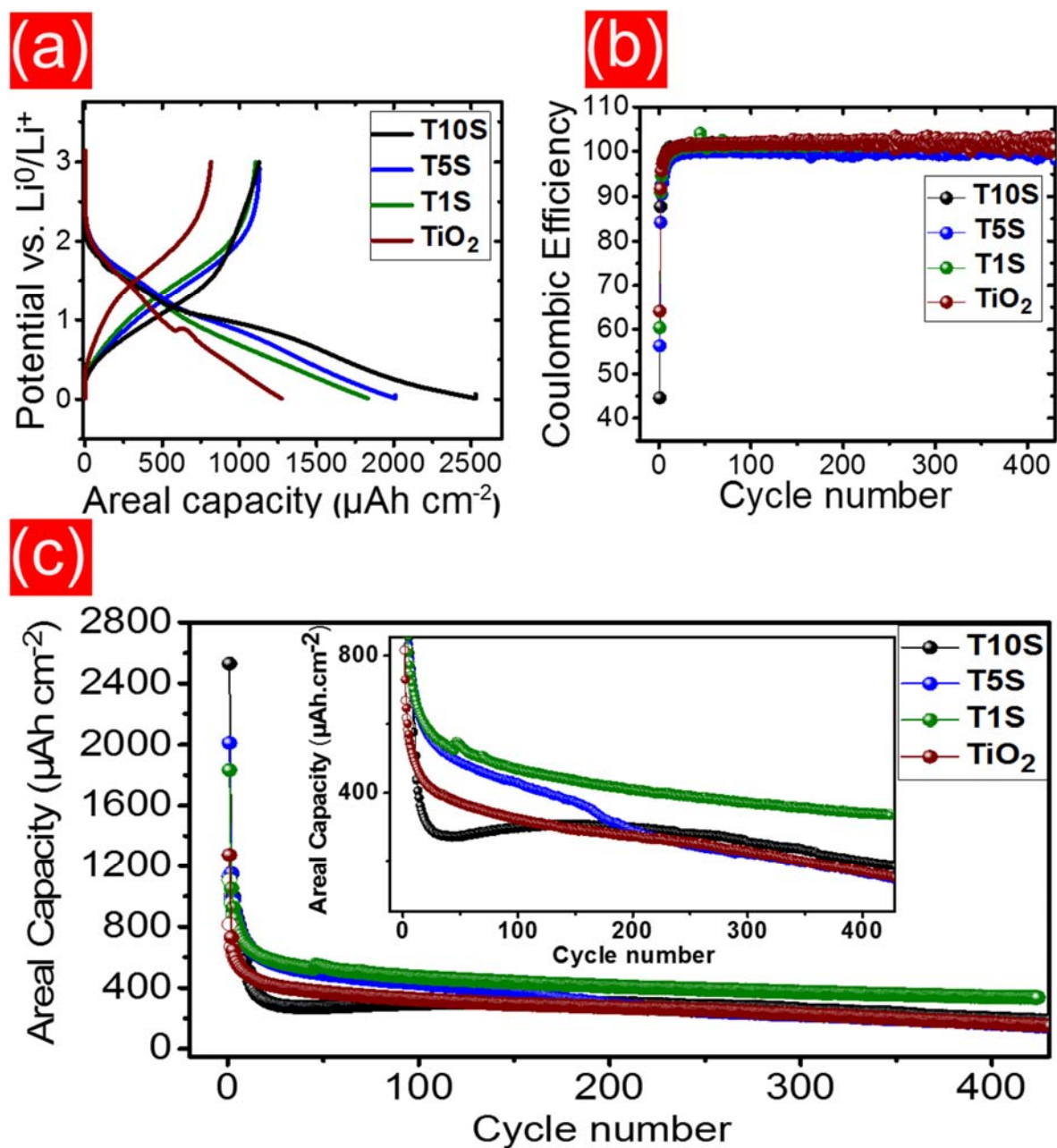
Fig. 6.14. *(a) Typical voltage profiles for the 1st charging/discharging cycle against areal capacity for pure TiO$_2$, T1S, T5S and T10S electrodes, prepared at 40 V anodization voltage, obtained at a current density of 504 μA cm^{-2}. (b) The corresponding coulombic efficiency of the electrodes over 450 charging/discharging cycles. (c) Galvanostatic areal discharging capacities as a function of cycle number obtained at the same current density for pure TiO$_2$ (dark red circles) and TiO$_2$-SnO$_2$ anodes (T1S electrode (green circles), T5S electrode (blue circles) and T10S electrode (black circles). The mass of each electrode was 1.91 mg.cm^{-2}.*

It is known that SnO$_2$ reacts with Li$^+$ ion according to a conversion mechanism described by equations **6.1** and **6.2** thus producing a higher theoretical capacity (782 mAh g^{-1}) than pure TiO$_2$ (335 mAh g^{-1}) reacting by an intercalation mechanism [235].

$$\text{SnO}_2 + 4\,\text{Li}^+ + 4e^- \leftrightarrow \text{Sn} + 2\,\text{Li}_2\text{O} \tag{6.1}$$

$$\text{Sn} + x\,\text{Li}^+ + x\,e^- \leftrightarrow \text{Li}_x\text{Sn}\ (0 \leq x \leq 4.4) \tag{6.2}$$

In the lithiation step, SnO$_2$ decomposes into metallic Sn and Li$_2$O resulting in a reduction capacity of 711 mAh g^{-1} (eq. **6.1**) [236]. Afterwards, the reduced Sn undergoes an alloying step in which it reversibly interacts with lithium ions to form Li$_x$Sn where, $0 \leq x \leq 4.4$ [239]. Taking into account that the first reaction is partially reversible, the total capacity obtained from both reactions is 782 mAh g^{-1}.

Figure 6.14c displays the galvanostatic cycling carried out at a current density of 504 µAh cm^{-2} for more than 400 cycles. All samples show an irreversible discharging/charging capacity in the first cycle assigned to the formation of the solid electrolyte interface (SEI) layer between the electrolyte and the electrode. After the first cycle, the specific capacity drops rapidly into a plateau lasting for over 20 cycles. Such rapid capacity fading was reported in previous studies as a common characteristic for amorphous TiO$_2$ and attributed to the increased overpotential during the lithiation/delithiation processes [10].

Note that, cycling the electrodes in a voltage window below 1 V may be partially another reason for the substantial loss in the specific capacity due to SEI formation at roughly 0.8 V *vs.* Li/Li$^+$ as a result of electrolyte decomposition which can also explain the low CE values. As presented in the inset of **Fig. 6.14c**, the T1S electrode shows the highest discharging/charging capacity. Compared to T0S, the T1S sample exhibits an average 1.4-fold increase in the specific capacity with excellent cycling stability over 420 cycles. For the T5S electrode, a gradual decrease in the capacity is observed up to about 200 cycles where the specific capacity of pure TiO$_2$ is met. The T10S electrode displays the lowest capacity over around 115 cycles. A significant

increase in the specific capacity is noticed when starting from cycle number 50 to number 200 a higher capacity compared to both T5S and pure T0S samples is reached. The main reason for the lower capacity of the T10S electrode before 115 cycles may originate from the partially irreversible conversion reaction of SnO$_2$. Due to the partial irreversibility of the conversion reaction, SnO$_2$ becomes inactive upon cycling resulting in a large loss of capacity of the electrode. This behavior is similar to the cyclic performance of the T5S electrode which contains half the amount of SnO$_2$ compared to T10S. In the case of T1S, the effect of the SnO$_2$ mass on the total electrode mass is small. This fact implies that, the presence of such a significant amount of SnO$_2$ in the TiO$_2$-SnO$_2$ electrode may have a positive effect to improve its ionic conductivity, resulting in a higher electrochemical performance. Note that the remarkably better cycling performance is additionally attributed to the high surface area of the T1S sample, exhibiting a thinner tube wall thickness [174]. Moreover, the thinner tube wall thickness promotes an accelerated Li ion diffusion towards the TiO$_2$-SnO$_2$ electrode as a result of the shorter Li ion diffusion path. Besides, the thinner tube wall thickness promotes accelerated Li ion diffusion towards the TiO$_2$-SnO$_2$ electrode as a result of the shorter Li ion diffusion path [174,238].

6.3.3 Specific surface area of the fabricated TiO$_2$-SnO$_2$ nanotubes

In order to further quantify the amount of accessible surface area of the samples, nitrogen physisorption experiments were carried out. The respective isotherms are shown in **Figure 6.15**. All investigated samples show similar sorption isotherms which feature an IUPAC Type-III shape. The initial uptake of nitrogen at low relative pressures is rather low, indicating the absence of microporosity. However, at high relative pressures (p/p0 > 0,8) a steep increase in the nitrogen uptake is noticed. Considering the fact that the diameter of the tubes in all samples exceeds 50 nm, a pronounced effect of macroporosity is expected. Thus, the increase of the nitrogen uptake at high relative pressures is attributed to condensation effects. The samples discussed here show a decrease of the specific surface area with increasing Sn content, from 58 m^2 g^{-1} for T1S to 27 m^2 g^{-1} for T10S, as shown in **Table**

6.3. These values also correlate with the thickness of the tube walls, which become thicker with increasing amount of Sn (**Tab. 6.3**). Since the T1S sample shows the highest specific surface area, for this electrochemical reactions, which in turn leads to a high areal capacity, as shown in **Figure 6.14c**. The comparatively lower specific surface area of T10S hinders quick and complete reaction, leading to the lowest areal capacity of all samples already after about 10 cycles.
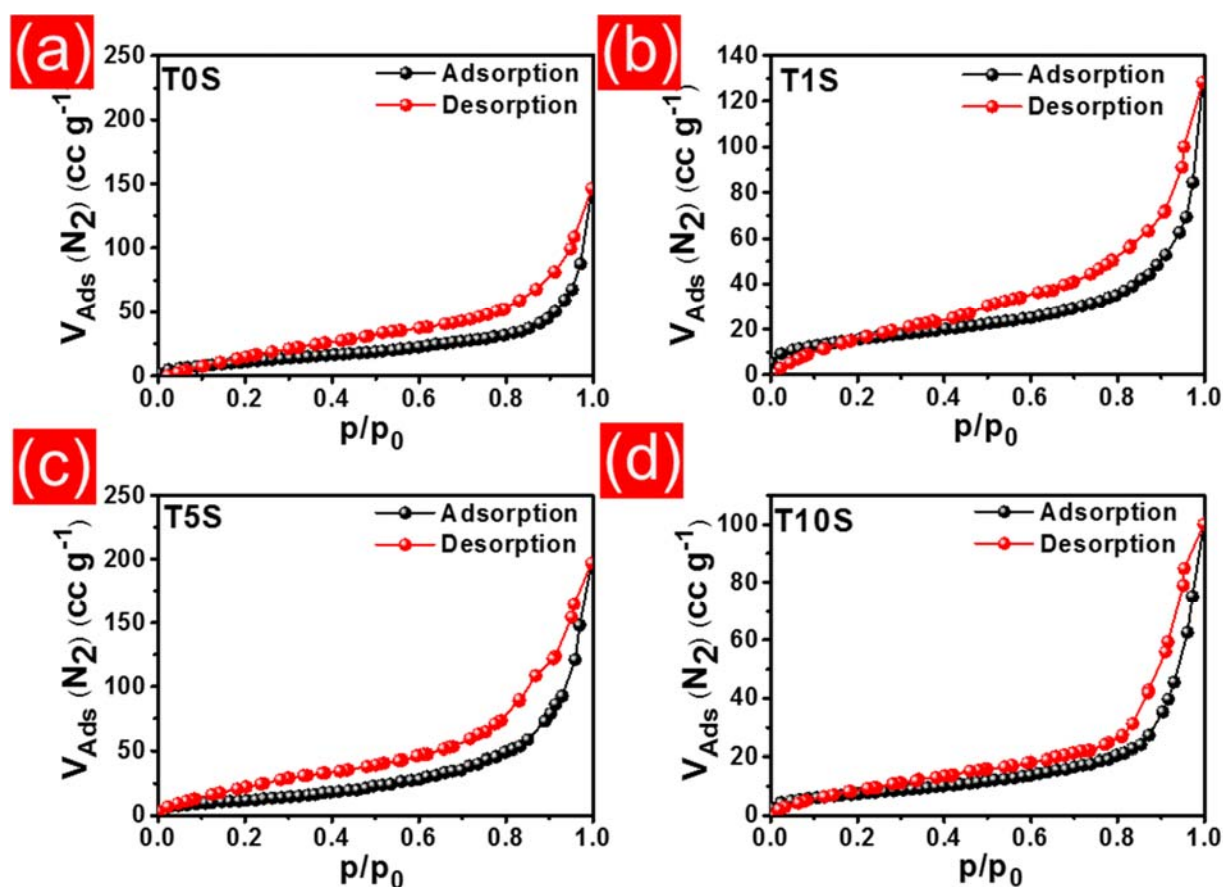
Fig. 6.15. *Nitrogen physisorption isotherms obtained at 77 K for (a) pure TiO$_2$ (b) T1S (c) T5S and (d) T10S nanotubes prepared at 40 V.*

Tab. 6.3. Specific surface areas of the investigated samples, obtained from nitrogen physisorption experiments.

Sample	Specific Surface Area (m^2 g^{-1})
T0S	47 ± 0.2
T1S	58 ± 0.2
T5S	45 ± 0.2
T10S	27 ± 0.2

6.3.4 Electrochemical impedance spectroscopy (EIS) and rate performance tests of the fabricated TiO$_2$-SnO$_2$ nanotubes

To investigate the effect of SnO$_2$ on the ionic conductivity of the electrodes, electrochemical impedance spectroscopy (EIS) measurements for all samples were conducted. The Nyquist plots of pure TiO$_2$ and the TiO$_2$-SnO$_2$ electrodes recorded at 1.7 V *vs.* Li/Li$^+$ are shown in **Figure 6.16a**. The spectra are characterized by semicircles at high-to-medium frequencies and inclined lines in the low frequency region. Generally, the semicircles at high-to-medium frequencies represent the charge transfer resistance whilst lithium ions diffuse from the electrolyte across the solid electrode/electrolyte interface [12,144]. The inclined lines correspond to solid state diffusion processes of lithium inside the TiO$_2$-SnO$_2$ nanotubes. Interpreted from these plots, all TiO$_2$-SnO$_2$ electrodes exhibit smaller semicircle diameters than the pure TiO$_2$ electrode. The T10S electrode shows the smallest diameter followed by the T5S and the TS1 electrodes indicating a higher ionic conductivity with increasing SnO$_2$ content. Majorly the Li$_2$O originating from the SnO$_2$ decomposition (equation 1) is suggested to be responsible for the enhanced ionic conductivity, similar to silicon nanostructures [240]. The EIS measurements of the T1S electrode were also conducted after 100 charge/discharge cycles at a current density of 504 µA cm^{-2} and

presented in **Figure 6.16b**. Only negligible changes in the EIS spectra were observed indicating that the T1S preserves its electrical conductivity even over cycling. All electrodes were further tested at different current densities from 50 to 1008 µA cm^{-2} to demonstrate its rate capability as depicted in **Figure 6.16c**. Although both of T5S and T10S electrodes showed higher charging/discharging capacities in comparison with T1S electrode at a low current density (50 µA cm^{-2}), the capacities decay sharply within the first ten cycles and finally meet the capacity values of the T1S electrode when the current density increases to 125 µA cm^{-2}. The rapid decrease in the charging/discharging capacities in the first few cycles is in accordance with the general behaviors of T5S and T10S electrodes in the cycling performance presented in **Figure 6.14c** which attributed to the irreversible conversion reaction of SnO$_2$.

Both T5S and T10S electrodes display a steep decrease in the charging/discharging capacities by increasing the current density stepwise to higher values. At the same rate, the T1S electrode exhibits the highest rate capability with a slower decrease in the charging/discharging capacity. The T1S electrode can deliver average capacities of 780, 660, 490 and 405 µA cm^{-2} at current densities of 50, 100, 252, 504 and 1008 µA cm^{-2}, respectively. The T1S electrode therefore exhibits an outstanding reversible rate capability. The electrode can be utilized for practical applications with these high values which is also supported of the morphological stability. To assess the morphological stability, further TEM investigations have been performed for the T1S sample after 450 charging/discharging cycles at a current density of 504 µA cm^{-2}. From the TEM image in **Figure 6.16d** it is deduced that the electrode sustains the original tubular structure with a marginal deformation of the tube walls.
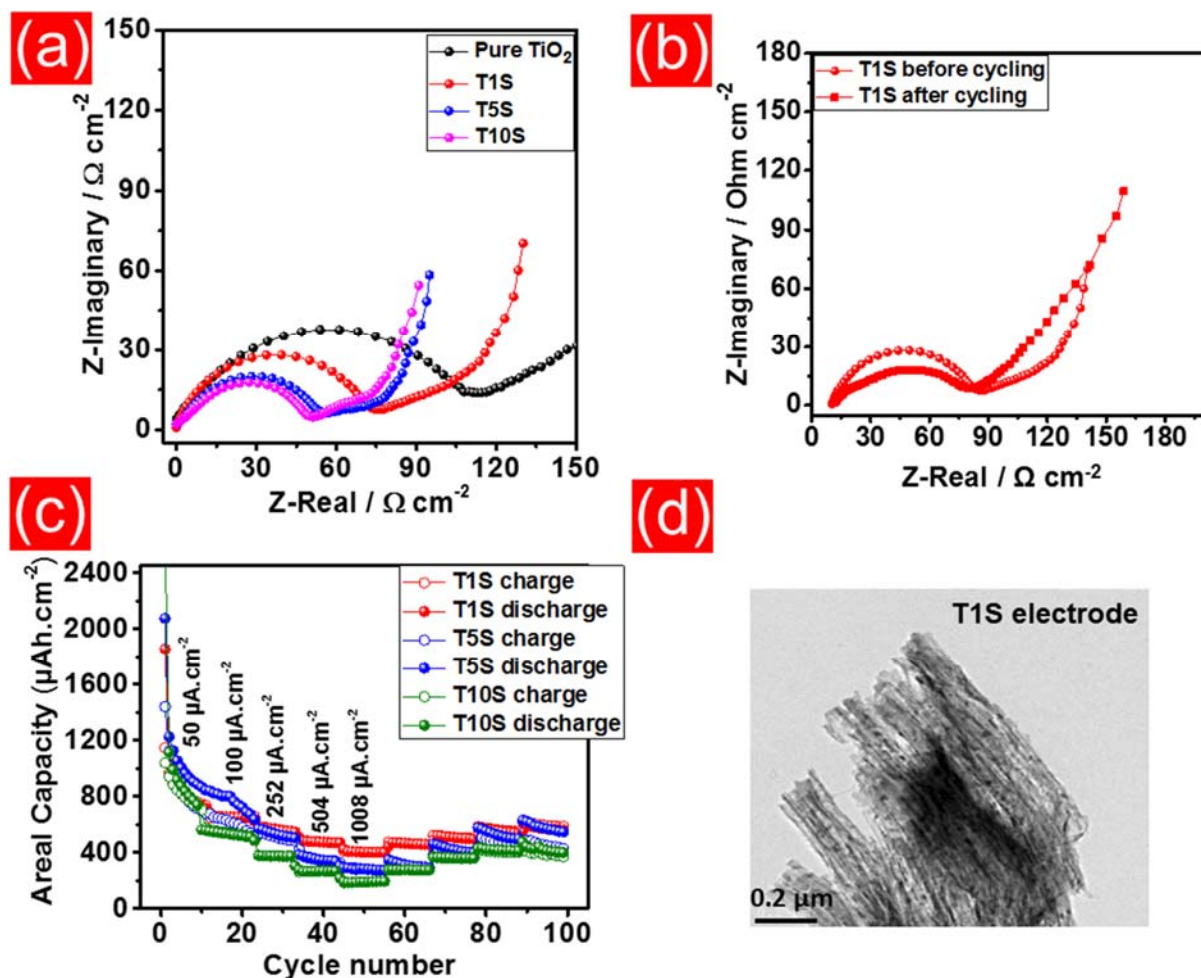
Fig. 6.16. *Nyquist plots of pure TiO$_2$ T0S (black circles) and TiO$_2$-SnO$_2$ anodes T1S electrode (red circles), T5S electrode (blue circles) and T10S electrode (magenta circles), prepared at 40 V in the frequency range of 100 kHz to 0.1 Hz at a potential of 1.7 V vs. Li/Li$^+$ (a); EIS spectra of T1S electrode before and after 100 charging/discharging cycles (b); Rate capability of the T1S electrode formed at 40 V (c). The filled red circles represent the discharging and black circles for the charging process; Morphological characterization of the T1S electrode formed at 40 V after 450 charging/discharging cycles at a current density of 504 µA cm^{-2} (d).*

6.4 Summary of chapter 6

In the present work, the electrochemical growth of self-organized mixed titanium and tin oxide nanotubes on the Ti-Sn alloys with different Sn concentrations (1, 5 and 10 at.%) as a practicable way to obtain TiO$_2$/SnO$_2$ nanotubes was investigated. The as-formed nanotubes are amorphous and their diameters depend on the formation voltage. The characterization results of the oxide films confirmed that the grown nanotubes are comprised of mixed TiO$_2$ and SnO$_2$. The electrochemical tests revealed that the SnO$_2$ contributes to the total capacity of the TiO$_2$/SnO$_2$ electrodes. The TiO$_2$/SnO$_2$ anode grown on the TiSn$_1$ alloy at 40 V displays a 1.4 times increase in the areal capacity compared to pure TiO$_2$ nanotube anodes fabricated and tested under the same conditions over 420 cycles. The enhanced electrochemical performance of TiO$_2$/SnO$_2$ nanotubes is related to the increased lithium ion diffusion resulting from the improved ionic conductivity of TiO$_2$ due to the presence of SnO$_2$ or secondary products. The morphological features of the TiO$_2$/SnO$_2$ nanotubes are well-sustained upon the electrochemical cycling.

Chapter **7**

Summary and outlook

7.1 Summary

In the present work, the electrochemical growth of self-organized, highly ordered and well-aligned mixed titanium and cobalt oxide nanotubes on the two-phase alloy $Ti_{80}Co_{20}$ were explored as a practicable way to obtain TiO_2-CoO nanotubes. The current density changes during the dynamic anodization processes and correlates with the morphology depending on the crystal structure of the two phases. The crystallinity of the fabricated TiO_2-CoO oxides was tuned by heat

treatment at 450 °C. The structural and spectroscopic characterizations of the oxide films confirm the formation of TiO_2-CoO and TiO_2-SnO_2 mixed nanotubes.

The electrochemical performance of the grown nanotubes was evaluated against a Li/Li$^+$ electrode at different current densities. On one hand, the TiO_2-CoO nanotube anodes displayed a 1.6 times increased areal capacity compared to pure TiO_2 nanotube anodes fabricated under the identical conditions with a capacity retention of 88 % over 100 cycles.

On the other hand, the Ti-Sn system with different Sn concentrations (1, 5 and 10 at.%) was utilized as starting materials to successfully grow TiO_2-SnO_2 nanotubes. The electrochemical tests revealed that the SnO_2 contributes to the total capacity of the TiO_2-SnO_2 electrodes. The TiO_2-SnO_2 anode grown on the $TiSn_1$ alloy at 40 V displays a 1.4 times increase in the areal capacity compared to pure TiO_2 nanotube anodes fabricated and tested under the same conditions over 420 cycles.

The fabrication of a novel ternary carbon nanotubes (CNTs)@TiO_2/CoO nanotubes composite by a two-step synthesis method was also investigated to improve further the electrochemical performance of TiO_2/CoO NT. The preparation includes an initial anodic fabrication of well-ordered TiO_2/CoO NTs from a Ti-Co alloy, followed by growing of CNTs horizontally on the top of the oxide films using a simple spray pyrolysis technique. The unique 1D structure of such a hybrid nanostructure with the inclusion of CNTs demonstrates significantly enhanced areal capacity and rate performances compared to pure TiO_2 and TiO_2/CoO NTs without CNTs tested under identical conditions. The findings revealed that CNTs provide a highly conductive network that improves Li$^+$ ion diffusivity promoting a strongly favored lithium insertion into the TiO_2/CoO NT framework, and hence results in high capacity and extremely reproducible high rate capability.

The improved electrochemical performance of TiO_2-CoO and TiO_2-SnO_2 nanotubes is attributed to the following reasons: (1) the high surface area of the TiO_2-CoO and TiO_2-SnO_2 mixed nanotubes, and (2) the increased lithium ion diffusion

resulting from the improved ionic conductivity of TiO_2 due to the presence of either CoO or SnO_2 or other secondary products. Such improvement essentially facilitates the Li^+ ion insertion and enhances its reversible capacity. The morphological features of the mixed oxide electrodes are well-sustained upon electrochemical cycling.

7.2 Outlook

In future work, the aim will be to optimize both of CoO and SnO_2 contents in the mixed oxide nanotubes using low atomic concentrations of Co and Sn in the alloy substrate in order to achieve higher lithium ion storage capacity. In addition, investigations are required in order to achieve a deeper understanding of the growth mechanism of TiO_2-CoO nanotubes, which may allow for identifying the reasons behind the formation of nanotubes on Ti_2Co phase with heights different from those nanotubes grown on β-Ti. In addition, studying the effect of annealing treatment (temperature and atmosphere) on each mixed oxide electrode on their electrochemical properties is precious to be investigated.

The applications, where such mixed oxides of the unique morphology may be used, are an important issue. Both of TiO_2-CoO and TiO_2-SnO_2 nanotubes may be applied as photoanodes in solar cell applications, solar hydrogen production or in sensors and catalysis.

Appendix

Supplementary information:

Table S1. List of the prepared samples

No.	Sample name	Synthesis method	Preparation conditions	Heat treatment
1	TiO_2-CoO NT 20 V	Anodization in Formamide based-electrolyte	20 V for 5 h	450 °C for 3 h
2	TiO_2-CoO NT 40 V	Anodization in Formamide based-electrolyte	40 V for 5 h	450 °C for 3 h
3	TiO_2-CoO NT 60 V	Anodization in Formamide based-electrolyte	60 V for 5 h	450 °C for 3 h
4	TiO_2-CoO NT 60 V	Anodization in Formamide based-electrolyte	60 V for 5 h	as-prepared
5	TiO_2 NT 20 V	Anodization in Formamide based-electrolyte	20 V for 5 h	450 °C for 3 h
6	TiO_2 NT 40 V	Anodization in Formamide based-electrolyte	40 V for 5 h	450 °C for 3 h
7	TiO_2 NT 60 V	Anodization in Formamide based-electrolyte	60 V for 5 h	450 °C for 3 h
8	TiO_2 NT 60 V	Anodization in Formamide based-electrolyte	60 V for 5 h	as-prepared
9	CNTs@TiO_2-CoO NT	Anodization followed by a spray pyrolysis	60 V for 5 h (anodization) and 860 °C for 25 min (spray pyrolysis)	as-prepared
10	CNTs@TiO_2 NT	Anodization followed by a spray pyrolysis	60 V for 5 h (anodization) and 860 °C for 25 min (spray pyrolysis)	as-prepared
11	TiO_2-SnO2 NT 40 V (T1S)	Anodization of Ti-Sn_1 alloy in Ethylene glycol based-electrolyte	40 V for 5 h	as-prepared
12	TiO_2-SnO_2 NT 40 V (T5S)	Anodization of Ti-Sn_5 alloy in Ethylene glycol based-electrolyte	40 V for 5 h	as-prepared
13	TiO_2-SnO_2 NT 40 V (T10S)	Anodization of Ti-Sn_{10} alloy in Ethylene glycol based-electrolyte	40 V for 5 h	as-prepared
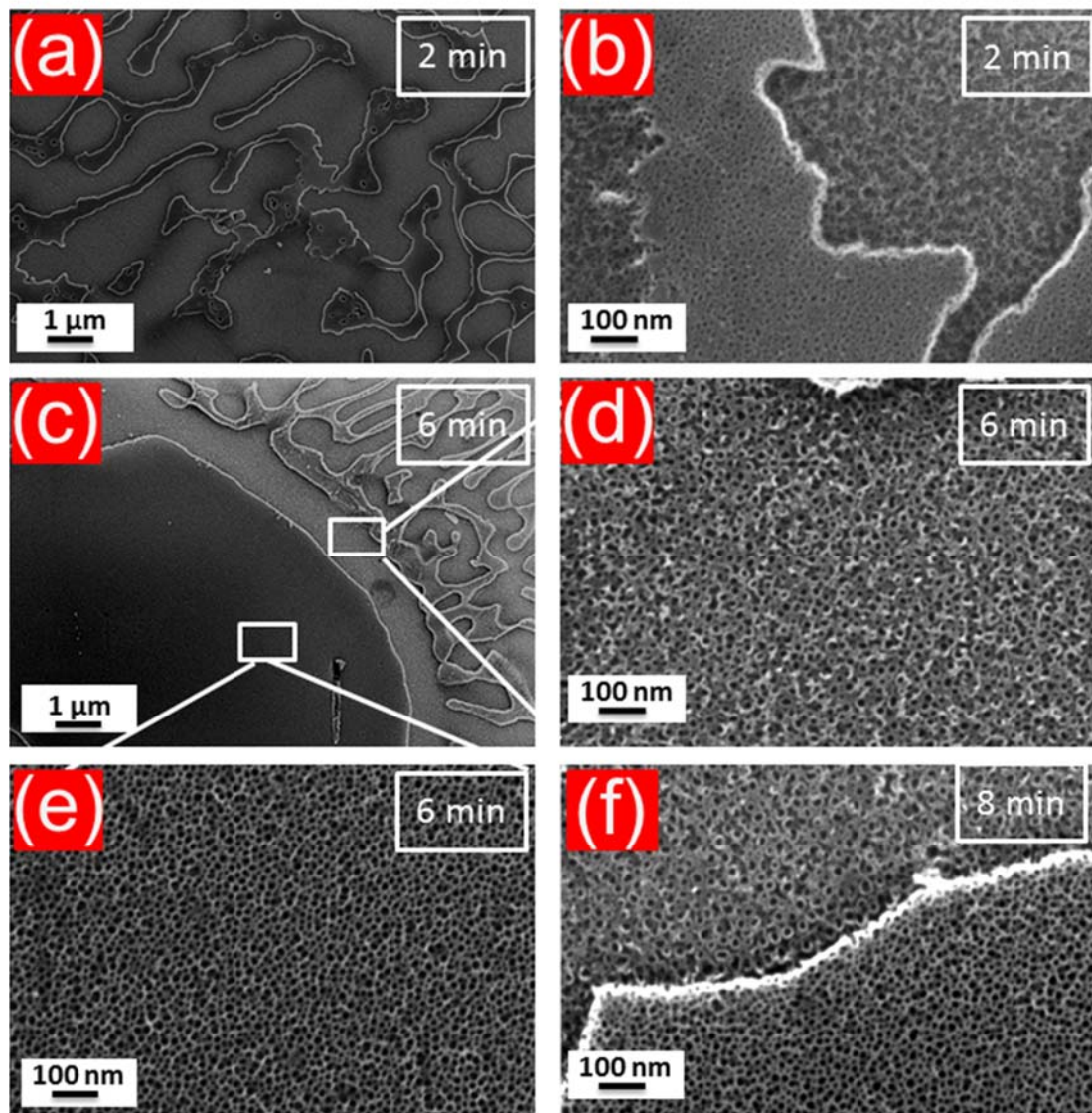
Fig. S1. *SEM micrographs of the Ti-Co alloy anodized for 2 min (a,b), anodized for 6 min (c), magnified for the β-Ti phase anodized for 6 min (d) and magnified for the Ti2Co phase anodized for 6 min(e) as well as the phase boundary of the sample anodized for 8 min (f).*
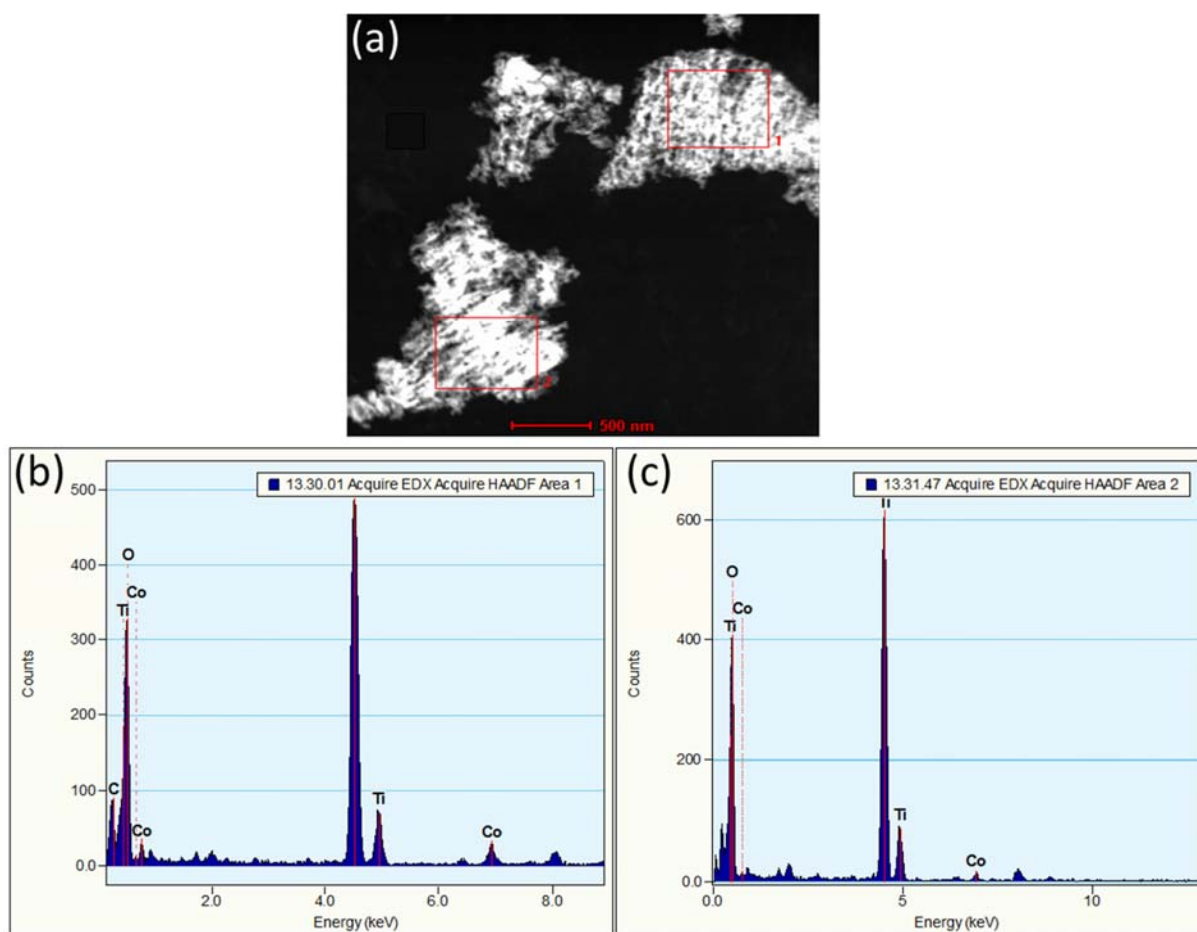
Fig. S2. STEM image of individual nanotubes (a) and the STEM-EDXS analysis confirming that the tubes are composed of Ti and Co oxides (b, c).
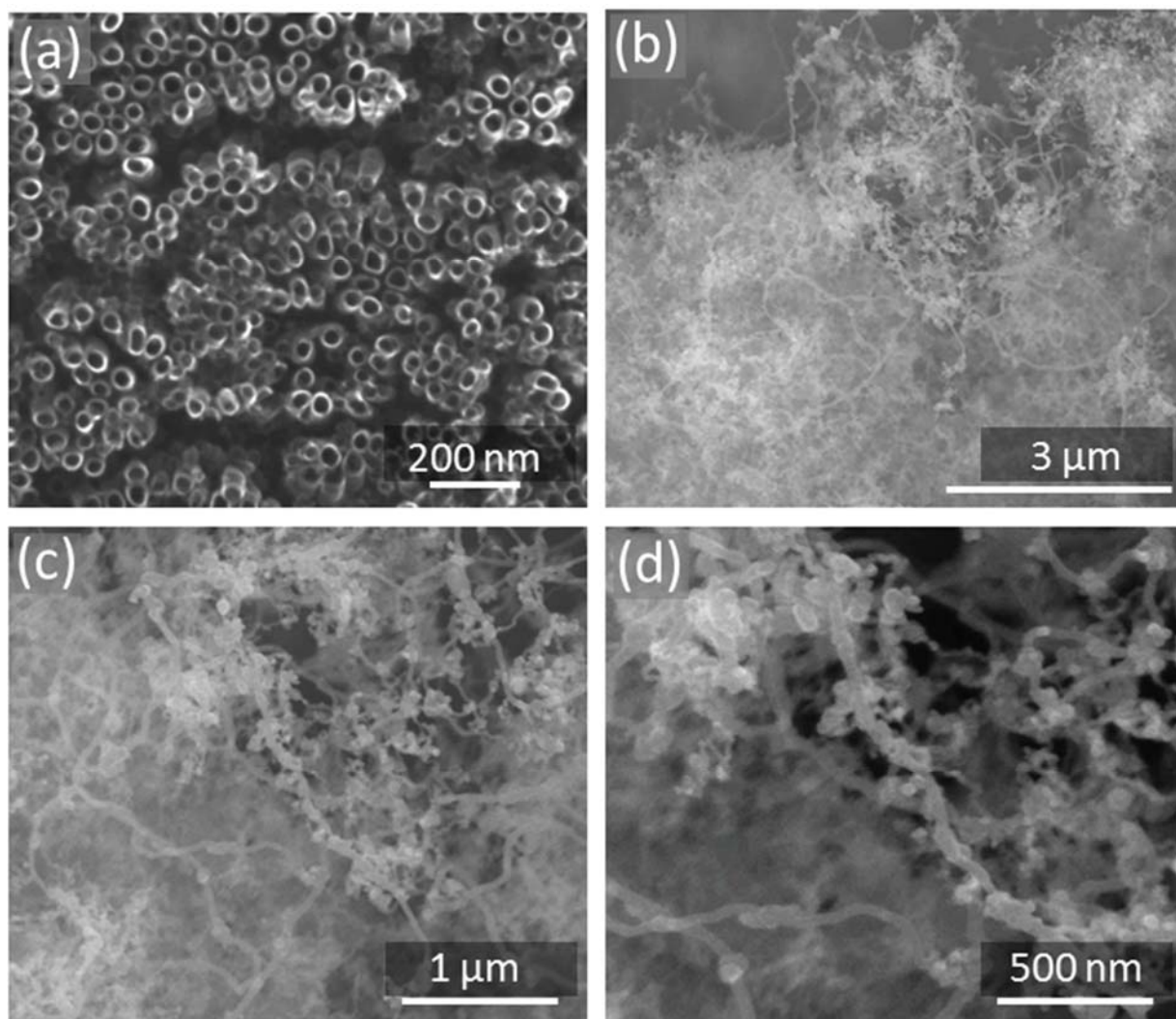
Fig. S3. SEM images showing pure TiO₂ nanotubes prepared at 60 V on the Ti substrate (a) and surface overview after CNT covering at different magnifications (b-d).
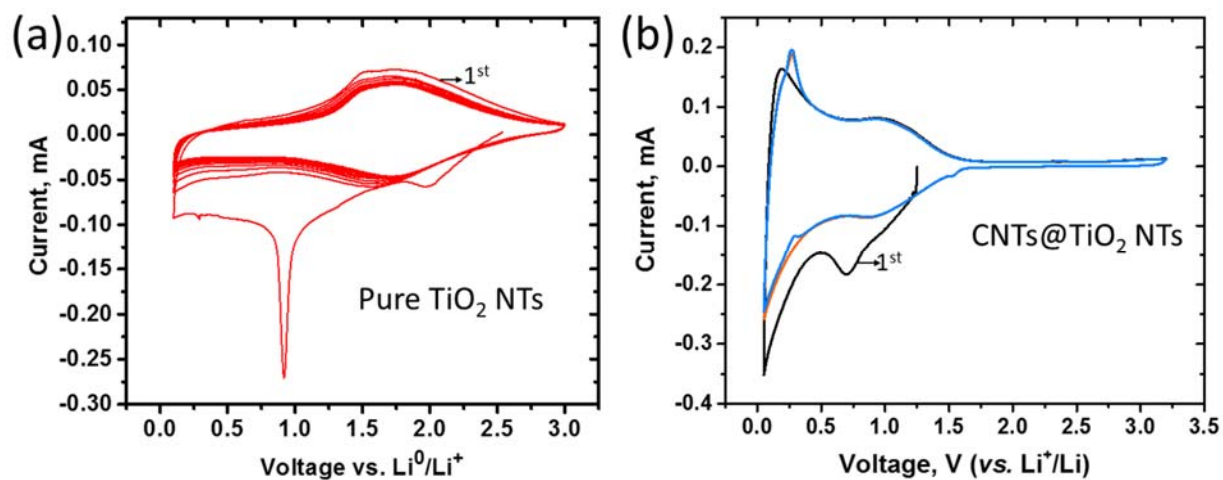
Fig. S4. *Cyclic voltammograms of pure TiO₂ nanotubes (a) and CNTs@TiO₂ NTs, measured at scan rates of 0.1 mVs⁻¹.*
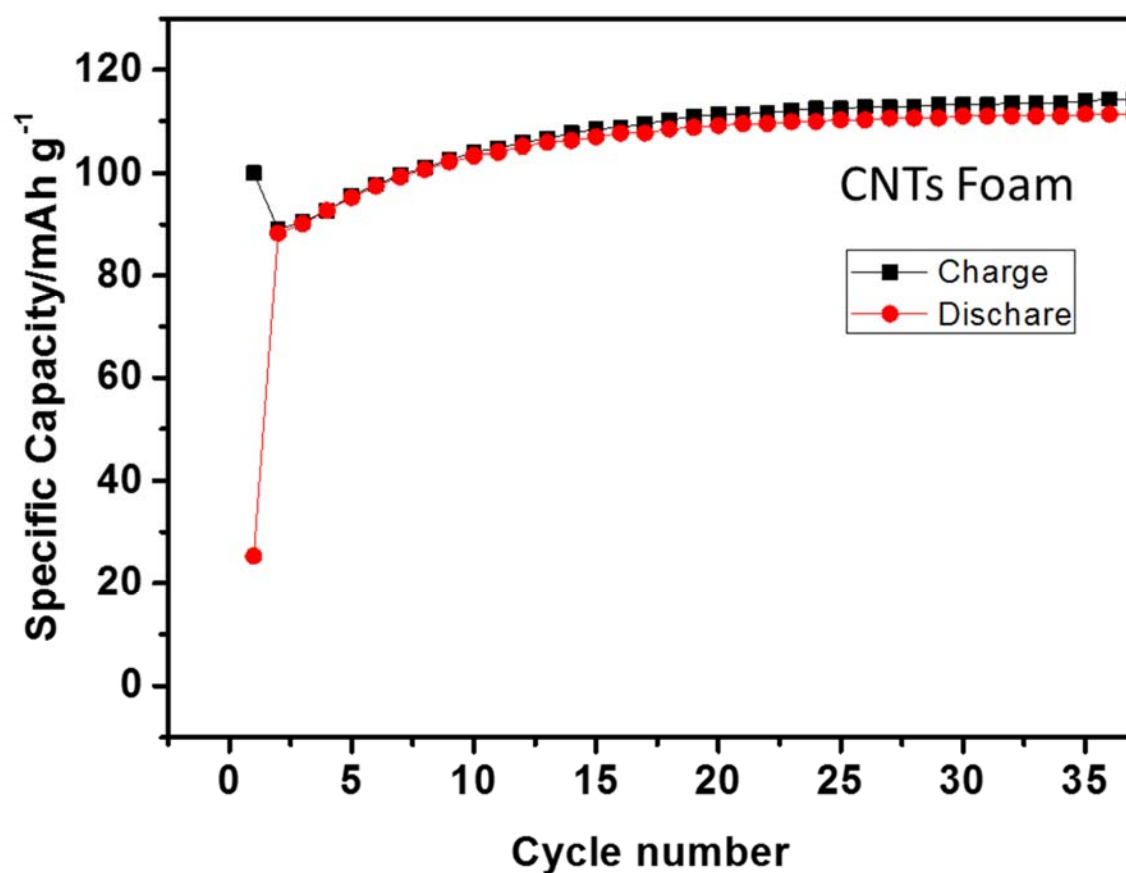
Fig. S5. Galvanostatic cycling of CNTs foam at a current rate of 446 mA g⁻¹ between 0.1 – 3 V.
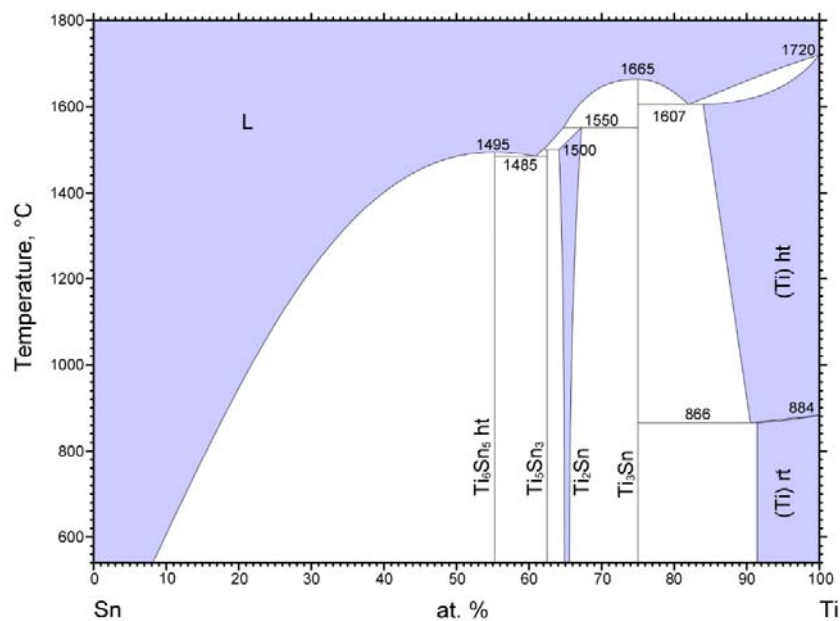
Fig. S6. *Phase diagram of binary Ti-Sn alloy.*
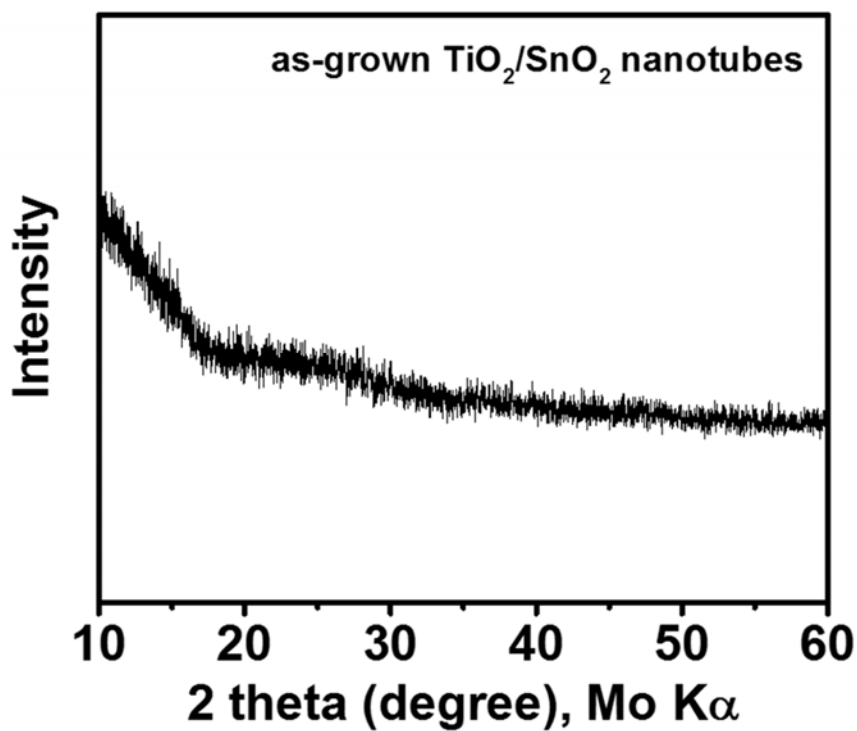
Fig. S7. *XRD pattern of the as-grown TiO₂-SnO₂ nanotubes (T10S sample) prepared at 40 V represents the amorphous state of the as-grown nanotubes.*
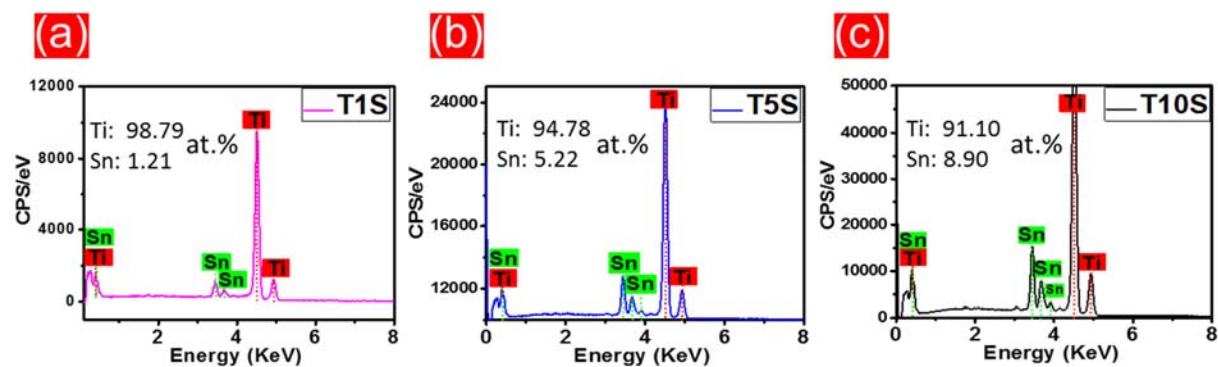
Fig. S8. *Quantitative analysis of Ti and Sn contents in T1S (a), T5S (b) and T10S (c) electrodes obtained from EDX elemental mapping.*
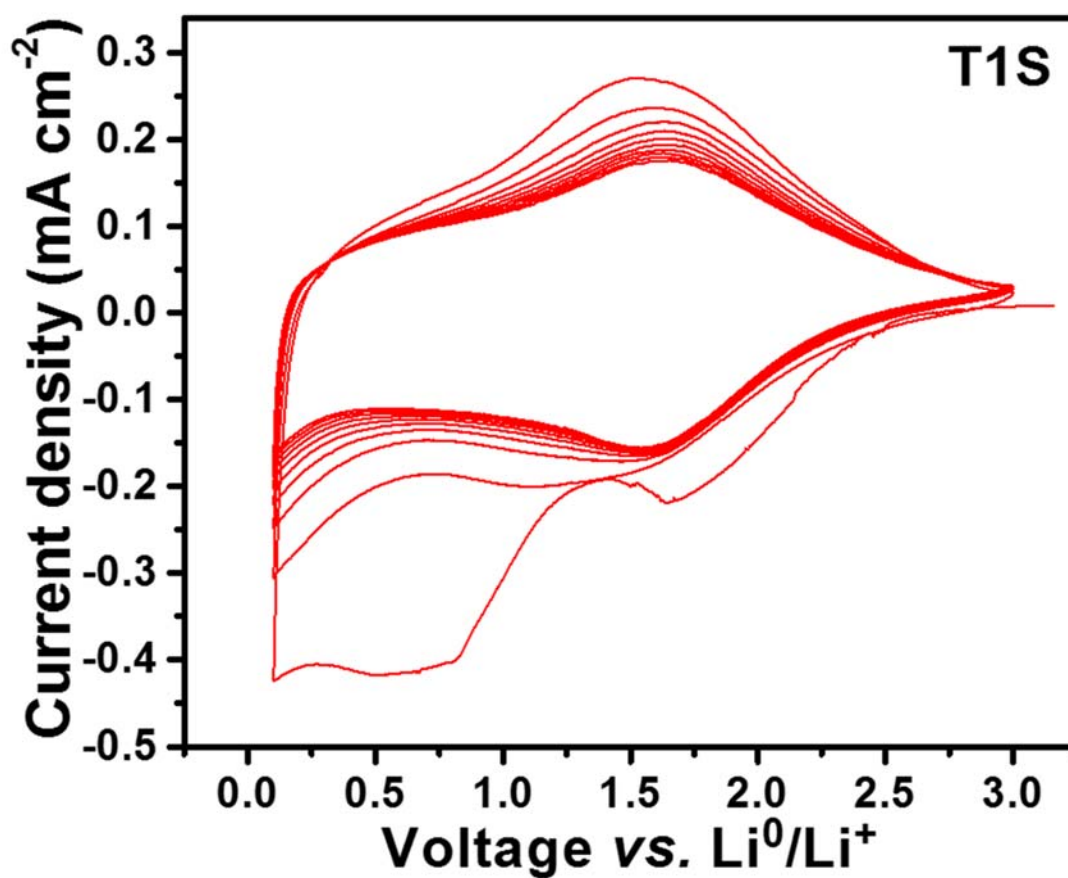
Fig. S9. *Cyclic Voltammograms of TiO$_2$-SnO$_2$ nanotubes (formed on the TiSn1 alloy), prepared at 40 V, and measured at scan rate of 1 mV s^{-1}.*
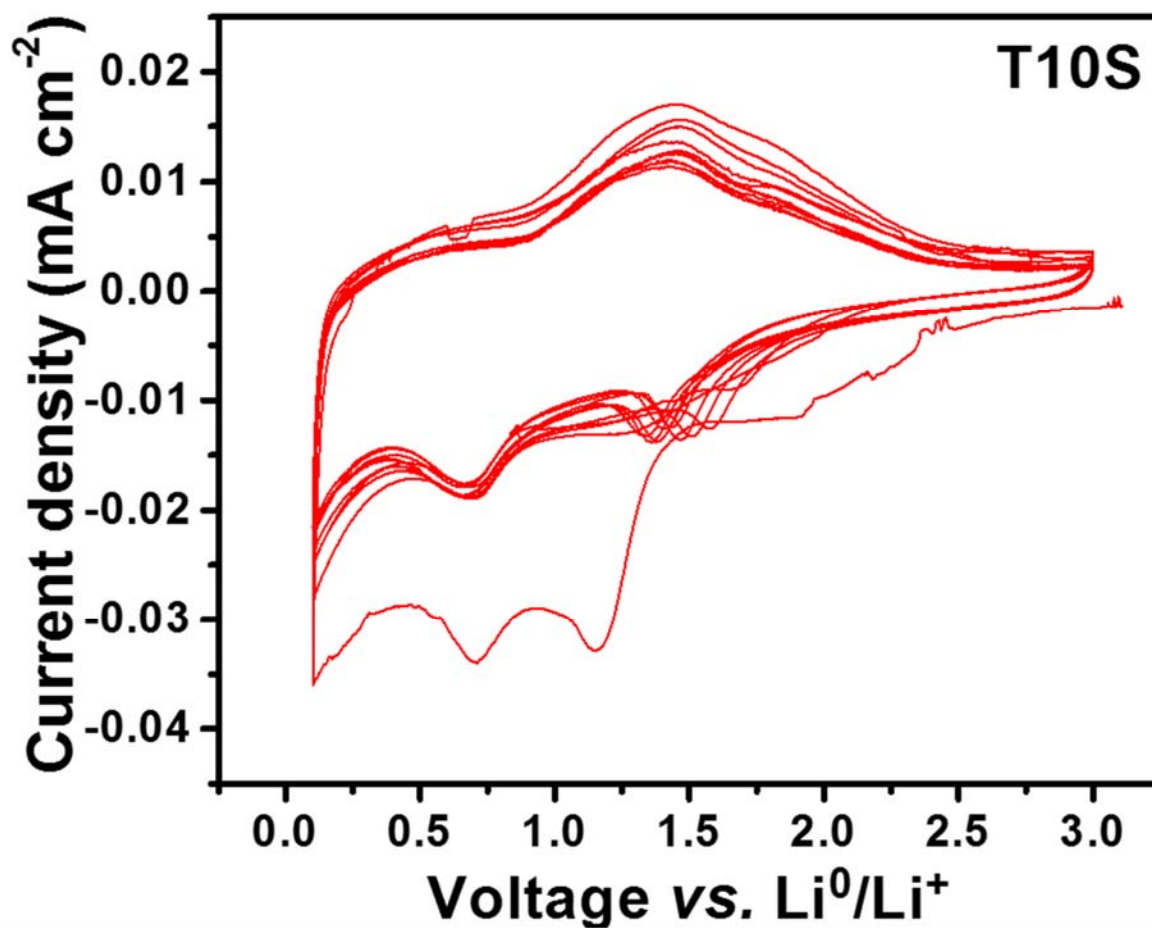
Fig. S10. *Cyclic Voltammograms of TiO$_2$-SnO$_2$ nanotubes (formed on the TiSn10 alloy), prepared at 40 V, and measured at scan rate of 1 mV s^{-1}.*
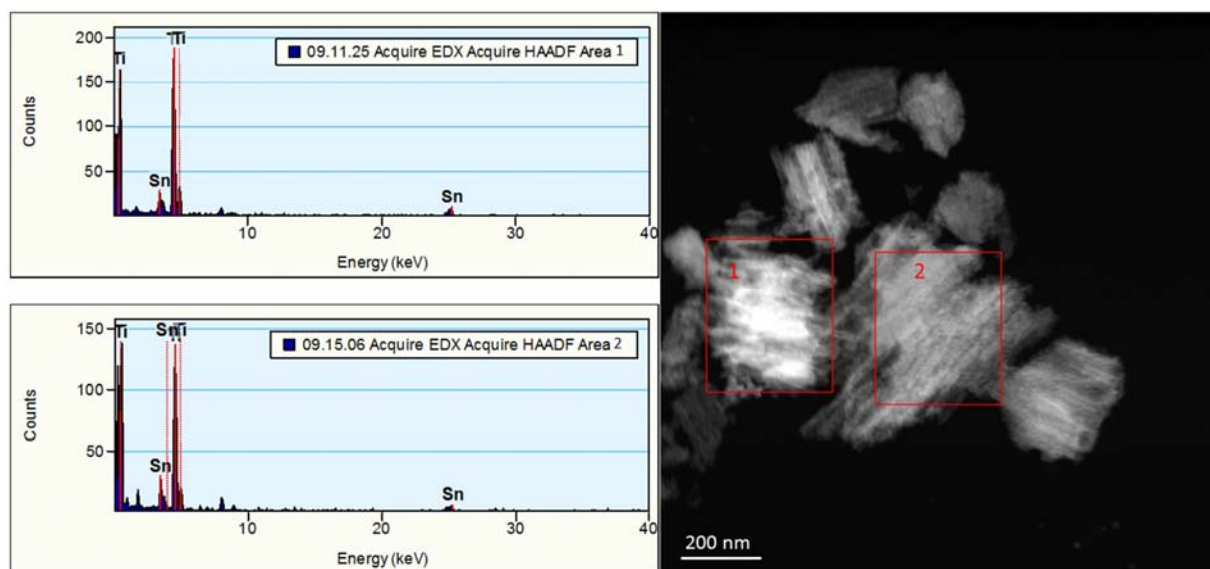
Fig. S11. *STEM images for the as-grown nanotubes on the TiSn$_1$ alloy formed at 40 V and the corresponding STEM-EDXS analysis of two diffident areas market with red rectangles.*
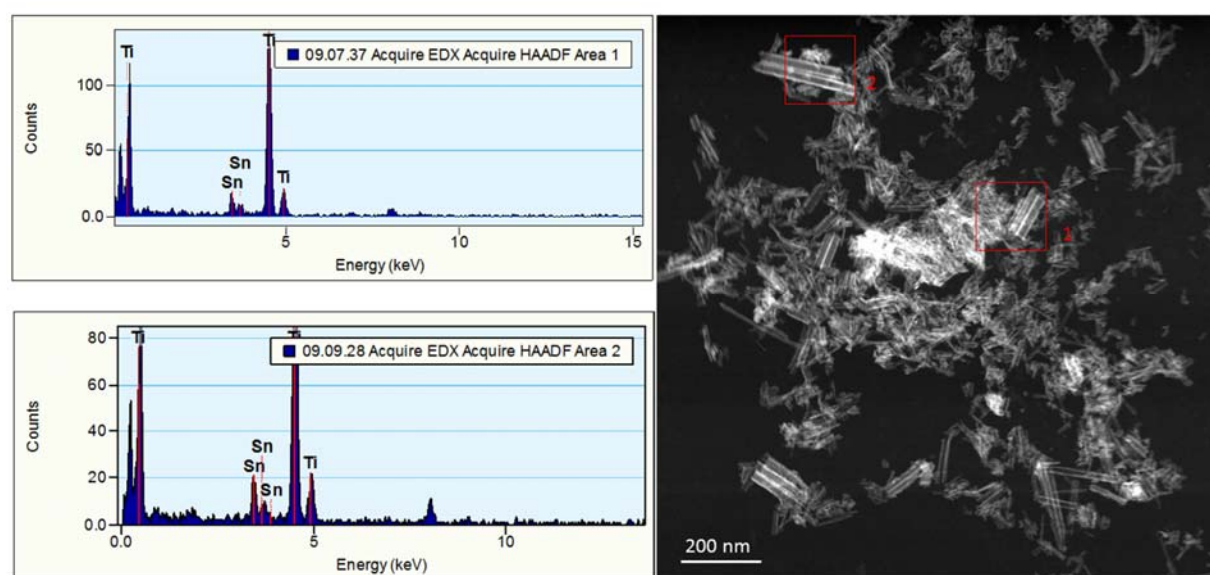
Fig. S12. *STEM images for the as-grown nanotubes on the TiSn$_5$ alloy formed at 40 V and the corresponding STEM-EDXS analysis of two diffident areas market with red rectangles.*
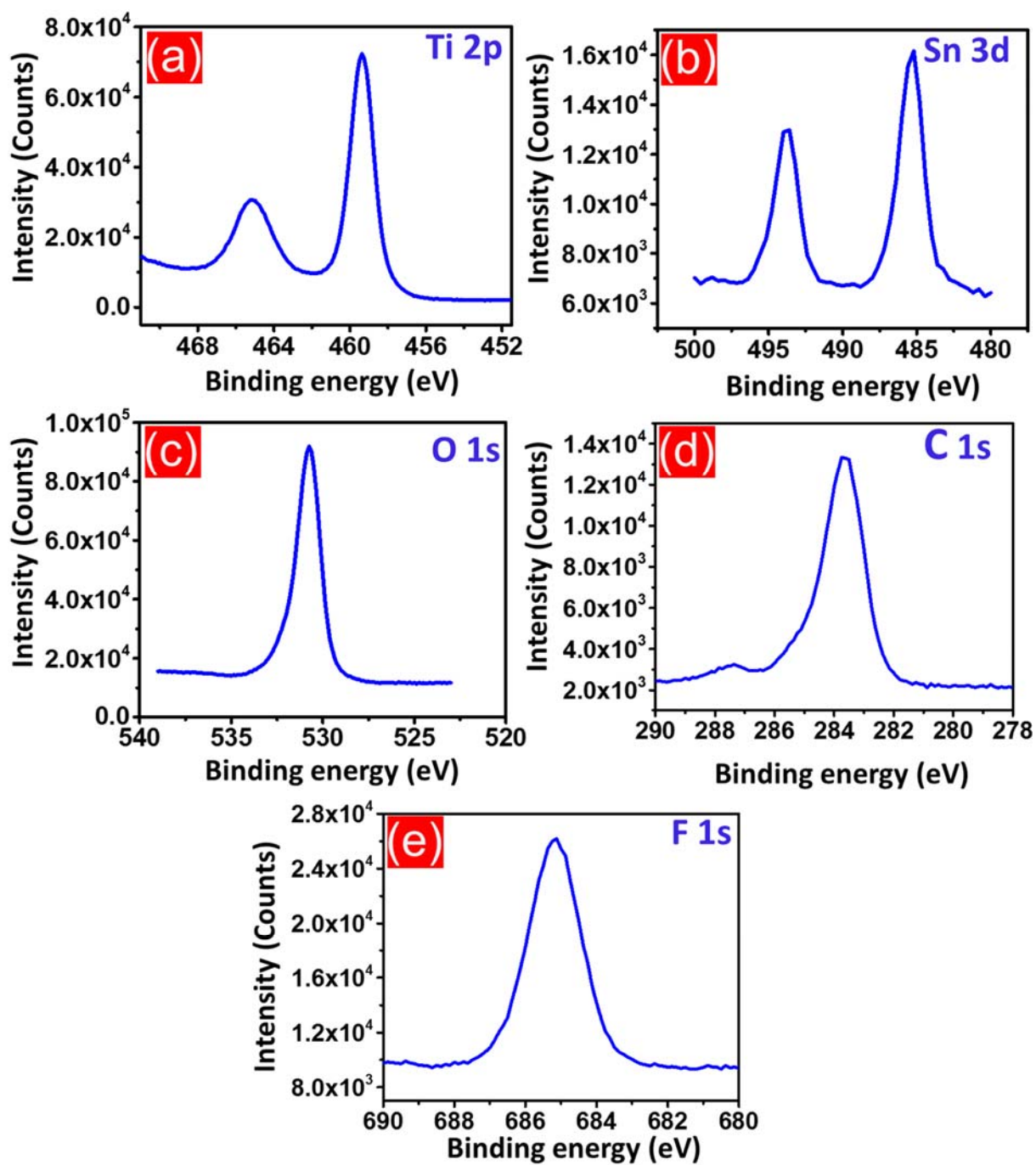
Fig. S13. *X-ray photoelectron spectra of the grown nanotubes on the TiSn₁ substrate (T1S sample) at 40 V for the binding energies Ti 2p (a), Sn 3d (b), O 1s (c), C 1s (d) and F 1s (e).*
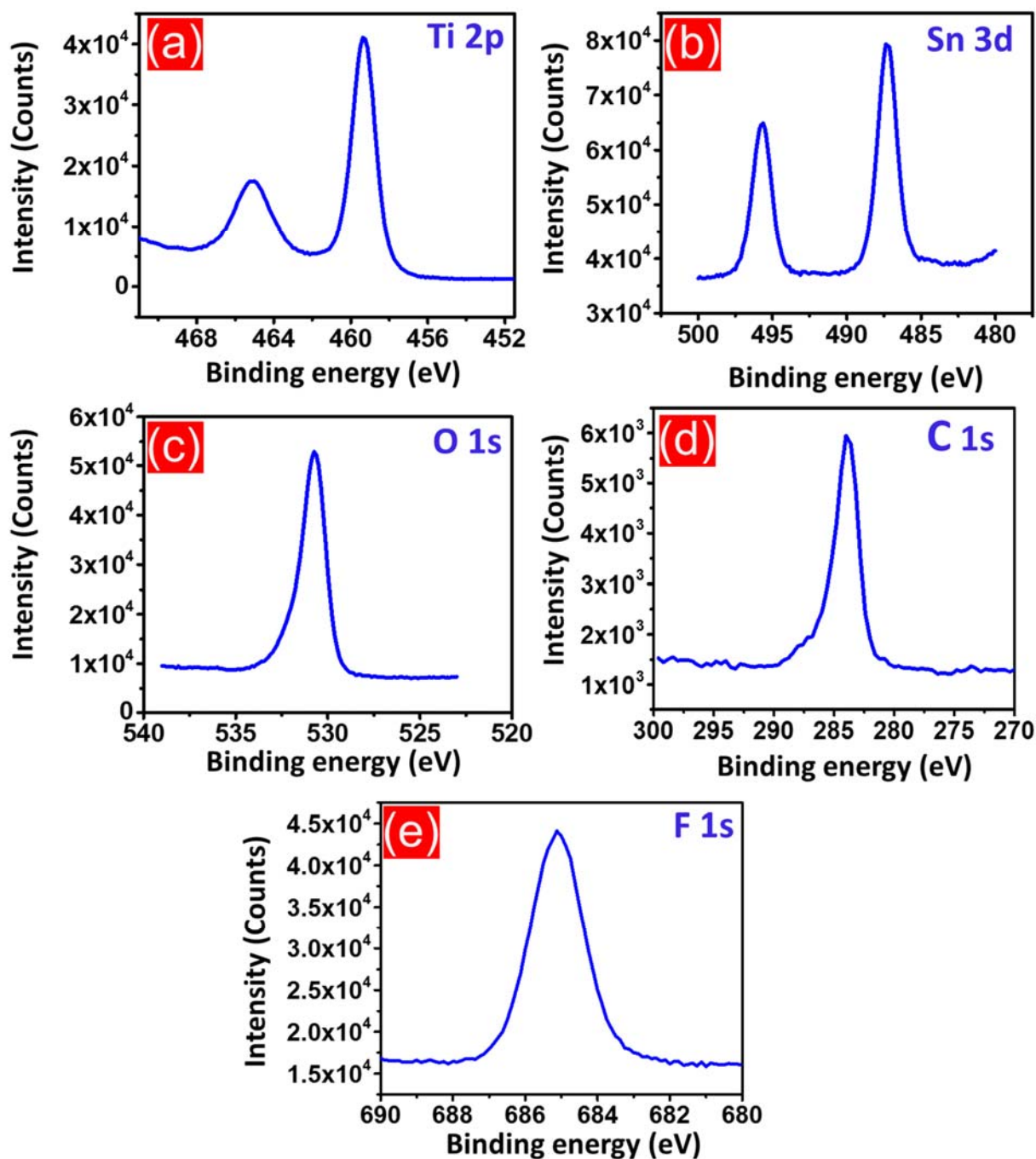
Fig. S14. *X-ray photoelectron spectra of the grown nanotubes on the TiSn₅ substrate (T5S sample) at 40 V for the binding energies Ti 2p (a), Sn 3d (b), O 1s (c), C 1s (d) and F 1s (e).*

Bibliography

[1] O. Travesset-Baró, B. P. Ó Gallachóir, E. Jover, and M. Rosas-Casals, "Transport energy demand in Andorra: Assessing private car futures through sensitivity and scenario analysis," *Energy Policy*, vol. 96, pp. 78–92, 2015.

[2] M. Hoeven, "World Energy Outlook 2012," *International Energy Agency, IEA publication, Paris, France,* pp. 31–46, 2012. ISBN: 978 92 64 180840. http://www.iea.org/publications/freepublications/publication/world-energy-outlook-2012.html

[3] G. L. Soloveichik, "Flow Batteries : Current status and trends," *Chem. Rev.*, vol. 115, no. 20, pp. 11533–11558, 2015.

[4] M. Wagemaker, G. J. Kearley, A. a. Van Well, H. Mutka, and F. M. Mulder, "Multiple Li positions inside oxygen octahedra in lithiated TiO_2 anatase," *J. Am. Chem. Soc.*, vol. 125, no. 3, pp. 840–848, 2003.

[5] M. Mancini, F. Nobili, R. Tossici, M. Wohlfahrt-Mehrens, and R. Marassi, "High

performance, environmentally friendly and low cost anodes for lithium-ion battery based on TiO_2 anatase and water soluble binder carboxymethyl cellulose," *J. Power Sources*, vol. 196, no. 22, pp. 9665–9671, 2011.

[6]   X. Su, Q. Wu, X. Zhan, J. Wu, S. Wei, and Z. Guo, "Advanced titania nanostructures and composites for lithium ion battery," *J. Mater. Sci.*, vol. 47, no. 6, pp. 2519–2534, 2011.

[7]   M. D. Earle, "The electrical conductivity of titanium dioxide," *Phys. Rev.*, vol. 61, no. 15, pp. 56–62, 1942.

[8]   A. K. Rai, L. T. Anh, J. Gim, V. Mathew, J. Kang, B. J. Paul, J. Song, and J. Kim, "Simple synthesis and particle size effects of TiO_2 nanoparticle anodes for rechargeable lithium ion batteries," *Electrochim. Acta*, vol. 90, pp. 112–118, 2013.

[9]   W. Wen, J. Wu, Y. Jiang, S. Yu, J. Bai, M. Cao, and J. Cui, "Anatase TiO_2 ultrathin nanobelts derived from room-temperature-synthesized titanates for fast and safe lithium storage," *Sci. Rep.*, vol. 5, no. February, pp. 1–10, 2015.

[10]   W. Wei, G. Oltean, C. W. Tai, K. Edström, F. Björefors, and L. Nyholm, "High energy and power density TiO_2 nanotube electrodes for 3D Li-ion microbatteries," *J. Mater. Chem. A*, vol. 1, no. 28, pp. 8160–8169, 2013.

[11]   P. Roy, S. Berger, and P. Schmuki, "TiO_2 nanotubes: synthesis and applications.," *Angew. Chem. Int. Ed. Engl.*, vol. 50, no. 13, pp. 2904–2939, 2011.

[12]   H. Han, T. Song, E. K. Lee, A. Devadoss, Y. Jeon, J. Ha, Y. C. Chung, Y.-M. Choi, Y. G. Jung, and U. Paik, "Dominant factors governing the rate capability of a TiO_2 nanotube anode for high power lithium ion batteries.," *ACS Nano*, vol. 6, no. 9, pp. 8308–8315, 2012.

[13]   Y. Chen, Y. Tang, S. Luo, C. Liu, and Y. Li, "TiO_2 nanotube arrays co-loaded with Au nanoparticles and reduced graphene oxide: Facile synthesis and promising photocatalytic application," *J. Alloys Compd.*, vol. 578, pp. 242–248, Nov. 2013.

[14] P. Zhang, J. Qiu, Z. Zheng, G. Liu, M. Ling, W. Martens, H. Wang, H. Zhao, and S. Zhang, "Free-standing and bendable carbon nanotubes/TiO_2 nanofibres composite electrodes for flexible lithium ion batteries," *Electrochim. Acta*, vol. 104, pp. 41–47, 2013.

[15] Y. Fan, N. Zhang, L. Zhang, H. Shao, J. Wang, J. Zhang, C. Cao, "Co_3O_4-coated TiO_2 nanotube composites synthesized through photo-deposition strategy with enhanced performance for lithium-ion batteries," *Electrochim. Acta*, vol. 94, pp. 285–293, 2013.

[16] J. H. Kim, K. Zhu, Y. Yan, C. L. Perkins, and A. J. Frank, "Microstructure and pseudocapacitive properties of electrodes constructed of oriented NiO-TiO_2 nanotube arrays," *Nano Lett.*, vol. 10, pp. 4099–4104, 2010.

[17] X. Wu, S. Zhang, L. Wang, Z. Du, H. Fang, Y. Ling, and Z. Huang, "Coaxial SnO_2@TiO_2 nanotube hybrids: from robust assembly strategies to potential application in Li+ storage," *J. Mater. Chem.*, vol. 22, no. 22, pp. 11151–11158, 2012.

[18] D. Guan, J. Li, X. Gao, and C. Yuan, "Controllable synthesis of MoO_3-deposited TiO_2 nanotubes with enhanced lithium-ion intercalation performance," *J. Power Sources*, vol. 246, pp. 305–312, 2014.

[19] Y. Yang, D. Kim, M. Yang, and P. Schmuki, "Vertically aligned mixed V_2O_5-TiO_2 nanotube arrays for supercapacitor applications.," *Chem. Commun.*, vol. 47, no. 27, pp. 7746–7748, 2011.

[20] R. Hang, Y. Liu, L. Zhao, A. Gao, L. Bai, X. Huang, X. Zhang, B. Tang, and P. K. Chu, "Fabrication of Ni-Ti-O nanotube arrays by anodization of NiTi alloy and their potential applications," *Sci. Rep.*, vol. 4, pp. 1–9, 2014.

[21] G. K. Mor, H. E. Prakasam, O. K. Varghese, K. Shankar, and C. A Grimes, "Vertically oriented Ti-Fe-O nanotube array films: toward a useful material architecture for solar spectrum water photoelectrolysis.," *Nano Lett.*, vol. 7, no. 8, pp. 2356–64, 2007.

[22] N. K. Allam, N. M. Deyab, and N. Abdel Ghany, "Ternary Ti-Mo-Ni mixed oxide nanotube arrays as photoanode materials for efficient solar hydrogen

production.," *Phys. Chem. Chem. Phys.*, vol. 15, no. 29, pp. 12274–82, 2013.

[23] B. Luo, H. Yang, S. Liu, W. Fu, P. Sun, M. Yuan, Y. Zhang, and Z. Liu, "Fabrication and characterization of self-organized mixed oxide nanotube arrays by electrochemical anodization of Ti-6Al-4V alloy," *Mater. Lett.*, vol. 62, no. 30, pp. 4512–4515, 2008.

[24] J. H. Thomas, "Electrical properties of thin cobalt oxide films on cobalt," *Thin Solid Films*, vol. 44, pp. 155–161, 1977.

[25] F. Lange and M. Martin, "The electrical conductivity of CoO: experimental results and a new conductivity model," *Ber. Bunsenges Phys. Chem.*, vol. 101, pp. 176–184, 1997.

[26] K. P. Constant, T. O. Mason, S. J. Rothman, "Non-stoichimetry, electrical properties, and cation diffusion in highly non.stoichimetric $Co1_{-x}O$-I. Experimental," *J. Phys. Chem. Solids*, vol. 53, no. 3, pp. 405–411, 1992.

[27] K. Hübener, G. Leonhardt "Ionicity and electrical conductivity in transition-metal oxides," *Phys. Status Solidi*, vol. 68, no. 175, pp. 175–179, 1975.

[28] G. M. Joshi, M. Pai, H. R. Harrison, C. J. Sandberg, R. Aragon, J. M. Honig, "Electrical properties of un doped single CoO crystals," *Mater. Res. Bull.*, vol. 15, pp. 1575–1579, 1980.

[29] I. A. Courtney, J. R. Dahn, "Electrochemical and in situ X-Ray diffraction studies of the reaction of uthium with tin oxide composites," *J. Electrochem. Soc.*, vol. 144, no. 6, pp. 2045–2052, 1997.

[30] M. Kim, J. Lee, S. Lee, S. Seo, C. Bae, and H. Shin, "Nanotubular heterostructure of tin dioxide/titanium dioxide as a binder-free anode in lithium-ion batteries," *ChemSusChem*, vol. 8, pp. 2363–2371, 2015.

[31] M. Radecka, A. Wnuk, A. Trenczek-Zajac, K. Schneider, and K. Zakrzewska, "TiO_2/SnO_2 nanotubes for hydrogen generation by photoelectrochemical water splitting," *Int. J. Hydrogen Energy*, vol. 40, no. 1, pp. 841–851, 2015.

[32] J. Wang, N. Du, H. Zhang, J. Yu, and D. Yang, "Large-scale synthesis of SnO_2 nanotube arrays as high-performance anode materials of Li-ion batteries," pp.

11302–11305, 2011.

[33]   L. Zaraska, N. Czopik, M. Bobruk, G. D. Sulka, J. Mech, and M. Jaskuła, "Synthesis of nanoporous tin oxide layers by electrochemical anodization," *Electrochim. Acta*, vol. 104, pp. 549–557, 2013.

[34]   M. S. Whittingham, "Lithium batteries and cathode materials," *Chem. Rev.*, vol. 104, no. 10, pp. 4271–4301, 2004.

[35]   B. Scrosati, "Lithium rocking chair batteries: An old concept," *J. Electrochem. Soc.*, vol. 139, no. 10, pp. 2776–2781, 1992.

[36]   P. T. Moseley, Jürgen Garche, "*Electrochemical energy storage for renewable sources and grid balancing,*" *Elsevier.* ISBN: 9780444626103, 2014.

[37]   Y. Wang, B. Liu, Q. Li, S. Cartmell, S. Ferrara, Z. D. Deng, and J. Xiao, "Lithium and lithium ion batteries for applications in microelectronic devices: A review," *J. Power Sources*, vol. 286, pp. 330–345, 2015.

[38]   P. Yang, "*The Chemistry of Nanostructured Materials,*" *World Scientific, New Jersey,* pp. 1–37, 2003. ISBN: 978-981-256-004-9.

[39]   K. M. Abraham, "Prospects and limits of energy storage in batteries," *J. Phys. Chem. Lett.*, pp. 830–844, 2015.

[40]   V. Petr, "*Electrochemical Series,*" *Handbook of Chemistry and Physics*, 92nd ed, Editor: W. M. Haynes, *CRC Press*, pp. 5-80–5-86, 2011. ISBN:1439855129.

[41]   Y. Nishi, "Lithium ion secondary batteries; past 10 years and the future," *J. Power Sources*, vol. 100, pp. 101–106, 2001.

[42]   T. Djenizian, I. Hanzu, and P. Knauth, "Nanostructured negative electrodes based on titania for Li-ion microbatteries," *J. Mater. Chem.*, vol. 21, no. 27, pp. 9925–9937, 2011.

[43]   L. Xu, C. Kim, A. K. Shukla, A. Dong, T. M. Mattox, D. J. Milliron, and J. Cabana, "Monodisperse Sn nanocrystals as a platform for the study of mechanical damage during electrochemical reactions with Li," *Nano Lett.*, vol. 13, no. 4, pp. 1800–1805, 2013.

[44]   R. A. H. Wen, C. John, B. A. Boukamp, "Thermodynamic and mass transport properties of LiAl,'" *J. Electrochem. Soc.*, vol. 126, no. 12, pp. 2258–2266, 1979.

[45] J. Saint, M. Morcrette, D. Larcher, and J. M. Tarascon, "Exploring the Li-Ga room temperature phase diagram and the electrochemical performances of the Li$_x$Ga$_y$ alloys *vs.* Li," *Solid State Ionics*, vol. 176, no. 2, pp. 189–197, 2005.

[46] S. Yoon, C. M. Park, H. J. Sohn, "Electrochemical characterizations of germanium and carbon-coated germanium composite anode for lithium-ion batteries," *Electrochem. Solid-State Lett.*, vol. 11, no. 4, pp. A42–A45, 2008.

[47] M. Martos, J. Morales, L. Sánchez, "Lead-based systems as suitable anode materials for Li-ion batteries," *Electrochim. Acta*, vol. 48, no. 6, pp. 615–621, 2003.

[48] A. Dailly, J. Ghanbaja, P. Willmann, and D. Billaud, "Lithium insertion into new graphite-antimony composites," *Electrochim. Acta*, vol. 48, no. 8, pp. 977–984, 2003.

[49] H. Li, X. Huang, X. Huang, L. Chen, Z. Wu, Y. Liang, "A high capacity nano-Si composite anode material for lithium rechargeable batteries," *Electrochem. Solid-State Lett.*, vol. 2, no. 11, pp. 547–549, 1999.

[50] F. F. Cao, J. W. Deng, S. Xin, H. X. Ji, O. G. Schmidt, L. J. Wan, Y. G. Guo, "Cu-Si nanocable arrays as high-rate anode materials for lithium-ion batteries," *Adv. Mater.*, vol. 23, no. 38, pp. 4415–4420, 2011.

[51] X. Fan, H. Zhang, N. Du, P. Wu, X. Xu, Y. Li, and D. Yang, "Vertically ordered Ni3Si2/Si nanorod arrays as anode materials for high-performance Li-ion batteries," *Nanoscale*, vol. 4, p. 5343–5347, 2012.

[52] L. Ji, Z. Lin, M. Alcoutlabi, X. Zhang, "Recent developments in nanostructured anode materials for rechargeable lithium-ion batteries," *Energy Environ. Sci.*, vol. 4, no. 8, pp. 2682–2699, 2011.

[53] L. Kavan, M. Grätzel, S. E. Gilbert, C. Klemenz, and H. J. Scheel, "Electrochemical and photoelectrochemical investigation of single-crystal anatase," *J. Am. Chem. Soc.*, vol. 118, no. 28, pp. 6716–6723, 1996.

[54] F. Dachille, P. Y. Simons, R. Roy, "Pressure-temperature studies of anatase, brookite rutile, and TiO$_2$(II)," *Amer. Mineral.*, vol. 53, pp. 1929–1939, 1968.

[55]   Z. F. Yin, L. Wu, H. G. Yang, Y. H. Su, "Recent progress in biomedical applications of titanium dioxide," *Phys. Chem. Chem. Phys.*, vol. 15, no. 14, pp. 4844–4858, 2013.

[56]   Z. Chen, I. Belharouak, Y. K. Sun, and K. Amine, "Titanium-based anode materials for safe lithium-ion batteries," *Adv. Funct. Mater.*, vol. 23, no. 8, pp. 959–969, 2013.

[57]   R. Van De Krol, A. Goossens, and J. Schoonman, "Spatial Extent of Lithium Intercalation in Anatase TiO_2," *J. Phys. Chem. B*, vol. 103, pp. 7151–7159, 1999.

[58]   Y. Zhang, Z. Jiang, J. Huang, Y. W. L. Lim, W. Li, J. Deng, D. Gong, Y. Tang, Y. Lai, and Z. Chen, "Titanate and titania nanostructured materials for environmental and energy applications: A review," *RSC Adv.*, vol. 5, no. 97, pp. 79479–79510, 2015.

[59]   X. Yan, Z. Wang, M. He, Z. Hou, T. Xia, G. Liu, and X. Chen, "TiO_2 nanomaterials as anode materials for lithium-ion rechargeable batteries," *Energy Technol.*, vol. 3, no. 8, pp. 801–814, 2015.

[60]   M. V. Koudriachova, N. M. Harrison, and S. W. De Leeuw, "Diffusion of Li-ions in rutile. An ab initio study," *Solid State Ionics*, vol. 157, no. 4, pp. 35–38, 2003.

[61]   B. Zachau-Christiansen, K. West, T. Jacobsen, and S. Atlung, "Lithium insertion in different TiO_2 modifications," *Solid State Ionics*, vol. 28–30, no. 2, pp. 1176–1182, 1988.

[62]   H. Lindström, S. Södergren, A. Solbrand, H. Rensmo, J. Hjelm, A. Hagfeldt, and S. E. Lindquist, "Li + ion insertion in TiO_2 (anatase). A voltammetry on nanoporous films," *J. Phys. Chem. B*, vol. 101, no. 97, pp. 7717–7722, 1997.

[63]   G. Sudant, E. Baudrin, D. Larcher, and J. M. Tarascon, "Electrochemical lithium reactivity with nanotextured anatase-type TiO_2," *J. Mater. Chem.*, no. 1, pp. 1263–1269, 2005.

[64]   A. Vittadini, M. Casarin, A. Selloni, "Structure and stability of TiO_2-B surfaces: A density functional study," *J. Phys. Chem. C*, vol. 113, no. 44, pp. 18973–18977, 2009.

[65]   Z. Yang, D. Choi, S. Kerisit, K. M. Rosso, D. Wang, J. Zhang, G. Graff, and J.

Liu, "Nanostructures and lithium electrochemical reactivity of lithium titanites and titanium oxides: A review," *J. Power Sources*, vol. 192, no. 2, pp. 588–598, 2009.

[66] M. Zukalova, M. Kalbac, L. Kavan, M. Zukalová, M. Kalbáč, I. Exnar, and M. Graetzel, "Pseudocapacitive lithium storage in TiO$_2$ (B)," *Chem. Mater.,* vol. 17, no. 5, pp. 1248–1255, 2005.

[67] D. Deng, M. G. Kim, J. Y. Lee, and J. Cho, "Green energy storage materials: Nanostructured TiO$_2$ and Sn-based anodes for lithium-ion batteries," *Energy Environ. Sci.*, vol. 2, no. 8, p. 818–837, 2009.

[68] L. Kavan, J. Rathouský, M. Grätzel, V. Shklover, and A. Zukal, "Surfactant-templated TiO$_2$ (Anatase): Characteristic features of lithium insertion electrochemistry in organized nanostructures," *J. Phys. Chem. B*, vol. 104, no. 50, pp. 12012–12020, 2000.

[69] G. Nuspl, K. Yoshizawa, and T. Yamabe, "Lithium intercalation in TiO$_2$ modifications," *J. Mater. Chem.*, vol. 7, no. 12, pp. 2529–2536, 1997.

[70] C. Jiang, J. Zhang, "Nanoengineering titania for high rate lithium storage: A review," *J. Mater. Sci. Technol.*, vol. 29, no. 2, pp. 97–122, 2013.

[71] M. Wagemaker, W. J. H. Borghols, and F. M. Mulder, "Large impact of particle size on insertion reactions," *J.Am.Chem.Soc.*, vol. 129, pp. 4323–4327, 2007.

[72] C. Jiang, M. Wei, Z. Qi, T. Kudo, I. Honma, and H. Zhou, "Particle size dependence of the lithium storage capability and high rate performance of nanocrystalline anatase TiO$_2$ electrode," *J. Power Sources*, vol. 166, no. 1, pp. 239–243, 2007.

[73] C. Jiang, I. Honma, T. Kudo, and H. Zhou, "Nanocrystalline Rutile TiO$_2$ Electrode for High-Capacity and High-Rate Lithium Storage," *Electrochem. Solid State Lett.*, vol. 10, no. 5, p. A127, 2007.

[74] M. L. Sushko, K. M. Rosso, and J. Liu, "Size effects on Li+/electron conductivity in TiO$_2$ nanoparticles," *J. Phys. Chem. Lett.*, vol. 1, no. 13, pp. 1967–1972, 2010.

[75] P. Kubiak, T. Fröschl, N. Hüsing, U. Hörmann, U. Kaiser, R. Schiller, C. K.

Weiss, K. Landfester, M. Wohlfahrt-Mehrens, "TiO$_2$ anatase nanoparticle networks: Synthesis, structure, and electrochemical performance.," *Small*, vol. 7, no. 12, pp. 1690–1696, 2011.

[76] O. Wilhelm, S. E. Pratsinis, E. De Chambrier, M. Crouzet, I. Exnar, "Electrochemical performance of granulated titania nanoparticles," *J. Power Sources*, vol. 134, no. 2, pp. 197–201, 2004.

[77] J. Liang, Z. Wang, Z. Li, X. Wang, and K. Yu, "Fabrication of nanostructured TiO$_2$ using a solvothermal reaction for lithium-ion batteries," *Nanomater. Nanotechnol.*, vol. 6, no. 15, pp. 1–8, 2016.

[78] J. Kang, D. H. Kim, V. Mathew, J. S. Lim, J. Gim, and J. Kim, "Particle size effect of anatase TiO$_2$ Nanocrystals for lithium-ion batteries," *J. Electrochem. Soc.*, vol. 158, no. 2, pp. A59–A62, 2011.

[79] L. Liu, Q. Fan, C. Sun, X. Gu, H. Li, F. Gao, Y. Chen, and L. Dong, "Synthesis of sandwich-like TiO$_2$@C composite hollow spheres with high rate capability and stability for lithium-ion batteries," *J. Power Sources*, vol. 221, pp. 141–148, 2013.

[80] W. Wang, Q. Sa, J. Chen, Y. Wang, H. Jung, Y. Yin "Porous TiO$_2$/C nanocomposite shells as a high-performance anode material for lithium-ion batteries," *ACS Appl. Mater. Interfaces*, vol. 5, pp. 6478–6483, 2013.

[81] D. Wang, D. Choi, J. Li, Z. Yang, Z. Nie, R. Kou, D. Hu, C. Wang, L. V Saraf, J. Zhang, I. A. Aksay, and J. Liu, "Self-assembled TiO$_2$–graphene hybrid insertion," vol. 3, no. 4, pp. 907–914, 2009.

[82] F. F. Cao, Y. G. Guo, S. F. Zheng, X. L. Wu, L. Y. Jiang, R. R. Bi, L. J. Wan, and J. Maier, "Symbiotic coaxial nanocables: Facile synthesis and an efficient and elegant morphological solution to the lithium storage problem," *Chem. Mater.*, vol. 22, no. 17, pp. 1908–1914, 2010.

[83] H. C. Tao, L. Z. Fan, X. Yan, and X. Qu, "In situ synthesis of TiO$_2$-graphene nanosheets composites as anode materials for high-power lithium ion batteries," *Electrochim. Acta*, vol. 69, pp. 328–333, 2012.

[84] J. Jin, S. Z. Huang, Y. Li, H. Tian, H. E. Wang, Y. Yu, L. H. Chen, T. Hasan,

B. L. Su, "Hierarchical nanosheet-constructed yolk–shell TiO_2 porous microspheres for lithium batteries with high capacity, superior rate and long cycle capability," *Nanoscale*, vol. 7, no. 30, pp. 12979–12989, 2015.

[85]   D. Wang, D. Choi, Z. Yang, V. Viswanathan, Z. Nie, C. Wang, Y. Song, J. Zhang, J. Liu, "Synthesis and Li-ion insertion properties of highly crystalline mesoporous rutile TiO_2 synthesis and Li-ion insertion properties of highly crystalline mesoporous rutile TiO_2," *Chem. Mater.*, no. 1, pp. 3435–3442, 2008.

[86]   H. Qiao, D. Tao, Y. Wang, Y. Cai, F. Huang, X. Yang, J. Wei, and Q. Wei, "Electrochemical charge storage of flowerlike rutile TiO_2 nanorods," *Chem. Phys. Lett.*, vol. 490, no. 4–6, pp. 180–183, 2010.

[87]   Y. Lan, X. Gao, H. Zhu, Z. Zheng, T. Yan, F. Wu, S. P. Ringer, D. Song, "Titanate nanotubes and nanorods prepared from rutile powder," *Adv. Funct. Mater.*, vol. 15, no. 8, pp. 1310–1318, 2005.

[88]   J. Kim and J. Cho, "Rate Characteristics of Anatase TiO_2 nanotubes and nanorods for lithium battery anode materials at room temperature," *J. Electrochem. Soc.*, vol. 154, pp. A542–A546, 2007.

[89]   S. J. Bao, Q. L. Bao, C. M. Li, Z. L. Dong, "Novel porous anatase TiO_2 nanorods and their high lithium electroactivity," *Electrochem. Commun.*, vol. 9, no. 5, pp. 1233–1238, 2007.

[90]   X. Gao, H. Zhu, G. Pan, S. Ye, Y. Lan, F. Wu, and D. Song, "Preparation and electrochemical characterization of anatase nanorods for lithium-inserting electrode material," *J. Phys. Chem. B*, vol. 108, no. 9, pp. 2868–2872, 2004.

[91]   R. B. Khomane, "Microemulsion-mediated sol-gel synthesis of mesoporous rutile TiO_2 nanoneedles and its performance as anode material for Li-ion batteries," *J. Colloid Interface Sci.*, vol. 356, no. 1, pp. 369–372, 2011.

[92]   Y. Wang, M. Wu, and W. F. Zhang, "Preparation and electrochemical characterization of TiO_2 nanowires as an electrode material for lithium-ion batteries," *Electrochim. Acta*, vol. 53, pp. 7863–7868, 2008.

[93]   F. Wu, X. Li, Z. Wang, H. Guo, L. Wu, X. Xiong, and X. Wang, "A novel method

to synthesize anatase TiO_2 nanowires as an anode material for lithium-ion batteries," *J. Alloys Compd.*, vol. 509, no. 8, pp. 3711–3715, 2011.

[94] A. R. Armstrong, G. Armstrong, J. Canales, and P. G. Bruce, "TiO_2-B nanowires," *Angew. Chemie - Int. Ed.*, vol. 116, no. 17, pp. 2286–2288, 2004.

[95] S. Goriparti, E. Miele, M. Prato, A. Scarpellini, S. Marras, S. Monaco, A. Toma, G. C. Messina, A. Alabastri, F. De Angelis, L. Manna, C. Capiglia, R. P. Zaccaria, "Direct Synthesis of carbon-doped TiO_2-bronze nanowires as anode materials for high performance lithium-ion batteries," *ACS Appl. Mater. Interfaces*, vol. 7, no. 45, pp. 25139–25146, 2015.

[96] J. Wang, Y. Zhou, B. Xiong, Y. Zhao, X. Huang, and Z. Shao, "Fast lithium-ion insertion of TiO_2 nanotube and graphene composites," *Electrochim. Acta*, vol. 88, pp. 847–857, 2013.

[97] L. He, R. Ma, N. Du, J. Ren, T. Wong, Y. Li, and S. T. Lee, "Growth of TiO_2 nanorod arrays on reduced graphene oxide with enhanced lithium-ion storage," *J. Mater. Chem.*, vol. 22, no. 36, pp. 19061–19066 , 2012.

[98] L. Xiao, M. Cao, D. Mei, Y. Guo, L. Yao, D. Qu, and B. Deng, "Preparation and electrochemical lithium storage features of TiO_2 hollow spheres," *J. Power Sources*, vol. 238, pp. 197–202, 2013.

[99] K. Saravanan, K. Ananthanarayanan, P. Balaya, "Mesoporous TiO_2 with high packing density for superior lithium storage," *Energy Environ. Sci.*, vol. 3, p. 939–948, 2010.

[100] H. E. Wang, J. Jin, Y. Cai, J. M. Xu, D. S. Chen, X. F. Zheng, Z. Deng, Y. Li, I. Bello, B. L. Su, "Facile and fast synthesis of porous TiO_2 spheres for use in lithium ion batteries," *J. Colloid Interface Sci.*, vol. 417, pp. 144–151, 2014.

[101] H. E. Wang, H. Cheng, C. Liu, X. Chen, Q. Jiang, Z. Lu, Y. Y. Li, C. Y. Chung, W. Zhang, J. A. Zapien, L. Martinu, and I. Bello, "Facile synthesis and electrochemical characterization of porous and dense TiO_2 nanospheres for lithium-ion battery applications," *J. Power Sources*, vol. 196, no. 15, pp. 6394–6399, 2011.

[102] Z. H. Zhang, L. D. Zhang, W. Li, A. S. Yu, and P. Y. Wu, "Carbon-coated

mesoporous TiO_2 nanocrystals grown on graphene for lithium-ion batteries," *ACS Appl. Mater. Interfaces*, vol. 7, no. 19, pp. 10395–10400, 2015.

[103] Y. M. Jiang, K. X. Wang, X. X. Guo, X. Wei, J. F. Wang, J. S. Chen, "Mesoporous titania rods as an anode material for high performance lithium-ion batteries," *J. Power Sources*, vol. 214, pp. 298–302, 2012.

[104] D. Bresser, E. Paillard, E. Binetti, S. Krueger, M. Striccoli, M. Winter, and S. Passerini, "Percolating networks of TiO_2 nanorods and carbon for high power lithium insertion electrodes," *J. Power Sources*, vol. 206, pp. 301–309, 2012.

[105] Y. Cai, H. E. Wang, S. Z. Huang, M. F. Yuen, H.-H. Cai, C. Wang, Y. Yu, Y. Li, W. J. Zhang, and B. L. Su, "Porous TiO_2 urchins for high performance Li-ion battery electrode: facile synthesis, characterization and structural evolution," *Electrochim. Acta*, vol. 210, pp. 206–214, 2016.

[106] X. Wang, Z. Jia, F. Liu, H. Liang, X. You, K. Wang, X. Lou, W. Shuang, L. Xiao, B. Cai, and L. Yang, "The template-free synthesis of hierarchically porous anatase TiO_2 via acid-etching for enhancing the cycling stability and reversible capacity of lithium ion batteries," *RSC Adv.*, vol. 6, no. 54, pp. 48985–48994, 2016.

[107] J. Y. Shin, D. Samuelis, and J. Maier, "Sustained lithium storage performance of hierarchical, nanoporous anatase TiO_2 at high rates: Emphasis on interfacial storage phenomena," *Adv. Funct. Mater.*, vol. 21, no. 18, pp. 3464–3472, 2011.

[108] G. Lui, G. Li, X. Wang, G. Jiang, E. Lin, M. Fowler, A. Yu, and Z. Chen, "Flexible, three-dimensional ordered macroporous TiO_2 electrode with enhanced electrode-electrolyte interaction in high-power li-ion batteries," *Nano Energy*, vol. 24, pp. 72–77, 2016.

[109] J. Ye, A. C. Baumgaertel, Y. M. Wang, J. Biener, and M. M. Biener, "Structural optimization of 3D porous electrodes for high rate Performance lithium ion batteries," *Nano Lett.*, no. 2, pp. 2194–2202, 2015.

[110] M. Ge, C. Cao, J. Huang, S. Li, Z. Chen, K.-Q. ZHANG, S. S. Al-deyab, Y. Lai, "A review of one-dimensional TiO_2 nanostructured materials for environmental

and energy applications," *J. Mater. Chem. A*, vol. 4, pp. 6772–6801, 2016.

[111] M. A. V. Zwilling, E. Darque-Ceretti, "Anodic oxidation of titanium and TA6V alloy in chromic media. An electrochemical approach," *Electrochim. Acta*, vol. 45, pp. 921–929, 1999.

[112] J. J. Kelly, "The influence of fluoride ions on the passive dissolution of titanium," *Electrochim. Acta*, vol. 24, no. 12, pp. 1273–1282, 1979.

[113] D. Gong, C. A. Grimes, O. K. Varghese, W. Hu, R. S. Singh, Z. Chen, and E. C. Dickey, "Titanium oxide nanotube arrays prepared by anodic oxidation," *J. Mater. Res.*, vol. 16, no. 12, pp. 3331–3334, 2001.

[114] M. Madian, L. Giebeler, M. Klose, T. Jaumann, M. Uhlemann, A. Gebert, S. Oswald, N. Ismail, A. Eychmüller, and J. Eckert, "Self-Organized TiO_2/CoO nanotubes as potential anode materials for lithium ion batteries," *ACS Sustain. Chem. Eng.*, vol. 3, no. 5, pp. 909–919, 2015.

[115] G. K. Mor, O. K. Varghese, M. Paulose, N. Mukherjee, and C. A. Grimes, "Fabrication of tapered, conical-shaped titania nanotubes," *J. Mater. Res.*, vol. 18, no. 11, pp. 2588–2593, 2003.

[116] C. Ruan, M. Paulose, O. K. Varghese, G. K. Mor, and C. A Grimes, "Fabrication of highly ordered TiO_2 nanotube arrays using an organic electrolyte," *J. Phys. Chem. B*, vol. 109, no. 33, pp. 15754–15759, 2005.

[117] J. M. Macak, H. Tsuchiya, L. Taveira, S. Aldabergerova, and P. Schmuki, "Smooth anodic TiO_2 nanotubes," *Angew. Chemie - Int. Ed.*, vol. 44, no. 45, pp. 7463–7465, 2005.

[118] X. Quan, S. Yang, X. Ruan, and H. Zhao, "Preparation of titania nanotubes and their environmental applications as electrode," *Environ. Sci. Technol.*, vol. 39, no. 10, pp. 3770–3775, 2005.

[119] S. P. Albu, A. Ghicov, J. M. Macak, and P. Schmuki, "250 μm long anodic TiO_2 nanotubes with hexagonal self-ordering," *Phys. status solidi – Rapid Res. Lett.*, vol. 1, no. 2, pp. R65–R67, 2007.

[120] M. Paulose, K. Shankar, S. Yoriya, H. E. Prakasam, O. K. Varghese, G. K. Mor, T. A. Latempa, A. Fitzgerald, C. A. Grimes, U. V Park, and V. Pennsyl, "Anodic

growth of highly ordered TiO_2 nanotube arrays to 134 µ m in length," pp. 16179–16184, 2006.

[121] H. E. Prakasam, K. Shankar, M. Paulose, O. K. Varghese, and C. A. Grimes, "A new benchmark for TiO_2 nanotube array growth by anodization," *J. Phys. Chem. C*, vol. 111, no. 20, pp. 7235–7241, 2007.

[122] J. M. Macak, K. Sirotna, and P. Schmuki, "Self-organized porous titanium oxide prepared in Na_2SO_4/NaF electrolytes," *Electrochim. Acta*, vol. 50, no. 18, pp. 3679–3684, 2005.

[123] H. Tsuchiya, J. M. Macak, L. Taveira, E. Balaur, A. Ghicov, K. Sirotna, and P. Schmuki, "Self-organized TiO_2 nanotubes prepared in ammonium fluoride containing acetic acid electrolytes," *Electrochem. Commun.*, vol. 7, no. 6, pp. 576–580, Jun. 2005.

[124] R. Beranek, H. Hildebrand, and P. Schmuki, "Self-organized porous titanium oxide prepared in H_2SO_4/HF Electrolytes," *Electrochem. Solid-State Lett.*, vol. 6, no. 3, pp. B12–B14, 2003.

[125] C. A. Grimes, "Synthesis and application of highly ordered arrays of TiO_2 nanotubes," *J. Mater. Chem.*, vol. 17, no. 15, pp. 1451–1457, 2007.

[126] O. Jessensky, F. Müller, and U. Gösele, "Self-organized formation of hexagonal pore arrays in anodic alumina," *Appl. Phys. Lett.*, vol. 72, no. 10, pp. 1173–1175, 1998.

[127] D. D. Macdonald, "On the formation of voids in anodic oxide films on aluminum," *J. Electrochem. Soc.*, vol. 140, no. 3, pp. L27–L30, 1993.

[128] V. P. Parkhutik and V. I. Shershulsky, "Theoretical modelling of porous oxide growth on aluminium," *J. Phys. D. Appl. Phys.*, vol. 25, pp. 1258–1263, 1992.

[129] G. E. Thompson, "Porous anodic alumina: fabrication, characterization and applications," *Thin Solid Films*, vol. 297, no. 2, pp. 192–201, 1997.

[130] J. Siejka, "An O^{18} study of field-assisted pore formation in compact anodic oxide films on aluminum," *J. Electrochem. Soc.*, vol. 124, no. 6, pp. 883–891, 1977.

[131] A. Jaroenworaluck, D. Regonini, C. R. Bowen, R. Stevens, and D. Allsopp,

"Macro, micro and nanostructure of TiO_2 anodised films prepared in a fluorine-containing electrolyte," *J. Mater. Sci.*, vol. 42, no. 16, pp. 6729–6734, 2007.

[132] M. M. Lohrengel, "Thin anodic oxide layers on aluminium and other valve metals: High field regime," *Mater. Sci. Eng. Rep.*, vol. R11, pp. 243–294, 1993.

[133] K. Shimizu, K. Kobayashi, G. E. Thompson, and G. C. Wood, "Development of porous anodic films on aluminium," *Philos. Mag. A*, vol. 66, no. 4, pp. 643–652, 1992.

[134] R. Kirchgeorg, M. Kallert, N. Liu, R. Hahn, M. S. Killian, and P. Schmuki, "Key factors for an improved lithium ion storage capacity of anodic TiO_2 nanotubes," *Electrochim. Acta*, vol. 198, pp. 56–65, 2016.

[135] Z. Wei, Z. Liu, R. Jiang, C. Bian, T. Huang, and A. Yu, "TiO_2 nanotube array film prepared by anodization as anode material for lithium ion batteries," *J. Solid State Electrochem.*, vol. 14, no. 6, pp. 1045–1050, 2009.

[136] H. Li, S. K. Martha, R. R. Unocic, H. Luo, S. Dai, and J. Qu, "High cyclability of ionic liquid-produced TiO_2 nanotube arrays as an anode material for lithium-ion batteries," *J. Power Sources*, vol. 218, pp. 88–92, 2012.

[137] R. D. Shannon, "Phase transformation studies in TiO_2 supporting different defect mechanisms in vacuum-reduced and hydrogen-reduced rutile," *J. Appl. Phys.*, vol. 35, no. 11, pp. 3414–3416, 1964.

[138] I. Roman, R. D. Trusca, M.-L. Soare, C. Fratila, E. Krasicka-Cydzik, M. S. Stan, and A. Dinischiotu, "Titanium dioxide nanotube films: Preparation, characterization and electrochemical biosensitivity towards alkaline phosphatase," *Mater. Sci. Eng. C. Mater. Biol. Appl.*, vol. 37, pp. 374–82, 2014.

[139] S. Ivanov, L. Cheng, H. Wulfmeier, D. Albrecht, H. Fritze, A. Bund, "Electrochemical behavior of anodically obtained titania nanotubes in organic carbonate and ionic liquid based Li ion containing electrolytes," *Electrochim. Acta*, vol. 104, pp. 228–235, 2013.

[140] W. H. Ryu, D. H. Nam, Y. S. Ko, R. H. Kim, H. S. Kwon, "Electrochemical performance of a smooth and highly ordered TiO_2 nanotube electrode for Li-ion batteries," *Electrochim. Acta*, vol. 61, pp. 19–24, 2012.

[141] H. T. Fang, M. Liu, D. W. Wang, T. Sun, D.-S. Guan, F. Li, J. Zhou, T. K. Sham, H. M. Cheng, "Comparison of the rate capability of nanostructured amorphous and anatase TiO_2 for lithium insertion using anodic TiO_2 nanotube arrays.," *Nanotechnology*, vol. 20, no. 22, pp. 225701–225708, 2009.

[142] A. Tighineanu, T. Ruff, S. Albu, R. Hahn, and P. Schmuki, "Conductivity of TiO_2 nanotubes: Influence of annealing time and temperature," *Chem. Phys. Lett.*, vol. 494, no. 4–6, pp. 260–263, 2010.

[143] D. Guan, C. Cai, and Y. Wang, "Amorphous and crystalline TiO_2 nanotube arrays for enhanced Li-ion intercalation properties," *J. Nanosci. Nanotechnol.*, vol. 11, no. 4, pp. 3641–3650, 2011.

[144] Y. Wang, S. Liu, K. Huang, D. Fang, and S. Zhuang, "Electrochemical properties of freestanding TiO_2 nanotube membranes annealed in Ar for lithium anode material," *J. Solid State Electrochem.*, vol. 16, pp. 723–729, 2012.

[145] D. Liu, P. Xiao, Y. Zhang, B. B. Garcia, Q. Zhang, Q. Guo, R. Champion, and G. Cao, "TiO_2 nanotube arrays annealed in N2 for efficient lithium-ion intercalation," *J. Phys. Chem. C*, pp. 11175–11180, 2008.

[146] Z. Lu, C. T. Yip, L. Wang, H. Huang, and L. Zhou, "Hydrogenated TiO_2 nanotube arrays as high-rate anodes for lithium-Ion Microbatteries," *Chempluschem*, vol. 77, no. 11, pp. 991–1000, 2012.

[147] G. Liu, N. Hoivik, and K. Wang, "Small diameter TiO_2 nanotubes with enhanced photoresponsivity," *Electrochem. Commun.*, vol. 28, pp. 107–110, Mar. 2013.

[148] N. Kilinç, E. Şennik, M. Işik, A. Ş. Ahsen, O. Öztürk, and Z. Z. Öztürk, "Fabrication and gas sensing properties of C-doped and un-doped TiO_2 nanotubes," *Ceram. Int.*, vol. 40, no. 1 Part A, pp. 109–115, 2014.

[149] F. Mole, J. Wang, D. A. Clayton, C. Xu, and S. Pan, "Highly conductive nanostructured C- TiO_2 electrodes with enhanced electrochemical stability and double layer charge storage capacitance.," *Langmuir*, vol. 28, no. 28, pp. 10610–9, 2012.

[150] C. L. Cao, C. G. Hu, W. D. Shen, S. X. Wang, H. Liu, and J. L. Wang, "Cobalt oxide modified highly ordered TiO_2 nanotube arrays: enhanced visible light photoelectrochemical properties," *Sci. Adv. Mater.*, vol. 5, no. 9, pp. 1256–1263, 2013.

[151] J. M. Macak, B. G. Gong, M. Hueppe, and P. Schmuki, "Filling of TiO_2 nanotubes by self-doping and electrodeposition," *Adv. Mater.*, vol. 19, no. 19, pp. 3027–3031, 2007.

[152] S. K. Mohapatra, S. Banerjee, and M. Misra, "Synthesis of Fe_2O_3/ TiO_2 nanorod-nanotube arrays by filling TiO_2 nanotubes with Fe," *Nanotechnology*, vol. 19, no. 31, p. 315601–315601, 2008.

[153] X. W. (David) Lou, "TiO_2 nanotube arrays grafted with Fe_2O_3 hollow nanorods as integrated electrodes for lithium-ion batteries," *J. Mater. Chem. A*, pp. 122–127, 2013.

[154] J. E. Herrera, T. T. Isimjan, I. Abdullahi, A. Ray, and S. Rohani, "A novel nanoengineered VO_x catalyst supported on highly ordered TiO_2 nanotube arrays for partial oxidation reactions," *Appl. Catal. A Gen.*, vol. 417, pp. 13–18, 2012.

[155] F. Gobal and M. Faraji, "Fabrication of nanoporous nickel oxide by de-zincification of Zn–Ni/(TiO_2 nanotubes) for use in electrochemical supercapacitors," *Electrochim. Acta*, vol. 100, pp. 133–139, 2013.

[156] G. F. Ortiz, I. Hanzu, P. Lavela, P. Knauth, J. L. Tirado, and T. Djenizian, "Nanoarchitectured TiO_2/SnO_2: A future negative electrode for high power density Li-ion microbatteries," *Chem. Mater.*, vol. 22, no. 5, pp. 1926–1932, Mar. 2010.

[157] M, C. López, G. F. Ortiz, J. R. González, R. Alcántara, J. L. Tirado, "Improving the performance of titania nanotube battery materials by surface modification with lithium phosphate," 2014.

[158] H. Jha, R. Hahn, and P. Schmuki, "Ultrafast oxide nanotube formation on TiNb, TiZr and TiTa alloys by rapid breakdown anodization," *Electrochim. Acta*, vol. 55, no. 28, pp. 8883–8887, 2010.

[159] N. K. Allam, A. J. Poncheri, M. A. El-Sayed, "Vertically oriented Ti-Pd mixed oxynitride nanotube arrays for enhanced photoelectrochemical water splitting.," *ACS Nano*, vol. 5, no. 6, pp. 5056–66, Jun. 2011.

[160] J. Y. Kim, K. H. Lee, J. Shin, S. H. Park, J. S. Kang, K. S. Han, M. M. Sung, N. Pinna, and Y.-E. Sung, "Highly ordered and vertically oriented TiO_2/Al_2O_3 nanotube electrodes for application in dye-sensitized solar cells," *Nanotechnology*, vol. 25, no. 50, pp. 504003–504010, 2014.

[161] N. T. C. Oliveira, J. F. Verdério. C. Bolfarini "Obtaining self-organized nanotubes on biomedical Ti-Mo alloys," *Electrochim. Acta*, vol. 35, no. 2, pp. 139–141, 2013.

[162] I. Paramasivam, Y. C. Nah, C. Das, N. K. Shrestha, and P. Schmuki, "WO_3/TiO_2 nanotubes with strongly enhanced photocatalytic activity," *Chem. Eur. J.*, vol. 16, no. 30, pp. 8993–8997, 2010.

[163] K. S. Raja, M. Misra, "Ordered arrays of Ti-Mn oxide nanotubes for high capacity Li-ion battery," *ECS Trans*. vol. 33, no. 29, pp. 31–44, 2011.

[164] E. Filova, J. Fojt, M. Kryslova, H. Moravec, L. Joska, and L. Bacakova, "The diameter of nanotubes formed on Ti-6Al-4V alloy controls the adhesion and differentiation of Saos-2 cells," *Int. J. Nanomedicine*, vol. 10, pp. 7145–7163, 2015.

[165] M. Yang, G. Yang, E. Spiecker, K. Lee, and P. Schmuki, "Ordered 'superlattice' TiO_2/Nb_2O_5 nanotube arrays with improved ion insertion stability," *Chem. Commun.*, vol. 49, no. 5, pp. 460–462, 2013.

[166] E. D. Stoica, F. Fedorov, M. Nicolae, M. Uhlemann, A. Gebert, and L. Schultz, "Ti6Al7Nb Surface modifications by anodization in electrolysis containing HF," *U.P.B. Sci. Bull., Series B.*, vol. 74, pp. 277–288, 2012.

[167] R. Ummethala, M. Fritzsche, T. Jaumann, J. Balach, S. Oswald, R. Nowak, N. Sobczak, I. Kaban, M. H. Rümmeli, L. Giebeler, "Lightweight, free-standing 3D interconnected carbon nanotube foam as a flexible sulfur host for high performance lithium-sulfur battery cathodes," *Energy Storage Mater.*, 2017.

[168] B. D. Cullity, "*Elements of X-ray diffiraction*," 2nd ed. Addison-Wesley Publishing Company Inc., 1978.

[169] H. M. Rietveld, "A profile refinement method for nuclear and magnetic structures," *J. Appl. Crystallogr.*, vol. 2, no. 2, pp. 65–71, 1969.

[170] H. L. Ma, J. Y. Yang, Y. Dai, Y. B. Zhang, B. Lu, and G. H. Ma, "Raman study of phase transformation of TiO_2 rutile single crystal irradiated by infrared femtosecond laser," *Appl. Surf. Sci.*, vol. 253, pp. 7497–7500, 2007.

[171] S. Brunauer, P. H. Emmett, and E. Teller, "Adsorption of gases in multimolecular layers," *J. Am. Chem. Soc.*, vol. 60, no. 1, pp. 309–319, 1938.

[172] C. Glaize and S. Geniès, "Definitions and Measuring Methods," *Lithium Batter. Other Electrochem. Storage Syst.*, pp. 21–87, 2013.

[173] R. V. Kumar and T. Sarakonsri, "Introduction to electrochemical cells," 2010.

[174] Y. Wang, S. Liu, K. Huang, D. Fang, and S. Zhuang, "Electrochemical properties of freestanding TiO_2 nanotube membranes annealed in Ar for lithium anode material," *J. Solid State Electrochem.*, vol. 16, no. 2, pp. 723–729, 2011.

[175] J. L. Murray, "The Co-Ti (cobalt-titanium) system," *Bull. Alloy Phases Diagrams*, vol. 3, no. 1, pp. 74–85, 1982.

[176] W. G. Burgers, F.M. Jacobs, "Crystal structure of ß-titanium," *Z. Kristallogr.*, vol. 94, pp. 299–300, 1936.

[177] A. V. Skripov, a. L. Buzlukov, a. V. Soloninin, V. I. Voronin, I. F. Berger, T. J. Udovic, Q. Huang, and J. J. Rush, "Hydrogen motion and site occupation in $Ti_2CoHx(D_x)$: NMR and neutron scattering studies," *Phys. B Condens. Matter*, vol. 392, no. 2, pp. 353–360, Apr. 2007.

[178] R. A. Patterson, "Crystal structure of titanium and chromium," *Phys. Rev.*, vol. 26, no. 1, pp. 56–59, 1925.

[179] S. G. Chebotareva, E.S.; Nuzhdina, "Observation of ω-titanium in a composite hard facing alloy based on fine-grain diamonds," *Phys. Met. Metallogr.*, vol. 36, pp. 200–202, 1973.

[180] C. P. Ferreira, M. C. Gonçalves, R. Caram, R. Bertazzoli, and C. a. Rodrigues,

"Effects of substrate microstructure on the formation of oriented oxide nanotube arrays on Ti and Ti alloys," *Appl. Surf. Sci.*, vol. 285, pp. 226–234, Nov. 2013.

[181] V. S. Saji, H. C. Choe, and W. a. Brantley, "Nanotubular oxide layer formation on Ti-13Nb-13Zr alloy as a function of applied potential," *J. Mater. Sci.*, vol. 44, pp. 3975–3982, 2009.

[182] W. G. Kim, H. C. Choe, Y. M. Ko, and W. a. Brantley, "Nanotube morphology changes for Ti-Zr alloys as Zr content increases," *Thin Solid Films*, vol. 517, no. 17, pp. 5033–5037, 2009.

[183] K. Shankar, J. I. Basham, N. K. Allam, O. K. Varghese, G. K. Mor, X. Feng, M. Paulose, J. a Seabold, K.-S. Choi, and C. a Grimes, "Recent advances in the use of TiO_2 nanotube and nanowire arrays for oxidative photoelectrochemistry," *J. Phys. Chem. C*, vol. 113, no. 16, pp. 6327–6359, 2009.

[184] C. A. Zarco V.I. Gette A.V., Kozub G.M. Sushko R.V. "Structural and electrophysical characteristics of titanium-containing silicon dioxide," *Inorg. Mater*, vol. 19, pp. 215–217, 1983.

[185] K. Sakata, "Study of the phase transition in $Nb_xTi_{1-x}O_2$," *Phys. Soc. Japan*, vol. 26, p. 1067, 1969.

[186] J. L. Dorémieux, R. Poilblanc, "Sur la présence de restes acétates dans un composé chimiquement proche de CoO," *Séances Acad. Sci. Série C,* vol. 264, pp. 1278–1281, 1967.

[187] C. Legrand, M. Louis, "Sur les paramètres cristallins du rutile et del'anatase," *C.R. Hebd. Séances Acad. Sci. Série C*, vol. 236, pp. 944–946, 1953.

[188] G. Fierro, M. Lo Jacono, M. Inversi, R. Dragone, and P. Porta, "TPR and XPS study of cobalt–copper mixed oxide catalysts: evidence of a strong Co–Cu interaction," *Top. Catal.*, vol. 10, pp. 39–48, 2000.

[189] D. Barreca, C. Massignan, S. Daolio, M. Fabrizio, C. Piccirillo, L. Armelao, and E. Tondello, "Composition and microstructure of cobalt oxide thin films obtained from a novel cobalt(II) precursor by chemical vapor deposition," *Chem. Mater.*, vol. 13, no. 2, pp. 588–593, 2001.

[190] S. Bauer, S. Kleber, and P. Schmuki, "TiO$_2$ nanotubes: Tailoring the geometry in H$_3$PO$_4$/HF electrolytes," *Electrochem. Commun.*, vol. 8, no. 8, pp. 1321–1325, 2006.

[191] K. Esquivel, M. G. García, F. J. Rodríguez, M. V. González, L. Escobar-Alarcón, L. Ortiz-Frade, and L. a. Godínez, "Titanium dioxide doped with transition metals (M$_x$ Ti$_{1-x}$ O$_2$, M: Ni, Co): synthesis and characterization for its potential application as photoanode," *J. Nanoparticle Res.*, vol. 13, pp. 3313–3325, 2011.

[192] F. Hardcastle, "Raman spectroscopy of titania (TiO$_2$) nanotubular water-splitting catalysts," *J. Ark. Acad. Sci.*, vol. 65, pp. 43–48, 2011.

[193] Y. Yu, J. C. Yu, J. G. Yu, Y. C. Kwok, Y. K. Che, J. C. Zhao, L. Ding, W. K. Ge, and P. K. Wong, "Enhancement of photocatalytic activity of mesoporous TiO$_2$ by using carbon nanotubes," *Appl. Catal. A Gen.*, vol. 289, pp. 186–196, 2005.

[194] C. W. Tang, C. Bin Wang, and S. H. Chien, "Characterization of cobalt oxides studied by FTIR, Raman, TPR and TG-MS," *Thermochim. Acta*, vol. 473, pp. 68–73, 2008.

[195] H. C. Choi, Y. M. Jung, I. Noda, and S. Bin Kim, "A study of the mechanism of the electrochemical reaction of lithium with CoO by two-dimensional soft X-ray absorption spectroscopy (2D XAS), 2D Raman, and 2D heterospectral XAS-Raman correlation analysis," *J. Phys. Chem. B*, vol. 107, pp. 5806–5811, 2003.

[196] M. Koudriachova, N. Harrison, and S. de Leeuw, "Effect of diffusion on lithium intercalation in titanium dioxide," *Phys. Rev. Lett.*, vol. 86, no. 7, pp. 1275–1278, 2001.

[197] D. V. Bavykin, F. C .Walsh, *Titanate and titania nanotubes*. RSC Nanoscience & Nanotechnology no. 12, Cambridge 2010. ISBN: 978-1-84755-910-4.

[198] G. F. Ortiz, I. Hanzu, P. Lavela, P. Knauth, J. L. Tirado, and T. Djenizian, "Nanoarchitectured TiO$_2$/SnO$_2$: A future negative electrode for high power density Li-ion microbatteries," *Chem. Mater.*, vol. 22, no. 5, pp. 1926–1932, 2010.

[199] J. H. Kim, K. Zhu, J. Y. Kim, and A. J. Frank, "Tailoring oriented TiO$_2$ nanotube morphology for improved Li storage kinetics," *Electrochim. Acta*, vol. 88, pp.

123–128, 2013.

[200] K. Zhu, Q. Wang, J. Kim, A. A. Pesaran, and A. J. Frank, "Pseudocapacitive lithium-ion storage in oriented anatase TiO_2 nanotube arrays," *J. Phys. Chem. C*, vol. 116, pp. 11895–11899, 2012.

[201] Z. Lu, C. T. Yip, L. Wang, H. Huang, and L. Zhou, "Hydrogenated TiO_2 nanotube arrays as high-rate anodes for lithium-ion microbatteries," *Chempluschem*, vol. 77, no. 11, pp. 991–1000, 2012.

[202] M. C. Yang, Y. Y. Lee, B. Xu, K. Powers, and Y. S. Meng, "TiO_2 flakes as anode materials for Li-ion-batteries," *J. Power Sources*, vol. 207, pp. 166–172, 2012.

[203] S. Yoon, B. H. Ka, C. Lee, M. Park, and S. M. Oh, "Preparation of nanotube TiO_2-carbon composite and its anode performance in lithium-ion batteries," *Electrochem. Solid-State Lett.*, vol. 12, no. 2, pp. A28–A32, 2009.

[204] E. C. Self, R. Wycisk, and P. N. Pintauro, "Electrospun titania-based fibers for high areal capacity Li-ion battery anodes," *J. Power Sources*, vol. 282, pp. 187–193, 2015.

[205] M. Zou, Z. Ma, Q. Wang, Y. Yang, S. Wu, L. Yang, S. Hu, W. Xu, R. P. S. Han, R. Zou, and A. Cao, "Coaxial TiO_2-carbon nanotube sponges as compressible anodes for lithium-ion batteries," *J. Mater. Chem. A*, vol. 4, pp. 7398–7405, 2016.

[206] K. Hemalatha, a. S. Prakash, G. K, and M. Jayakumar, "TiO_2 coated carbon nanotubes for electrochemical energy storage," *J. Mater. Chem. A*, vol. 2, no. 6, p. 1757–1766, 2014.

[207] J. Liu, H. Feng, J. Jiang, D. Qian, J. Li, S. Peng, and Y. Liu, "Anatase-TiO_2/CNTs nanocomposite as a superior high rate anode material for lithium-ion batteries," *J. Alloys Compd.*, vol. 603, pp. 144–148, 2014.

[208] J. Wang, R. Ran, M. O. Tade, and Z. Shao, "Self-assembled mesoporous TiO_2/carbon nanotube composite with a three dimensional conducting nanonetwork as a high-rate anode material for lithium-ion battery," *J. Power Sources*, vol. 254, no. 5, pp. 18–28, 2014.

[209] N. T. H. Trang, Z. Ali, and D. J. Kang, "Mesoporous TiO_2 spheres interconnected by multiwalled carbon nanotubes as an anode for high-performance lithium ion batteries," *ACS Appl. Mater. Interfaces*, vol. 7, no. 6, pp. 3676–3683, 2015.

[210] P. Zhu, Y. Wu, M. V. Reddy, A. Sreekumaran Nair, B. V. R. Chowdari, and S. Ramakrishna, "Long term cycling studies of electrospun TiO_2 nanostructures and their composites with MWCNTs for rechargeable Li-ion batteries," *RSC Adv.*, vol. 2, no. 2, pp. 531–537, 2012.

[211] Y. Peng, Z. Chen, Z. Le, Q. Xu, H. Li, and Y. Lu, "Mesoporous crystalline amorphous oxide nanocomposite network for high performance lithium storage," *Chem. Commun.*, vol. 51, no. 60, pp. 12056–12059, 2015.

[212] K. Roy, D. J. Smith, R. Vajtai, B. G. Sumpter, V. Meunier, H. Terrones, M. Terrones, and P. M. Ajayan, "Covalently bonded three-dimensional carbon nanotube solids via boron induced nanojunctions," *Sci. Rep.*, vol. 2, no. 363, pp. 1–8, 2012.

[213] Z. Wen, S. Ci, S. Mao, S. Cui, G. Lu, K. Yu, S. Luo, Z. He, and J. Chen, "TiO_2 nanoparticles-decorated carbon nanotubes for significantly improved bioelectricity generation in microbial fuel cells," *J. Power Sources*, vol. 234, pp. 100–106, 2013.

[214] L. W. Zhu, L. K. Zhou, H. X. Li, H. F. Wang, and J. P. Lang, "One-pot growth of free-standing $CNTs/TiO_2$ nanofiber membrane for enhanced photocatalysis," *Mater. Lett.*, vol. 95, pp. 13–16, 2013.

[215] R. Kumar and S. B. Cronin, "Raman scattering of carbon nanotube bundles under axial strain and strain-induced debundling," *Phys. Rev. B - Condens. Matter Mater. Phys.*, vol. 75, no. 15, pp. 1–4, 2007.

[216] H. C. Choi, Y. M. Jung, I. Noda, and S. Bin Kim, "A study of the mechanism of the electrochemical reaction of lithium with CoO by two-dimensional soft X-ray absorption spectroscopy (2D XAS), 2D Raman, and 2D heterospectral XAS-Raman correlation analysis," *J. Phys. Chem. B*, vol. 107, pp. 5806–5811, 2003.

[217] V. Likodimos, T. Stergiopoulos, P. Falaras, J. Kunze, and P. Schmuki, "Phase composition, size, orientation, and antenna effects of self-assembled anodized

titania nanotube arrays: A polarized micro-raman investigation," *J. Phys. Chem. C*, vol. 112, no. 33, pp. 12687–12696, 2008.

[218] C. Rüdiger, M. Favaro, C. Valero-Vidal, L. Calvillo, N. Bozzolo, S. Jacomet, C. Hejny, L. Gregoratti, M. Amati, S. Agnoli, G. Granozzi, and J. Kunze-Liebhäuser, "Fabrication of Ti substrate grain dependent C/TiO$_2$ composites through carbothermal treatment of anodic TiO$_2$," *Phys. Chem. Chem. Phys.*, vol. 18, no. 13, pp. 9220–9231, 2016.

[219] J. K. Burdett, T. Hughbanks, G.J. Miller, J.W. Richardson, "Structural-electronic relationships in inorganic solids: Powder neutron diffraction studies of the rutile and anatase polymorphs of titanium dioxide at 15 and 295 K," *J. Am. Chem. Soc*, vol. 109, pp. 3639–3646, 1987.

[220] R.D. Shannon, "Kinetics of the anatase-rutile transformation," *J. Am. Cer. Soc.*, vol. 48, pp. 391–398, 1965.

[221] M. Madian, M. Klose, T. Jaumann, A. Gebert, S. Oswald, N. Ismail, A. Eychmüller, J. Eckert, and L. Giebeler, "Anodically fabricated TiO$_2$–SnO$_2$ nanotubes and their application in lithium ion batteries," *J. Mater. Chem. A*, vol. 2, pp. 5542–5552, 2016.

[222] M. Xie, X. Sun, C. Zhou, A. S. Cavanagh, H. Sun, T. Hu, G. Wang, J. Lian, and S. M. George, "Amorphous ultrathin TiO$_2$ atomic layer deposition films on carbon nanotubes as anodes for lithium ion batteries," *J. Electrochem. Soc.*, vol. 162, no. 6, pp. A974–A981, 2015.

[223] R. T. Wen, G. A. Niklasson, and C. G. Granqvist, "Eliminating electrochromic degradation in amorphous TiO$_2$ through Li-ion detrapping," *ACS Appl. Mater. Interfaces*, vol. 8, no. 9, pp. 5777–5782, 2016.

[224] P. Kubiak, M. Pfanzelt, J. Geserick, U. Hörmann, N. Hüsing, U. Kaiser, and M. Wohlfahrt-Mehrens, "Electrochemical evaluation of rutile TiO$_2$ nanoparticles as negative electrode for Li-ion batteries," *J. Power Sources*, vol. 194, no. 2, pp. 1099–1104, 2009.

[225] S. Ding, J. S. Chen, and X. W. D. Lou, "One-dimensional hierarchical structures

composed of novel metal oxide nanosheets on a carbon nanotube backbone and their lithium-storage properties," *Adv. Funct. Mater.*, vol. 21, no. 21, pp. 4120–4125, 2011.

[226] D. Guan, C. Cai, and Y. Wang, "Amorphous and crystalline TiO_2 nanotube arrays for enhanced Li-ion intercalation properties," *J. Nanosci. Nanotechnol.*, vol. 11, no. 4, pp. 3641–3650, 2011.

[227] H. Xiong, H. Yildirim, E. V Shevchenko, V. B. Prakapenka, B. Koo, M. D. Slater, M. Balasubramanian, S. K. R. S. Sankaranarayanan, P. Greeley, S. Tepavcevic, N. M. Dimitrijevic, P. Podsiadlo, C. S. Johnson, and T. Rajh, "Self-improving anode for lithium-ion batteries based on amorphous to cubic phase transition in TiO_2 nanotubes," *J. Phys. Chem. C*, pp. 3181–3187, 2012.

[228] H. Okamoto, "Sn-Ti (Tin-Titanium)," *J. Phase Equilibria Diffus.*, vol. 31, no. 2, pp. 202–203, 2010.

[229] I. Szanto, "The determination of high-purity a-titanium lattice parameters," *Acta Tech. Acad. Sci. Hungaricae*, vol. 13, pp. 363–372, 1955.

[230] H. W. Worner, " The structure of titanium-tin alloys in the range 0-25 atomic % tin," *J. Inst. Met.*, vol. 81, pp. 521–528, 1953.

[231] G. K. Mor, O. K. Varghese, M. Paulose, and C. A. Grimes, "Transparent highly ordered TiO_2 nanotube arrays via anodization of titanium thin films," *Adv. Funct. Mater.*, vol. 15, no. 8, pp. 1291–1296, 2005.

[232] S. P. Albu, D. Kim, and P. Schmuki, "Growth of aligned TiO_2 bamboo-type nanotubes and highly ordered nanolace," *Angew. Chemie Int. Ed.*, vol. 47, no. 10, pp. 1916–1919, 2008.

[233] D. Kim, A. Ghicov, and P. Schmuki, "TiO_2 nanotube arrays: Elimination of disordered top layers ('nanograss') for improved photoconversion efficiency in dye-sensitized solar cells," *Electrochem. Commun.*, vol. 10, no. 12, pp. 1835–1838, 2008.

[234] L. V. Taveira, J. M. Macak, K. Sirotna, L. F. P. Dick, and P. Schmuki, "Voltage oscillations and morphology during the galvanostatic formation of self-organized TiO_2 nanotubes," *J. Electrochem. Soc.*, vol. 153, no. 4, pp. B137–B143,

2006.

[235] X. Liu, J. Zhang, W. Si, L. Xi, S. Oswald, C. Yan, and O. G. Schmidt, "High-rate amorphous SnO_2 nanomembrane anodes for Li-ion batteries with a long cycling life," *Nanoscale*, vol. 7, pp. 282–288, 2015.

[236] S. Sreekantan, K. A. Saharudin, Z. Lockman, and T. W. Tzu, "Fast-rate formation of TiO_2 nanotube arrays in an organic bath and their applications in photocatalysis.," *Nanotechnology*, vol. 21, no. 36, p. (365603) P1-P8, 2010.

[237] J. Lin, J. Chen, X. Chen, "Facile fabrication of free-standing TiO_2 nanotube membranes with both ends open via self-detaching anodization," *Electrochem. Commun.*, vol. 12, no. 8, pp. 1062–1065, 2010.

[238] Q. L. Wu, J. Li, R. D. Deshpande, N. Subramanian, S. E. Rankin, F. Yang, Y. Cheng, "Aligned TiO_2 nanotube arrays as durable lithium-ion battery negative electrodes," *J. Phys. Chem. C,* vol. 116, pp. 18669–18677 2012.

[239] N. Li and C. R. Martin, "A high-rate, high-capacity nanostructured Sn-based anode prepared using sol-gel template synthesis," *J. Electrochem. Soc.*, vol. 148, no. 2, pp. A164–A170, 2001.

[240] T. Jaumann, J. Balach, M. Klose, S. Oswald, U. Langklotz, A. Michaelis, J. Eckert, and L. Giebeler, "SEI-component formation on sub 5 nm sized silicon nanoparticles in Li-ion batteries: The role of electrode preparation, FEC addition and binders," *Phys. Chem. Chem. Phys.*, vol. 17, no. 38, pp. 24956–24967, 2015.

List of figures

Glossary

PV systems	Photovoltaic systems
EVs	hybrid or electric powered vehicles
SEI	Solid electrolyte interface
LIBs	Lithium ion batteries
CNTs	Carbon nanotubes
ALD	Atomic layer deposition
BET	Brunauer-Emmett-Teller
EC	Ethylene carbonate
0D	Zero-dimensional
1D	One-dimensional
2D	Two-dimensional
3D	Three-dimensional
RGO	Reduced graphene oxide
NT	Nanotube

NTs	Nanotubes
EIS	Electrochemical Impedance Spectroscopy
EC	Ethylene carbonate
DMC	Dimethyl carbonate
LP30	1 M solution of $LiPF_6$ in EC:DMC 1:1
DC	Direct current
XRD	X-ray diffraction
SEM	Scanning electron microscopy
EDXS	Energy-dispersive X-ray spectroscopy
FESEM	Field-emission scanning electron microscopy
HRSEM	high resolution scanning electron microscopy
XPS	X-ray photoelectron spectroscopy
TEM	Transmission electron microscopy
HRTEM	High resolution transmission electron microscopy
A.h	Ampere-hour
BE	Binding energy
eV	Electron volt
S_{BET}	Specific surface area
CE	Coulombic efficiency

List of Publications

- **Peer-review papers originated from this work**

  Published

  1. **M. Madian**, R. Ummethala, A. O. Abo El Naga, N. Ismail, M. H. Rümmeli, A. Eychmüller, L. Giebeler. *Ternary CNTs@TiO$_2$/CoO Nanotube Composites: Improved Anode Materials for High Performance Lithium Ion Batteries.* Materials, 10, 678 (2017), $1 - 13$.

  2. **M. Madian**, M. Klose, T. Jaumann, A. Gebert, S. Oswald, N. Ismail, J. Eckert, A. Eychmüller, L. Giebeler. *Anodically fabricated TiO$_2$-SnO$_2$ nanotubes and their application in lithium ion batteries.* Journal of Materials Chemistry A, 4 (2016) 5542 $- 5552$.

  3. **M. Madian**, L. Giebeler, M. Klose, T. Jaumann, M. Uhlemann, A. Gebert, S. Oswald, N. Ismail, A. Eychmüller, J. Eckert. *Self-organized TiO$_2$/CoO nanotubes as potential anode materials for lithium ion batteries.* ACS Sustainable Chemistry & Engineering, 3, 5 (2015) 909-919.

- **Other peer-review papers**

    4. N. Ismail, **M. Madian**, M. S. El-Shall. *Reduced Graphene Oxide doped with Ni/Pd nanoparticles for Hydrogen storage application.* Journal of Industrial and Engineering Chemistry, 30 (2015) 328-335.

    5. A. El-Meligi, **M. Madian**, N. Ismail. *Fabrication and Characterization Single Crystal of FePS₃ Layered Material.* International Advanced Research Journal in Science, Engineering and Technology, 2, 12 (2015) 117-120.

    6. N. Ismail, **M. Madian**, A. El-Meligi. *Synthesis of NiPS₃ and CoPS and its hydrogen storage capacity.* Journal of Alloys and Compounds, 588 (2014) 573 - 577.

    7. A. El-Meligi, N. Ismail, **M. Madian**. *Characterizing Layered Structure of MgPS₃ and New Application as a Hydrogen Storage Material.* International Journal of Nanopatricles, 4, 4 (2011) 326 -335.

    8. A. El-Meligi, N. Ismail, **M. Madian**. *Synthesis and Characterization of FePS₃ for Hydrogen Uptake.* International Journal of Hydrogen Energy, 35(2010) 7827 -7834.

    9. N. Ismail, Y. M. Temerk, A. A. El-Meligi, M.A.Badr, **M.Madian.** *Synthesis and characterization of MnPS₃ for hydrogen sorption.* Journal of Solid State Chemistry,183(2010) 984-987.

- **Book**

    - **M. Madian**, N. Ismail, A. A. El-Meligi. *Layered Chalcogenides for Hydrogen Storage*, LAP LAMBERT Academic Publishing GmbH & Co. KG, Germany (2012), ISBN- 978-3-659-17084-3.

Curriculum Vitae

Date, Place of birth	1st of January 1983, in Asiut, Egypt.
Citizenship	Egyptian
Experience	**April 2013 – present**
	PhD studies at Electrochemical energy storage group (IFW Dresden),

- Fabrication of highly ordered and well-aligned mixed transition metal oxide nanotubes by anodic oxidation
- Assembly and construction of lithium ion batteries from novel TiO_2-based anodes

July 2008 – October 2012

Researcher assistant at the Physical Chemistry Department, National Research Centre, Egypt.

July 2009 – October 2009

Short-term internship (three months), Chemistry Department, Virginia Commonwealth University, USA,

Education

May 2004

B.Sc. Chemistry Department, Alazhar University, Asiut, Egypt

Grade: *Excellent*.

May 2007

Pre-Master Courses in Non Organic Chemistry, Asiut University, Egypt

June 2010

Master Degree in Non Organic Chemistry, Asuit University, Egypt.

Awards

- PhD stipend from DAAD (German Academic Exchange Service) 2012.
- Misr El-khair Foundation award for the best publications 2010.

Languages   Arabic (mother tongue), English, German (basics).

• Attended conferences and research schools

- **International Conference Materials Science Engineering,** Darmstadt, Germany, 23-25.09.2014.
- **DAAD-scholarship holders Meeting,** Chemnitz, Germany, 22-24.03.2013.
- **4th International IUPAC Conference on Green Chemistry,** Foz do Igua¸cu, PR, Brazil, 25-29.08.2012.

- **3th Annual International workshop on Advanced Materials (IWAM2011)** Ras Elkhima, United Arab Emirates, 20-22.02.2011.

- **US-Egypt (ASI) "Nanomaterials and Nanocatalysis for Energy, Petrochemicals and Environmental Application",** Cairo, Egypt, 28.03-04.04.2010.

- **American Chemical Society, ACS National Meeting& Exposition ,** Washington DC, USA, 16.2-20.08.2009.

- **Material Science and Nanotechnology "Future Challenges" ,**Cairo, Egypt, 2-4.12.2008.

Acknowledgement

First and foremost, all thanks and appreciation to Allah (God) for providing me the power, patience and the motivation to accomplish this thesis. This dissertation would not have been possible without the guidance, supports and encouragements from many people whose extended their valuable assistance in the preparation and completion of this study.

Special gratitude and sincere thanks go to my Father, Mother, brothers and sisters for their unfailing emotional support, supplication, pray and good wishes. Thank you my beloved family, Samar, Muaz and Leen for your joyfulness, love, encouragement, patience and the time for making me carefree.

I am deeply indebted to Dr. Lars Giebeler for his day to day supervision of the work during my PhD. His worthy guidance, fruitful discussions, patient explanations, brilliant suggestions and encouragements along with his passionate interest in my results helped me a lot to jump over many challenges and obstacles I faced.

Eidesstattliche Erklärung

Hiermit versichere ich, dass ich die vorliegende Arbeit ohne unzulässige Hilfe Dritter und ohne Benutzung anderer als der angegebenen Hilfsmittel angefertigt habe, die aus fremden Quellen direkt oder indirekt übernommenen Gedanken sind als solche kenntlich gemacht. Die Arbeit wurde bisher weder im Inland noch im Ausland in gleicher oder ähnlicher Form einer anderen Prüfungsbe- hörde vorgelegt. Diese Arbeit wurde unter Betreuung von Prof. Dr. Alexander Eychmüller am Physikalische Chemie. Es haben keine früheren erfolglosen Promotionsverfahren stattgefunden. Ich erkenne hiermit die Promotionsordnung der Fakultät Mathematik und Naturwissenschaften der Technischen Universität Dresden vom 23.02.2011 an.

Mahmoud MADIAN

Dresden, Juli 24, 2017